

Morphological evolution of galaxies over the last 8 billion years

Maurilio Pannella



München 2007

Morphological evolution of galaxies over the last 8 billion years

Maurilio Pannella

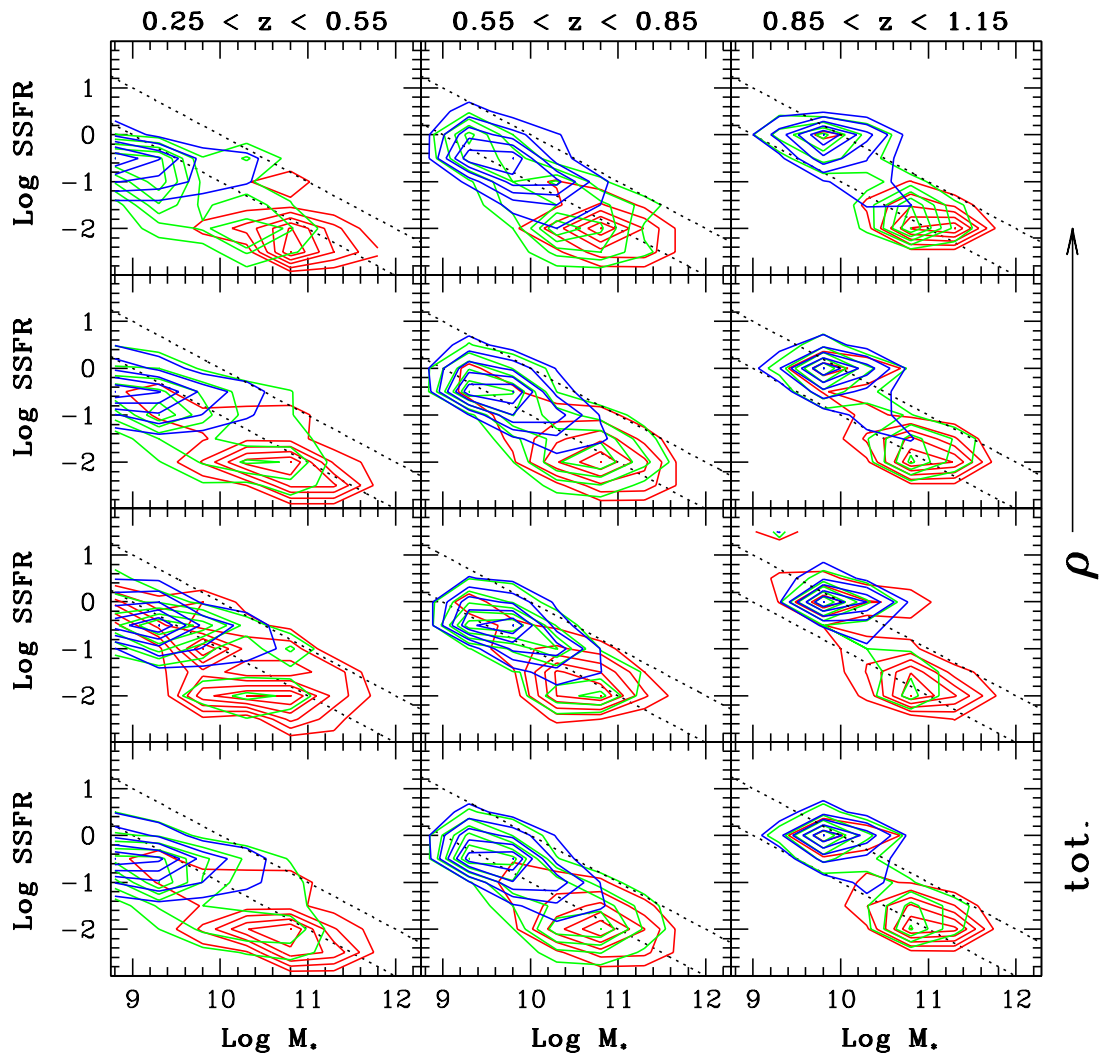
Dissertation
an der Fakultät für Physik
der
Ludwig-Maximilians-Universität München

vorgelegt von Maurilio Pannella
aus Turin (Italien)

München, den 1 August 2007

Erstgutachter: Prof. Dr. Ralf Bender
Zweitgutachter: Prof. Dr. Hans Böhringer
Tag der mündlichen Prüfung: 18. September 2007

Morphological evolution of galaxies over the last 8 billion years



Maurilio Pannella

*“... benvenuto raggio di sole, avrai matite per giocare
e un bicchiere per bere forte, e un bicchiere per bere piano
un sorriso per difenderti
e un passaporto per andare via lontano ...
... benvenuto figlio di nessuno, benvenuto in questo paese.”*

Contents

Zusammenfassung (Summary in German)	5
Summary	9
1 Galaxy formation and evolution in the cosmological framework	13
1.1 The hierarchical Universe	13
1.2 The formation and evolution of galaxies	15
1.2.1 Morphological properties	17
1.2.2 Star formation and colors	21
1.2.3 The Cosmic Star Formation History and Mass assembly	21
1.2.4 The Environmental dependence of galaxy evolution	24
1.3 This Thesis	26
2 Observing the coloured Universe: the large deep surveys	29
2.1 The FORS Deep Field	30
2.1.1 Source detection and multi-band photometry	30
2.1.2 Photometric redshifts in the FORS Deep Field	32
2.2 The Great Observatories Origins Deep Survey South Field	34
2.2.1 A Ks-band selected galaxy sample in GOODS-S	35
2.2.1.1 Source detection and multi-band photometry	35
2.2.1.2 Photometric redshift	38
2.2.1.3 Source catalogue	44
2.2.1.4 Redshift distribution	47
2.3 The Cosmic Evolution Survey	49
2.3.1 A deep galaxy catalogue in the COSMOS field	49
2.3.1.1 NIR imaging data: acquisition	50
2.3.1.2 NIR imaging data: reduction, photometry and cataloging	51
2.3.1.3 The i-selected catalogues	54
2.3.1.4 Spectroscopic redshifts	58
2.3.1.5 Photometric redshifts	60
3 Morphological characterization of high redshift galaxies	65

Contents

3.1	The Advanced Camera for Surveys on board the HST	65
3.2	The morphological analysis	68
3.2.1	GIM2D	68
3.2.2	PSF influence on the morphological parameters	69
3.2.3	Results on the overlapping COSMOS ACS tiles	69
3.2.4	Results on simulated objects	70
3.2.5	GIM2D vs. GALFIT	71
3.2.6	Parametric profile fitting versus visual classification	73
4	Morphological evolution in FDF and GOODS-S	77
4.1	Introduction	78
4.2	Ground-based data, photo-z and M _* /L ratios	79
4.3	HST imaging and the morphological analysis	80
4.4	Evolution of the morphological mass function, total mass density and SSFR	81
4.5	Conclusions	85
5	Bulges and disks in the last 8 Gyrs of the COSMOS	87
5.1	Ground-based data and photometric redshifts	90
5.2	Computing mass-to-light ratios	91
5.3	HST Advanced Camera for Surveys imaging	94
5.3.1	Sources extraction, star-galaxy classification and cataloging	95
5.4	The morphological analysis	95
5.5	The evolution of the morphological mass function and mass density	97
5.6	A hole in the sky at z~0.5	100
5.7	The environmental effect on morphological evolution	101
5.7.1	8 Giga years of morphology density relation	104
5.8	Red sequence and blue cloud up to redshift 1.15	104
5.9	The specific star formation rate in the last 8 Gyrs	106
5.10	The ages of early-type objects in different environments	110
5.11	Discussion and conclusions	111
6	Further work	115
6.1	The dark side of star formation: chasing the dusty Universe	116
6.1.1	The GOODS-S test	116
6.2	Field to Clusters variation	118
6.2.1	Virial masses of cluster galaxies through scaling relations	118
6.3	The UV morphology of high redshift star forming galaxies	122
6.3.0.1	Analysis of the UV morphology of high redshift galaxies	123
6.3.0.2	Morphological properties and extinction curve	124
6.4	The star formation rate history	126
6.4.1	The Star Formation Rate	127

Contents

6.4.2	Conclusions	131
6.5	The stellar mass function of galaxies to $z \sim 5$	131
6.5.1	The stellar mass function	134
6.5.2	Stellar mass density and number densities	135
6.6	The supermassive black hole in NGC 4486a	137
	References	139

Contents

Zusammenfassung

Der Schwerpunkt dieser Arbeit lag in der Untersuchung der Entstehung und Entwicklung von Feldgalaxien auf Grundlage von Beobachtungen.

Mit Hilfe von weiträumigen und tiefen Durchmusterungen habe ich die Entstehungs geschichte von Galaxien bzgl. ihrer stellaren Materie, die Entwicklung ihrer strukturellen Eigenschaften und die gesamtheitliche Entwicklung des Aufbaus stellarer Materie im Universum untersucht.

In kürzlich veröffentlichter Arbeit haben meine Mitarbeiter und ich zeigen können, dass schon bei $z \approx 1$ - d.h. als das Universum nur halb so alt war wie heute - etwa die Hälfte der heute existierenden Sterne vorhanden waren. Wir haben bestätigt, dass die Entwicklungs geschichte von Galaxien durch ihre Masse beeinflusst ist. Massereichere Objekte haben den Großteil ihrer stellaren Materie früher aufgebaut als entsprechend masseärmere Objekte, ein Phänomen das gemeinhin als *downsizing scenario* bezeichnet wird.

Trotz der Erfolge der vergangenen Jahre sind die vorliegenden Daten noch nicht in der Lage die heutigen, hierarchischen Modelle der Galaxienentwicklung mit Sicherheit zu bestätigen oder zu widerlegen. Hierarchische Modelle versuchen die beobachteten Eigen schaften von Galaxien im Rahmen der hierarchisch gewachsenen Strukturen Dunkler Mate rie, die in kosmologischen N-Körper-Simulationen beobachtet werden, zu verstehen. Hierzu müssen vereinfachende - jedoch physikalisch und aus Beobachtungen motivierte - Annah men über die Entwicklung der diffusen baryonischen Komponente gemacht werden. Laut dieser Modelle entstehen zum einen massereiche Galaxien durch Verschmelzung kleinerer Objekte, zum anderen werden Bulge-dominierte Galaxien durch Verschmelzungen aus Scheiben oder durch dynamische Instabilitäten gebildet. Daher ist zu erwarten, dass gleichzeitig die Zahl der extrem massereichen Objekte sowie die Anzahl der Bulge-dominierten Galaxien mit zunehmender Rotverschiebung abnehmen.

Aus diesem Grund stellt neben der Entwicklung der Masse die Untersuchung der Struktur von Galaxien als Funktion der Rotverschiebung einen wichtigen Test der hierarchischen Modelle dar.

So ist das Ziel meiner Arbeit dem weitgehend akzeptierten *downsizing scenario* eben diese strukturellen Charakterisierungen hinzuzufügen.

In der Anfangsphase meiner Arbeit war ich an dem Aufbau von tiefen Multiwellenlängen Katalogen beteiligt, die sich als wichtige Grundlage für aktuelle extragalaktische Astronomie erwiesen haben. Die vorliegende Arbeit macht intensiv Gebrauch von solchen Katalogen.

Zusammenfassung

Sie erlauben die Bestimmung photometrischer Rotverschiebungen, stellaren Massen und der Entwicklung von Sternentstehungsraten der katalogisierten Galaxien. Natürlich ist die Genauigkeit der abgeleiteten Eigenschaften dabei eine direkte Folge der Sorgfalt mit der diese Kataloge erstellt wurden.

Unter Verwendung von hochauflösenden HST/ACS Bildern habe ich eine parametrische, morphologische Analyse für große, tiefe Stichproben von Galaxien aus dem Forn Deep Field (FDF), dem GOODS-South Feld und dem Cosmic Evolution Survey (COSMOS) durchgeführt. Die zweidimensionale Flächenhelligkeitsverteilung jeder Galaxie wurde jeweils durch ein Sérsic-Profil, welches mit der entsprechenden Punktverbreiterungsfunktion (PSF) des Bildes gefaltet wurde, modelliert. Hierbei habe ich großes Gewicht auf die Absicherung der Zuverlässigkeit und Robustheit der Methode gelegt. Zum einen wurden systematische Effekte wie zum Beispiel die Variation des Signal-zu-Rausch-Verhältnisses oder der PSF über das Sichtfeld und zum anderen die Zuverlässigkeit der verwendeten Software und Klassifikationsmethoden einer genaueren Betrachtung unterzogen. Die Ergebnisse verschiedener Algorithmen und klassischer visueller Klassifikation wurden detailliert verglichen. Simulierte Bilder mit den gleichen Charakteristiken wie denen von echten Daten wurden mit genau denselben Methode untersucht, um eine Aussage über die Zuverlässigkeit der ermittelten Ergebnisse treffen zu können.

Wie oben dargestellt, werden neben einer zuverlässigen morphologischen Charakterisierung außerdem die stellaren Massen der Galaxien benötigt. Diese habe ich auf Grundlage der Multiwellenlängen-Kataloge durch Anpassung von Modellen zur stellaren Populationssynthese an die spektralen Energieverteilungen (SEDs) der Galaxien abgeleitet. Durch Gegenüberstellung der Ergebnisse der morphologischen Untersuchung zum einen und der stellaren Massen zum anderen konnte ich die Entwicklung der stellaren Massendichten für verschiedene Klassen von Galaxien untersuchen: In Abhängigkeit von ihrem Sérsic-index n wurden die Galaxien als "frühe" ($n > 3.5$), "mittlere" ($2 < n < 3.5$) oder "späte" Typen ($n < 2$) klassifiziert.

Einige andere Arbeiten haben sich kürzlich mit der Gegenüberstellung der Entwicklung von Morphologie und stellarer Masse als Funktion der Rotverschiebung beschäftigt. Während dies in vergleichbarer Art und Weise wie in der vorliegenden Arbeit geschah, sind all diese Arbeiten auf Grund der relativ kleinen Felder der meisten tiefen Durchmusterungen potentiell durch kosmische Varianz betroffen. Aus diesem Grund widmete ich mich in dem letzten Teil meiner Arbeit einer Studie im COSMOS-Feld. Auf Grund seiner nie zuvor erreichten Fläche und Tiefe erlaubt COSMOS systematische Effekte der kosmischen Varianz auszuschließen.

Darüber hinaus erlaubte die große Anzahl von Galaxien in COSMOS erstmals die Entkopplung der Effekte des Umfeldes der Galaxien auf ihre Entwicklung für eine große, homogene Menge von Feld-Galaxien. So war es mir möglich die Entwicklung der stellaren Massen in drei verschiedenen Kategorien des Umfeldes bzgl. der lokalen Massenhäufung (unterdicht, durchschnittlich und überdicht) zu untersuchen.

Die Definition einer "Übergangsmasse" erlaubte die Quantifizierung der relativen Beiträge

von Galaxien unterschiedlichen Morphologischen Typs zur Massenfunktion. Die Übergangsmasse wurde für jede Rotverschiebung definiert als diejenige Masse bei der der Übergang vom Bulge- zu Scheiben-dominierten Massenbudget stattfindet. Die Untersuchung der Entwicklung mit der Rotverschiebung hat eine monotone Entwicklung mit der Zeit ergeben: Je größer die Rotverschiebung, desto stärker ist die Gesamtmasse durch Scheibensysteme dominiert. Während bei einer Rotverschiebung von $z \sim 0.7$ der Wert der Übergangsmasse ungefähr dem heutigen Wert entspricht, so tragen bei $z \sim 1$ Galaxien frühen und späten Typs im annähernd gleichen Maße zur Gesamtmasse bei.

Der Verlauf der stellaren Massenfunktion von Scheiben-dominierten Galaxien erscheint konstant bzgl. der Rotverschiebung. Die Anzahl der Scheibengalaxien nimmt im Massebereich von $\log M_* = 10.6$ bis $\log M_* = 12$ um mehr als eine Größenordnung ab. Dahingegen ist die Massenfunktion von Bulge-dominierten Galaxien ungefähr flach. Die Anzahldichte der Galaxien erscheint also konstant bzgl. ihrer Masse. Der Normierungswert dieser Massenfunktion scheint jedoch mit zunehmender Rotverschiebung kontinuierlich abzunehmen. Aus der Steigung der Massenfunktion von Scheiben-dominierten Galaxien zum einen und der Änderung der Gesamtzahl von Bulge-dominierten Galaxien bei ungefähr flacher Massenfunktion zum anderen resultiert in natürlicher Weise die beschriebene Entwicklung der Übergangsmasse mit der Rotverschiebung.

Meine Untersuchungen haben ergeben, dass bei $z \sim 1$ die in massereichen Objekte enthaltene stellare Masse ungefähr halb so groß war wie die in massiven Objekten enthaltene Masse im lokalen Universum. Dabei entwickelt sich nicht die Form der Massenfunktion sondern ihre Normalisierung.

Erstmalig habe ich die Entwicklung der spezifischen Sternentstehungsrate (SSFR), also der Sternentstehungsrate pro stellaren Einheits-Masseintervall, als Funktion des morphologischen Typs und der Umgebung untersucht. Es hat sich ergeben, dass die Positionen von Galaxien frühen und späten Typs in der stellaren Masse–SSFR–Ebene für alle Rotverschiebungen unterschiedlich sind. Galaxien mittleren Typs fallen dabei zwischen diese beiden Regionen, was ihre Natur als Übergangsobjekte bestätigt. Galaxien frühen und späten Typs weisen einen signifikanten Unterschied in der Masse auf: Scheibengalaxien dominieren die Systeme mit niedrigen Massen, während Galaxien frühen Typs das massenreiche Ende dominieren. Galaxien frühen Typs sind also maßgeblich für die Abnahme der Sternentstehungsrate in massereichen Objekten von Rotverschiebung 1 bis zum lokalen Universum verantwortlich. Während dieses generelle Bild für alle Umgebungen ähnlich zu sein scheint, existiert in Umgebungen von geringer Massendichte eine Population von relativ massereichen Galaxien frühen Typs mit großen SSFRs und blauen Farben.

All dies weist in Richtung eines Szenarios, in dem massereiche Objekte ihre Massen von $z \sim 1$ bis 0 annähernd verdoppeln und zunehmend Bulge-dominieren werden. Durch Bestimmung der Sternentstehungsraten konnte ich zeigen, dass *in situ* Sternentstehung nicht ausreichend ist, um die Entwicklung des Massenbudgets in massiven Galaxien zu erklären. Hieraus schließe ich, dass Verschmelzungen oder noch wahrscheinlicher die Einverleibung vieler kleinerer Objekte durch größere eine Schlüsselrolle im “Massenfluss” von Scheiben-

Zusammenfassung

zu Bulge-dominierten Systemen spielen.

Wie schon oben beschrieben erlaubte die große Fläche von COSMOS die Untersuchung des Einflusses der lokalen Massendichte auf die Eigenschaften der Galaxien. Ich konnte die bereits etablierte Morphologie-Massendichte-Beziehung für alle Rotverschiebungen bestätigen: Lokal überdichte Regionen enthalten einen relativ größeren Anteil von Bulges gegenüber Regionen mit niedrigerer lokaler Massendichte.

Schließlich konnte ich Dank des sehr homogenen COSMOS Datensatzes das Alter von massereichen Galaxien frühen Typs als Funktion der lokalen Massendichte untersuchen. Die Altersverteilung weist signifikant unterschiedliche Mittelwerte für alle Rotverschiebungen auf. Die Untersuchungen in dieser Arbeit bestätigen die Ergebnisse anderer aktueller Studien. Unser Ergebnis zeigt, dass sich junge (blaue), massereiche Galaxien frühen Typs vorzugsweise in Umgebungen mit niedriger lokaler Massendichte aufhalten, wohingegen diejenigen Galaxien, die die ältesten Sterne beherbergen, sich vorzugsweise in Regionen mit großer lokaler Massendichte aufhalten. Nichtsdestotrotz weisen die meisten Systeme frühen Typs ähnliche charakteristische Alter, Farben und SSFRs auf, was auf einen ähnlichen Entstehungszeitpunkt schließen lässt.

Summary

This thesis work has been focused on the formation and evolution of field galaxies from an observational perspective.

I have used large deep surveys to study the mass assembly history of galaxies, the evolution of their structural properties, and the history of star formation in the Universe.

In recent work, my collaborators and I have shown that about half of the present day stars were already in place at $z \approx 1$, i.e. when the age of the Universe was half of its present value. We have also confirmed that galaxy evolution depends on mass, more massive objects having assembled the bulk of their stellar mass earlier than their lower mass counterparts. This behavior is commonly termed as *the downsizing scenario*.

Despite continuous progress has been made in the last years, present data are not yet able to put firm constraints on current models of galaxy formation and evolution within the hierarchical paradigm. These latter try to link the hierarchical growth of dark matter structures derived using cosmological N-body simulations to the observed galaxy properties, by means of simplified, yet physically and/or observationally motivated assumptions about the evolution of the diffuse baryonic component. According to these models not only massive galaxies form by merging of smaller ones, but also bulge dominated galaxies form from disks, either through mergers or by dynamical instabilities. Therefore, at the same time, both the number density of the most massive objects and the fraction of bulge-dominated galaxies are expected to decrease at high redshift.

For this reason, effective constraints can be put on such models if, beside the study of the redshift evolution of the galaxy stellar mass function, one is able to understand where the stars were located at different look-back times, in other words what was the morphology of their host galaxies.

This has been the main aim of my thesis work, namely the addition of a morphological characterization to the well established *downsizing* scenario.

During the first stages of my PhD research, I have been involved in the build-up of deep multiwavelength catalogs, which turn out to be an essential tool of modern extragalactic astronomy. Such catalogs are the fundamental basis of all the work presented in this Thesis. They allow to estimate photometric redshifts, stellar masses and star formation histories for each galaxy in the catalog. The attention which is put in producing catalogs in a careful way, directly reflects in the accuracy of the derived galaxy properties.

I have then taken advantage of the superior quality, in particular the very high angular resolution, of the HST/ACS images to perform a parametric morphological analysis of large,

Summary

deep galaxy samples extracted from the Fors Deep Field (FDF), the GOODS-South and the Cosmic Evolution Survey (COSMOS). The two-dimensional surface brightness distribution of each galaxy was modelled by a Sersic profile convolved with the point spread function (PSF) of the image. I put extensive effort in understanding and quantifying the reliability and robustness of the modelling, both in terms of systematics due to characteristics of the data (as for instance dependence on the signal-to-noise ratio or PSF variations over the field of view), and in terms of reliability of the codes and classifications used, comparing the results obtained with different softwares as well as with the classical visual classification. Simulated images, with the same characteristics of true images and analyzed in exactly the same way as the original data, were used to accurately quantify the reliability of the fit results.

Beside a robust morphological characterisation of the galaxy samples, the pursuit of the line of research described above requires an estimate of the galaxy stellar masses. I thus derived stellar masses from the multiwavelength catalogs, by means of SED fitting with stellar population synthesis models.

By adding together the morphological and stellar mass properties of the whole galaxy sample, I have been able to investigate the evolution of the stellar mass density for different classes of galaxies: according to their Sérsic index n , galaxies were in fact classified as “early”, “intermediate” and “late” types ($n > 3.5$, $2 < n < 3.5$, and $n < 2$, respectively).

While recently also a few other studies have been carried out by cross-correlating the morphological and stellar mass evolution with redshift in deep galaxy surveys, in a similar fashion as I did in this work, all these works were potentially significantly affected by cosmic variance, due to the small areas of most deep surveys. For this reason, the last part of my PhD work has been devoted to a follow-up study in the COSMOS field. Due to its unprecedented coupling of wide area and depth, COSMOS allows cosmic variance to be beaten.

Moreover, thanks to its huge statistic, I could also disentangle for the first time the environmental effects on galaxy evolution for an homogeneous sample of *field* galaxies. Therefore, I also studied the evolution of the morphologically split galaxy stellar mass density in three different environments (underdense, average, and overdense).

In both my works on the FORS Deep Field plus GOODS-South and on COSMOS, I have found that, at all redshifts, early-type galaxies dominate the high-mass end. Going to progressively lower stellar masses, the relative contribution of late-type objects becomes more and more important, tending to dominate the total mass density.

To better quantify this change in the relative contribution of galaxies of different morphologies to the total mass function, a *transition mass* can be defined at each redshift, as the mass where the transition from a bulge-dominated to a disk-dominated stellar mass budget takes place. By studying the redshift evolution of this transition mass, I found that the morphological mix evolves monotonically with time: the higher the redshift, the more disk systems dominate the total mass content. While at $z \sim 0.7$ the value of the transition mass is approximately consistent with the local value, at $z \sim 1$ the contribution from early and late type galaxies to the total mass budget is found to be nearly equal.

The shape of the stellar mass function of disk dominated galaxies is consistent with being

constant with redshift; the number density of disk galaxies declines by more than one order of magnitude from masses of $\log M_* = 10.6$ to $\log M_* = 12$. Instead, the stellar mass function of bulge dominated galaxies is roughly flat (number densities are similar at all masses), but its normalisation constantly declines with increasing redshift. The steepness of the disks stellar mass function, together with the decline in normalisation of the bulges stellar mass function, naturally sets the evolution of the transition mass with redshift.

I have found that at $z \sim 1$, massive objects host nearly half the mass contained in similarly massive objects in the local universe: this means that the global mass function does not evolve in shape but only in normalization with redshift.

For the first time, I investigated the evolution of the specific star formation rate (SSFR, i.e. the star formation rate per unit stellar mass) as a function of morphological type and environment. I have found that the locations of early and late-type galaxies in the stellar mass vs. SSFR plane are very well separated at all redshifts and in all environments. The intermediate type galaxies fall in between, confirming their nature of transition objects. The early- and late-type galaxy populations exhibit a significant segregation in mass: disk galaxies dominate at low masses while early-type objects completely dominate the high mass tail. Therefore early-type galaxies drive the global decline of star formation from redshift 1 to the local Universe in massive galaxies. While in general this picture seems to be quite similar in all environments, in low density regions there is a population of relatively massive, early-type galaxies, having high SSFR and blue colours.

All together these findings point towards a scenario in which massive objects almost double their mass from $z \sim 1$ to 0, and become more and more bulge-dominated as time goes by. By means of estimates of the star formation rates for the whole sample, I have shown that *in situ* star formation is not sufficient to explain the evolving mass budget in massive objects. This argument let me conclude that merging events, or more likely the accretion of numerous small mass objects, must play a key role in the *mass pouring* from disks to bulges.

As explained above, thanks to the wide area of COSMOS I was able to investigate also the influence of the local environmental density on galaxy properties. I have found evidence of an established morphology density relation at all the redshifts probed in this work: overdense regions contain a higher relative fraction of bulges with respect to lower density regions.

Finally, thanks to the very homogeneous COSMOS dataset, I have studied the ages of stellar populations in massive early-type galaxies stellar as a function of environment. The age distributions show significantly different mean ages at all redshifts. The results found in this work are in agreement with other recent studies. Our results suggest that young (blue) massive early-type galaxies preferentially live in low density environments, while the galaxies hosting the oldest stars in the Universe preferentially belong to the highest density regions. Nonetheless, most early-type galaxies have similar characteristic ages, colors, and SSFRs, hence a similar formation redshift.

Summary

1

Galaxy formation and evolution in the cosmological framework

Abstract

In this chapter I describe the motivation behind this Thesis work. I briefly review the main theoretical aspects and the very broad observational scenario, explaining the fundamental goals of this work and summarizing its most relevant contributions to the study of galaxy evolution. The review of previous work, both observational and theoretical, is by no means to be intended as exhaustive nor complete, and I certainly by-pass to mention several important steps in extragalactic astronomy research, as well as to address many issues which are still relevant today. It is only meant to set this work in a context, thus allowing its fundamental aspects to be highlighted.

1.1 The hierarchical Universe

The Aristotelian cosmology (see Figure 1.1) dominated the Western thinking for nearly 2000 years. Aristotle's Cosmos was a brilliantly integrated whole, which holistically linked Matter, Place, Motion, Cause, and Value. The relations between Man, Nature, and God were never in doubt. Everything was connected and reinforcing. That mainly explains why the Copernicus' innocent suggestion raised such furor.

The current, only few tens of years old, standard model for our Universe, the Hot Big Bang model, draws everything we see today from an initial state of exceedingly high temperature and density. Starting from this initial condition, the Universe expanded for almost 14 billion

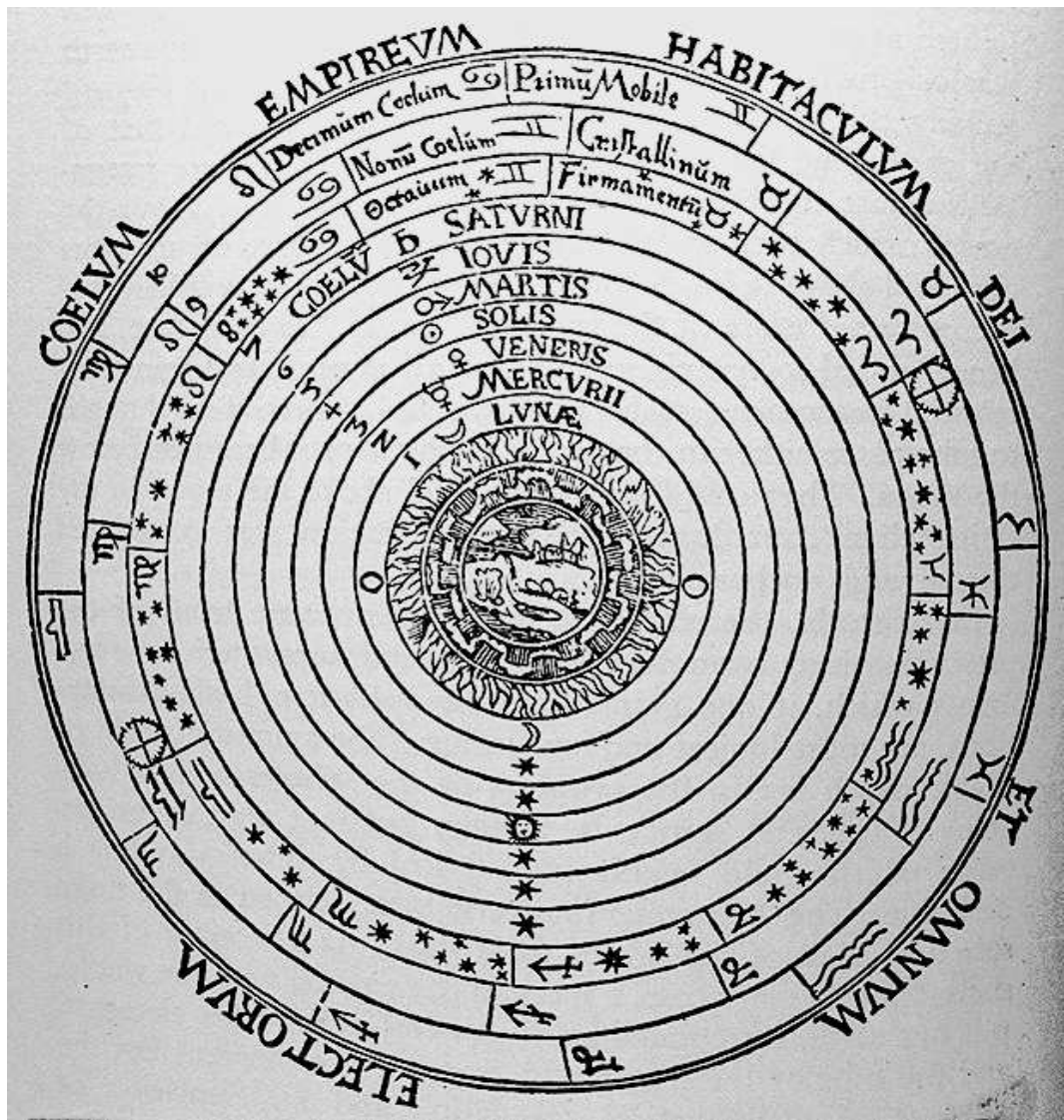


Figure 1.1: The Aristotelic Ptolemaic astronomical system, engraving from Peter Apian’s *Cosmographia* (1524).

years, and continues expanding, following Einstein’s theory of General Relativity. Today’s concordance model is a low-density, vacuum dominated Universe ($\Omega_M=0.3$, $\Omega_\Lambda=0.7$).

Most of the matter in the Universe is thought to be non-baryonic “cold dark matter”, which only interacts through gravitation. Dark matter is fundamental in explaining the origin of the structures observed in the Universe starting from the highly homogeneous initial density field

1.2 The formation and evolution of galaxies

observed as the Cosmic Microwave Background.

Being weakly interacting with the radiation, cold dark matter detaches earlier than baryons from the relativistic matter-radiation plasma. The structure formation is then due to gravitational instability, starting from primordial quantum fluctuations in the global density field which were amplified during the inflation epoch. Later on, at the epoch of recombination, baryons decouple from the relativistic radiation field and start falling in the “structure seeds” already present in the density field. While more and more matter is accreted onto the seeds, these overdense regions will no longer follow the general expansion of the Universe, but will slow down and eventually detach from the so-called Hubble flow, collapsing to form bound systems. In the currently favored Cold Dark Matter scenario, this process leads to the formation of small systems (sub-galactic scales) that will then merge to form larger systems: the bottom-up hierarchical process of structure formation.

1.2 The formation and evolution of galaxies

The modern picture of galaxy formation and evolution has the beautiful feature to naturally place the existence of galaxies into the cosmological framework (see Figure 1.2 for a schematic picture). Indeed, what we observe as a galaxy is, in this picture, a baryonic component in such a hierarchically assembled (mainly) dark matter system – a dark halo.

Baryons fall in the cores of the dark haloes inducing “typically baryonic” processes: baryonic gas cools, collapsing to form stars in a complex, poorly known process.

The modelling of galaxy formation and evolution is an essential tool to provide predictions to be contrasted with the observations, and at the same time to help the interpretation of what we observe, as well as possibly to devise new observations.

At the same time, observations give fundamental inputs to such modelling at the present stage. In fact, while the gravitational processes involving dark matter appear to be convincingly reproduced, the physical processes related to baryonic matter are much less known.

On the theoretical side, two approaches have been used thus far: the hydrodynamical simulation (which directly follows the dynamics of the gas, thus being very numerically-expensive), and the so-called semi-analytic models coupled with the calculated/simulated evolution of dark matter structure (which model each known process by means of physically and/or observationally motivated prescriptions).

On the other hand, galaxy evolution is observed in two different ways: i) the observation of galaxies at high redshifts, providing a direct view of the galaxy populations at previous cosmic times, and ii) the exploitation of the so-called fossil record, that is the imprint left by the evolutionary history on the populations of nearby galaxies.

This work relies on the first approach, to study the evolution of massive galaxies in the last 9 billion years. While this may look the more natural approach, and in some sense even the more straightforward, nonetheless it is complicated by a series of problems and caveats. First, this approach assumes that the portion of the Universe that we observe at high redshift

1 Galaxy formation and evolution in the cosmological framework

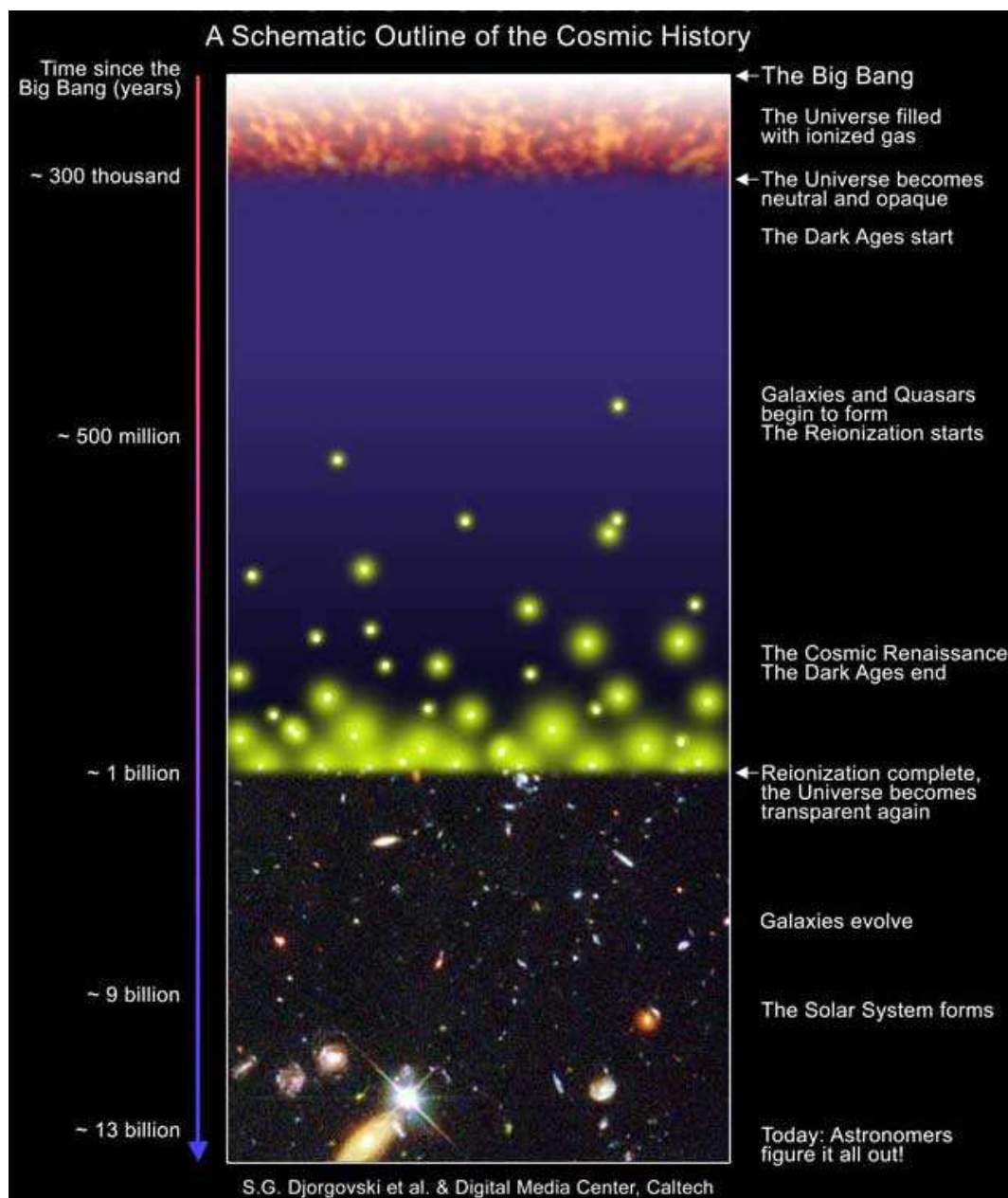


Figure 1.2: A schematic outline of the cosmic history (<http://abyss.uoregon.edu/~js>)

will evolve into the local Universe. This is in principle true only on very large scales, and until very recently there were no surveys at the same time deep and wide enough to assure the observation of the distant Universe without being limited by the influence of cosmic variance. Moreover, to compare galaxy populations at different redshifts it is essential to define complete, well defined samples whose galaxy properties can be meaningfully contrasted with each other. This often implies observational challenges, and both the definition of such samples and the derivation of their galaxy properties always rely, at least to some extent, on assumptions and models.

I will now briefly describe the different aspects of galaxy evolution that are considered in this work.

1.2.1 Morphological properties

The discovery of ‘nebula’, fuzzy objects in the sky that were not planets, comets or stars, is attributed to Charles Messier in the late 1700’s. His collection of 103 objects is the first galaxy catalog. Herschel (1792–1871) used a large reflecting telescope to produce the first General Catalog of galaxies. Edwin Hubble showed in the 1930’s that most of the ‘nebula’ seen in the sky are, in fact, external galaxies, systems composed of billions of stars well outside the Milky Way.

Once the existence of external galaxies was definitively established, it became customary to divide them into a number of classes based on their morphology, that is, their apparent shape and structure. The goal of any classification system, either in biology or astronomy, is to reveal underlying physical properties, which in our case may lead to understanding the formation and evolution of galaxies. Almost all current systems of galaxy classification are outgrowths of the initial scheme proposed by Edwin Hubble in 1926. In Hubble’s scheme, which is based on the optical appearance of galaxy images on photographic plates, galaxies are divided into three general classes: ellipticals, spirals, and irregulars (see Figure 1.3).

Trying to link physical observables to the morphological appearance, astronomers started to use fitting formulae to describe the light profile of galaxies. These fitting formulae had no physical motivation but at the same time they did such a good job in describing the galaxy light profiles that it was put much effort in building dynamical models that could explain such formulae. The de Vaucouleurs profile (de Vaucouleurs 1948) for giant ellipticals and the exponential profile (Freeman 1970) became for decades the standard ways to describe analytically the galaxy morphology. In fact they turned out to be the main ingredients of galaxy scaling laws such as the Fundamental Plane relation for elliptical galaxies (Dressler et al. 1987; Djorgovski & Davis 1987; Bender et al. 1992) and the Tully–Fisher (1977) relation for disk galaxies.

More generally speaking, ellipticals have light profiles well described by the more general Sérsic law (1968). The Sérsic profile has the following form:

$$\Sigma(r) = \Sigma_e e^{-\kappa[(\frac{r}{r_e})^{1/n} - 1]} \quad (1.1)$$

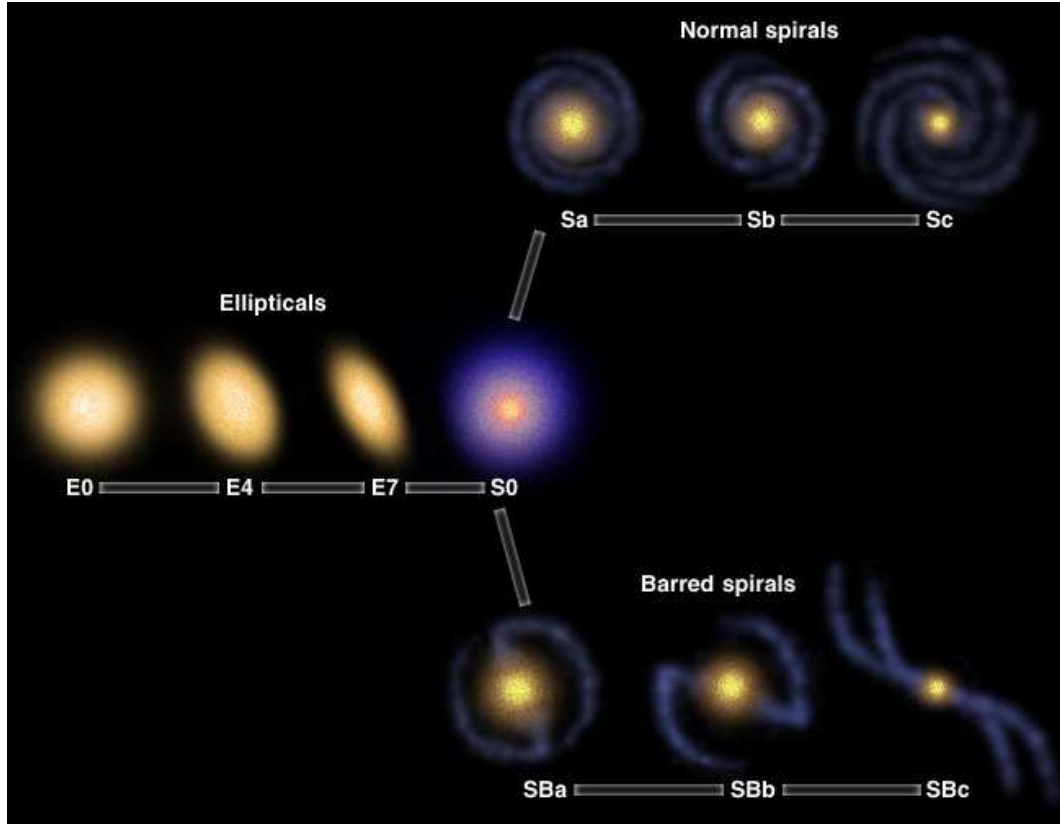


Figure 1.3: The Hubble tuning fork (courtesy of “Windows to the Universe”, <http://www.windows.ucar.edu>).

where r_e is the effective radius of the galaxy, Σ_e is the surface brightness at r_e , n is the power-law index, and κ is coupled to n such that half of the total flux is always within r_e .

The original de Vaucouleurs (1948) profile is a special case with $n = 4$ and $\kappa = 7.67$. While the de Vaucouleurs profile is well suited for “classical” bulges, some bulges, the pseudo bulges, may be better represented by exponential profiles (e.g., Kormendy & Bruzual 1978; Shaw & Gilmore 1989).

The Sérsic index n for elliptical galaxies shows a relatively wide distribution with values in between 2 and 6. The Sérsic index results to be correlated to the absolute luminosity of the galaxy: more luminous the galaxy, the higher its Sérsic index.

The light profile of the bulges in spiral galaxies have been found to be very similar to elliptical galaxies of similar luminosities; i.e., they are well-described by a Sérsic profile.

The advantage of the Sérsic profile is that it can easily describe the whole galaxy zool-

1.2 The formation and evolution of galaxies

ogy, with a continuous sequence from a Gaussian ($n = 0.5$) to an exponential ($n = 1$) to a de Vaucouleurs ($n = 4$) profile, simply by varying the n exponent.

For this reason by fitting a Sérsic profile to the surface brightness of each galaxy in the sample, and defining a criterion for the separation of different galaxy classes based on the Sérsic index (see for instance chapter 4), one can divide the galaxies in the sample in broad morphological classes.

The study of galaxy structures yields considerable information on the way they have formed. In fact, the structure of a galaxy mainly reflects its dynamical status: disk galaxies have exponentially declining light profiles and their dynamics is made of ordered motions of stars around the azimuthal axis. The total angular momentum is relatively high and such galaxies are usually classified as *cold* systems because of the low velocity dispersion around the mean velocity.

Bulge galaxies instead have centrally concentrated light profiles and their dynamics is made of chaotic motions of stars around the object center. The total angular momentum is quite low and these galaxies are usually referred to as *hot* systems because of the high velocity dispersion.

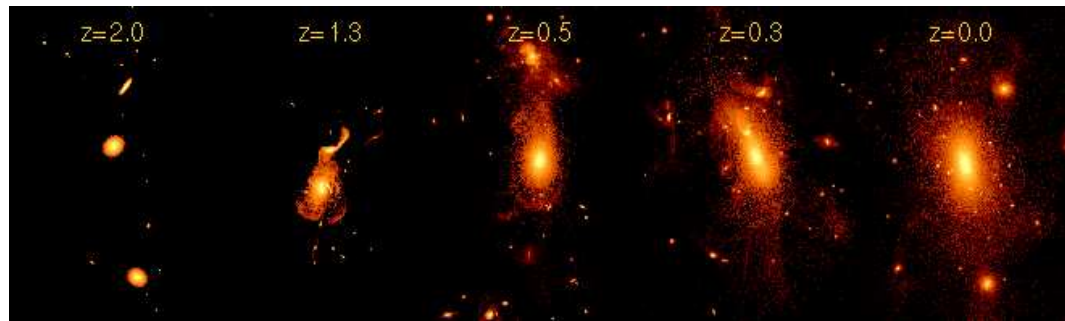


Figure 1.4: Three disk galaxies at $z = 2$ are interacting and finally merging all together at $z = 0$ to form a giant elliptical (Dubinski et al. 1998).

In the currently favored scenario, the bulk of the stars generally start forming in disk structures, thus creating disk galaxies first. Later on, these disk galaxies may transform into bulge galaxies through processes of gravitational instability and/or merging (e.g. Toomre & Toomre 1972, see figure 1.4).

On the other hand, in the “historical” picture for the formation of elliptical galaxies, the so-called monolithic collapse (e.g. Eggen et al. 1962; Larson 1974), such galaxies formed as already massive objects in one single star formation event at high redshift.

Even though peculiar objects are indeed observed which are considered as evidence of the occurrence of the transformations in galaxy structures, and in particular of merging events, it is not yet clear in which measure merging is actually important in the galaxy formation and evolution process, nor its consequences in terms of induced star formation in the remnant

1 Galaxy formation and evolution in the cosmological framework

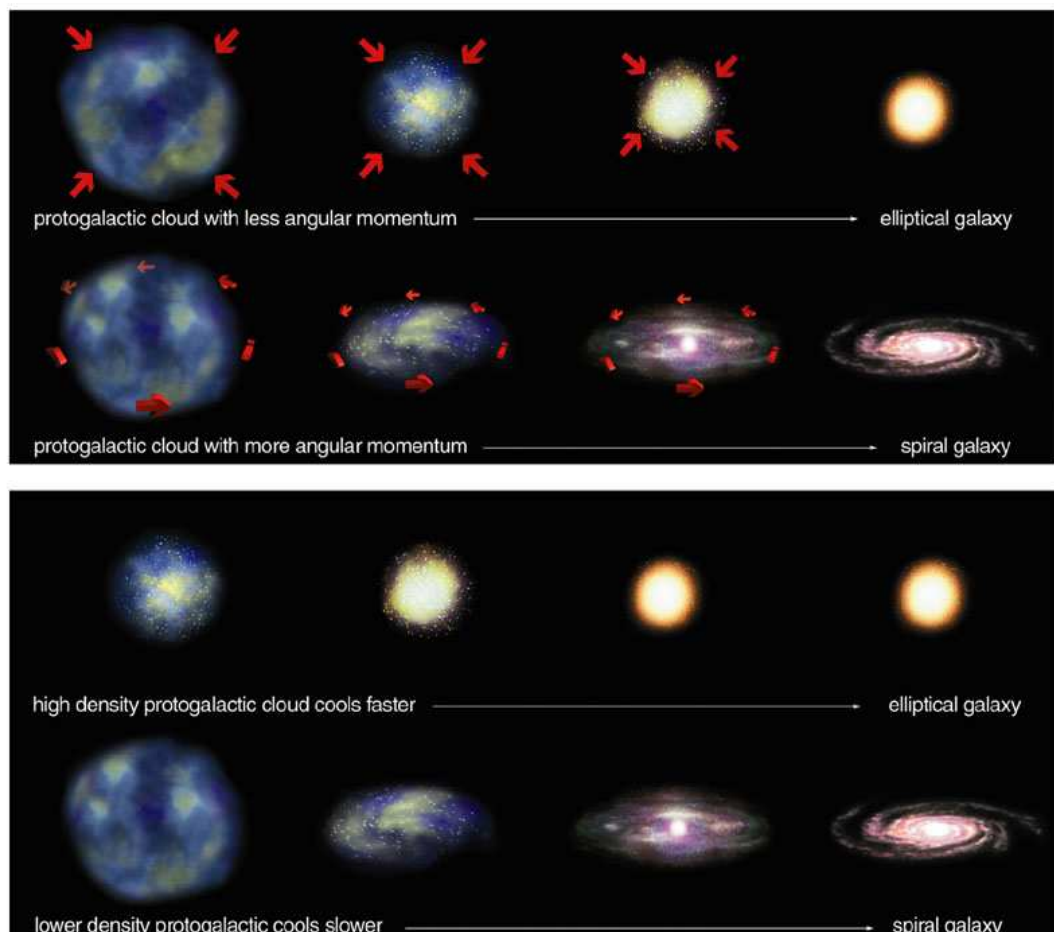


Figure 1.5: The influence of initial conditions of the protogalactic cloud on the resulting galaxy structure (© 2004 Pearson Education, publishing as Addison Wesley).

galaxy, as well as structural modifications, are yet completely understood.

Moreover, apart from the general cosmological framework, the details of the galaxy formation process might be determined also by the initial conditions in the protogalactic cloud (such as angular momentum and density of the protogalactic gas, see figure 1.5).

The morphological analysis of large and unbiased galaxy samples is thus able to discriminate between the predictions of different formation and evolutionary scenarios. For this reason, it became very important to obtain morphological analysis of thousands of galaxies up to high redshift, with a method as much as possible objective and whose results could be reliably reproduced by different observers. While visual morphological analysis (that is, visual classification of a galaxy by eye) was the natural approach in the beginning of morphological

1.2 The formation and evolution of galaxies

studies, nowadays – especially for large samples in deep fields – the most common choice is morphological classification by comparison with analytic surface brightness profiles.

1.2.2 Star formation and colors

Star formation is the process that actually forms what we observe as a galaxy. When a star formation event occurs in a galaxy, the newborn population of stars is formed according to the initial mass function (IMF, i.e. the mass distribution of stars). The IMF is parametrised by a power law: $\phi_{IMF}(M) \propto M^\alpha$, with $\alpha < 0$. Therefore, massive stars are much less numerous than low mass stars.

Massive stars burn their hydrogen fuel, by thermonuclear fusion, extremely fast. Thus, they are bright and hot (i.e. the maximum of their Planckian emission is at blue/UV wavelengths). Low mass stars instead are much cooler in surface temperature (thus their emission peaks in the red) and much fainter. All this is shown in the Hertzsprung-Russell Diagram (see figure 1.6).

A young stellar population has a mean color that is blue, since most of the light is coming from the massive, hot stars. However, since such massive, blue stars use their core fuel much faster than the fainter, cooler red ones, they die sooner. Therefore, a progressively older stellar population turns redder because all the massive blue stars have died off (turned into red giant stars) leaving the faint, cool, red stars.

The stellar populations hosted by a galaxy mainly determine the galaxy colour, together – and unfortunately in a degenerate fashion – with other properties like the metal enrichment history and dust content of the interstellar medium.

In the nearby Universe, the galaxy colour is found to strongly correlate with the galaxy structure: elliptical galaxies (as well as dominating bulges in spiral galaxies) show red colours, while disks and irregular galaxies exhibit bluer colours. In fact, in a single galaxy different components (like bulge, disk, bars, etc.) may have different colours depending on the local stellar population properties. Looking at their colours, it is found that in general, and modulo the just cited degeneracies, elliptical galaxies host old stellar populations while younger populations inhabit disk galaxies. This means that the star formation history of these two classes of galaxies is clearly different, pointing toward a short, intense episode of star formation at high redshift for the ellipticals, and a more quiet and prolonged star formation history in spirals, as shown in figure 1.7.

1.2.3 The Cosmic Star Formation History and Mass assembly

Even though the star formation process is still poorly understood from the theoretical point of view, the star formation rate of a galaxy may be quantified by using several different indicators. As explained above, the light distribution (spectral energy distribution, SED) emitted by a galaxy is indicative of its stellar populations, and more specifically of the amount of present/recent star formation.

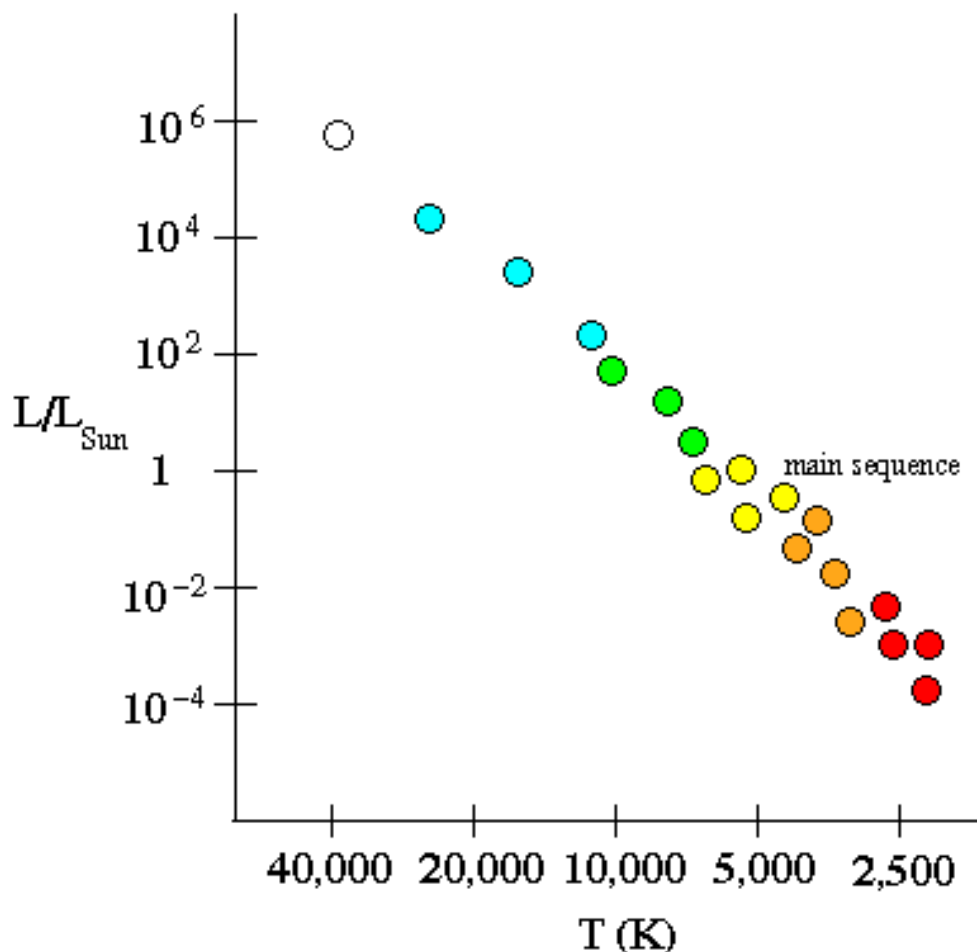


Figure 1.6: The Hertzsprung–Russel Diagram. The Temperature on the horizontal axis refers to the photospheric stellar temperature. On the vertical axis the solar luminosities emitted from the different kind of stars are shown . Colors refer to the wavelength at which the stellar (pseudo–plankian) emission has its maximum. The star locus shown is the *main sequence* stage of the stellar evolution: this is the locus where stars spend most of their life and it is actually the period over which stars burn their hydrogen and transform it into helium (<http://abyss.uoregon.edu/~js>).

At the same time, the SED of a galaxy allows an estimate of the galaxy mass in stars. In fact, as explained above, the red/near-infrared part of the galaxy SED is dominated by the light from low mass stars, which dominate in mass the stellar populations. Therefore, from the galaxy flux emitted at red wavelengths it is possible to estimate, in a relatively robust

1.2 The formation and evolution of galaxies

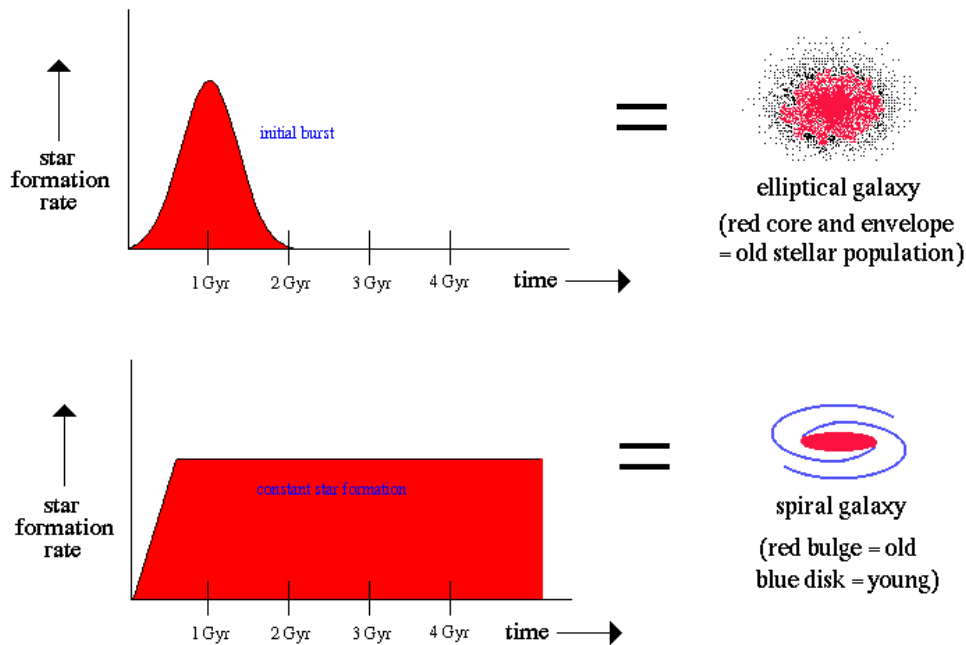


Figure 1.7: The different star formation histories of typical elliptical and spiral galaxies (<http://abyss.uoregon.edu/~js>).

way, the total mass of the galaxy stellar populations, as will be explained in more details in chapter 5.

These two quantities, namely the instantaneous star formation rate and the total stellar mass of a galaxy, are fundamental tools in modern astronomy. By observing galaxy samples at different redshifts, and measuring their star formation rates, it is possible to trace the star formation history of the Universe.

In recent years, several deep extragalactic surveys allowed the cosmic star formation history to be measured: all these studies point towards a substantial amount of star formation at early cosmic epochs (see figure 1.8).

At the same time, a number of studies have been able to measure directly the stellar mass density up to high redshifts. The two independent approaches are in a remarkably good agreement, and consistently suggest that about half of the present-day stars were already in place at $z \approx 1$, when the Universe was half of its present age (see figure 1.9).

The assembly of the stellar mass through cosmic time is a crucial test for models of galaxy formation and evolution. As explained in section 1.2, in the currently favored models bulge dominated galaxies are thought to form from disks, either through mergers or by dynamical

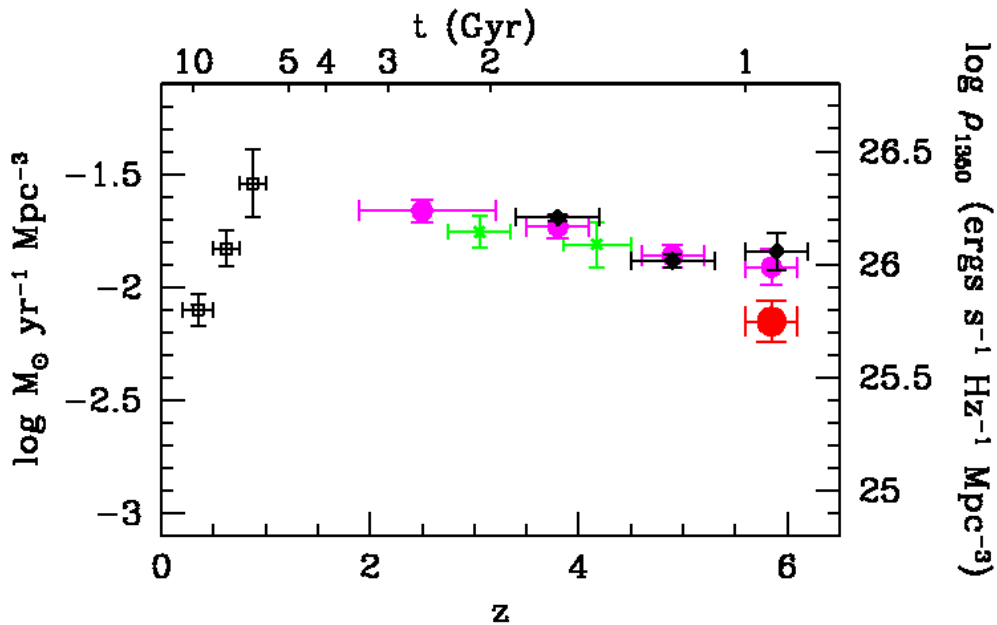


Figure 1.8: The cosmic star formation history from a compilation of different surveys (Bowens et al., 2004).

instabilities. Therefore, even though detailed predictions do not exist, the qualitative expectation is that the fraction of bulge-dominated galaxies decreases at higher redshifts. As also stated in section 1.2, in a hierarchical picture one also expects massive galaxies to assemble at later cosmic times, by merging of smaller objects.

In order to put sensitive constraints on the models, it is thus very important to measure at the same time the mass assembly and the evolution of the structural properties of galaxies as a function of cosmic time. In chapters 4 and 5 I present a study based on the measurement of stellar masses and structural properties of large samples of galaxies up to redshift 1. Since, in a hierarchical scenario, merging is driving both mass assembly and dynamical evolution, these studies offer a direct probe of the role of this process in galaxy evolution.

1.2.4 The Environmental dependence of galaxy evolution

The link between galaxy evolution and environmental properties has been observed since years as being very tight. The hostile clusters environment influences through different processes, namely strangulation, ram-pressure and close-encounters, both the dynamical status and the star formation activity of a galaxy.

Elliptical galaxies living in galaxy clusters are always found to show a tight relation between their magnitudes and colours, the so-called red sequence, which is expected to be the

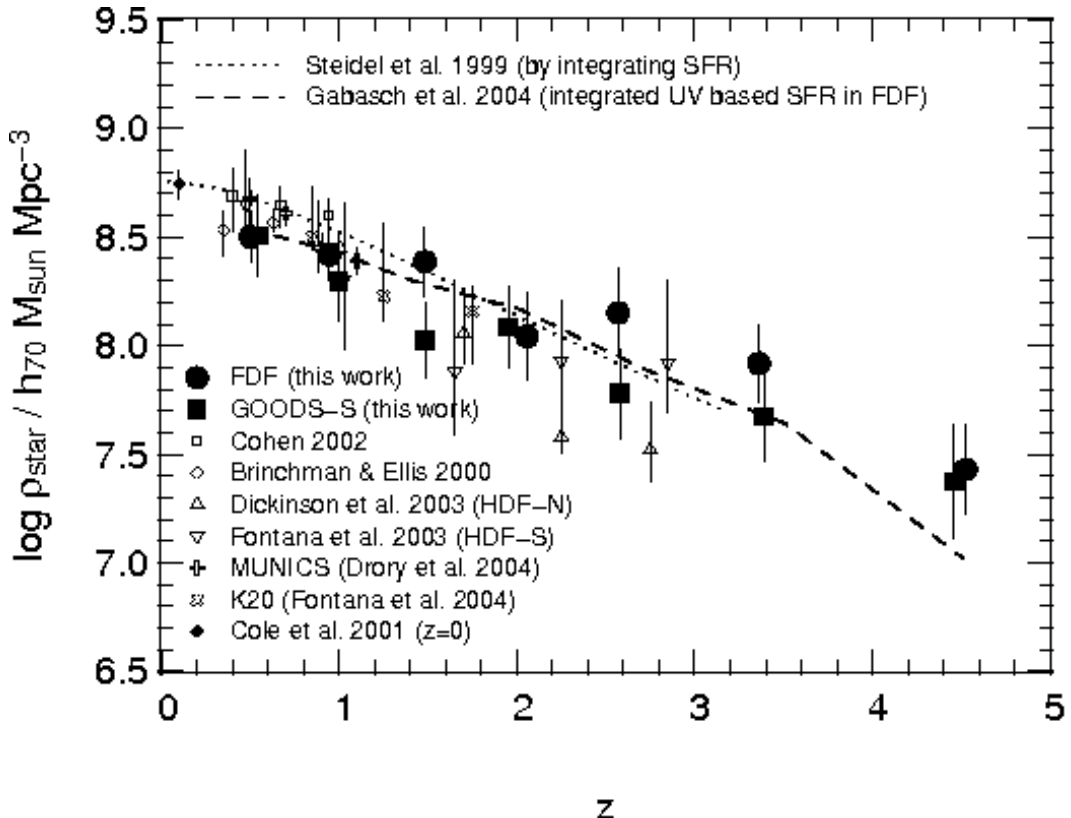


Figure 1.9: The total stellar mass density as a function of redshift, from a compilation of different surveys (Drory et al., 2005).

outcome of processes which stop the star formation activity, so that the stellar populations of red sequence galaxies result to be all consistently red/old.

Furthermore, it is well observed that in overdense regions the fraction of elliptical galaxies increases with respect to average density environments, while that of spirals/irregulars decreases. This morphology–density relation is also thought to be the outcome of the processes typical of overdense environment, which transform the galaxy structural properties.

The linear theory of the structure growth predicts that, starting from the initial density fluctuations field, overdense regions tend to become more and more overdense as time goes by. Conversely, underdense regions tend to loose more and more matter. As described in section 1.1, the highest density peaks of the dark matter large scale structure are supposed to first detach from the Hubble flow and collapse. Therefore, these are the places where also the first galaxies are supposed to start out and grow during the cosmic time. The higher the density the earlier star formation is supposed to start in small sub-galactic units. These sub-galactic units will ultimately merge together to form the biggest objects. Such biggest

objects will hence be made of the oldest stars in the Universe.

Such a picture nicely explains the observed *downsized* flavour of the Universe: the most massive objects are observed to host the oldest stellar populations, and their contribution to the cosmic star formation history is very early in cosmic times. This was originally thought to be in contradiction with the hierarchical picture of galaxy formation, because the most massive galaxies, which were predicted to be the younger, latest products of the hierarchical assembly, were instead found to be the older ones when examining the age of their stars. However, if no significant star formation is triggered by the subsequent merging events, the hierarchical merging process goes on by assembling small galaxies with already evolved stellar populations, thus while the resulting massive galaxy is actually assembled very recently (so its “age” as a single object is very young), the stellar populations it hosts were formed much before in the smaller galaxies, thus being much older.

1.3 This Thesis

The main aim of my thesis work has been to add a morphological characterization to the well-established *downsizing* scenario.

I have performed a parametric morphological analysis based on the deep high resolution HST/ACS imaging available for three deep surveys, the Forn Deep Field (FDF), the GOODS-South surveys and the Cosmic Evolution Survey (COSMOS). I modeled the two-dimensional surface brightness of each galaxy in these large samples up to redshift $z \sim 1$ (down to a limiting magnitude $I_{AB}=24$) with Sérsic profiles, obtaining a quantitative measure of the morphological properties of these objects. I put extensive effort in understanding and quantifying how various kinds of systematics could affect the modelling results. An exhaustive description of the data used in this work is given in chapter 2, while the morphological analysis is explained in full details in chapter 3.

Also the technical treatment of the data took an important part in this work. For instance, the last part of this work, which is based on the HST/ACS COSMOS survey dataset, consists of the morphological analysis of about 1 square degree of the sky. While such a huge volume allows us to put firmer constraints on our results, it involved the morphological analysis of more than 400 separate ACS images, and it has been possible thanks to a deep use of Python scripting which let me handle this “Tera-byte domain” amount of data in a reasonable time.

Once a robust morphological characterisation was secured for the whole sample, I estimated by means of SED fitting the stellar masses of the galaxies, making use of the very high-quality, multiwavelength datasets available for all the three deep fields studied. Putting together the information about structural properties and stellar masses, I have been able to investigate the evolution of the stellar mass density for three different classes of galaxies, i.e. early, intermediate and late types, selected according to the Sérsic index, n ($n > 3.5$, $2 < n < 3.5$, and $n < 2$, respectively). Chapters 4 and 5 present the results of this analysis, obtained on the FORS Deep Field, the GOODS-South and on the COSMOS

survey, respectively. As of today, this is the analysis of combined mass and morphological evolution in galaxies based on the largest galaxy sample.

Thanks to the huge statistic available in the COSMOS survey, I could also, for the first time, disentangle the environmental effect on galaxy evolution for a homogeneous sample of *field* galaxies. Therefore, I also studied the evolution of the morphologically split galaxy stellar mass density in three different environments (underdense, average, and overdense).

I have also analysed both the bulge-to-total and the bulge-to-disk fractions at different redshifts and for different environments. Firstly, at all redshifts I have found evidence of a well established morphology–density relation: more dense volumes contain a higher relative fraction of bulges as respect to lower density volumes.

Furthermore, in this work for the first time the evolution of the specific star formation rate (SSFR, i.e. the star formation rate per unit stellar mass) was investigated as a function of morphological type and environment. In agreement with previous studies, this work found that the most massive galaxies have the lowest amount of star formation per unit stellar mass up to the highest redshift probed, and hence they cannot have formed the bulk of their stars in this redshift range (i.e. the last 9 billion years). This pushes the bulk of their star formation at much earlier cosmic epochs, in agreement with the downsizing scenario. In fact, previous studies have generally neglected both galaxy morphological properties and environmental conditions. I have been able to plug in also these two further variables, thus producing a wider view of this complex picture. In particular, the SSFR in massive early–types is found to significantly evolve with redshift, while it remains pretty constant since $z \sim 1$ in massive disks. On the other hand, the high–mass end of the galaxy populations is always dominated by early–type objects, which thus drive the decline in star formation rate at high masses. While in general this picture seems to be quite similar in all environments, in low density regions there is a population of relatively massive, early–type galaxies, having high SSFR and blue colours.

Finally, I have studied, with the highly homogeneous dataset available, the ages of the stellar populations in massive early–type galaxies as a function of the environment. The age distributions show different mean ages at all redshifts, in agreement with other recent studies. The results found in this work suggest that young (blue) massive early–type galaxies preferentially live in low density environments, while the galaxies hosting the oldest stars in the Universe preferentially belong to the highest density regions. Nonetheless, most early–type galaxies have similar characteristic ages, colors, and SSFRs, hence a similar formation redshift.

In chapter 6, I summarise some results obtained in complementary studies I was involved in, and provide a short description of some of the follow–up work which is already under way.

1 Galaxy formation and evolution in the cosmological framework

2

Observing the coloured Universe: the large deep surveys

Abstract

In this chapter I describe the spectro–photometric data used in this work. These consist of multiwavelength UV–to–NIR observations of three extragalactic deep fields. In this chapter, details are given about the quality and characteristics of such data, as well as about the process of building multicolor catalog and estimating photometric redshifts.

Wide and deep surveys are a vital tool in modern astronomy: they provide the large datasets of objects needed (both at high and low redshifts) to improve our knowledge of the physical mechanisms driving galaxy formation and evolution.

Recent wide field surveys, such as 2MASS, SDSS and 2DF, (Jarrett et al. 2000; York et al. 2000; Colless et al. 2001) provide an unprecedented wealth of information on the structure of the *local* Universe.

On the other hand, the complementary *pencil beam* deep surveys (i.e. relatively small patches of the sky observed in several bands with high angular resolution and high S/N ratios at faint magnitude levels) allow us to investigate the high- z Universe ($z \gtrsim 1$), providing large sets of distant galaxies to constrain the different evolutionary scenarios.

The Hubble Deep Fields (Williams et al. 1996) has marked a cornerstone in our understanding of galaxy evolutionary processes, providing unprecedented constraints on the theoretical scenarios for galaxy formation and evolution.

Later on more deep surveys have been performed using space and ground–based telescopes of the 10m class generation: the Subaru Deep Field (Maihara et al. 2001), the Fors

2 Observing the coloured Universe: the large deep surveys

Deep Survey (Heidt et al. 2003), Gemini Deep Deep Survey (Abraham et al. 2004) and GOODS (Giavalisco et al. 2004).

However, an important drawback of these deep surveys is that the typical field of view has angular sizes that at $z \sim 1$ convert to physical scales relatively small with respect to those relevant for large-scale structure. Thus, in order to study the properties of distant galaxies at high redshift in different large scale environments, it is mandatory to control field-to-field variations, by means of deep surveys along many different lines of sight or extended to larger contiguous sky areas.

Very recently, the Cosmic Evolution Survey (COSMOS, Scoville et al. 2007) addressed this issue, by observing a 2 square degree contiguous patch of the sky, providing the whole community with an unprecedented view of galaxy evolution *with in the large scale structure* up to high redshift.

2.1 The FORS Deep Field

The FORS Deep Field (Appenzeller et al. 2000) is a multi-color photometric and spectroscopic survey of a $7' \times 7'$ region near the south galactic pole including the QSO Q 0103-260 at redshift $z = 3.36$. The data have been taken with FORS1 and FORS2 at the ESO VLT and SofI at the NTT.

The data were reduced and calibrated as described in Heidt et al. (2003). The reduction of the images in the z-band and the medium-band filter at 834 nm required an additional step to remove the characteristic fringing pattern.

The formal 50% completeness limits for point sources are 26.5, 27.6, 26.9, 26.9, 26.8, ~ 25.5 , ~ 25.8 , 23.8, 22.6 in U, B, g, R, I, 834 nm, z, J and Ks, respectively. The seeing varied from 0.5 arcsec in the I and z band to 1.0 arcsec in the U-band. As the depth of the images decreases towards the borders, we limited our analysis to the inner 39.81 arcmin^2 of the survey field, thus ensuring an optimal photometric homogeneity and preventing any possible bias in the photometric redshifts determination.

2.1.1 Source detection and multi-band photometry

Object detection was done in the I-band image using SExtractor (Bertin & Arnouts 1996), and the catalogue for this ‘deep’ part of the FDF includes 5636 objects.

Accurate multicolor photometry of the objects is crucial to derive accurate photometric redshifts, therefore we checked the accuracy of the absolute calibration of our multicolor catalog by means of color-color plots of stars. We compared the colors of FDF stars with the colors of stellar templates from the library of Pickles (1998) convolved with the FORS filter system. In general, corrections to the photometric zeropoints of only a few hundredth of a magnitude were needed to obtain an optimal match to the stars and best results for the photometric redshifts.



Figure 2.1: The FORS Deep Field.

After checking the accuracy of the photometric calibration, we can measure the broad-band spectral energy distribution (SED) of galaxies as sampled by our passbands. In order to take into account that different images had different point spread function (PSF), all the images were convolved to the same PSF of FWHM = 1''. Object fluxes were measured in a fixed aperture of 1.5''.

To avoid contamination from stars, we rely on three sources of information: the star-galaxy classifier of the detection software SExtractor, the goodness of fit for galaxy objects of the photometric redshift code and, if available, on the spectroscopic information. We first exclude all bright ($I < 22^m$) starlike objects (SExtractor star galaxy classifier > 0.95). Then we exclude all objects whose best fitting stellar spectral energy distribution (SED) – according to the photometric redshift code – gives a better match to the flux in the different wavebands than any galaxy template ($2\chi^2_{star} < \chi^2_{galaxy}$). These objects are subsequently flagged as star and removed from our catalogue. Further inspection of the images confirms, that none of

2 Observing the coloured Universe: the large deep surveys

these flagged objects are extended. Finally, we reject all objects spectroscopically classified as stars. In total 78 objects were classified as stars and removed from our sample. Our final I-band selected catalogue comprises therefore 5558 objects.

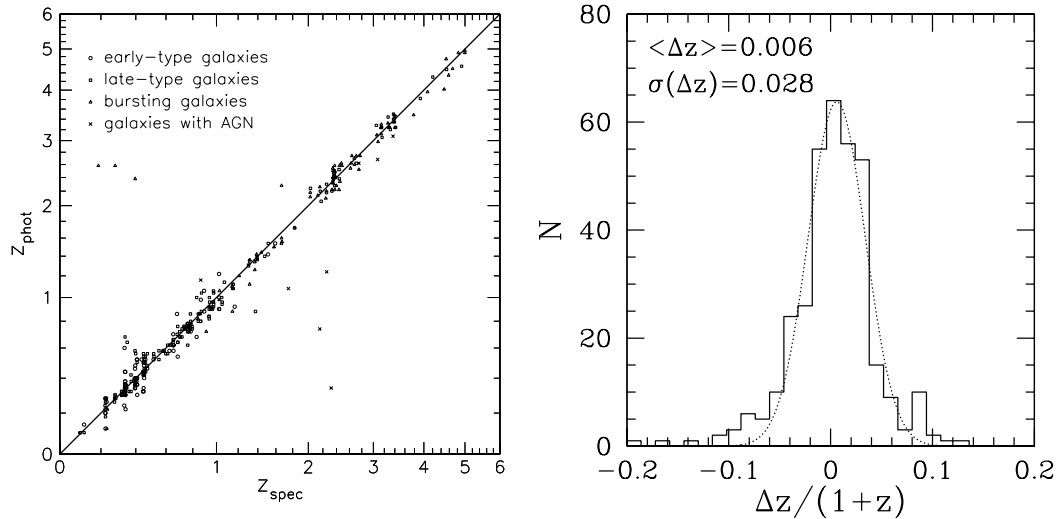


Figure 2.2: Left panel: comparison of spectroscopic (Noll et al. 2004; Böhm et al. 2004) and photometric redshifts for different galaxy types and quasars in the FDF. Right panel: histogram of the photometric redshift errors. The error distribution can be approximated by a Gaussian centered at 0.006 with an rms of 0.028 (dotted line). Reproduced from Gabasch et al. (2004a).

2.1.2 Photometric redshifts in the FORS Deep Field

A redshift probability function $P(z)$ was determined for each object by matching the object's fluxes to a set of 29 template SEDs redshifted between $z = 0$ and $z = 10$ and covering a wide range of ages and star formation histories. As templates we used (a) local galaxy templates from Mannucci et al. (2001), and Kinney et al. (1996) and (b) semi-empirical templates more appropriate for modest to high redshift galaxies. The semi-empirical templates were constructed by fitting combinations of theoretical spectral energy distributions of different ages from Maraston (1998) and Bruzual & Charlot (1993) with variable reddening (Kinney et al. 1994) to the observed broad band colors of about 100 galaxies in the Hubble Deep Field and about 180 galaxies from the FDF with spectroscopic redshifts. Lyman forest absorption was parameterized following Madau (1995) and references therein.

The remaining 180 galaxies in the FDF with spectroscopic redshift were used as an independent control sample.

In the left panel of Fig. 2.2 the comparison of photometric and spectroscopic redshifts

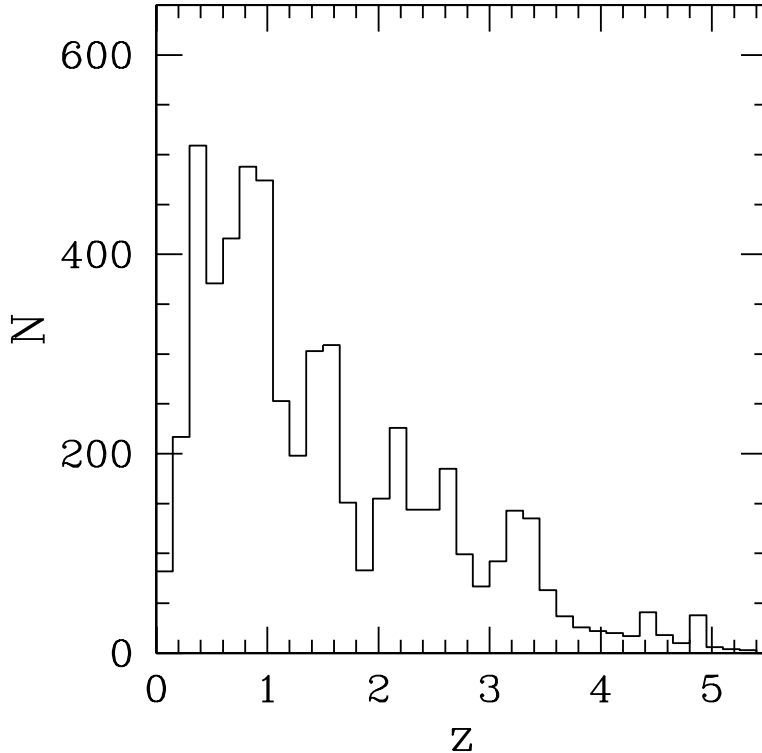


Figure 2.3: Redshift distribution of all galaxies in the FDF sample. The clustering observed in photometric redshift space is probably mostly real, as we see clustered *spectroscopic* redshifts at $z = 0.22$, $z = 0.33$, $z = 0.39$, $z = 0.45$, $z = 0.77$, $z = 2.35$ and possibly at $z = 0.95$, $z = 3.15$, and $z = 3.4$. Reproduced from Gabasch et al. (2004a).

of 362 galaxies and QSOs in the FDF is shown (see Noll et al. 2004; Böhm et al. 2004 for the spectroscopic redshifts). The agreement is very good and we have only 6 outliers with a redshift error larger than $\Delta z > 1$. Three of the outliers are quasars or galaxies with a strong power-law AGN component (crosses). The others are very blue objects with an almost feature-less continuum (triangles).

In the right panel of Fig. 2.2 the distribution of the redshift errors is shown. It is nearly Gaussian and scatters around zero with an rms error of $\Delta z/(z_{spec} + 1) \approx 0.03$.

The redshift histogram of all objects in the FDF is shown in Fig. 2.3. Most if not all peaks in the distribution are due to real clustering in redshift space. From the 362 spectroscopic redshifts, clusters, groups or filaments of galaxies with more than 10 identical or almost identical redshifts were identified at $z = 0.22$, $z = 0.33$, $z = 0.39$, $z = 0.45$, $z = 0.77$, $z = 2.35$. Other structures are possibly present at $z = 0.95$, $z = 3.15$, and $z = 3.4$.

2.2 The Great Observatories Origins Deep Survey South Field

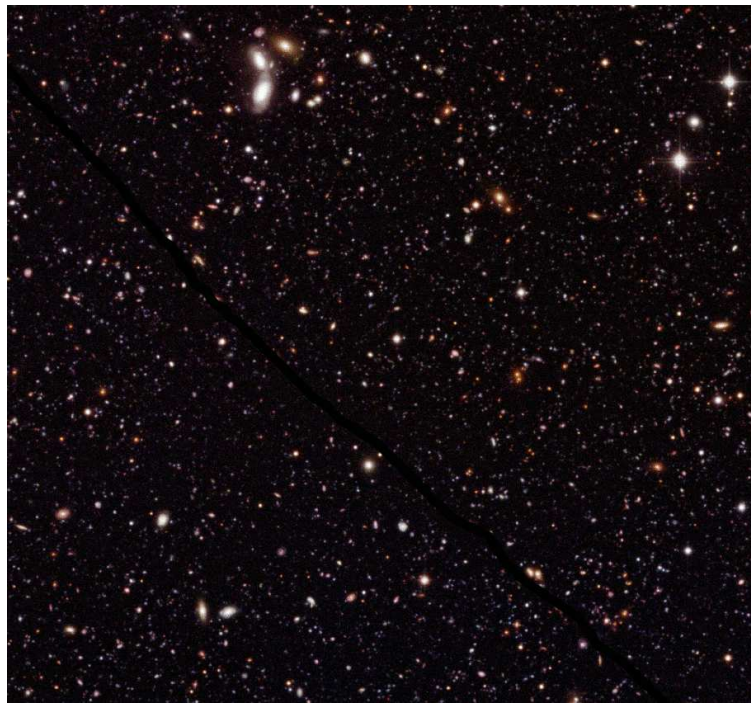


Figure 2.4: The portion of the GOODS-South field discussed in this section

The Great Observatories Origins Deep Survey (GOODS) combines extremely deep observations from the NASA's space observatories Spitzer, Hubble, and Chandra, ESA's XMM-Newton, and from the most powerful ground-based facilities, to survey the distant universe across the broadest range of wavelengths.

A fundamental goal of the GOODS survey is the study of galaxy formation and evolution over a wide range of cosmic lookback time, addressing the mass assembly history of galaxies, the evolution of their stellar populations, and the energetic output from star formation and active nuclei.

GOODS will survey approximately 300 square arcmin divided into two fields centered on the Hubble Deep Field North (GOODS-N) and the Chandra Deep Field South (GOODS-S). These are among the best observed portions of the sky, and are the sites of the deepest observations ever made from Spitzer, Hubble, Chandra, and XMM-Newton. The space-based observations are complemented by ground-based imaging and spectroscopy, including an extensive commitment of ESO and NOAO observing time. While GOODS is a deep (and not wide) survey, it is much larger than most previous deep surveys. Only recently the COSMOS survey sampled a significantly wider area.

2.2 The Great Observatories Origins Deep Survey South Field

GOODS includes an HST Treasury Program which uses the Advanced Camera for Surveys (ACS) to image the two GOODS fields through four broad, non-overlapping filters: F435W (B), F606W (V), F775W (i), and F850LP (z) (exposure times are 3, 2.5, 2.5 and 5 orbits per filter, respectively). Thanks to the superior resolution of ACS, the combination of this treasury program with GOODS observations at other wavelengths allows us to map the evolution of the Hubble sequence with redshift, reconstructing the history of galaxy mass assembly and star formation of different galaxy populations.

2.2.1 A K_s-band selected galaxy sample in GOODS-S

Adapted from M. Salvato et al, “A K_s-band selected galaxy sample in GOODS-S”, A&A submitted

The study presented here is based on ground-based optical and near-infrared images obtained by ESO on the GOODS-S field. Optical observations in the *U*, *B*, *V*, *R* and *I* bands have been carried out with the Wide-Field Imager (WFI) at the 2.2-m MPG/ESO telescope. The datasets have been reduced by two different groups: *U* and *I* images are taken from the field Deep2c of the GOODS/ESO Deep Public Survey (Arnouts et al. 2001), and images in the *B*, *V* and *R* bands have been provided by the Garching-Bonn Deep Survey (Schirmer et al. 2003). *U* and *I* images have a total exposure time of 13.2 and 7.47 hours, respectively. The latter were obtained by stacking the images from the GOODS/ESO Deep Public Survey and supplementing them with archival WFI images. A total exposure times of 15.8, 15.6 and 17.8 hours were reached in the *B*, *V* and *R* bands, respectively. All optical observations were obtained under very similar seeing conditions (1'') with a marginal spread of less than 5%.

The *J*, *H* and *K_s*-band data were observed with ISAAC at the VLT and are part of the GOODS/ESO release 0.5¹. The near-infrared observations are split into eight sub-fields, with a size of 3'×3' each (plate scale 0''.148/pixel). They cover the central part of the optical images which have a field of view of 30'×30' (0''.238/pixel). The sub-fields are overlapping by ∼25'', which reduces the total analyzed area to 50.64 arcmin². The exposure times in each filter differ between the eight sub-fields and range from 2.2 to 4.2, 3.9 to 5 and 5.8 to 7.9 hours in the *J*, *H* and *K_s* bands, respectively. Moreover, the seeing conditions varied significantly for the eight sub-fields and between the three near-infrared bands (see Tab. 2.1).

2.2.1.1 Source detection and multi-band photometry

Source detection and multi-band photometry was performed using YODA (Drory 2003). This package was specifically designed for multi-band imaging surveys. It takes into account that in mosaiced frames as well as in dithered images the background noise is often inhomogeneous across the field. Furthermore, the frames do not usually share a common coordinate system and/or pixel scale, due to the use of multiple telescopes and imagers. This is a severe issue, since re-sampling the images to a common coordinate system inevitably

¹ Available at <http://www.eso.org/science/goods/>

2 Observing the coloured Universe: the large deep surveys

introduces considerable noise, especially for faint sources. The methodology used here is resembling the method described in Drory et al. (2001b). Below, details on the detection, image registration and photometric measurements, specific for this analysis, are given.

Detection

Source detection was performed in the K_s -band sub-images. Because of the considerable seeing variability between the individual sub-fields this results in varying limiting depths for the sub-fields. Compared to a degradation of the quality of all images to that with the worst point spread function (PSF), this has the advantage of reaching the optimum depth for each sub-field.

For a given image, the number of detected sources mainly depends on three parameters, namely (i) the threshold level above the background, (ii) the minimum number of connected pixels above that threshold which define an object and (iii) the minimum number of pixels above the detection threshold in splitted objects. Playing with the parameters can increase the number of (faint) detected sources, but most of these sources are actually noise. In order to obtain the optimal choice, simulations with different parameter combinations have been performed for each K_s -band sub-field on the original image as well as on its inverted version which was simply obtained by multiplying with -1. Original and inverted image show the same fluctuations in the sky background, thus, object candidates found with the given parameter combination can be only false detections. Naturally, the same parameter set will select false detections of the same kind in the original image. Variation of the search parameters can either yield a vanishing amount of false detections on the inverted image which goes hand in hand with a small number of detection on the original image obviously cutting at relatively bright magnitude and leaving real objects undetected. The opposite extrem is a catalogue containing securely all visible objects but also a huge amount of false detections on the inverted image indicating that most of the faint sources in the obtain catalog are not real ones. As we intend to derive statistical investigations (e.g. luminosity functions) from the catalog we found a false detection rate of 1% as indicated by the inverted image technique acceptable. We chose a detection threshold of 3.5σ and minimum numbers of 7 and 5 consecutive pixels above the threshold for single and split objects, respectively. A source catalogue for each subfield was generated accordingly.

Due to dithering, the borders of the images were not homogeneously exposed, thus leading to numerous false detections and objects with unreliable photometry. Moreover, ISAAC images are effected by distortion which can reach $0.2''$ at the corners of the images. In order to limit these effects, all detections located within 50 pixels from the borders were removed. Nevertheless, an overlap of few arcseconds still remains between neighboring sub-fields. A cross check between the 8 catalogues revealed the presence of 65 sources with multiple detections. For these sources only the detection with the largest distance to the border of the image was included into the final source lists. The resulting catalogues consist of 3294 sources split into 450 in F09, 461 in F10, 427 in F11, 409 in F14, 351 in F15, 336 in F16,

2.2 The Great Observatories Origins Deep Survey South Field

Table 2.1: Seeing of the near-infrared images for the 8 sub-fields. The completeness and surface brightness limits for the K_s -band images, based on the re-calibrated photometry are given as well.

Field	<i>J</i>	<i>H</i>	K_s	50% compl.	s. b. lim.
	"	"	"	mag	mag/arc s^2
F09	0.36	0.43	0.39	24.71	24.47
F10	0.51	0.57	0.45	24.45	24.57
F11	0.46	0.48	0.44	24.73	24.54
F14	0.45	0.42	0.48	24.95	24.78
F15	0.47	0.67	0.49	24.69	24.75
F16	0.41	0.60	0.55	24.12	24.32
F20	0.46	0.50	0.39	25.04	24.60
F21	0.40	0.49	0.39	24.98	24.68

408 in F20 and 452 in F21.

The 50% completeness limits for point-sources were estimated following the procedure described in Snigula et al. (2002), where the authors made an extensive completeness simulation for imaging surveys of faint galaxies, taking into account their known size-surface-brightness relation.

The resulting value for each sub-field, together with the surface brightness limit, is listed in Tab. 2.1. Note that the quantities were computed *after* the tuning of the photometry as explained in Sect. 2.2.1.2.

Multi-band photometry

After source detection, all optical and near-infrared images were convolved to the worst seeing among the images in the dataset, namely to the 1'' seeing of the *B*-band frame. In the next step, each convolved image was registered to the pixel coordinate system of the corresponding un-convolved K_s -band image in which the detection was performed. The registration has been performed in IRAF environment, using a modified version of the task *imatch*. As first step, for each K_s image (reference image) the center of at least 5 bright and isolated sources have been measured and identified in all the other bands, in order to make a first order registration. Following, the task detects all the others bright sources in the reference image and looks for the corresponding source in the other images, defining the matrix to transform the coordinates of the reference image in the new images. The procedure has the advantage to be unaffected by the distortion of ISAAC data.

After transforming the coordinates the count rates in all filters were measured in fixed apertures of 1''.5 (i.e. 1.5 times the seeing). Furthermore, the total magnitudes included

2 Observing the coloured Universe: the large deep surveys

in Kron-like apertures (Kron 1980) were derived. The small fixed aperture was chosen in order to avoid the flux contamination from neighboring objects. As a further advantage the colour gradient of extended objects far from the center are ignored. Thus, later spectral energy distribution (SED) fitting will not take into account colour gradients outside of the aperture. The fluxes were measured with both YODA and SExtractor (Bertin & Arnouts 1996), and the values were found to be consistent. Preliminary magnitudes of the sources were computed based on the zero-points and associated uncertainties provided in the image headers. More precise magnitudes were achieved after the tuning of the zero-points of the images as described in the following section.

2.2.1.2 Photometric redshift

Photometric redshifts for the detected sources were computed as described in section 2.1.2. In brief, the templates were obtained by grouping approximately 300 observed spectra of galaxies from the FORS Deep Field (FDF; Heidt et al. 2003) and the Hubble Deep Field North (HDF; Williams et al. 1996) according to their spectral properties and extending them by fitting a combination of different stellar population models by Maraston (1998) with different ages and dust extinction values. As a result, representative SED templates with variable star-formation activity, age, metalicity, and dust extinction were obtained. The complete set of 29 SED templates is shown in Fig. 2.5.

In addition to the galaxy templates, each source of the catalogue was also compared with the stellar SEDs from the Pickles compilation of stars with solar abundance, metal-weak and metal-rich F-K dwarf and G-K giant components (Pickles 1998). The χ^2 obtained for the best galaxy and best stellar SEDs will be used to discriminate between stars and galaxy (see section 2.2.1.3).

The calibration

As it has been demonstrated in CADIS (Wolf et al. 2001) and in FDF (Bender et al. 2001), main sequence stars provide the most robust check of photometric zero-points.

Since only a handful of stars were present in each of the 8 sub-fields, this method could not be used to calibrate the photometry. Nonetheless stellar photometry was used as an *a posteriori* photometric sanity check as described later in this section.

Photometric zero-points of the images and photometric redshifts were calibrated using the observed spectra of 135 galaxies. 120 of these were taken from the GOODS/EIS webpage available prior to the release of the spectroscopic master catalogue². In addition 15 spectra of non-active galaxies were taken from the follow-up of X-ray observations in the Chandra Deep Field South (Szokoly et al. 2004). The redshift distribution of these 135 galaxies ranges from $z = 0.2$ to $z = 6.0$, with the majority of them lying between $z = 0.5$ and $z = 1.4$.

²http://www.eso.org/science/goods/spectroscopy/CDFS_Mastercat/

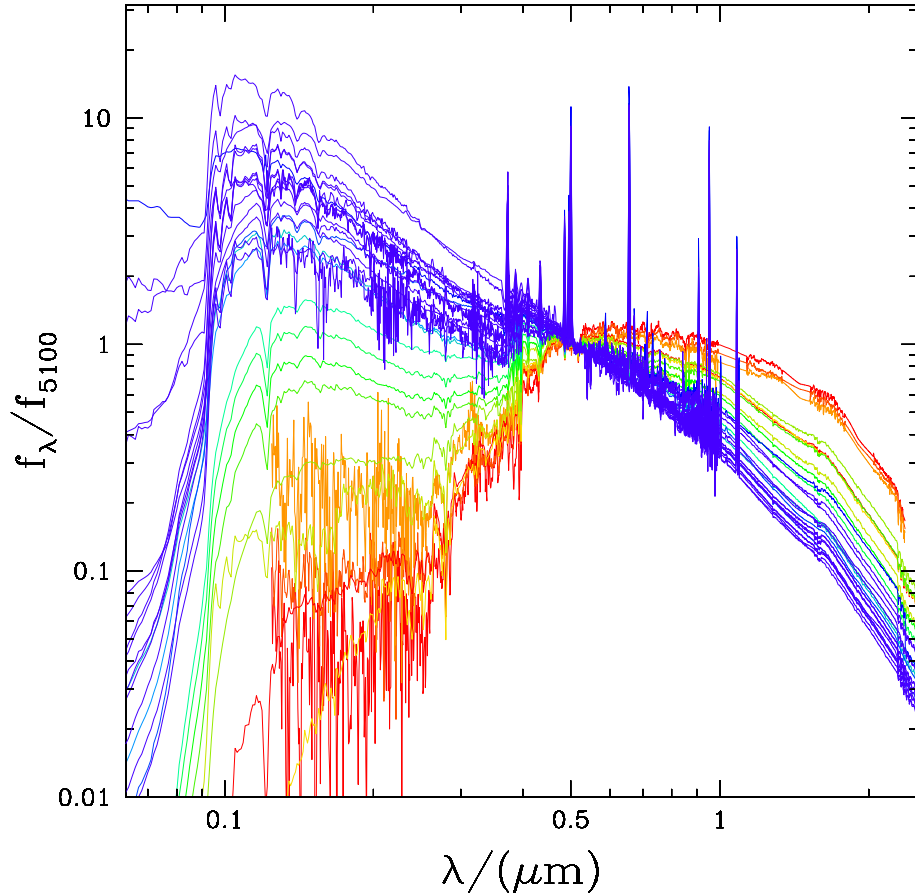


Figure 2.5: SED template library used for the photometric redshift determination. All templates are normalized to the flux at $\lambda = 5100\text{\AA}$.

The technique of photometric redshift is in general very sensitive to uncertainties in the photometry (see Bolzonella et al. (2000) for a complete discussion). Therefore, precise zero-points of the individual images are mandatory. Unfortunately, the first release of the optical GOODS/EIS images suffered from significant inaccuracies of the zero-points in the U and I bands (see Arnouts et al. 2001; Manfroid & Selman 2001; Hildebrandt et al. 2005). In addition, field-to-field variations of the order of 0.1 mag in J and 0.2 mag in K_s were already noted when the data were released. For the H -band data field-to-field variations were not ruled out in the release.

Being aware of these uncertainties, we allowed for small changes in the zero-points of the images in order to increase the accuracy of the photometric redshift solution. In a given

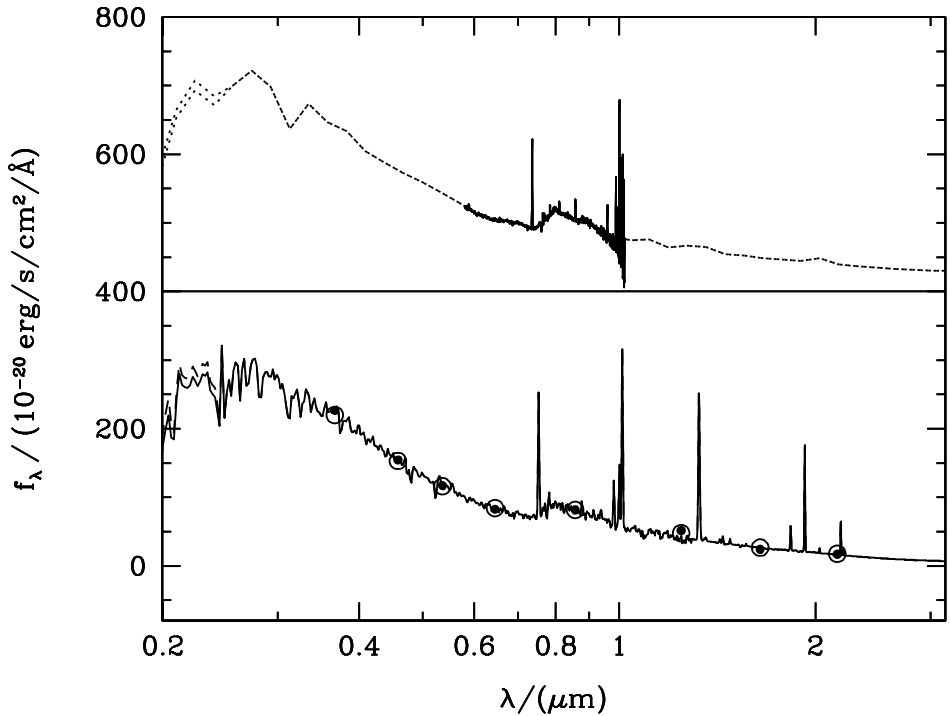


Figure 2.6: Template fitting to the photometric points for a galaxy with $R=23$ mag (bottom panel). The best photo-z fit is obtained with a late-type galaxy template at $z = 1.02 \pm 0.05$. The galaxy has actually a spectroscopic redshift of $z = 0.97$ and is shown for comparison in the top panel.

optical band, the same correction to the zero-point was applied in all sub-fields, as single images cover the whole area. In the near-infrared, new zero-points were independently obtained for each of the eight sub-fields. The zero-points were considered appropriate when for each object with an available spectrum (*i*) the photometric redshift was consistent with the spectroscopic one and (*ii*) the selected galaxy template was resembling the actual spectrum. A typical example is shown in Fig. 2.6, where the best fitting SED template is compared to the real observed spectrum of a galaxy with $R=23$ mag. The resulting photometric redshift of $z=1.02\pm0.05$ is perfectly consistent with the spectroscopic redshift of $z=0.97$.

The final corrections to the zero-points in the B , V and R bands are only marginal, while U and I required a systematic brightening of the order of 0.25 magnitudes. In the J band the necessary correction was on average -0.1 mag, while the H and K_s -band zero-points needed a modification in a range of -0.45 to $+0.19$ mag depending on the sub-field. Applying these corrections, a set of new zero-points was computed for all bands. The obtained values were used to compute the actual surface brightness limits of the K_s -band images and the

2.2 The Great Observatories Origins Deep Survey South Field

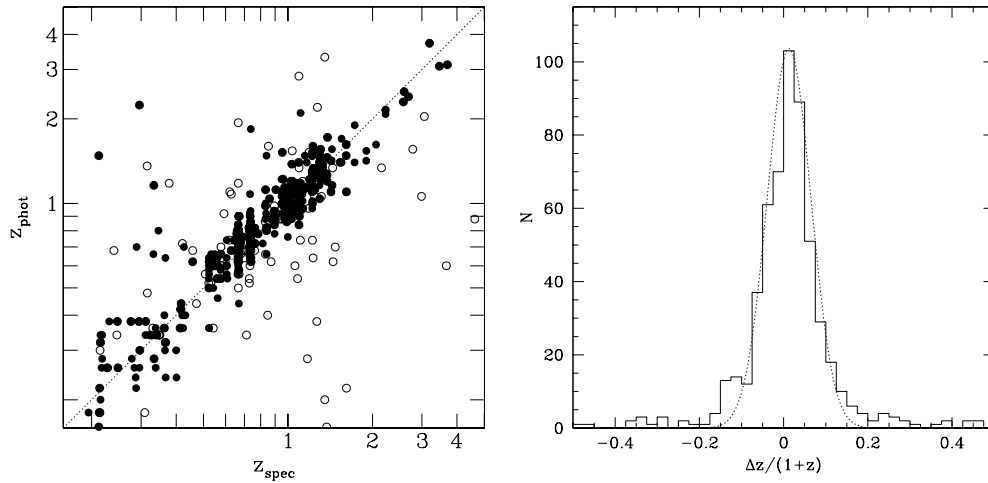


Figure 2.7: Left panel: Comparison between the photometric redshifts presented in this chapter and publicly available spectroscopic redshifts for galaxies in GOODS-S. This includes objects in common with the VVDS (Le Fèvre et al. 2004), observed with the VLT/FORS2 (Vanzella et al. 2005), from the spectroscopic follow-up of *Chandra* selected sources (Szokoly et al. 2004) and from K20 (Mignoli et al. 2005). The filled circles indicate objects for which the spectroscopic redshifts were flagged as highly reliable (flag(VVDS)=4, flag(VLT/FORS2)=A, flag(Szokoly)=2, flag(K20)=1). Empty circles mark galaxies with lower reliability. Right panel: Distribution of the uncertainties in the photometric redshift (solid histogram). It can be fitted by a Gaussian distribution (dotted line) centered at $\Delta z/(1+z) = 0.012$ with a σ of 0.05.

aforementioned completeness limits of the catalogues presented in Table 2.1.

Fig. 2.7 shows the comparison between our photometric redshift and the now available spectroscopic redshift for a sample of approximately 500 galaxies (i. e. including the 135 galaxies used for the calibration above; see figure caption for details). Considering only galaxies with highly reliable spectroscopic redshifts, an accuracy of $\Delta z/(1+z) = 0.05$ is reached independent of redshift, the highest precision achieved for this specific dataset of images so far.

Verification of the zero-points

Although the achieved accuracy of the photometric redshifts is a crucial test of our re-calibrated zero-points, we performed additional tests using (i) color of the stars in the 8 subfield compared with theoretical stellar color, (ii) photo-z comparison for sources detected in more than one sub-field, (iii) the H -band catalogue of the Las Campanas Infrared Survey (Chen et al. 2002), (iv) photometry and (v) photometric redshifts provided by COMBO-17 (Wolf et al. 2004). Moreover, in September 2004 the release v1.5 of the ISAAC images became available. Although the new release has a more accurate photometry, the images are shallower than the previous ones. For that reason we decided to stick to the release v0.5 and to use the release v1.5 to verify our correction.

After computing the new zero-points it was possible to look at the color color diagrams of the stars (Fig. 2.8, open circles), and compare them with the expected color of main sequence stars with solar (red solid line) and low (blue dashed line) metallicity. The colours of synthetic stars as function of metallicity have been computed on the Kurucz (1979) theoretical model atmospheres, as in the compilation of Lejeune et al. (1998). In general, the observed distribution of stars is reasonably well reproduced by the color distributions of library stars with a metal spread as observed in disk and halo of the Milky Way. As discussed above, 65 sources were detected in more than one of the eight K_s -band images. For each of these sources and for a given near-infrared band, the photometry of the multiple detections (after the zero-point correction) is in agreement within 0.05 mag or better. The resulting values for the photometric redshifts of the individual sources are consistent within $\Delta z_{phot} = 0.03$.

Observations of the GOODS-S field in V , R , I , z and H are also included in the Las Campanas Infrared Survey. Chen et al. (2002) provide the H -band photometry for sources brighter than $H \sim 20.8$ mag in a fixed aperture of $2''$. In order to allow a comparison with their results, we recomputed the flux measurements in the H band using the same aperture. The magnitude difference $\Delta M_H = M_{H, \text{Las Campanas}} - M_{H, \text{this work}}$ for common sources, before and after the zero-point correction, are shown in the left panel of Fig. 2.9. Using the original zero-points, the distribution showed an offset of $\Delta M_H = 0.04$ mag and a non-negligible asymmetry due to field-to-field variations. With the new zero-points this asymmetry disappears and the distribution is centered at $\Delta M_H = 0.03$ mag with an RMS of 0.1 mag.

We further compared our photometry and photometric redshifts with the results of COMBO-17 (Wolf et al. 2004), a survey based on photometry in 17 optical filters, including 12 medium-band filters.

These filters are sensitive to individual emission lines and therefore allow a photometric redshift accuracy of up to 1% for sources brighter than $R = 21$. The precision decreases for fainter objects, reaching 10% at $R > 24$. A total of 499 targets with photometric redshifts and classified as *galaxy* in COMBO-17 are also present in our catalogues. A comparison of the photometric redshifts is shown in the right panel of Fig. 2.9.

Following Wolf et al. we estimated the precision of our photometric redshift in different

2.2 The Great Observatories Origins Deep Survey South Field

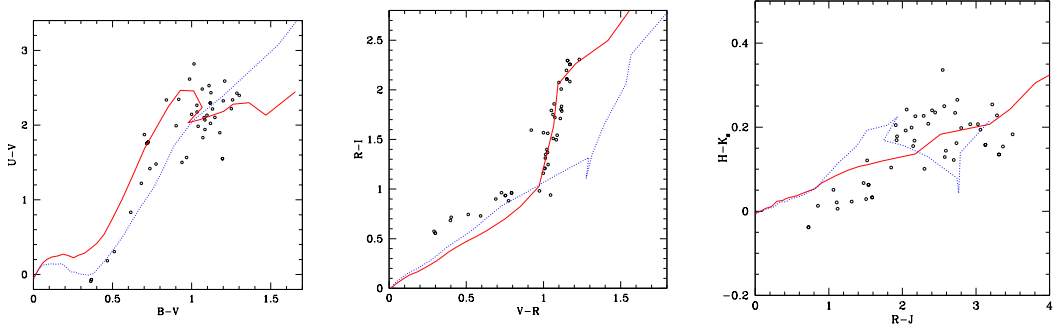


Figure 2.8: Three examples of color color diagram for main sequence stars with solar (red solid line), and low (blue dashed line) metallicity and stars in the GOODS field, after correction of the zero-points.

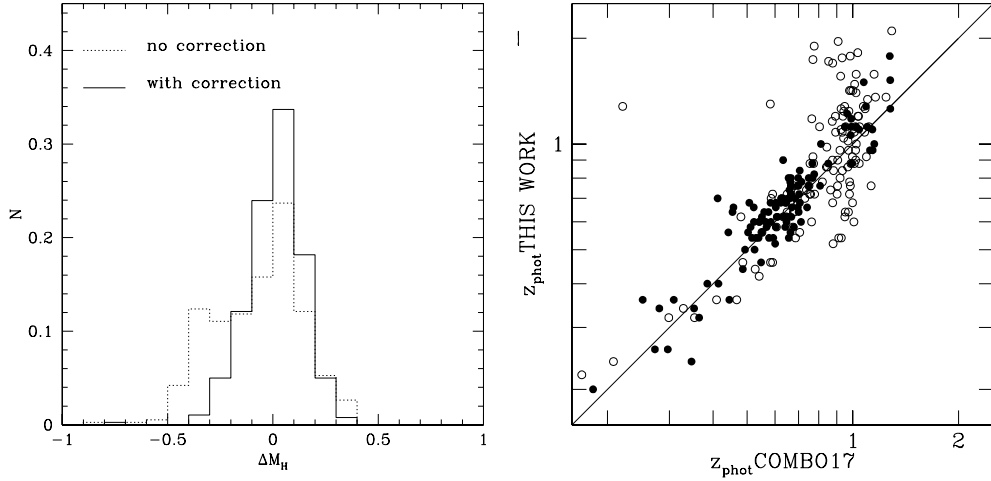


Figure 2.9: *Left panel:* Histogram of magnitude differences between the H -band photometry from the Las Campanas Survey and this work computed within a fixed aperture of $2''$. The dashed and solid lines show the distribution before and after the correction of the zero-points, respectively. After the correction the asymmetry of the distribution disappears. *Right panel:* Comparison between the photometric redshifts presented in this work and those provided by COMBO-17 for the galaxies in common. Filled circles represent galaxies brighter than $R = 23.5$ mag and empty circles mark fainter sources.

magnitude intervals. We defined $\Delta z = (z_{\text{COMBO-17}} - z_{\text{this work}})/(1+z_{\text{COMBO-17}})$, assuming the photometric redshift of COMBO-17 as *true redshift* and we computed the deviation of our photometric redshift from them. For galaxies brighter than $R = 21$ an accuracy of $\Delta z \sim 0.02$

2 Observing the coloured Universe: the large deep surveys

was achieved. This value corresponds to the intrinsic binning of our photometric redshift procedure. Sources with $21 < R < 23.5$ have a Δz of 0.05. For galaxies fainter than $R = 23.5$, the photometric redshifts of COMBO–17 exhibit significant uncertainties. Therefore, these sources could not be used for further verification of the quality of our results.

Finally, a comparison of the photometry of the sources using both, the release version 0.5 (after zero-point correction) and the newest version 1.5, was due. The zero-points in the new release are computed by comparing photometry of stars in photometrically calibrated SOFI images and, as clearly stated in the web page of GOODS/ESO, "uncertainties are not negligible due to the calibration procedure and residual non-uniformities in the images (either ISAAC or SOFI)". A calibration using photometric standard stars is still missing and need to be done. For the comparison we used between 300 and 400 sources per field for which the match in R.A. and DEC coordinates was better than $0.5''$. In many frames the averaged difference in the photometry is close to zero (see for example F21 in the H and K_s band) with a scatter driven by the faint sources. The general agreement with the new released version 1.5 confirms that our recalibration is reliable.

2.2.1.3 Source catalogue

After removing the field-to-field variations of the photometry and the verification of the photometric redshift accuracy, we applied our method to all eight K_s -band source catalogues. Below we describe how stars are identified and how we treated AGN for the subsequent analysis of the galaxy luminosity function.

Stars

The catalogue contains 57 stars. 14 of them have known spectral type provided by SIMBAD and for 22 for which stellar spectra have been observed in the follow-up by VVDS, VLT/FORS2 spectroscopy in GOODS-S and K20. As demonstrated in Gobasch et al. (2004a), stars can be also identified by the photometric redshift technique. We classify as stars all objects for which the best fitting stellar SED gives a better match than any galaxy template ($2\chi^2_{\text{star}} < \chi^2_{\text{galaxy}}$). According to this criterion 41 stars were selected, out of which $\sim 50\%$ were also spectroscopically confirmed.

AGN

The K_s -band selection naturally does not distinguish between normal and active galaxies, thus also AGN and quasars are contained in the final source catalogue. As no specific AGN template is included in our photometric redshift code, a separate verification of the reliability of the photometric redshift for those galaxies was required.

For this purpose, we compared the photometric redshifts for 36 X-ray selected sources from our catalogue with secure spectroscopic redshifts provided by Szokoly et al. (2004).

2.2 The Great Observatories Origins Deep Survey South Field

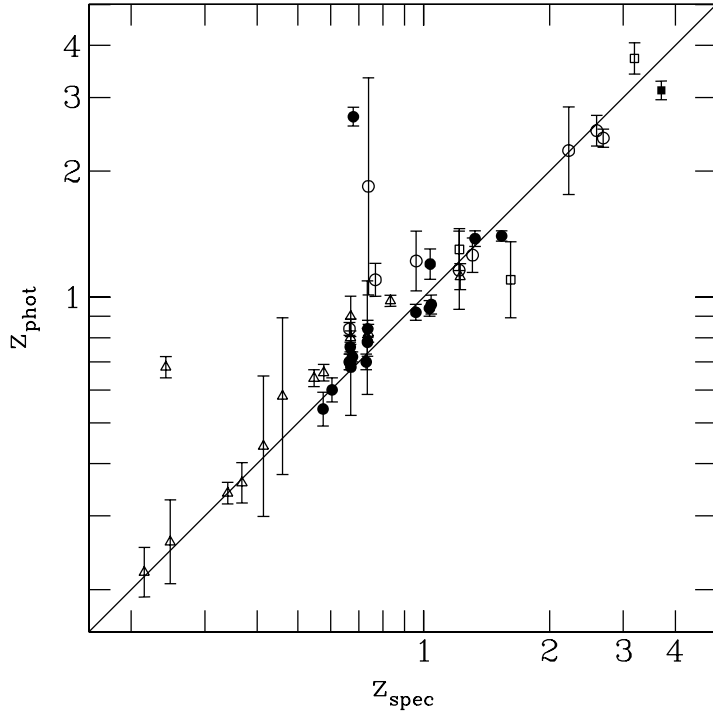


Figure 2.10: Comparison of the photometric redshift presented in this work with the spectroscopic redshift for 36 X-ray selected galaxies. Symbols are as defined in Zheng et al. (2004), where open circles represent type-I AGN, open squares type-I quasars, filled circles type-II AGN, filled squares type-II AGN and triangles galaxies. The accuracy is $\Delta z/(1 + z) \sim 0.05$. Note that no specific AGN SED template was used. This suggests that the light of the host galaxies dominates over the nuclear emission.

15 of those were classified as *galaxies* on the base of their optical spectra and already used for the photometric calibration method described above. The remaining sources include 7 type-I and 14 type-II AGN.

We find a good match of the photometric and spectroscopic redshifts for all 36 sources with an accuracy of $\Delta z/(1 + z) = 0.05$ (see Fig. 2.10). Irrespective of the small sample size, the achieved precision overcomes results obtained from previous applications of photometric redshift codes on X-ray selected samples, including those using AGN templates (e.g., Zheng et al. 2004).

As no specific AGN SED templates were used to obtain the photometric redshifts, the accurate match with the templates of normal and star-forming galaxies suggests that the optical emission of the X-ray selected sources is dominated by the host galaxy rather than

2 Observing the coloured Universe: the large deep surveys

the central engine. Therefore, these galaxies remained included in the final source catalogue.

Only for two sources significant deviations between the photometric and spectroscopic redshifts were found, namely (ii) a normal galaxy, and (iii) a type II AGN. In both cases the algorithm has picked up the right redshift as second solution.

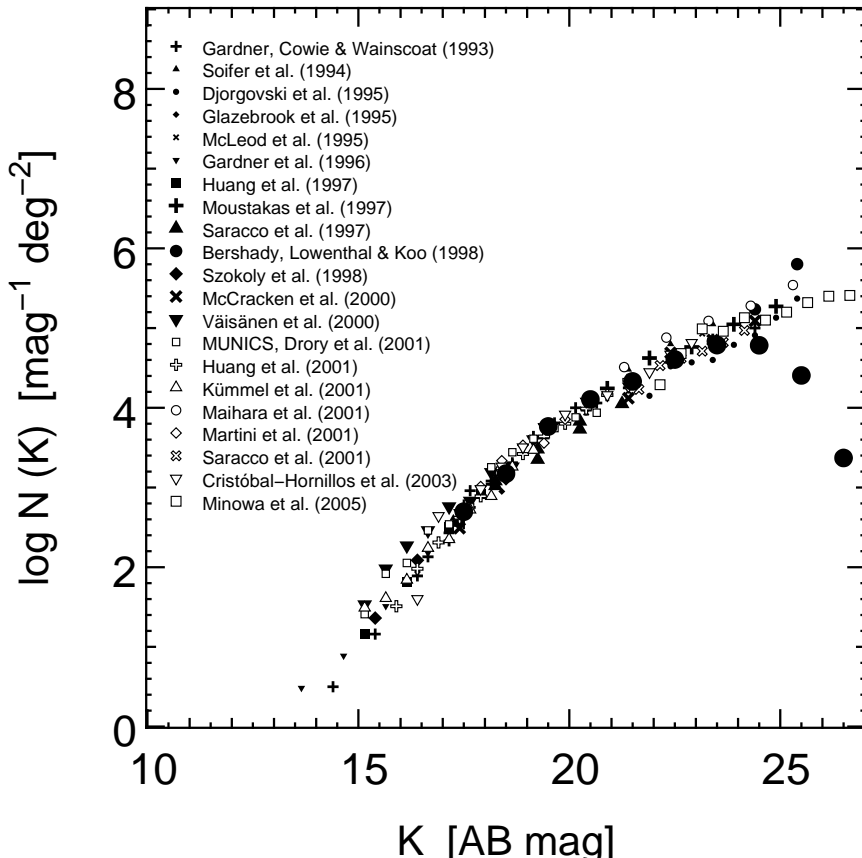


Figure 2.11: Galaxy number counts in the K_s band from our catalogue, not corrected for incompleteness (filled red circles) and from previous studies (other symbols).

The final catalogue

After removal of the stars, the galaxy number counts for the 3237 galaxies of the final catalogue have been computed (Tab. 2.2) and a good agreement has been found when comparing the results to previous studies (Fig. 2.11). This is the catalogue that has been already used, together with the FDF, in Gabasch et al. (2004b), Drory et al. (2005), Feulner et al. (2005a) and Pannella et al. (2006) for deriving the star formation history, the evolution of

2.2 The Great Observatories Origins Deep Survey South Field

Table 2.2: Differential K_s -band galaxy number counts and Poisson errors in the GOODS-S field. The counts are not corrected for incompleteness.

K_s [mag]	$\log N(K)$ [mag $^{-1}$ deg $^{-1}$]	$\delta \log N(K)$ [mag $^{-1}$ deg $^{-1}$]
17.50	2.70	0.17
18.50	3.17	0.10
19.50	3.77	0.05
20.50	4.10	0.03
21.50	4.33	0.03
22.50	4.61	0.02
23.50	4.79	0.01

the stellar mass, the specific star formation rate and the evolution of galaxy morphology of field galaxies within a vast redshift regime. In the following section we analyze the redshift distribution obtained in our deep catalog.

2.2.1.4 Redshift distribution

To better characterize the galaxy population probed by our sample we study the distribution of the absolute I -band magnitude with redshift for the various SED templates (see left panel of Fig. 2.12). It confirms that early-type galaxies are present out to relatively high redshifts of $z \sim 2$ in a deep K_s -band selected catalogue (Cimatti et al. 2004). Later types can be traced to even higher redshifts.

This trend can be seen also in the right panel of Fig. 2.12, where we reproduce the redshift distribution of the sample galaxies as a function of their SED (as attributed by the photo-z code). Galaxies classified as early type (red) appear mostly at redshift less than 1.5, while those classified as intermediate type (green) reach redshifts up to 4. On the other hand, objects with a starburst/irregular-type SED (blue) span the full redshift range. Only in a few cases, the photo-z code has attributed an early-type SED to objects at redshifts as high as 2.5. This can be naturally explained as follows. The rest-frame UV-to-optical SED of a heavily dust obscured starburst at these high redshifts is very similar to that of an old, passively evolving galaxy, so that the photometric redshift technique selects the wrong SED. This is particularly true in absence of any prior on the maximum redshift allowed for an early-type galaxy. In fact, when early-type SEDs are forced not to characterize galaxies at redshifts higher than 1.5, the new solutions of the photo-z code for the previous objects do correspond to a starburst-like SED. Furthermore, only 2% of these objects have a new redshift that differs by more than 0.2 from the original one, the fraction of those with a difference in redshift larger than 0.5 being only 1%. In the same panel, the total redshift distribution of

2 Observing the coloured Universe: the large deep surveys

the objects is shown as a black line. Large scale structures spectroscopically detected at $z \sim 0.7$ (Cimatti et al. 2002; Gilli et al. 2003; Le Fèvre et al. 2004), $z \sim 1.1$ (Vanzella et al. 2002), $z \sim 1.61$ (Gilli et al. 2003), and $z \sim 3.5$ (Caputi et al. 2005) can be also seen in the histogram of photometric redshifts.

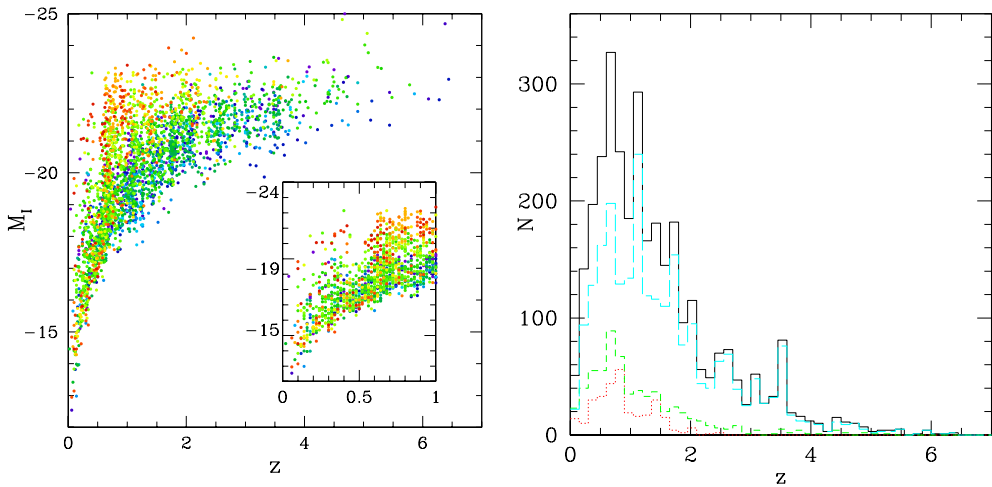


Figure 2.12: *Left panel:* Absolute I-band magnitude versus photometric redshift. (color version of the figure is available online where a smooth colour transition from red to blue indicates the different SED template of the galaxies, where red corresponds to early types, and blue to late types. Note the lack of galaxies in the redshift range 0.2 to 0.6 (see inset). *Right panel:* Redshift number distribution of all galaxies in the GOODS-S sample, where, for simplicity galaxy types have been grouped in early type (red), late type (cyan) and intermediate type (green). The clustering visible at $z \sim 0.7, 1.1$, and 1.6 is spectroscopically confirmed.

2.3 The Cosmic Evolution Survey

The Cosmic Evolution Survey (COSMOS) (Scoville et al., in preparation) is an HST Treasury Project to survey a 2 square degree equatorial field with the Advanced Camera for Surveys (ACS). It is the largest survey that HST has ever done (640 orbits, see Figure 2.13 for a comparison with previous ACS efforts). The project also incorporates major contributions from other observatories around the world, including the VLA radio telescope, ESO's VLT in Chile, ESA's XMM X-ray satellite, and Japan's 8-meter Subaru telescope in Hawaii.

COSMOS combines deep to very-deep multi-waveband information in order to extend the analysis of deep pencil beam surveys to a much bigger volume, thus being able to drastically increase the statistics and detect also very rare objects.

The primary goal of COSMOS is to study the relationship between large scale structure (LSS) in the universe and the formation of galaxies, dark matter, and nuclear activity in galaxies. This includes a careful analysis of the dependence of galaxy evolution on environment. The wide field coverage of COSMOS will sample a larger range of LSS than any previous HST survey. Therefore, COSMOS allows us to map the morphology of galaxies as a function of local environment (density) and epoch, all the way from high redshift ($z > 3$) to the nearby ($z < 0.5$) Universe.

Combined with the follow-up observations from space- and ground-based facilities, COSMOS addresses fundamental issues in observational cosmology, including the evolution of LSS, the formation, assembly and evolution of galaxies and star formation as a function of environment, morphology and redshift. In particular, the wide-area COSMOS-ACS survey yields 10^5 galaxies with multi-waveband color information. Combined with photometric and spectroscopic redshifts, COSMOS thus allows the measurement of the evolution of the galaxy population properties with redshift and environment. This is of fundamental importance in constraining galaxy formation scenarios.

2.3.1 A deep galaxy catalogue in the COSMOS field

Adapted from A. Gabasch et al., “A deep galaxy catalogue in the COSMOS field”, MNRAS submitted

In this work we combine publicly available u, B, V, r, i, z, and K COSMOS data with proprietary imaging in the H band to derive a homogeneous multi-waveband catalogue suitable for deriving accurate photometric redshifts. Our observing strategy was designed to follow-up the publicly available COSMOS observations with proprietary imaging in H band. The whole area is covered by 25 pointings (15.4'x15.4' each) to a depth adequate to the public NIR data. The programme was carried out as a joint effort between three large extragalactic survey projects currently being pursued at the Centro Astronómico Hispano Alemán (CAHA), on Calar Alto: ALHAMBRA (Moles et al. 2005), MANOS-wide(Röser et al. 2004) and MUNICS-Deep (Goranova et al., in prep.). In addition, as a part of the MUNICS-Deep project, in one of the pointings (01c) we have also collected deep Js- and K'-band data.

2 Observing the coloured Universe: the large deep surveys

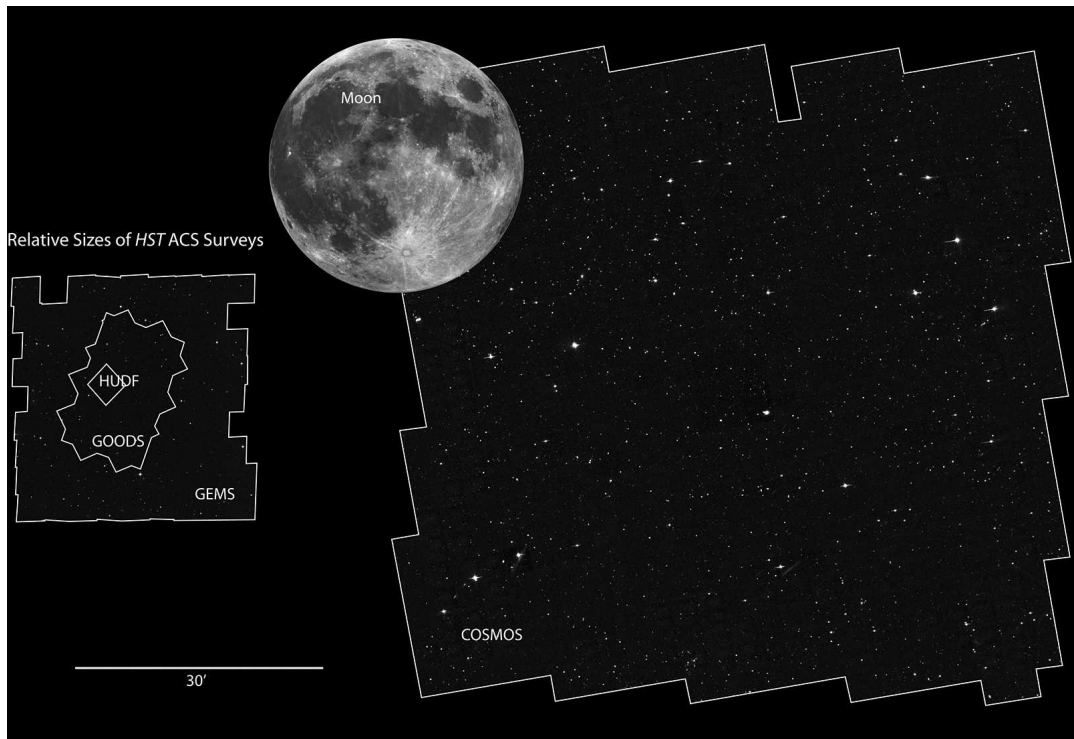


Figure 2.13: The COSMOS field compared with the Moon angular size and also with other ACS deep field surveys.

2.3.1.1 NIR imaging data: acquisition

The observations in H, Js and K' bands were carried out using the NIR wide-field imager OMEGA2000³, operating at the prime focus of the CAHA 3.5m telescope. OMEGA2000 is equipped with a HAWAII-2 HgCdTe 2048x2048 array. The instrument pixel scale is 0.45'' per pixel, providing a field-of-view of 15.4'x 15.4'.

Here we present the H-band observations in 15 pointings, collected during 11 nights spanned over 3 observing campaigns: December 2004, February 2005, and March/April 2005. Each pointing was observed for a total of 3 ksec. The individual exposure times were 3 sec, on-chip co-added to produce single frames of 60 sec each. Except for 05b, at least 50 such frames (depending on the weather conditions) were observed per pointing.

In addition, observations in Js and K' bands in one pointing were collected during 7 night in the observing campaigns November 2003 and February 2006. The total exposure time in Js-band data was 8.2 ksec with the same individual exposure time scheme like in the H band. The K'-band observations have a total of 7.7 ksec exposure time with individual exposures

³<http://w3.caha.es/CAHA/Instruments/O2000/index2.html>

of 2 sec, co-added internally into single frames of 30 sec each.

All observations were done using dithering pattern consisting of typically 20 positions shifted with respect to one another by $20''$. The consecutive dithering sequences were repeated with the same pattern but with an offset in the origin.

2.3.1.2 NIR imaging data: reduction, photometry and cataloging

In this section we present the NIR imaging data in the J, H, and K' bands. We developed a 2-pass reduction pipeline optimised for reducing and stacking images of different quality to get an optimal signal-to-noise ratio for faint (sky dominated) objects.

Since our final goal is the combination of our H-band data with public data to construct a multi-wavelength catalogue, we want to astrometrically align our H-band images to the publicly available images in the COSMOS field (Scoville et al., in prep.). Moreover, as we intend to use the same procedure as in the FDF in constructing the catalogue (Heidt et al. 2003), i.e. using SExtractor in the double image mode, the data sets in the different passbands must also be aligned by pixel. On the other hand, we do not want to shift the NIR images twice. This would smooth the images and destroy the signal of very faint objects. As it is also very challenging to shift single NIR images on top of deep optical images (where many bright starlike objects are e.g. saturated), we use the following approach:

First we compute the astrometric transformation between our stacked NIR image and the reference optical frame (Subaru z-band). This allows us to rely on hundreds of objects when computing the astrometric solution instead of only a few tens of objects visible in a single NIR image. Knowing the relative shifts of the single images to the stacked XDIMSUM image and the full astrometric solution of the latter (with respect to the Subaru z-band), we are able to calculate the astrometric solution also for each single, *unshifted* pre-reduced image. Restarting from these images, we do the alignment, the distortion correction, the regridding and the stacking of the individual images (with optimal signal-to-noise ratio, see below) in *one* step.

As the single exposures were not taken under the same observing conditions, the sky levels, the seeing, and the zeropoints can substantially differ from frame to frame. On the other hand this gives one the possibility to stack the single images with weighting factors in order to achieve a final combined frame with optimal signal-to-noise ratio (S/N).

Finally, we did the image alignment, the distortion correction, the regridding and the stacking of the individual images with optimal S/N in one step by using standard IRAF routines as well as SWarp (Bertin, E. 2003). The regridding has been done to the native pixel scale of the Subaru telescope ($0.2''$ per pixel). Please note that we do not interpolate any bad pixel or bad region in the single images, but set them to zero during the stacking procedure.

Since a different number of dithered frames contributed to each pixel in the co-added images (producing a position-dependent noise pattern) a combined weight map for each frame was constructed. The latter was used during source detection and photometry procedure to

properly account for the position-dependent noise level.

The absolute photometric calibration is based on the 2MASS (Jarrett et al. 2000) catalogue. First we cross-correlate the objects in all our reduced patches with sources in the 2MASS catalogue. We exclude all objects with possible problems in either one of the catalogues relying on the quality flags of 2MASS and SExtractor quality flags (only objects with a flag of ≤ 3 are considered). An error weighted fit between these objects (20 to 45, depending on the patch) then determines the zeropoint as well as its error. The accuracy of the zeropoint in the different fields is in the order of 0.01 magnitudes.

Based on the stacked images we derived 15 H-band selected catalogues as well as 1 J-band and 1 K-band selected catalogue (in field 01c, only). For this purpose we run SExtractor (Bertin & Arnouts 1996) with the detection threshold $t = 2$ (minimum signal-to-noise ratio of a pixel to be regarded as a detection) and $n = 3$ (number of contiguous pixels exceeding this threshold). Depending on the depth⁴ of the different patches, we detect between 2000 and 4000 objects (excluding patch 05b where we have only half of the minimum exposure time we wanted to achieve). The false detection rate are in the order of one percent or less (detected on the inverted image). Only around extremely bright and saturated objects (three in patch 02d and one in patch 03c) the false detection rate increases. As the regions around these four objects are not taken into account, we get an overall false detection rate in the order of 1 percent.

Because the depth of the patches decreases towards the borders, we limited our analysis to the inner field of each patch. This prevents a possible bias of the photometric redshifts due to a not completely homogeneous photometric information. In total we detected about 40 000 H-selected objects over an area of about 0.85d^o as well as about 4000 (3000) J (K) selected galaxies over an area of 205.44d^o .

The galaxy number counts can be used to check the calibration of the data set, to detect possible galaxy over or under-densities of a field as well as to determine the approximate depth of the data. We did not put much effort in star-galaxy separation at the faint end (as we did for the i-selected catalogue, see Sect. 2.3.1.3), where the galaxies dominate the counts. At the bright end, where SExtractor is able to disentangle a stellar and a galaxy profile, we used the star-galaxy classifier to eliminate obvious stellar objects. We present in Fig. 2.14 the H-band number counts of all patches and in Fig. 2.15 the Js and K' band number counts of patch 01c. Although the single patches show a scatter in the H-band number counts at the very bright end, there is a good to very good agreement between the literature number counts and our mean number counts (red dots) up to the 50 % completeness limit for point sources (Snigula et al. 2002). Comparing the Js and K' band number counts with data taken from the literature (Fig. 2.15) also shows a relatively good agreement, although patch 01c seems to be overdense with respect to most of the literature values. This is also true for the H-band number counts in 01c if compared to the other patches or to the literature, indicating an overdensity in this specific patch. Nevertheless, our results are compatible within the error

⁴as a result of the slightly varying seeing and total exposure times.

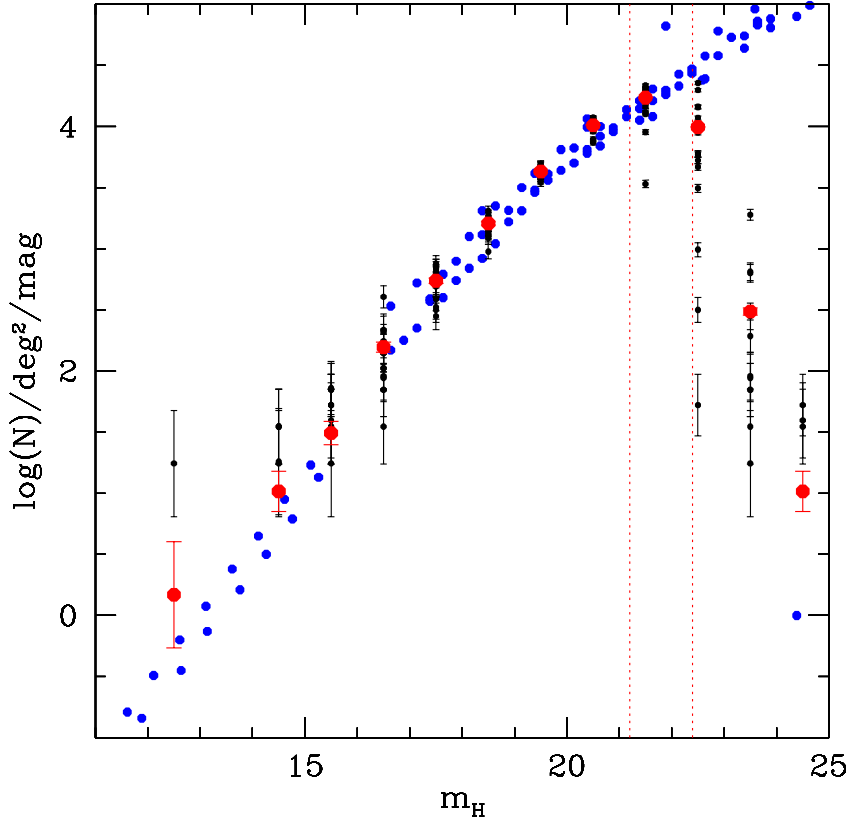


Figure 2.14: Galaxy number counts in the H-band (not corrected for incompleteness) as compared to the literature (blue dots). The black dots represent the number counts of the single patches, whereas the red dots show the average number counts of all fields. The vertical dotted lines indicates the 50% completeness limits of the shallowest (05a) and the deepest (02d) patches. The literature number counts are taken from Yan et al. (1998); Teplitz et al. (1998); Thompson et al. (1999); Martini (2001b); Chen et al. (2002); Moy et al. (2003); Frith et al. (2006); Metcalfe et al. (2006). The error bars show the 1σ Poissonian errors.

bars at a 1σ level.

Please note that the 50 % completeness levels for point sources (vertical red lines in Fig. 2.14 and Fig. 2.15) coincide very nicely with the faint-end region where the number counts start to drop. The values of the NIR galaxy number counts can be found in Table 2.3.

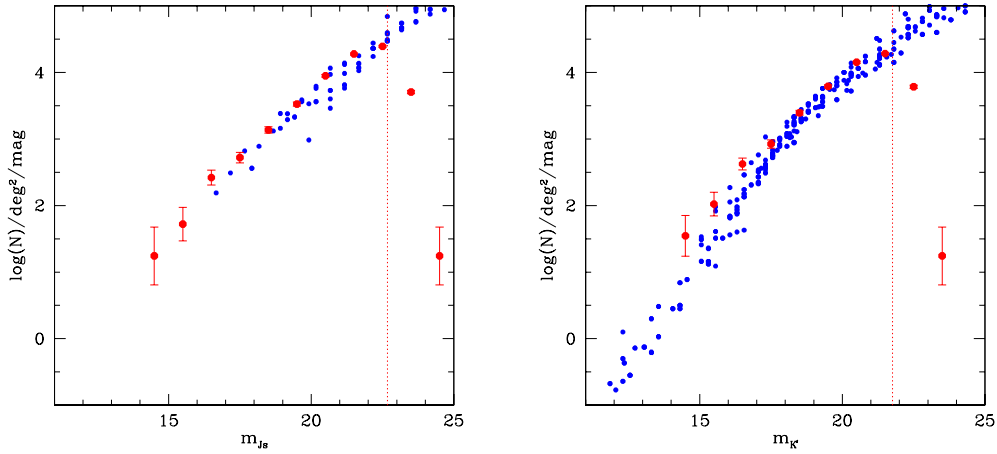


Figure 2.15: Left panel: Js-band galaxy number counts of patch 01c (red dots, not corrected for incompleteness) as compared to the literature (blue dots). The vertical dotted line indicates the 50% completeness limit. The literature number counts are taken from Saracco et al. (1999, 2001); Maihara et al. (2001); Teplitz et al. (1999). Right panel: K'-band galaxy number counts of patch 01c (red dots, not corrected for incompleteness) as compared to the literature (blue dots). The vertical dotted line indicates the 50% completeness limit. The literature number counts are taken from Gardner et al. (1993); Soifer et al. (1994); Djorgovski et al. (1995); Glazebrook et al. (1995); McLeod et al. (1995); Gardner et al. (1996); Huang et al. (1997); Moustakas et al. (1997); Saracco et al. (1997); Bershadsky et al. (1998); Szokoly et al. (1998); McCracken et al. (2000); Väistönen et al. (2000); Drory et al. (2001b); Huang et al. (2001); Kümmel & Wagner (2001); Maihara et al. (2001); Martini (2001a); Saracco et al. (2001); Cristóbal-Hornillos et al. (2003); Minowa et al. (2005). The error bars show the 1σ Poissonian errors.

2.3.1.3 The i-selected catalogues

Based on the publicly available optical and NIR data of the COSMOS field⁵ we build a Subaru i-band detected galaxy catalogue in 12 of our 15 patches. Because of the relatively bad H-band seeing ($> 1.3''$), we exclude three NIR patches.

We use a very similar approach as for the FDF (Heidt et al. 2003) in constructing a multi-waveband catalogue in the COSMOS field. First we align by pixel all available filters (u_{CFHT} , B_{Subaru} , V_{Subaru} , r_{Subaru} , i_{Subaru} , z_{Subaru} , K_{SKPNO} , afterwards referred to as u , B , V , r , i , z , and K) to our H-band patches and derive i-selected catalogues. Please note that we had

⁵The data were taken from:
<http://irsa.ipac.caltech.edu/data/COSMOS/>

2.3 The Cosmic Evolution Survey

Table 2.3: Galaxy number counts not corrected for incompleteness from COSMOS in the i (12 patches), J_s (1 patch), H (15 patches), and K' (1 patch) bands. $\log N$ and $\sigma_{\log N}$ are given, where N is in units of $\text{mag}^{-1}\text{deg}^{-2}$.

m	i		J_s		H		K'	
	$\log N$	$\sigma_{\log N}$						
14.5			1.244	0.434	1.015	0.164	1.545	0.307
15.5			1.721	0.250	1.492	0.094	2.022	0.177
16.5	0.465	0.307	2.420	0.112	2.195	0.042	2.624	0.088
17.5	1.465	0.097	2.721	0.079	2.738	0.022	2.925	0.062
18.5	2.304	0.036	3.136	0.049	3.206	0.013	3.393	0.036
19.5	3.127	0.014	3.525	0.031	3.631	0.008	3.790	0.023
20.5	3.598	0.008	3.949	0.019	4.010	0.005	4.152	0.015
21.5	3.996	0.005	4.277	0.013	4.236	0.004	4.283	0.013
22.5	4.350	0.003	4.390	0.011	3.995	0.005	3.784	0.023
23.5	4.677	0.002	3.705	0.025	2.486	0.030	1.244	0.434
24.5	4.970	0.001	1.244	0.434	1.015	0.164		
25.5	5.103	0.001			0.170	0.434		
26.5	4.983	0.001						
27.5	4.338	0.003						
28.5	2.702	0.023						
29.5	1.278	0.120						

Table 2.4: COSMOS (FDF) field characteristics for a SExtractor detection threshold of $t = 2.5$ ($t = 1.7$) and $n = 3$ ($n = 3$) contiguous pixels.

Filter	50 % CL. COSMOS	50 % CL. FDF	seeing [']
u_{CFHT}	25.6	26.5 (U)	0.90
B_{Subaru}	27.7	27.6 (B)	0.95
V_{Subaru}	26.5	26.9 (g)	1.30
r_{Subaru}	26.8	26.9 (R)	1.05
i_{Subaru}	26.7	26.8 (I)	0.95
z_{Subaru}	25.1	25.8 (z)	1.15
Ks_{KPNO}	21.2	22.6 (Ks)	1.28

to compute a new astrometric solution for the public K band, as the solution given in the images was not sufficiently accurate. The program SCAMP (Bertin 2006) was applied for

2 Observing the coloured Universe: the large deep surveys

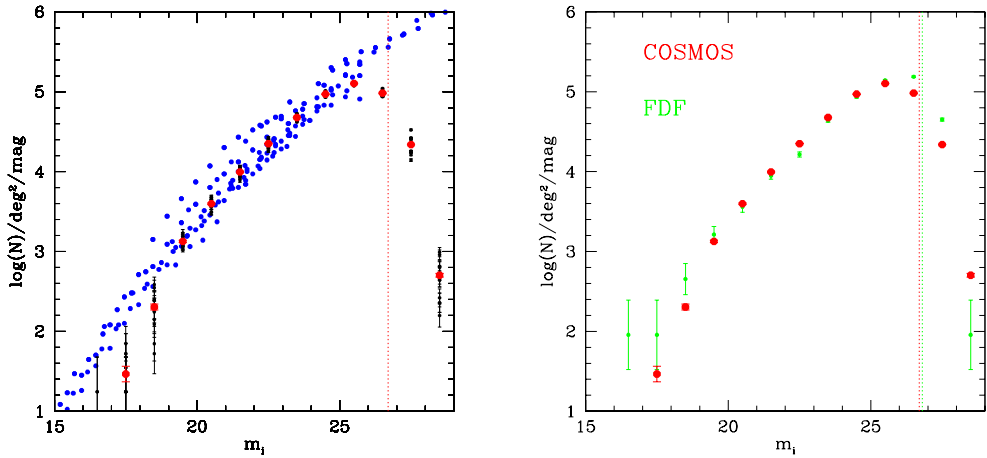


Figure 2.16: Left panel: Galaxy number counts in the i-band (not corrected for incompleteness) as compared to the literature. The black dots represent the number counts of the single COSMOS patches, whereas the red dots show the average number counts of all fields. The vertical dotted line indicates the 50% completeness limit. The literature number counts are taken from Hall & Mackay (1984); Tyson (1988); Lilly et al. (1991); Casertano et al. (1995); Driver et al. (1995); Williams et al. (1996); Huang et al. (1998); Postman et al. (1998); Arnouts et al. (1999); Metcalfe et al. (2001); Arnouts et al. (2001); Yasuda et al. (2001); Capak et al. (2004). Right panel: Galaxy number counts in the i-band (not corrected for incompleteness) as compared to the FDF. The red dots show the average number counts of all COSMOS fields, whereas the green dots show the number counts as derived from the deep part of the FDF. The vertical dotted lines indicate the 50% completeness limits of COSMOS and FDF. The error bars show the 1σ Poissonian errors.

this procedure. Then we convolved all images to the same seeing of $1.3''$ and ran SExtractor in the double image mode with the detection threshold of $t = 2.5$ and $n = 3$ contiguous pixels (we detect on the original i-band image with a seeing of $0.95''$). The 50 % completeness limits as well as the seeing of the different bands are listed in Table 2.4. The Table also compares the depth of the different bands with the depth in the FDF. Beside the u, z, and K bands, the COSMOS data set is roughly as deep as the FDF. In the u-band, z-band as well as in the K band the FDF is about 1 magnitude deeper.

In the FDF we did the source detection with $n = 3$ contiguous pixels and a threshold of $t = 1.7$. This results in only a few false detections (less than 1 percent). For the COSMOS data set we could not use the same detection threshold as this would result in too many false detections (measured on the negative image). We use a threshold of $t = 2.5$ in order to have false detections only at the 1 to 2 percent level. Depending on the patch, the false detections as measured on the negative image fluctuate between 0.6 percent and 2.6 percent. Never-

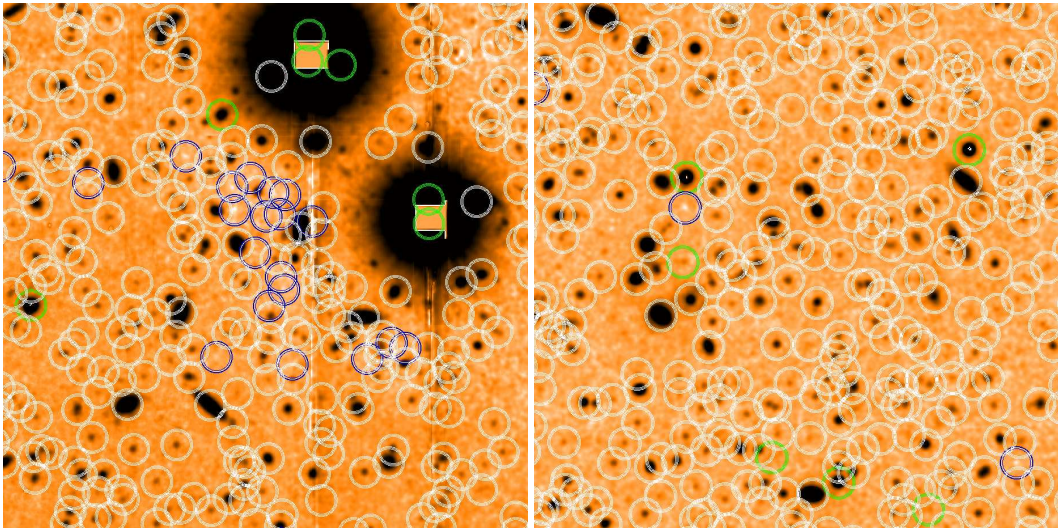


Figure 2.17: $1.5' \times 1.5'$ Subaru i-band image. White circles mark the detected objects from the final catalogue, green circles mark objects eliminated from the final catalogues (saturated or corrupted magnitude, see text for details), whereas the blue circles mark false detections as detected on the negative image. It illustrates the fact, that there are many more detections in the negative image around bright objects (left panel) than in other areas of the image (right panel).

theless this is not the real contamination rate, as a substantial fraction of these false objects detected on the negative image are distributed around bright objects. On the other hand the number density on the positive side does *not* increase around these bright objects. Therefore it is most likely, that these false detections are due to a reduction problem triggering false detections only in the negative image. This can be seen in Fig. 2.17 where we show a region around relative bright objects together with the positive and negative detections. Taking this into account, we conclude that we have a contamination rate of about 1 percent or less in our catalogues.

In total we detected about 300 000 objects in the 12 patches (3 contiguous pixels and a detection threshold of 2.5). These patches have a seeing of less than $1.3''$ (see above) in every band and reside in a region which has at least 90% of the maximum depth of each band. Moreover we exclude all objects (based on the weighting maps and SExtractor flags) with problems in the photometry (e.g. if some pixels of an object are saturated or the magnitude is corrupted) in at least one band in order to get a perfectly clean catalogue suitable to derive photometric redshifts. At this stage our clean i-selected catalogue comprises 293 377 objects. As we work on the individual patches and they slightly overlap, we analyse the objects and found that about 99% are unique entries.

A comparison between the i-band number counts in the COSMOS field and in the liter-

ature as well as with the FDF are shown in Fig. 2.16. There is a good agreement between the literature and COSMOS number counts up to the limiting magnitude. Moreover, the comparison with the FDF number counts shows an excellent agreement down to the faintest bins. Only at the very bright end the FDF number counts are slightly higher (most of the very bright objects are saturated in the COSMOS i-band and thus not taken into account), although not by more than 1σ to 2σ . The values of the galaxy number counts can be found in Table 5.2.

In order to avoid contamination from stars, we follow the same procedure adopted for the FDF data as described in section 2.1.1. The efficiency of our procedure was further tested by visual inspection (in one patch) on the public ACS data. It turned out that about half of these objects are extended in the ACS data and only half are point-like. Although this approach (see Gabasch et al. 2004a) of excluding stars works very well in the FDF where the seeing of the detection image is only $0.55''$, it is much less effective in the COSMOS i band with a seeing of $0.95''$.

In total 4803 (1.6 %) objects were classified as stars and removed from our sample (see also Fig. 2.22 for the photometric redshift distribution of all starlike objects excluded from the galaxy catalogue). Please note that most of the bright point-like objects are saturated in one of the bands and already removed in the first cleaning step (see above). Therefore our final i-band selected galaxy catalogue comprises 288 574 objects.

2.3.1.4 Spectroscopic redshifts

Photometric redshifts need to be calibrated by spectroscopic redshifts for objects covering a wide range of galaxy types and redshifts. Hence, we selected spectroscopic data of the COSMOS field (Scoville et al., in prep.) from the ESO archive taken with the VIMOS spectrograph (Le Fèvre et al. 2003) at the ESO VLT in the context of the zCOSMOS project (Lilly et al.; in prep.). zCOSMOS is a Large ESO Programme with 600 hr of observing time aiming at the characterisation of the distribution and properties of galaxies out to redshifts of $z \sim 3$. The project is divided into two parts. zCOSMOS-bright focuses on relatively bright galaxies with $I_{AB} < 22.5$ at redshifts $0.1 < z < 1.2$. In order to include such galaxies in our spectroscopic control sample we selected the VIMOS mask ‘zCOSMOS_4-4’ with 312 slits centred at $10h00m28.20s +02^\circ 15' 45.0''$. This mask was observed 1.5 h with the red low-resolution LR_red grism ($R \sim 210$), covering a wavelength range from 5500 to 9500 Å. zCOSMOS-deep aims at galaxies with $1.5 < z < 2.5$. For this Lilly et al. (in prep.) selected targets using the BzK criteria of Daddi et al. (2004) and the UGR ‘BX’ and ‘BM’ selection of Steidel et al. (2004). We obtained a representative sample of such galaxies, reducing the VIMOS mask ‘zCOSMOS_55_faint’ with 239 slits at $10h00m27.67s +02^\circ 10' 23.0''$, observed 4.5 h with the blue low-resolution LR_blue grism ($R \sim 180$), covering a wavelength range from 3700 to 6700 Å.

The spectra of both VIMOS masks were reduced using VIPGI (Scoveggio et al. 2005). This software package is designed to reduce the multi-object VIMOS spectra in a quite au-

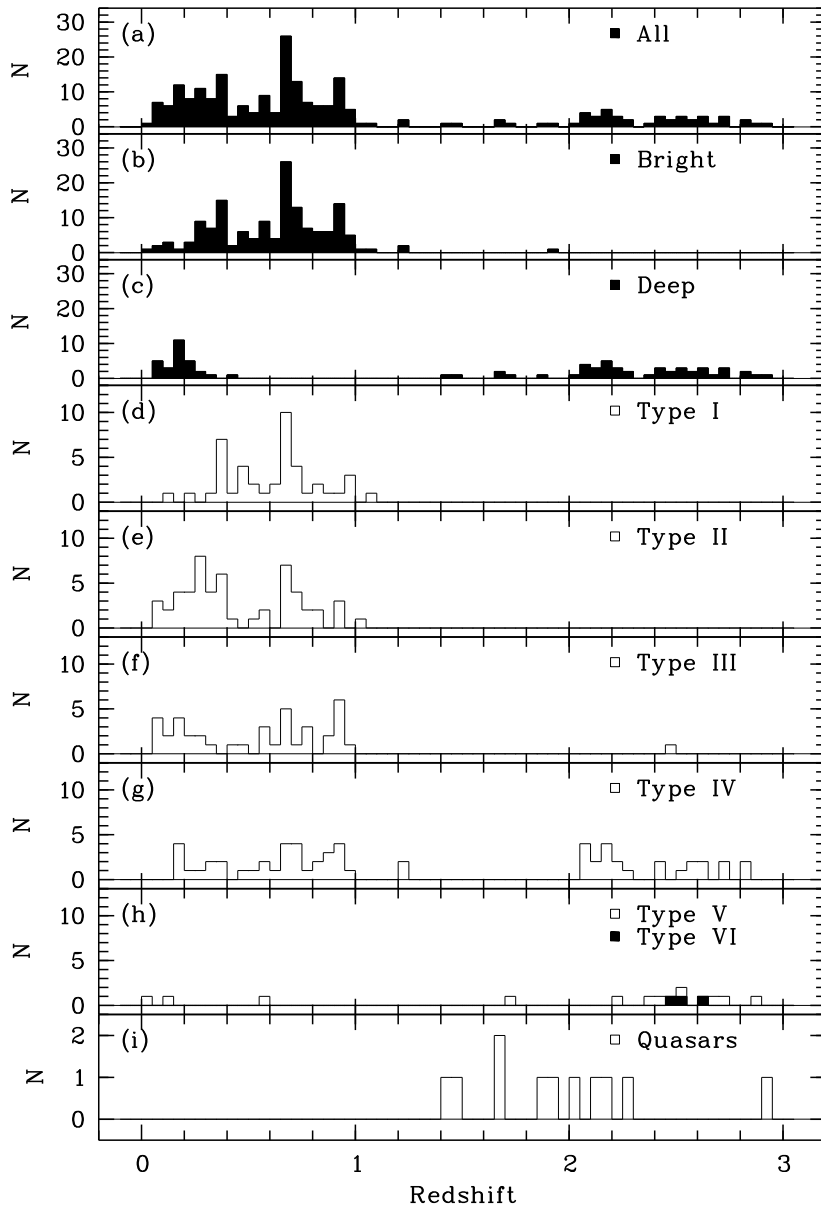


Figure 2.18: Redshift distribution of the COSMOS spectroscopic sample for (a) all extragalactic objects with trustworthy redshifts, (b) the corresponding objects of the bright-galaxies mask, (c) the corresponding objects of the zCOSMOS-deep mask, (d) – (h) galaxies of different object type, and (i) the quasars. The types range from I = ellipticals (or passively evolving) to V = extreme starbursts (see Noll et al. 2004). In diagram (h) galaxies of type V (white bars) as well as type VI (strong Ly α emitters, black bars) are plotted. The redshift resolution is $\Delta z = 0.05$.

tomatic way. The reduction was performed using essentially standard methods. The jittered sequences of individual exposures (five different positions) allowed to efficiently correct for fringing and to obtain a high-quality sky subtraction. The one-dimensional composite spectra were extracted by means of the S/N-optimised Horne (Horne 1986) algorithm. The final spectra are flux calibrated and corrected for atmospheric absorption bands.

Redshifts were derived using the cross-correlation based algorithm described by Noll et al. (2004). In order to obtain the redshift and a rough spectral type, we used a sequence of six empirical templates (see Noll et al. 2004) essentially differing in their UV-to-optical flux ratio, but also showing different strengths of nebular emission lines. For the comparison to photometric redshifts we consider galaxies with trustworthy ($> 90\%$ confidence) spectroscopic redshifts only. Due to low S/N (particular at high redshift) and the limited wavelength ranges of the spectra certain redshifts could only be derived for about half of the objects, i.e. 272 of 551 spectra. For the zCOSMOS-deep mask the success rate (33%) is significantly lower than for the bright-galaxy mask (62%). The total sample of 272 objects with trustworthy redshifts includes 49 stars and 12 quasars. Hence, the final sample of galaxies comprises 211 objects. The majority of them (147 or 70%) belongs to the bright-galaxy sample. On the other hand, the subsample of 36 galaxies with redshifts $1.5 < z < 3$ only consists of objects from the zCOSMOS-deep sample. These high-redshift galaxies (quasars excluded) correspond to 45% of the objects identified in the deep sample. Fig. 2.18 shows the redshift distribution of the full spectroscopic control sample, the ‘zCOSMOS_4-4’ mask, the ‘zCOSMOS_55_faint’ mask, the different galaxy types defined by Noll et al. (2004, I = ellipticals, V = extreme starbursts, VI = strong Ly α emitters), and the quasars.

After cross-correlating (by visual inspection) the 211 spectroscopic objects with the final i-band selected catalogue in the 12 patches (we excluded also objects, for which the identification was not unique) we end up with a final sample of 162 spectroscopic redshifts used to calibrate the photometric redshifts.

2.3.1.5 Photometric redshifts

A summary of the photometric redshift technique used to derive the distances to the galaxies can be found in Bender et al. (2001) and Gabasch et al. (2004a). Before deriving the photometric redshifts we checked and fine-tune the calibration of our photometric zeropoints by means of colour-colour plots of stars. We compared the colours of stars with the colours of stellar templates from the library of Pickles (1998) converted to the COSMOS filter system. In general, corrections to the photometric zeropoints of only a few hundredth of a magnitude were needed to obtain a good match to the stars and best results for the photometric redshifts (if compared to the spectroscopic ones). Only in the u-band and in the K-band, the correction were of the order of a few tens of a magnitudes. A comparison between the reduced KPNO K-band and our K-band (both convolved to the same seeing of $1.3''$) in patch 01c showed, that although the total magnitudes agreed very well, the fixed aperture magnitudes (especially of relatively faint sources) differ systematically by a few tens of a magnitude.

2.3 The Cosmic Evolution Survey

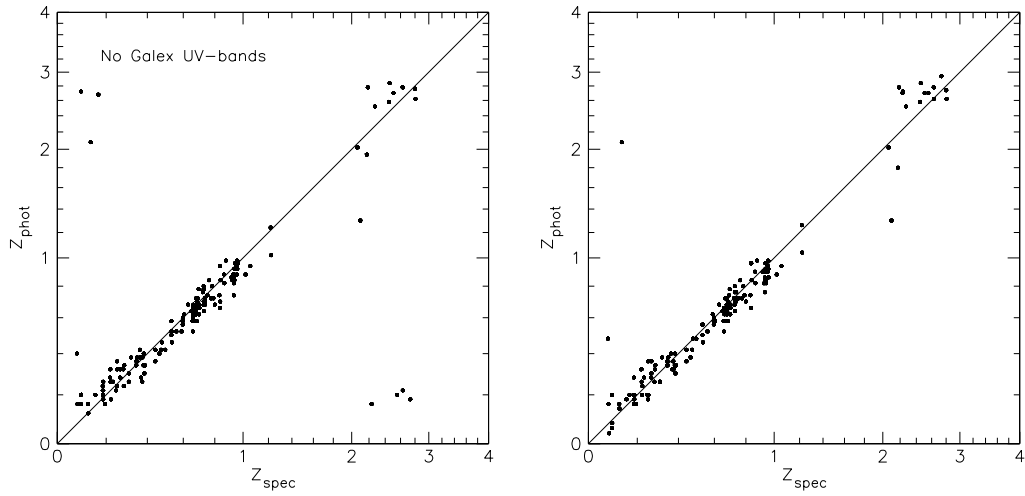


Figure 2.19: Comparison of spectroscopic and photometric redshifts in the COSMOS field (162 galaxies). Left panel: u band to K band are used to derive the photometric redshifts. Right panel: u band to K band as well as the GALEX FUV and NUV bands are used to derive the photometric redshifts.

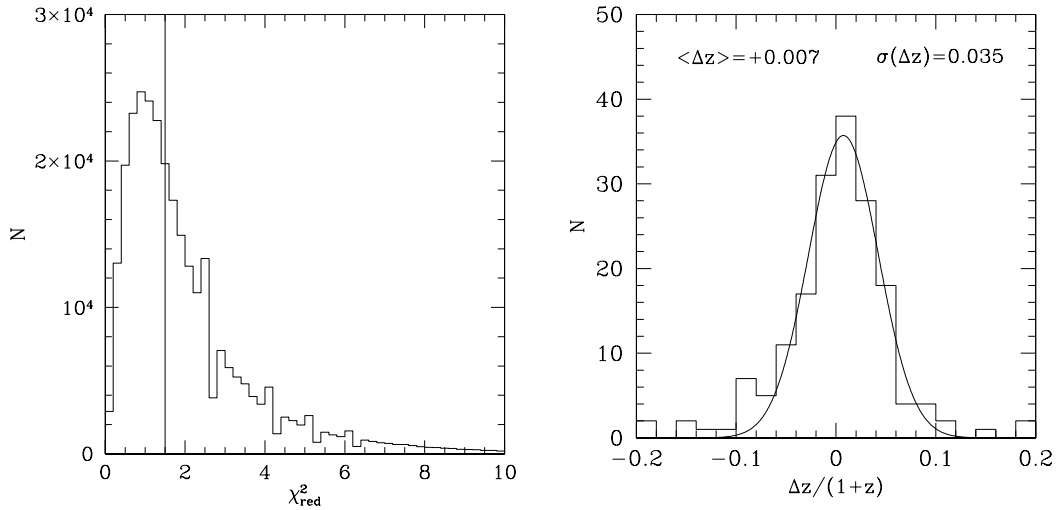


Figure 2.20: Left panel: Histogram of the reduced χ^2 for all galaxies in the COSMOS field as obtained for the best fitting template and redshift. The dotted vertical line indicates the median reduced χ^2 of 1.5. Right panel: Histogram of the photometric redshift errors. The error distribution can be approximated by a Gaussian centred at 0.007 with an rms of 0.035 (solid line).

2 Observing the coloured Universe: the large deep surveys

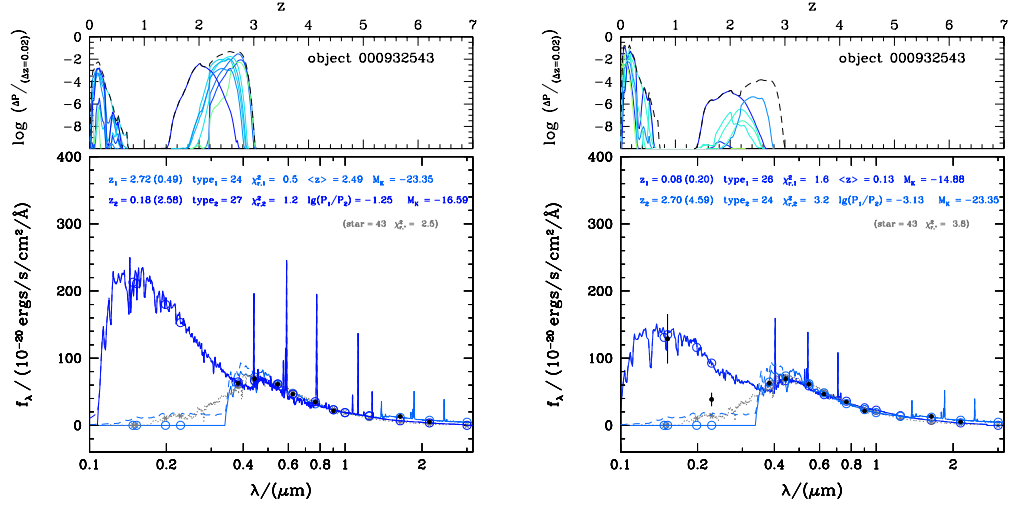


Figure 2.21: Redshift probability distribution (upper part) and photometric redshift fit (lower part) of the spectroscopic object 000932543 with $z_{spec} = 0.093$. The different SEDs are colour coded. The open circles (lower part) represent the SED integrated within the various filter transmission curves, whereas the black dots represent the measured fluxes. The redshift for the best fitting SED (z_1) as well as for the second best fit (z_2) are also given. Left panel: Only 8 bands (u-band to K-band) are used to derive the photometric redshift yielding a wrong z_{phot} of 2.72. Right panel: 10 bands (FUV, NUV, u-band to K-band) are used to derive the photometric redshift yielding a z_{phot} of 0.08 very close to the spectroscopic redshift.

Therefore we decided to correct the KPNO zeropoint by matching the faint sources in the KPNO image with those in our own field (in the fixed aperture used to derive the photometric redshifts). Moreover when calculating the photometric redshifts, we artificially increased the magnitude errors in the K-band by 0.25^m (added in quadrature to the SExtractor errors) to reduce the relative weight of this slightly problematic band. Therefore, we rely mostly on the accurate photometry of the NIR H band.

We derived object fluxes for a fixed aperture of $2.0''$ ($1.5 \times$ seeing) from images which had been convolved to the same point spread function (PSF; $1.3''$). In Fig. 2.19 (left panel) we compare 162 high quality galaxy spectroscopic redshifts with the photometric redshifts. Although there is a good agreement in the redshift range between $z \sim 0.2$ and $z \sim 1.2$, it is clear from Fig. 2.19, that there is a degeneracy between high redshift ($z \sim 2.5$) and low redshift ($z \sim 0.2$) objects (10 catastrophic outliers with $\Delta z/(z_{spec} + 1) \gtrsim 0.2$). This degeneracy stems from the relatively red u-band. In Fig. 2.21 we show the redshift probability function as well as the SED fits to the observed flux of the spectroscopic object 000932543. Although the spectroscopic redshift is $z_{spec} = 0.093$, the best fitting photometric redshift is

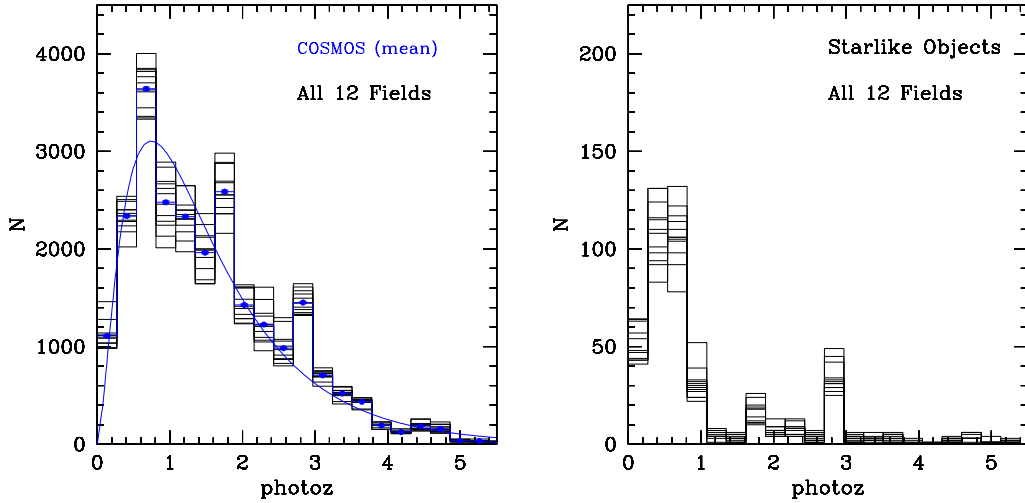


Figure 2.22: Left panel: Redshift number distribution of all galaxies in the 12 patches. The mean number distribution is shown as blue dots. The blue solid line represents a fit to the mean galaxy distribution using the approach of Brainerd et al. (1996) (see text for details). Right panel: Redshift distribution of objects classified as stars (see text for details) and eliminated from the final galaxy catalogues. Please note the different scaling by a factor of 20 in the left and right panel.

$z_{phot} = 2.72$. On the other hand, there is also a low redshift peak around $z_{phot} = 0.18$ in the redshift probability function (but with a lower probability). Moreover Fig. 2.21 also shows that both, the high redshift as well as the low redshift solutions are hard to be disentangled as long as no information in the UV is available (as they differ mainly in the UV). Therefore we decided to include in the determination of the photometric redshifts also the GALEX FUV and NUV bands⁶.

As we do not want to convolve all the images to a seeing of 5''(GALEX PSF), we decided to use another approach to include the UV fluxes in our photometric redshift estimation. Similar to the optical and NIR bands we used a fixed aperture of $\sim 1.5 \times$ PSF, i.e. 7.5''. As there were no obvious features in the colour-colour plots of stars including the UV bands, we could not fine-tuned the calibration of the zeropoints by means of colour-colour plots of stars. Therefore we optimised the zeropoints by using the SED fits of our galaxies with very good photometric redshifts (if compared with the spectroscopic ones). Please note that this approach can not derive accurate UV fluxes, but gives only a very rough flux estimation in the two UV bands. Nevertheless, it is now possible to break the degeneracy between the high redshift and low redshift solution. This can be best seen in Fig. 2.21 where we show

⁶The data were taken from:
<http://irsa.ipac.caltech.edu/data/COSMOS/>

2 Observing the coloured Universe: the large deep surveys

one of the catastrophic outliers. Only by including the NUV and FUV fluxes (right panel) we are able to obtain a photometric redshift of $z = 0.08$, hence very close to the spectroscopic redshift of $z_{spec} = 0.093$. This approach drastically reduces the number our catastrophic photometric redshift outliers (see Fig. 2.19).

In Fig. 2.19 (right panel) we compare the final photometric and spectroscopic redshifts of the 162 galaxies. The agreement is very good and we have only 3 catastrophic outliers. The right panel of Fig. 2.20 shows the distribution of the redshift errors. It is nearly Gaussian and scatters around zero with an rms error of $\Delta z/(z_{spec} + 1) \approx 0.035$. Fig. 2.20 (left panel) presents the χ^2 distribution of the best fitting templates and photometric redshifts for all the objects. The median value of the reduced χ^2 is 1.5 and demonstrates that the galaxy templates describe the vast majority of galaxies very well.

The galaxy redshift histogram of all objects in the different patches is shown in Fig. 2.22. The mean galaxy distribution can be very well described by Equation (2.1) introduced by Brainerd et al. (1996),

$$p_z(z) = Const \times \frac{\beta z^2}{\Gamma(3/\beta) z_0^3} \exp(-(z/z_0)^\beta) \quad (2.1)$$

where $Const$, $z_0 = < z > \frac{\Gamma(3/\beta)}{\Gamma(4/\beta)}$ and β are free parameters with $< z >$ being the first moment of the distribution. The best fitting values are: $Const = 6206$, $z_0 = 0.107$, and $\beta = 0.611$.

Please note that if we analyse the galaxy photometric redshift histogram with a binning of $\Delta z = 0.1$ there are three clearly visible peaks below redshift of $z = 2$: one at $z_{phot} = [0.6, 0.7]$, one at $z_{phot} = [0.9, 1.0]$, and one at $z_{phot} = [1.7, 1.8]$. Interestingly, we also find peaks in the spectroscopic redshift histogram (see also Fig. 2.18) with at least 10 galaxies at $z_{spec} = [0.657, 0.669]$, $z_{spec} = [0.672, 0.683]$, and $z_{spec} = [0.926, 0.941]$.

3

Morphological characterization of high redshift galaxies

Abstract

In this chapter, I describe the details of the procedure I used to derive the quantitative morphological characterisation for the galaxy samples presented in chapters 4 and 5. For all the samples, the morphological analysis was performed by means of two-dimensional fitting of the galaxy surface brightness profiles on deep i-band images obtained with the Advanced Camera for Surveys on the Hubble Space Telescope. This chapter is especially devoted to assess the robustness of the results obtained, both in terms of systematics due to characteristics of the data, as for instance signal-to-noise or PSF variations, and in terms of reliability of the codes and classifications used.

3.1 The Advanced Camera for Surveys on board the HST

The Hubble Space Telescope is a cooperative program of the European Space Agency (ESA) and the National Aeronautics and Space Administration (NASA) to operate a long-lived space-based observatory for the benefit of the international astronomical community. HST is an observatory first dreamt of in the 1940s, designed and built in the 1970 and 80s, and operational only in the 1990s. HST is a 2.4-meter reflecting telescope which was deployed in low-Earth orbit (600 kilometers) by the crew of the space shuttle Discovery (STS-31) on 25 April 1990. Because of HST's location above the Earth's atmosphere, its science instruments can produce high resolution images of astronomical objects.

The Advanced Camera for Surveys (ACS) is a third-generation Hubble Space Telescope

3 Morphological characterization of high redshift galaxies



Figure 3.1: The Hubble Space Telescope.

(HST) instrument. ACS¹ was installed by space shuttle Columbia during HST servicing mission 3B. The development of ACS is a collaborative effort between the Johns Hopkins University, the Goddard Space Flight Center, the Ball Aerospace and the Space Telescope Science Institute.

The very first images obtained with the first generation HST instruments demonstrated that HST could deliver superb spatial resolution pictures of the Universe but at the same time it was realised that the low efficiency and the small fields of view, of these first generation instruments, would have severely limited the HST's utility for deep high resolution imaging and for deep surveys.

The ACS was aimed exactly to improve the HST survey efficiency in the optical, and especially the I band by at least a factor of 10 with respect to the previous generations instruments.

ACS provided the astronomical community with very high quality, high resolution imaging of large patches of the sky, allowing a significant step forward in several research areas,

¹In January 2007, Hubble's Advanced Camera for Surveys (ACS) stopped working due to an electrical short.

3.1 The Advanced Camera for Surveys on board the HST

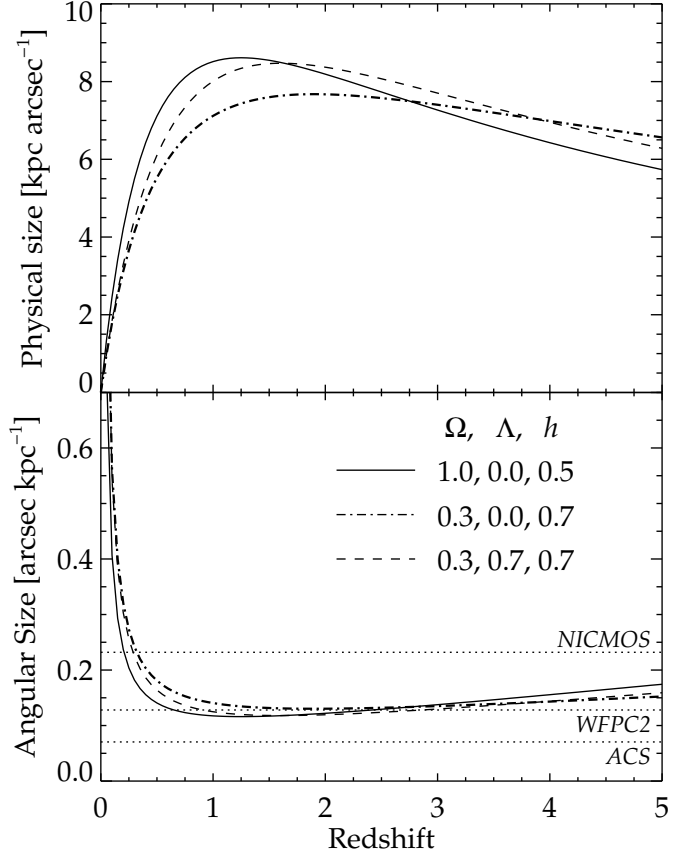


Figure 3.2: The cosmological angular diameter distance as a function of redshift for several fiducial world models. The panels illustrate the angular diameter distance, in units of the physical distance corresponding to an apparent angular size (*top* panel), and in units of the angular size corresponding to a fixed physical distance (*bottom* panel). The bottom panel also shows the nominal resolving capacity of the current HST instrumentation (as labeled; note that the WFPC2 resolution corresponds to that of the WF chips, and the NICMOS resolution is given for camera 3). . The figure is taken from Papovich et al. (2003).

and in particular in galaxy formation and evolution studies such as the one presented in this Thesis.

In the following we describe the analysis aimed at quantitatively determine the morpho-

3 Morphological characterization of high redshift galaxies

logical properties of the distant galaxy samples described in chapter 2. Such morphological analysis, based on ACS imaging of the FORS Deep Field, GOODS and COSMOS fields, combined with the spectrophotometrical data from chapter 2, is the basis of a study of the evolution of different galaxy populations in the past 8 billion years, which is the subject of chapters 4 and 5.

3.2 The morphological analysis

We make use of the package GIM2D (Simard et al. 1999) to fit PSF convolved Sersic (1968) profiles to the two-dimensional surface brightness distribution of each galaxy, for all galaxies in our samples down to a limit of F814W=24.

In the following we explain the details of the adopted procedure and the tests that were performed to assess the robustness of our results.

3.2.1 GIM2D

The GIM2D (Galaxy IMage 2D) code has been designed for the quantitative structural analysis of distant galaxies (Simard et al. 1999). The code comes embedded in an IRAF wrapping package to make it as friendly as possible. GIM2D uses the Metropolis algorithm to converge to the analytical model, i.e. it carries out a Monte Carlo sampling of the likelihood function $P(w|D, M)$, which measures the probability that the parameter combination w is the correct one given the data D and the model M . The Monte Carlo approach of sampling the complex multidimensional topology of parameter space has the virtue of converging consistently to the same best fit model for a wide range of initial guesses. The algorithm is at the same time very time-consuming, not really an issue with modern machines, and very robust.

We fit a simple single Sérsic (Sersic (1968)) profile to describe the two-dimensional surface brightness distribution of the galaxy light:

$$\Sigma(r) = \Sigma_e e^{-\kappa[(\frac{r}{r_e})^{1/n} - 1]} \quad (3.1)$$

where r_e is the effective radius of the galaxy, Σ_e is the surface brightness at r_e , n is the power-law index, and κ is coupled to n such that half of the total flux is always within r_e . For $n \geq 2$, $\kappa \approx 2n - 0.331$; at low n , $\kappa(n)$ flattens out towards 0 and is obtained by interpolation. The adjustable form of the Sérsic law has the advantage of parameterizing, through the variable exponent n , surface brightness distributions including the exponential radial fall-off of the light profile in bulgeless disks ($n = 1$), and the classical de Vaucouleur profile typical of elliptical galaxies ($n = 4$).

During the fitting process, the model is convolved with the user specified PSF, and then compared to the input image.

In the case of a single Sérsic model, GIM2D seeks the best fitting values for the following eight parameters: total flux, half-light radius, ellipticity, position angle, center of the galaxy, background level and value of the Sérsic index.

3.2.2 PSF influence on the morphological parameters

The accurate determination of the image PSF is important for the proper determination of the morphological parameters. The PSFs used to convolve the profiles were obtained for each individual ACS tile by stacking about 10 high S/N isolated stars.

Although we did not expect the outcome of single Sérsic fits to depend strongly on small variations of the PSF, we carried out some tests with varying PSFs on a few COSMOS tiles to assess the influence of the PSF on the retrieved morphological parameters. Such tests were performed by using: i) a single universal PSF obtained by stacking all the COSMOS high S/N isolated stars; ii) the PSF we derived for the FDF, which was observed in the same filter F814W and at almost the same depth as COSMOS. We found that the largest differences obtained in the output parameters were of order 3–5 %, meaning that single Sérsic fits are pretty robust against such PSF variations.

We also tested the accuracy of the PSF itself by fitting all the point-like sources as selected with the SExtractor catalog parameters. Specifically, we used the neural network star classifier (CLASS_STAR), the half-light radius, and the FWHM, to identify point-like sources, as shown in figure 3.3. Point-like classified objects are shown in red, the main stellar locus is clearly traced corresponding to a FWHM of 2.2 pixel. The tail of PSF objects at bright magnitudes and larger FWHM is due to saturated stars. When GIM2D-fitting such point-like sources, the vast majority – but the saturated stars – has a best-fit half-light radius smaller than 0.01 pixel, meaning that after the code convolves them with the provided PSF they are indeed recovered as point-like sources.

3.2.3 Results on the overlapping COSMOS ACS tiles

Since the COSMOS ACS tiles are slightly overlapping, we took advantage of this feature to further test the reliability of our fitting procedure as well as to assess many other possible systematics, like PSF variation in time and over the ACS field of view, photometric and astrometric distorsion.

All sources appearing in two tiles were fitted separately in each tile, and the fit results were compared. The outcome of this test is shown in fig. 3.4, where we plot one against the other the GIM2D output (Sérsic index and half-light radius) coming from the two fits for all such objects ($\approx 8\,000$). An overall accuracy of $\Delta n/n \sim 0.3$ and $\Delta r/r \sim 0.1$ is obtained. Taking into account that in the tile borders only three out of four dithers are overlapping, and hence that the image rms is greater than in the central part of the image, one should consider these uncertainties as safe upper limits.

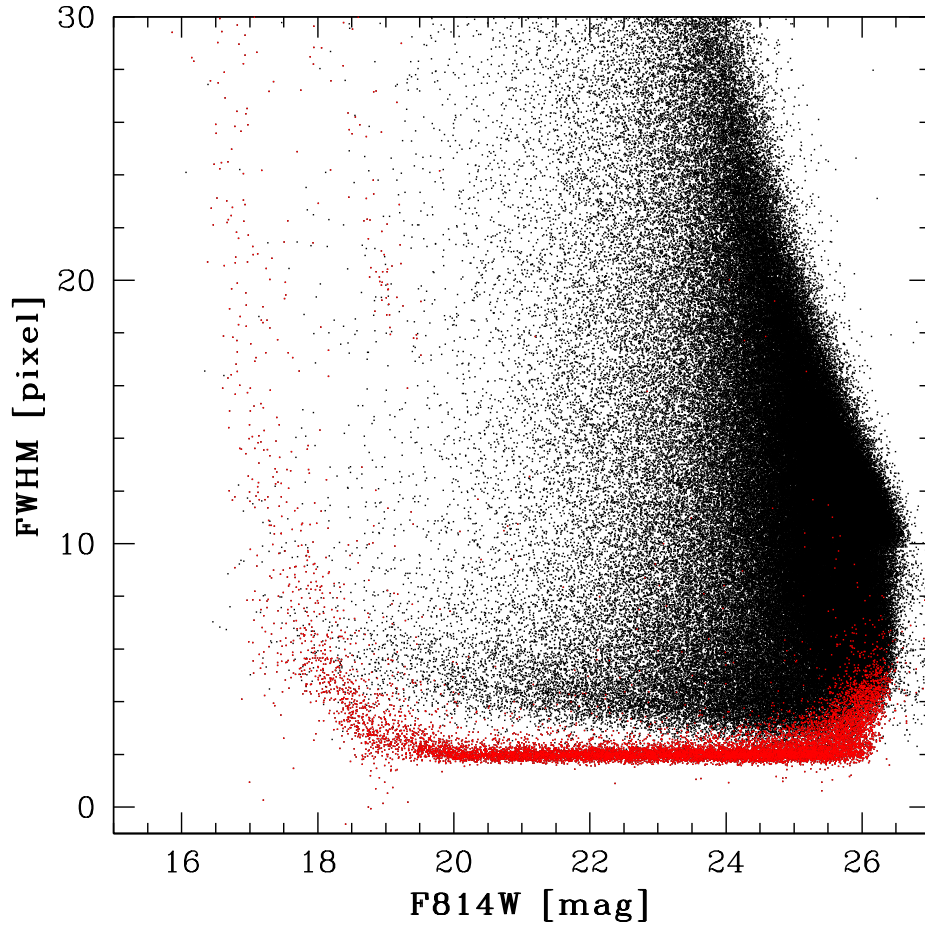


Figure 3.3: Example of diagnostic plot used to discriminate between point-like (red) and extended (black) objects in the COSMOS ACS/F814W catalog parameters space.

3.2.4 Results on simulated objects

We further tested the accuracy of our analysis by running GIM2D on simulated images. This test was performed by adding 3000 fake objects, one at a time, to the real image, in a blank, pure-sky region. The simulated galaxies were generated with the GIM2D task *gstimul*, by adding on the selected pure-sky region objects with structural parameters uniformly distributed in specified ranges (magnitude in [22.5 – 24.], ellipticity in [0.1 – 0.9], position angle in [0 – 90], effective radius in [0 – 60 pixel], Sérsic index in [0.2–6]). Each single object is first added into the image, then it is extracted with the same SExtractor configuration file used for the real images. It is then analyzed from GIM2D exactly as done for the real objects.

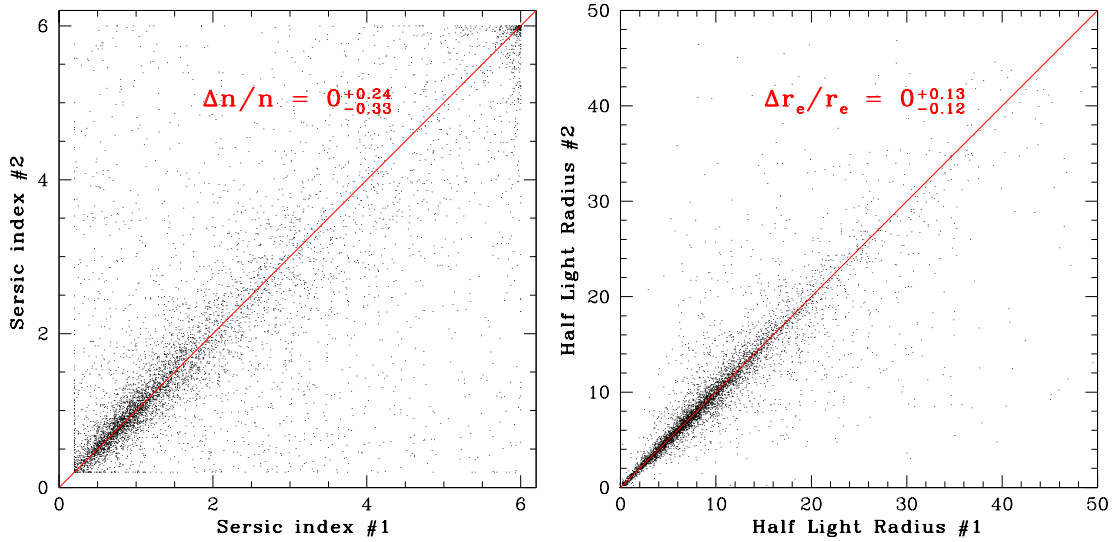


Figure 3.4: Comparison of morphological parameters obtained by fitting the surface brightness of all sources falling in two distinct ACS tiles. For each object, the fit was performed on both images, and the resulting Sérsic indexes and effective radii are compared in the left and right panels, respectively. The recovered median and 16th, 84th percentiles of the $\Delta n/n$ and $\Delta r/r$ distributions are indicated in red.

We find that the profile parameters of simulated objects are well recovered down to F814W=24 if their $\mu_e \geq \mu_{sky}$ (see figure 3.6).

The input magnitudes are generally better recovered for objects with $n_{ser} \lesssim 2$ than for objects with $n_{ser} \gtrsim 2$ with a median $\Delta M = 0.01$ and 0.06 , respectively (see fig. 3.5).

The recovered ellipticity and position angle as respect to the input ones show no trends with magnitude and are generally very well recovered (see fig. 3.6 for the ellipticity).

High Sérsic index objects have very extended wings that, depending on the total flux, can fall under the sky surface brightness, thus for these objects a lower Sérsic index, total flux and effective radii are usually recovered (see figure 3.7).

3.2.5 GIM2D vs. GALFIT

We tested our results by running also the GALFIT (Peng et al. 2002) code on four of the COSMOS ACS patches.

GALFIT is a 2D galaxy fitting software package more recent than GIM2D. It was designed to extract many structural components from galaxy images. It uses a Levenberg-Marquardt downhill-gradient (Press et al. 1992) method to derive the best fit, and therefore it is very fast. Furthermore it is very flexible and able to fit an arbitrary number of galaxies simultane-

3 Morphological characterization of high redshift galaxies

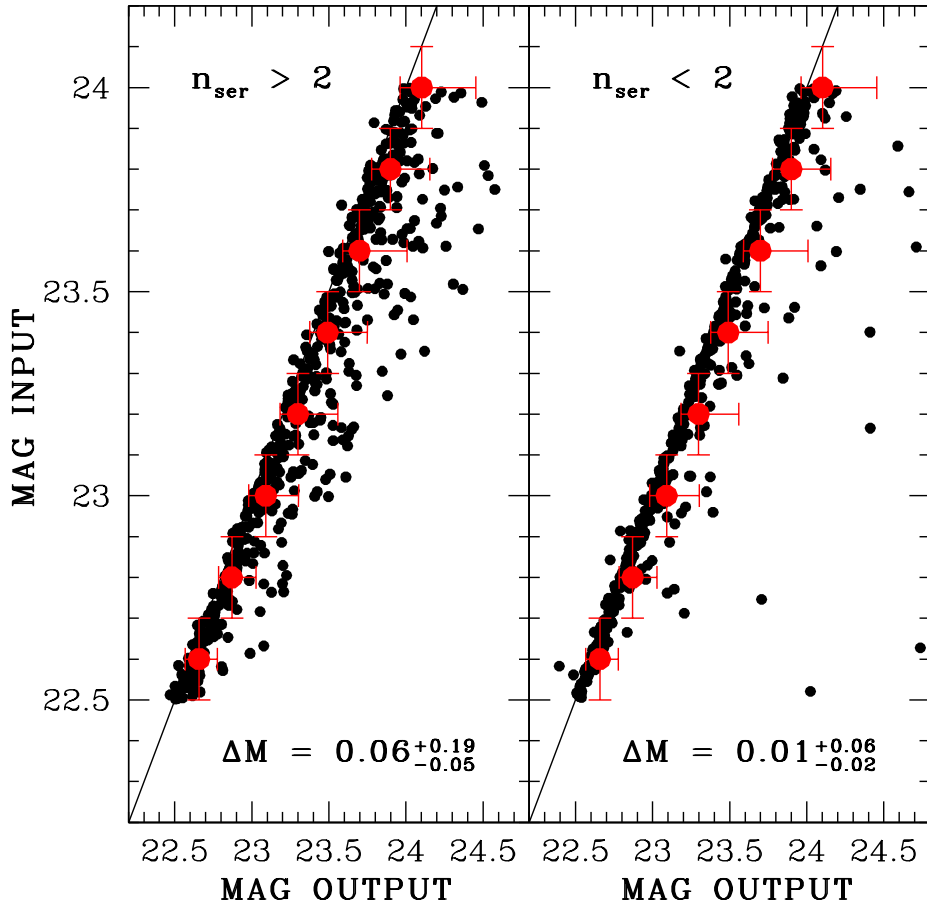


Figure 3.5: In the two panels output GIM2D recovered vs. input simulated magnitudes are shown for objects with $n_{\text{ser}} > 2$ (left) and $n_{\text{ser}} < 2$ (right). In each panel the median differences with errors are shown.

ously on an image, making it an ideal tool to fit neighboring objects in a sensitive way and not being biased from external informations such as the SExtractor segmentations used from GIM2D. This last characteristic makes obviously GALFIT an ideal tool for crowded field such as galaxy clusters or even confusion limited images.

During the fitting process, as for GIM2D, the model is convolved with the specified PSF, and then compared to the input image. The simple minimization algorithm could, in principle, fall in a local minimum and miss the global one more easily than the Metropolis solution. From the results we got this case is very rare, at least for the Sérsic profile fitting.

Figs. 3.8 shows a comparison between the two codes. No systematics are present, the

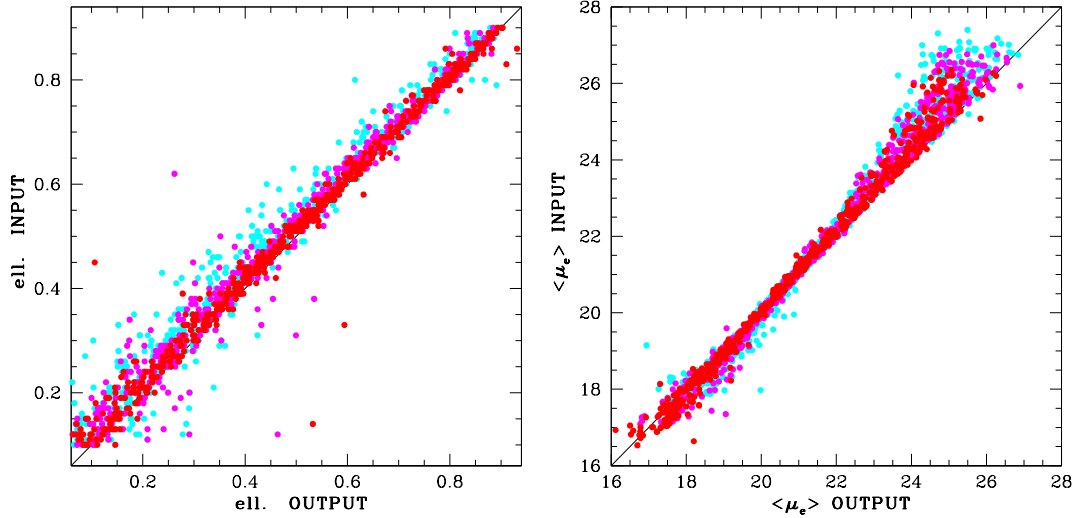


Figure 3.6: GIM2D test results on simulated objects. The plots show the output vs. input ellipticity (left panel) and μ_e (right panel). Points are colored according to the simulated objects total magnitudes in red ($I < 22.5$), magenta ($23.5 < I < 22.5$) and cyan ($23.5 < I < 24$)

medians for both the recovered Sérsic index and half light radius are very close to zero. The scatter is about 15% for the Sérsic index and 10% for the half light radius.

One can argue that the COSMOS ACS fields are not very crowded and that in more crowded fields one could see some systematic differences between the two codes. I had the chance to test both codes on the deep ACS images of A1689 (Halkola et al. 2006). The selected sample was made of bright ($I \lesssim 22.5$) red-sequence early type galaxies. Despite some obvious cases for which GALFIT performed best, again no systematics were found to be really worried about using one of the two code. Of course these considerations apply only for the single Sérsic fitting which we are dealing with here, no simulations and tests were done with regard to bulge/disk decomposition.

3.2.6 Parametric profile fitting versus visual classification

In order to further check our morphological classification, visual morphology was performed in the FDF and GOODS-S fields by Ulrich Hopp according to the de Vaucouleurs et al. (1991) classification scheme. A tight correlation is obtained between the average visual and automated classifications, parameterized by the morphological type T and the Sersic index n_{ser} , respectively (see Fig. 3.9). Using the visual or automated classification does not significantly affect the results presented in this study.

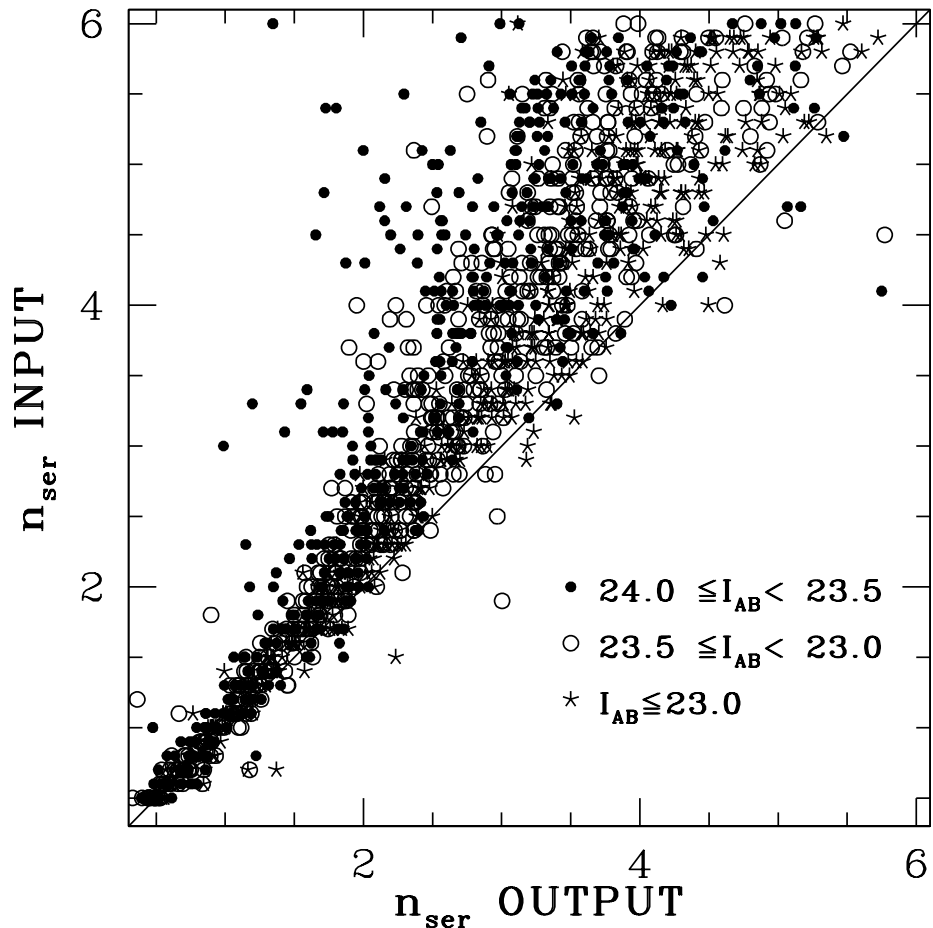


Figure 3.7: GIM2D recovered n_{ser} vs. simulated ones. High Sérsic index objects with magnitudes in the range 23.5/24, despite being easily detectable, fall with their extended wings under the sky surface brightness and suffer from a recovered lower value.

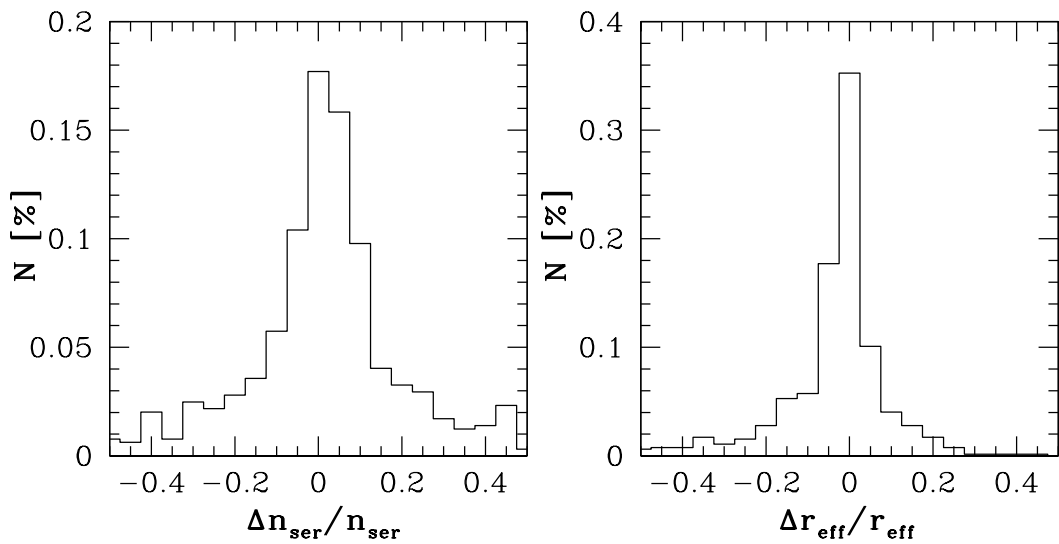


Figure 3.8: GIM2D vs GALFIT comparison. In figure the distribution obtained, on 4 COSMOS tile, of $\Delta n/n$ (left panel) and $\Delta r/r$ (right panel) from the two codes. The median is 0 and the width is less than 0.2 for $\Delta n/n$ and about 0.1 for $\Delta r/r$.

3 Morphological characterization of high redshift galaxies

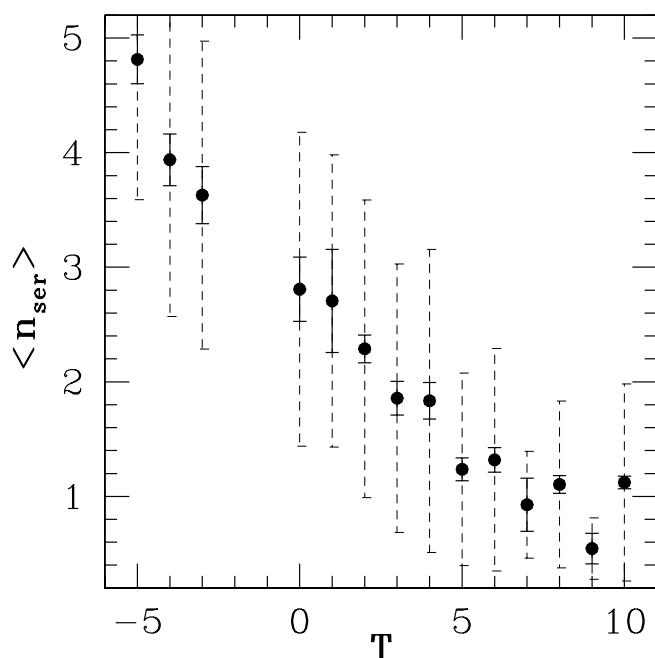


Figure 3.9: Correlation between the Sersic index and the visual classification T value for the GOODS-S subsample. Points are mean values. Solid error bars are the errors on the means, dashed error bars show the rms values.

4

Morphological evolution in FDF and GOODS-S

Adapted from M. Pannella et al., “The Evolution of the Mass Function Split by Morphology up to Redshift 1 in the FORS Deep and the GOODS-S Fields”, 2006, ApJ, 639L, 1

Abstract

In this chapter I present a study of the evolution of the stellar mass density for the separate families of bulge-dominated and disk-dominated galaxies over the redshift range $0.25 \leq z \leq 1.15$. I derive quantitative morphology for a statistically significant galaxy sample of 1645 objects selected from the FORS Deep and the GOODS-S Fields. I find that the morphological mix evolves monotonically with time: the higher the redshift, the more disk systems dominate the total mass content. At $z \sim 1$, massive objects ($M_* \geq 7 \times 10^{10} M_\odot$) host about half of the mass contained in objects of similar mass in the local universe. The contribution from early and late type galaxies to the mass budget at $z \sim 1$ is nearly equal. I show that *in situ* star formation is not sufficient to explain the changing mass budget. Moreover I find that the star formation rate per unit stellar mass of massive galaxies increases with redshift only for the intermediate and early morphological types while it stays nearly constant for late-type objects. This suggests that merging and/or frequent accretion of small mass objects has a key role in the shaping of the Hubble sequence as we observe it now, and also in decreasing the star formation activity of the bulge-dominated descendants of massive disk galaxies.

4.1 Introduction

Lilly et al. (1996), and soon after Madau et al. (1996), produced the first estimates of the cosmic star formation history. Since then, the growing number of deep extragalactic surveys has allowed galaxy evolution to be tackled in more and more detail, to higher and higher redshifts (e.g. Giavalisco et al. 2004b; Gabasch et al. 2004b; Bouwens et al. 2004; Juneau et al. 2005). All these recent studies point towards a substantial amount of star formation at early cosmic epochs.

More recently, a number of studies, mainly based on NIR selected surveys like 2MASS (Cole et al. 2001), MUNICS (Drory et al. 2004a), K20 (Fontana et al. 2004), FIRES (Rudnick et al. 2003), HDF (Dickinson et al. 2003) and GOODS+FDF (Drory et al. 2005), have been able to measure directly the stellar mass density up to high redshifts. The two independent approaches are in a remarkably good agreement, and suggest that about half of the present-day stars was already in place at $z \approx 1$, when the Universe was half of its present age.

The assembly of the stellar mass through cosmic time is a crucial test for models of galaxy formation and evolution (Kauffmann & Charlot 1998). Such models aim at linking the hierarchical growth of dark matter structures to the observed galaxy properties, by means of simplified prescriptions for the formation of baryonic systems in dark matter haloes (e.g. Cole et al. 2000; De Lucia et al. 2004). In this models bulges are thought to form from disks, either through mergers or from dynamical instabilities. Detailed predictions do not exist, but the qualitative expectation is that the fraction of bulge-dominated galaxies decreases at higher redshifts.

In a hierarchical picture one also expects massive objects to assemble at later cosmic times. It is possible however that their stars were already formed in smaller systems that subsequently merged to form more massive galaxies. Therefore their stellar populations could be old enough to explain the local observed spectral energy distributions (SEDs).

It is clear that quantitative predictions on both the processes of mass assembly and evolution from disk to bulge dominated systems depend crucially on the details of the models. Up to now studies on the evolution of the stellar mass density have not allowed to put stringent constraints on the models because in principle the presence of a substantial number of massive objects at high redshift is well contemplated (Fontana et al. 2004; Mo et al. 1998).

An effective way to put sensitive constraints on the models is to understand where the stars were located, specifically what was the morphology of their host galaxies, at different look-back times. In fact, this permits to directly probe how galaxies assembled their stars, and how their morphology (i.e., at least with some approximation, their dynamical status) evolves. Since merging is driving both mass assembly and dynamical evolution in a hierarchical scenario, these studies offer a direct probe of the role of this process in galaxy evolution.

Because of the lack of sufficient angular resolution, galaxies have been often classified, both at low and high redshift, as early or late types based on their broad band colors

4.2 Ground-based data, photo-z and M_{*}/L ratios

(Baldry et al. 2004; Fontana et al. 2004). However this kind of approach suffers, especially at high redshift, from the obvious drawback that a disk galaxy populated by an old stellar population would be classified as an early-type object (and vice versa). Bell et al. (2003) used the concentration parameter to discriminate between early and late type objects in a complete sample extracted from local surveys. They found that in the local Universe the *transition mass*, i.e. the mass at which disks become dominant in the relative contribution to the total stellar mass function, is $\approx 5 \times 10^{10} M_{\odot}$. The same mass value has recently been claimed to play a key role in the galaxy formation process by constraining the effectiveness of feedback processes (Dekel & Birnboim 2004; Kauffmann et al. 2004).

Taking advantage of the HST angular resolution, in the late 1990s, the MORPHS collaboration focused mainly on the evolution of the morphology-density relation in galaxy clusters up to $z \approx 0.5$ (Smail et al. 1997; Dressler et al. 1997; Ellis et al. 1997).

In this work we rely on a deep, complete and automatically morphologically classified sample to study the contribution of galaxies of different morphologies to the redshift evolution of the stellar mass density. Bundy et al. (2005), and also Brinchmann & Ellis (2000), have carried out a work qualitatively similar to the one we present here, but based on shallower samples and visual morphological classification. In particular, Bundy et al. (2005) find some evidence of the transition mass evolving with redshift, but such evolution was questioned by the same authors because of completeness issues.

In this work, for the first time, we rely on a deep, complete and automatically classified sample.

This chapter is organized as follows: in §4.2 we discuss the dataset on which this work is based, in §4.3 we present the surface brightness profiles modeling, and in §4.4 our results on the evolution of mass functions, mass densities and specific star formation rates (SSFR, i.e. star formation rate per unit stellar mass) split by morphological type. Finally, in §4.5 we draw our conclusions.

We use AB magnitudes and adopt a cosmology with $\Omega_M=0.3$, $\Omega_\Lambda=0.7$, and $H_0=70 \text{ km s}^{-1} \text{Mpc}^{-1}$.

4.2 Ground-based data, photo-z and M_{*}/L ratios

This study is based on photometric catalogs derived for the FORS Deep Field (FDF, Heidt et al. 2003; Gabasch et al. 2004a) and part of the GOODS-South Field (Salvato et al., in preparation, see chapter 2). The two fields cover approximately the same area (39.8 arcmin^2 for FDF and 50.6 arcmin^2 for GOODS-S). The FDF photometric catalog covers the UBgRIzJKs broad bands, plus an intermediate band centered at 834nm. The I-selected catalog used here lists 5557 galaxies down to $I_{lim} = 26.8$. For the GOODS-S field, our K-band selected catalog contains 3240 galaxies, and it consists of UBVR_IJHK broadband photometry (Arnouts et al. 2001; Schirmer et al. 2003, Vandame et al., in preparation). Number counts match the literature values down to $K_{lim} \approx 25$.

4 Morphological evolution in FDF and GOODS-S

Photometric redshifts are derived using the method described in Bender et al. (2001) (see also sections 2.1.2 and 2.2.1.2). Their accuracy is 3% and 5% for FDF and GOODS-S respectively, with $\approx 1\%$ outliers for both fields (for more details see Gabasch et al. 2004a).

For all galaxies in both catalogs, the M/L ratios were estimated with a log-likelihood based SED fitting technique, using a library of SEDs built with the Bruzual & Charlot (2003) code, assuming a Salpeter (1955) IMF. The procedure used is described in detail in Drory et al. (2004b). We use here the same mass catalog as in Drory et al. (2005), so we refer the reader to this paper for more details.

4.3 HST imaging and the morphological analysis

Both the FDF and GOODS-S fields were imaged with the ACS camera on board the HST. The FDF was imaged in the broad-band F814W filter, with 4 WFC pointings of 40 minutes exposure each, reaching a 10σ limit of 26 mag. The data reduction was performed with the standard CALACS¹ pipeline, and the combined final mosaic was produced with the multidrizzle package (Mutchler et al. 2002). The GOODS-S field was imaged in four different filters (BVIz) as part of the ACS GOODS legacy (Giavalisco et al. 2004b); the 10σ limit in the F775W band is 26.5 mag.

We make use of the publicly available packages GIM2D (Simard et al. 1999) and GALFIT (Peng et al. 2002) to fit PSF convolved Sersic (1968) profiles to the two-dimensional surface brightness of each object, down to a limit of F814W=24 (FDF) and F775W=24.5 (GOODS-S). The PSFs used to convolve the profiles were obtained for each individual tile by stacking about 10 high S/N isolated stars. The results from the two different codes are in excellent agreement, thus confirming the robustness both of our modeling and of the choice of flux limits.

More details on the surface brightness fitting procedure and on its validation are given in chapter 3. Also, as described in chapter 3, we compared our morphological classification with a classical visual classification (de Vaucouleurs et al. 1991), finding a good correlation between the two. Therefore, our results are not affected by the choice of using an automated, parametric classification.

We split our sample, according to the Sersic index, in early-type ($n \geq 3.5$, $\approx T \leq -3$), intermediate ($2 \leq n < 3.5$, $\approx -3 < T \leq 2$) and late-type ($n < 2$, $\approx T > 2$). We evaluated the effect of morphological k-correction on this coarse classification scheme by also performing the surface brightness modeling on B and z -band images for a subsample of the GOODS-S galaxies. We found that our broad classification is robust for objects at $z \leq 1.15$. Thus we restrict our analysis to $z \leq 1.15$.

Finally, we estimate the mass completeness of the two (FDF and GOODS-S) catalogs as the mass of a maximally old stellar population² having, at every redshift, an observed

¹www.stsci.edu/hst/acs/analysis

²We used a dust-free, passively evolving stellar population model, ignited by an instantaneous burst of sub solar

4.4 Evolution of the morphological mass function, total mass density and SSFR

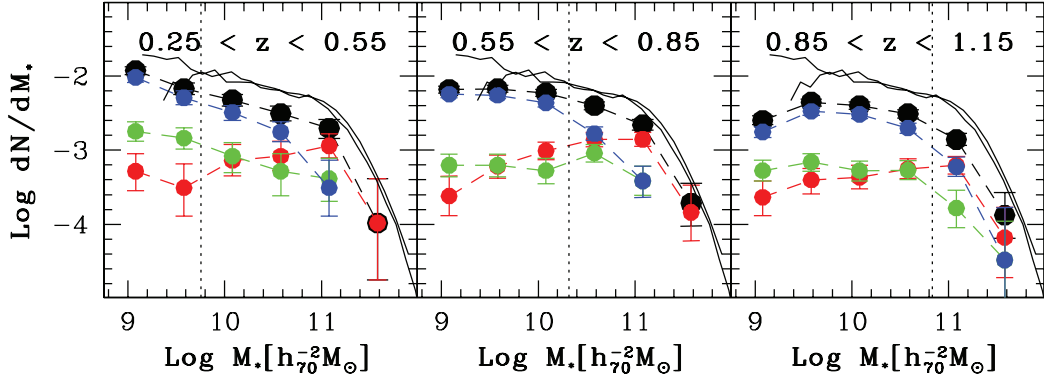


Figure 4.1: The mass function split by morphological types (early in red, intermediate in green, and late in blue) in three redshift bins. Black symbols refer to total values. The vertical axis is in units of [$h_{70}^3 \text{Mpc}^{-3} \text{dex}^{-1}$]. A vertical dotted line indicates the mass completeness limit in each redshift bin. Dashed colored lines are intended to guide the eye. Solid black lines show the local mass function determinations from Cole et al. (2001) and Bell et al. (2003).

magnitude equal to the catalog completeness magnitude (e.g. Dickinson et al. 2003). The final catalog contains 1645 galaxies.

4.4 Evolution of the morphological mass function, total mass density and SSFR

We performed extensive Monte-Carlo simulations to take into account the effect of mass uncertainties ($\approx 0.2\text{dex}$) on our results. Ten thousand simulations of the mass catalog were generated, perturbing each mass within a gaussian of sigma equal to its error. Unless stated differently in the relevant Figure captions, we use the median values of the Monte-Carlo simulations in all figures. Error bars take into account both poissonian errors on the median counts (Gehrels 1986), and 16-84th percentile values of each distribution.

In Fig. 4.1 we show the V/V_{max} corrected stellar mass functions, split by morphological type, in three redshift bins. The redshift intervals were chosen to have comparable numbers of objects in each bin. A dotted vertical line shows the mass completeness for each redshift bin. We find that, at all redshifts, the late-type objects dominate the low-mass end of the mass function, while the early- and intermediate-type objects dominate the high-mass end.

In addition, Fig. 4.1 shows that the relative contribution of disks to the high-mass end

metallicity at $z = 10$.

4 Morphological evolution in FDF and GOODS-S

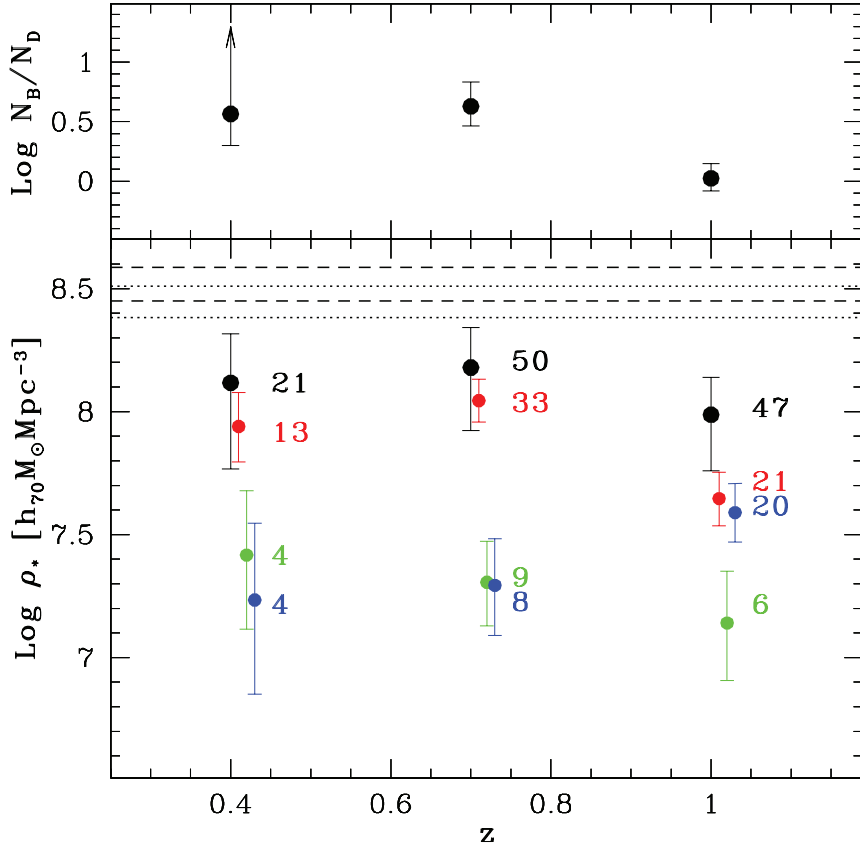


Figure 4.2: Top panel: The redshift evolution of the ratio of bulges and disks number densities. Error bars show the 5th and 95th percentiles of the ratio distributions. **Bottom panel:** Stellar mass densities for objects with $M_* \geq 7 \times 10^{10} M_\odot$ (color coding according to galaxy morphology, as in Fig. 4.1). Points are slightly shifted in redshift for clarity. The median numbers of objects in each class are also labeled. Error bars account for poissonian errors, mass uncertainties, and cosmic variance (for the total values only) as described in the text. Dotted and dashed lines indicate the 3 σ range estimate obtained at redshift 0, with the same mass cut and IMF, from Cole et al. (2001) and Bell et al. (2003), respectively.

of the mass function increases with redshift. This suggests that: *i*) the morphological mix at the high-mass end evolves with redshift; *ii*) the transition mass increases with redshift. The latter finding was already suggested in Bundy et al. (2005), but its significance was hampered by their mass completeness limit. In our case, the transition seems to happen well above the estimated mass completeness. As Fig. 4.1 shows, at $z \sim 1$ the disks' and bulges' contributions become comparable at $\approx 1 \times 10^{11} M_\odot$.

4.4 Evolution of the morphological mass function, total mass density and SSFR

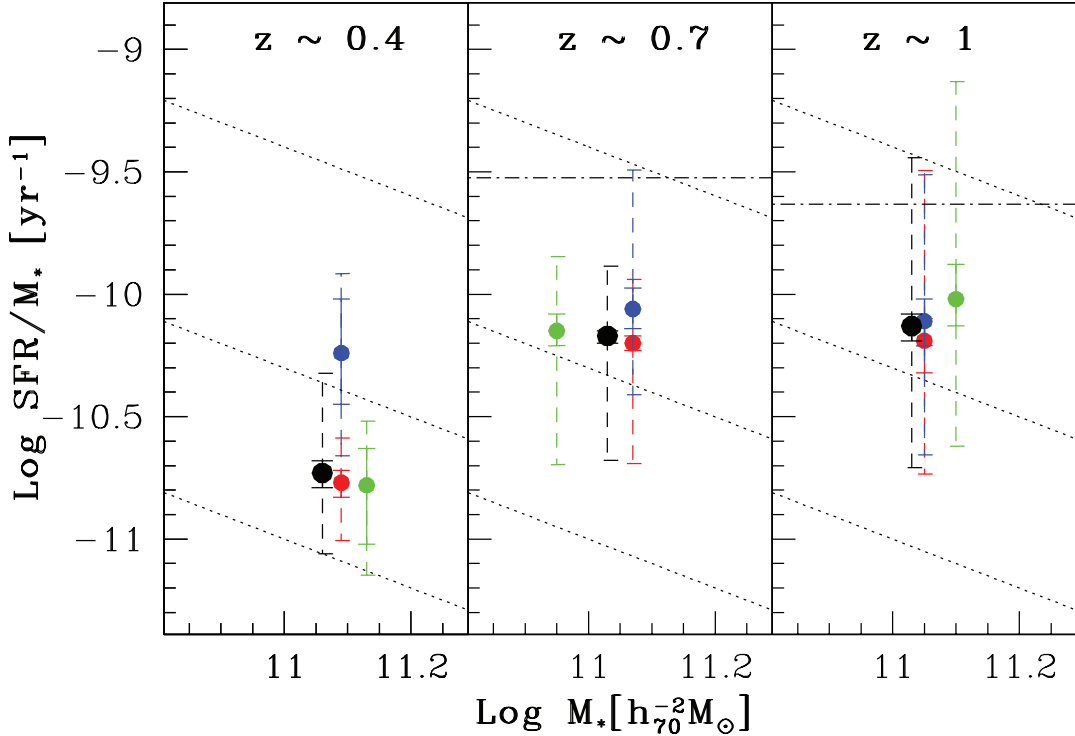


Figure 4.3: The median SSFR for different morphological types. The coloured symbols (same colour coding as in previous figures) show the median values in both stellar mass and SSFR. Dashed error bars represent the median 10th and 90th percentiles of the Monte-Carlo realizations, while the solid error bars show 1σ uncertainties on the median values. Tilted lines are constant SFR values (from the bottom 1,5,40 $M_\odot \text{yr}^{-1}$) while the horizontal lines mark the doubling mass lines (only for the last two redshift bins – see text for details).

In order to better explore the evolution of the morphological mix at the high-mass end, and to make a fair comparison between the three redshift bins, we cut hereafter the three subsamples at the same common mass completeness ($M_* \geq 7 \times 10^{10} M_\odot$).

The upper panel of Fig. 4.2 shows the behavior of the ratio of the number densities of bulges and disks. At increasing redshift, this ratio is found to systematically decrease with respect to the no-evolution hypothesis at more than 3σ significance. In the bottom panel of Fig. 4.2, we show the stellar mass density split by morphological type at different redshifts.

4 Morphological evolution in FDF and GOODS-S

The error estimates of the total values include the cosmic variance contribution, estimated as in Somerville et al. (2004).

In agreement with previous studies (see §1), we find that at $z \sim 1$ massive objects host almost half of the stellar mass contained in similarly massive objects at $z = 0$. In addition, we find that the contribution to the total mass budget from early and late type galaxies is almost equal at $z \sim 1$, but strongly evolves with redshift: there is a *mass pouring* from disk systems to bulge-dominated objects. Our findings require a scenario in which massive objects almost double their mass from redshift 1 to 0, and become more and more bulge-dominated systems as time goes by.

A possibility is that *in situ* star formation increases the mass and secular evolution modifies the morphology (Kormendy & Kennicutt 2004). Under simplified assumptions, we can estimate whether the star formation rates (SFR) of the galaxies in our three redshift subsamples can account for a doubling of the stellar mass by $z = 0$. Following Madau et al. (1998), the SFR of individual objects can be estimated from the restframe UV luminosity as $SFR_{2800} = 1.27 \times 10^{-28} \times L_{2800}$ in units of $M_\odot \text{yr}^{-1}$, where the constant factor is computed for a Salpeter IMF. We apply a dust attenuation correction of $A_{2800} = 1\text{mag}$ to the whole sample. This median value, assumed not to depend on redshift, is derived as in Gabasch (2004) by comparing the total stellar mass density and the integral of the SFR density at different look-back times. Fig. 4.3 shows the median SSFR values for the three redshift bins and for the different morphological types, cut at the same mass completeness as described above. Since it is not possible to know the individual star formation histories, we derive the median SFR decline with cosmic time from the massive galaxies subsample, and we assume that all the objects in our sample follow this median star formation history. In this way we can estimate, at every redshift, the minimum SSFR that enables an object to double its mass by $z = 0$. These minimum SSFRs are shown in the plot as horizontal lines at the last two redshift bins considered. It appears that only a small fraction of the $z \sim 1$ sample would be able to double its mass.

An alternative and more likely solution (see also Brinchmann & Ellis 2000) is a continuous accretion of smaller mass galaxies, and possibly the merging of massive disks, which can account for both the changing total mass budget and the morphological mix evolution.

In the past a number of works (e.g. Brinchmann & Ellis 2000; Feulner et al. 2005a,b; Bauer et al. 2005) have focused on the SSFR redshift evolution and consistently found an increase of the SSFRs with redshift. Hence the bulk of star formation in massive galaxies was pushed to $z \geq 2$, in agreement with the downsizing scenario (Cowie et al. 1996).

Here for the first time we explore the SSFR evolution split by different morphological types. We find, for objects with $M_* \geq 7 \times 10^{10} M_\odot$, a different behavior in the SSFR redshift evolution for the different morphological types. The median SSFR of late-type objects shows only a mild, if any, evolution up to redshift 1, while the median values of early and intermediate types are clearly increasing with redshift. Since these latter populations are dominating in numbers, they drive the redshift evolution of the whole massive galaxies distribution. This finding, together with the previous arguments, suggests that the morphological evolution of

massive disk galaxies toward more and more bulge dominated systems is accompanied by a decrease in the specific star formation rate of their end products.

Bell et al. (2005) show that a large part of the star formation in massive galaxies at $z \sim 0.7$ is due to normal spiral galaxies. Moreover, they conclude that turning off star formation in these objects is responsible for the observed decline of cosmic star formation thereafter. We find a good agreement at $z \sim 0.7$ with their result but also a hint that the decline of star formation in massive galaxies is linked more to the evolution of bulge-dominated galaxies.

4.5 Conclusions

In this work we have studied the contribution of disks and bulges to the evolution of the stellar mass function up to $z \sim 1$.

We agree with previous work (Bundy et al. 2005) that the transition mass, i.e. the mass at which disks become dominant in the relative contribution to the total mass function, increases with redshift. We estimate that at $z \sim 1$ the transition mass is up to a factor 2 larger than its measured local value.

We show that the morphological mix evolves with redshift. At $z \sim 1$ early and late type galaxies contribute nearly equally to the total mass budget in massive objects (i.e. with $M_* \geq 7 \times 10^{10} M_\odot$). We suggest that merging events must play a key role in the *mass pouring* from disks to bulges.

We find a different behavior of the SSFR, i.e. the star formation rate per unit stellar mass, as a function of redshift for the different morphological types. The median SSFR of late-type objects shows almost no evolution up to $z \sim 1$. Conversely, median SSFRs for early and intermediate types increase systematically. Since these latter morphological types are dominating in numbers, they drive the total SFR evolution of massive galaxies. This suggests a scenario where the morphological evolution of massive disk galaxies through merging is followed by the decrease of the star formation in their bulge-dominated descendants, maybe after a burst of star formation that exhausts the available gas.

Acknowledgments

We wish to thank the referee for valuable comments that pushed us to strengthen our results and to improve their presentation. M.P. is glad to thank G. De Lucia, D. Pierini, G. Rudnick and V. Strazzullo for a careful reading of the manuscript and for many insightful comments and suggestions. This work was supported by the Deutsche Forschungsgemeinschaft through the SFB 375 grant.

4 Morphological evolution in FDF and GOODS-S

5

Bulges and disks in the last 8 Gyrs of the COSMOS

Adapted from M. Pannella et al, “Bulges and disks in the COSMOS during the last 8 Gyrs”, 2007, A&A in preparation

Abstract

The Cosmic Evolution Survey (COSMOS) allows for the first time a highly significant census of environments and structures up to redshift 1 as well as a full morphological description of the galaxy population. In this chapter I present a study aimed to constrain the evolution of the morphological mix mass content up to redshift one and its dependency, if any, on the environmental density. I use a deep multicolor catalog, covering an area of $\sim 0.7 \text{ square degrees}$ inside the COSMOS field, to obtain accurate photometric redshift ($I \lesssim 25$ and $\Delta z/(z_{spec} + 1) \approx 0.035$). I estimate galaxy stellar masses by fitting the multi-color photometry to a grid of composite stellar population (CSP) models. I quantitatively describe the galaxy morphology by fitting PSF convolved Sérsic profile to the galaxy surface brightness distributions. I find an evolution of the morphological mix with redshift: the higher the redshift the more disks become important. I identify a mass underdensity in the COSMOS field at redshift 0.5. I find that the morphological mix is a strong function of the local comoving density at all the redshifts explored. I investigated the evolution of the specific star formation rate (SSFR) as a function of morphological type and environment, finding that the locations of early and late-type galaxies in the stellar mass vs. SSFR plane are very well separated at all redshifts and in all environments. The SSFR in massive early-types is found to significantly evolve with redshift, while it remains pretty constant since $z \gtrsim 1$ in massive disks. Since the high-mass end of the galaxy populations is always dominated by early-type objects, these drive the decline in star formation rate at high masses. While in general this

5 Bulges and disks in the last 8 Gyrs of the COSMOS

picture seems to be quite similar in all environments, in low density regions there is a population of relatively massive, early-type galaxies, having high SSFR and blue colours.

Galaxy formation and evolution has been a very actively debated topic of observational cosmology in the last years. Only recently models and observations are converging toward a unified and coherent picture.

On one side the observations of the Universe, with some controversies on the way, have finally agreed that half of the present-day stars was already in place at $z \approx 1$ and that the same mass deficit affects the high-mass end: the galaxy stellar mass function evolves basically from the local determination to redshift 1 only by a normalization factor of about 2. This means that at the high-mass end as well as at the low-mass one there is, at redshift 1, a factor 2 of missing objects in the comoving number density as respect to the local value (e.g. Dickinson et al. 2003; Rudnick et al. 2003; Drory et al. 2004a; Bundy et al. 2005; Borch et al. 2006; Fontana et al. 2006; Pozzetti et al. 2007; Arnouts et al. 2007). Measurements of the star formation rate density over cosmic times (e.g. Giavalisco et al. 2004b; Gabasch et al. 2004b; Bouwens et al. 2004) are in good agreement with being half of the present stars already born at redshift 1.

On the other side the models, linking the hierarchical growth of dark matter structures to the observed galaxy properties by means of simplified prescriptions for the formation of baryonic systems, predict that galaxies form in a bottom-up fashion by following the cosmological destiny of dark matter halos. Massive galaxies, in these models, assemble most (50%) of their stellar mass via merging only at $z < 1$ (De Lucia et al. 2006) but most of these accretion events are both red mergers (i.e. gas free mergers that imply no induced induced star-formation) and very rarely major mergers hence very difficult to detect from the observational point of view. The latest realizations of these models (e.g. Kitzbichler & White 2007; Bower et al. 2006) have been able to fully reproduce the galaxy stellar mass function up to high redshifts, thus reconciling the theoretical bottom-up assembly of dark matter halos to the claimed top-down assembly of galaxies (Cimatti et al. 2006).

In *hierarchical* models star formation is supposed to take place only in disk structures and in gas-rich mergers. This latter event would exhaust the residual gas and create a dynamically hot system: a bulge galaxy. Also dynamical instabilities, like minor merger events, are able to destroy the disk structures and finally create an elliptical galaxy. Detailed predictions in the literature do not exist but the general expectation is that the fraction of bulge-dominated massive galaxies increases with time.

The study of the evolution of the morphological mix in the galaxy stellar mass function is a decisive tool to put sensitive constraints on the models, because it could give unique insights in both the feedback and the merging processes in galaxy evolution (see for a detailed discussion Cole et al. 2000).

Because of the lack of sufficient angular resolution, galaxies have been often classified, both at low and high redshift, as early or late types based on their broad band colors

(Baldry et al. 2004; Fontana et al. 2004; Giallongo et al. 2005; Bundy et al. 2006). However this kind of approach suffers, especially at high redshift, from the obvious drawback that a disk galaxy populated by an old stellar population would be classified as an early-type object (and vice versa).

Thanks to the advent of the Advanced Camera for Surveys (ACS; Ford et al. 2003) on board the Hubble Space Telescope, it has become possible to investigate the optical restframe emission of galaxies up to redshift one and slightly beyond with sub-kiloparsec resolutions and on relatively wide fields.

In this context the COSMOS (Scoville et al. 2006a) survey is the ultimate effort to cover a sensitive patch of the sky (2 square degrees) with ACS, going factors of 10/100 wider than previous efforts like GEMS (Rix et al. 2004), the Great Observatories Origins Deep Survey (GOODS; Giavalisco et al. 2004b), the FORS Deep Field (FDF; Heidt et al. 2003) and others.

The high resolution imaging has been complemented in COSMOS by a state-of-the-art multiwavelength coverage all the way from the X-ray to the Radio regime. By observing the Universe in all its colors COSMOS is going to become a real breakthrough in the next years of the observational cosmology. The need to tackle and understand the Nature conspiracies embedded in the beautiful Universe variance makes of this wide and deep survey a unique and unprecedented possibility.

In this work we rely on a deep and accurate ($I \lesssim 25$ and $\Delta z/(z_{spec} + 1) \approx 0.035$) photometric redshift catalog, described in chapter 2, section 2.3, complemented by a morphologically classified sample ($F814 \lesssim 24$) to study the contribution of galaxies of different morphologies to the redshift evolution of the stellar mass density, as well as its dependency from the environmental density, over an area of $\sim 0.7 \text{ square degrees}$ in the COSMOS field.

Brinchmann & Ellis (2000), Bundy et al. (2005), Pannella et al. (2006) and also Franceschini et al. (2006), have carried out a work qualitatively similar to the one we present here, but based either on shallower samples and visual morphological classification or on much smaller areas heavily affected by cosmic variance.

This chapter is organized as follows: in § 5.1 we discuss the ground-based dataset and the photometric redshifts on which this work is based, in § 5.2 we discuss how galaxy stellar masses have been estimated, in § 5.4 we present the ACS data used in this work, the source extraction and the galaxy number counts, in § 5.4 we briefly describe the quantitative morphology analysis, referring to chapter 3 for a more detailed discussion, in § 5.5 we present the evolution of the morphological mass function and mass density, in § 5.6 we report on the identification of a mass underdensity in the COSMOS field at redshift 0.5, in § 5.7 we discuss the effect of local mass density on the galaxy morphological evolution and finally in § 6.4.2 we summarize our results and draw our conclusions.

Throughout this work, we use AB magnitudes and adopt a Λ cosmology with $\Omega_M = 0.3$, $\Omega_\Lambda = 0.7$, and $H_0 = 70 \text{ km s}^{-1} \text{ Mpc}^{-1}$.

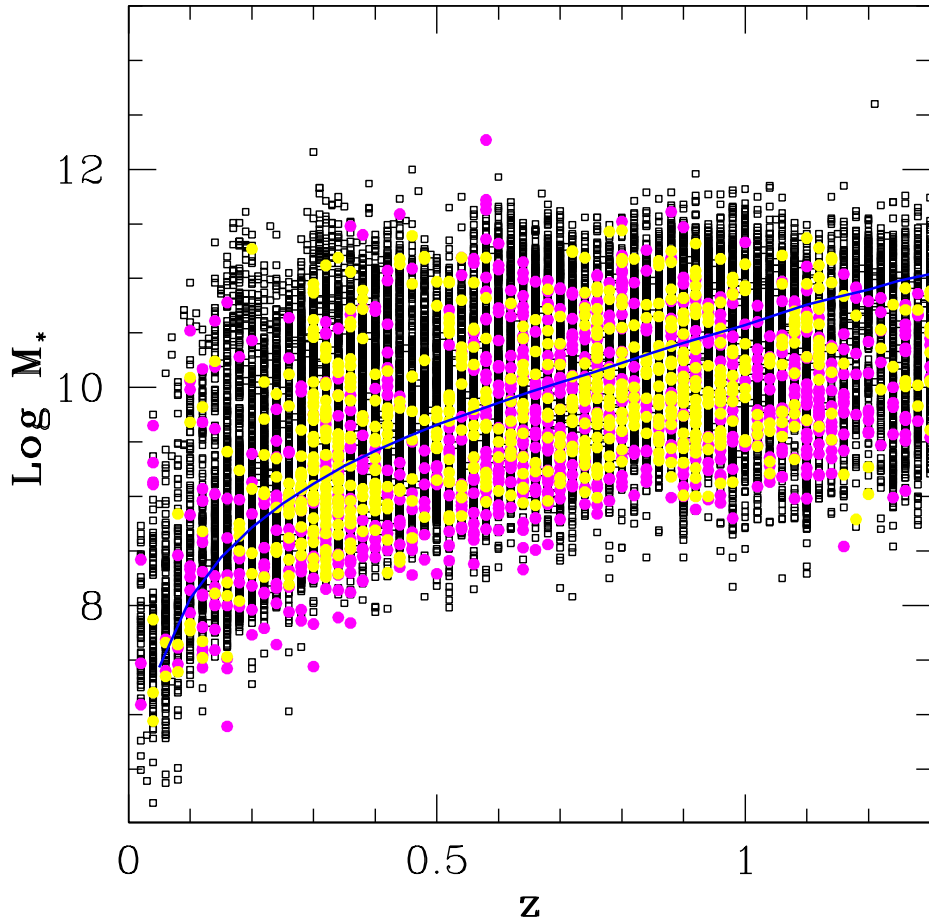


Figure 5.1: The distribution of galaxy stellar masses as function of redshift for the morphological catalog used in this work. Empty squares show the COSMOS catalog we are using here, for comparison and to show the improved statistic we over plot the morphological catalog used in Pannella et al. (2006) from the FDF(yellow) and GOODS-S(magenta) fields. The solid blue line sets the estimated mass completeness of the morphological sample at each redshift, see text for details.

5.1 Ground-based data and photometric redshifts

The ground-based data used in this paper combine the publicly available $uBVrizK$ COSMOS dataset with proprietary imaging in the H band. A highly homogeneous multi-wavelength i-band selected catalog is used to derive accurate photometric redshifts. A full description of the NIR data acquisition, data reduction and catalogue assembling, as well as for the photometric redshifts estimation, is presented in chapter 2, section 2.3. Here in the following,

for the sake of clarity, we give only a very brief summary.

Our *cleaned* i-selected catalogue comprises 293 377 objects over an area of $\sim 0.7 \text{ square degrees}$ and down to the limiting magnitude (~ 26), $\approx 118\,475$ objects brighter than 25 mag and $\approx 60\,000$ brighter than 24 mag. There is a good agreement between literature data and COSMOS number counts up to the 25th magnitude. At the bright end ($i \leq 21$) the literature number counts are sensibly higher since most of the very bright objects are saturated in the Subaru i-band images and thus not present in the final catalog.

Photometric redshifts were derived using the technique described in chapter 2 (Bender et al. 2001; Gabasch et al. 2004a). In short the method consists of : i) checking photometric zeropoints and, if necessary, determining photometric shifts by comparing theoretical and observed stellar *locii*, ii) computing object fluxes in a fixed aperture ($2.0''$) from seeing-matched images, iii) determining a redshift probability function $P(z)$ for each object by matching the object's fluxes against a set of template spectra covering a wide range of stellar population ages and star-formation histories.

The use of the GALEX FUV and NUV bands² allowed some photo-z degeneracies to be broken, and a final accuracy of $\Delta z/(z_{spec} + 1) \approx 0.035$ to be reached.

5.2 Computing mass-to-light ratios

The method we use to infer stellar masses from multi-color photometry is the one described in Drory et al. (2004b). It is based on the comparison of the observed multi-color photometry with a grid of stellar population synthesis models produced with the Bruzual & Charlot (2003) code.

We parameterize the possible star formation histories (SFHs) by a two-component model, consisting of a main, smooth component described by an exponentially declining star formation rate $\psi(t) \propto \exp(-t/\tau)$, linearly combined with a secondary burst of star formation. The main component timescale τ varies in $\in [0.1, \infty]$ Gyr, and its metallicity in $-0.6 < [\text{Fe}/\text{H}] < 0.3$. The age of the main component, t , is allowed to vary between 0.5 Gyr and the age of the Universe at the object's redshift.

The secondary burst of star formation is modeled as a 100 Myr old constant star formation rate episode of solar metallicity. We restrict the burst fraction to be lower than 15% in mass (higher values of the burst fraction are degenerate and unnecessary since such cases are described by models with a young main component).

We adopt a Salpeter (1955) initial mass function for both components, with lower and upper mass cutoffs of 0.1 and $100 M_\odot$.

Additionally, both the main component and the burst are allowed to exhibit a variable amount of extinction by dust with $A_V^{1,2} \in [0, 1.5]$ and $[0, 2]$ for the main component and the burst, respectively. This takes into account the fact that young stars are found in dusty environments and that the star light from the galaxy as a whole may be reddened by a (geometry dependent) different amount. We compare this set of models with multi-color photometry of

5 Bulges and disks in the last 8 Gyrs of the COSMOS

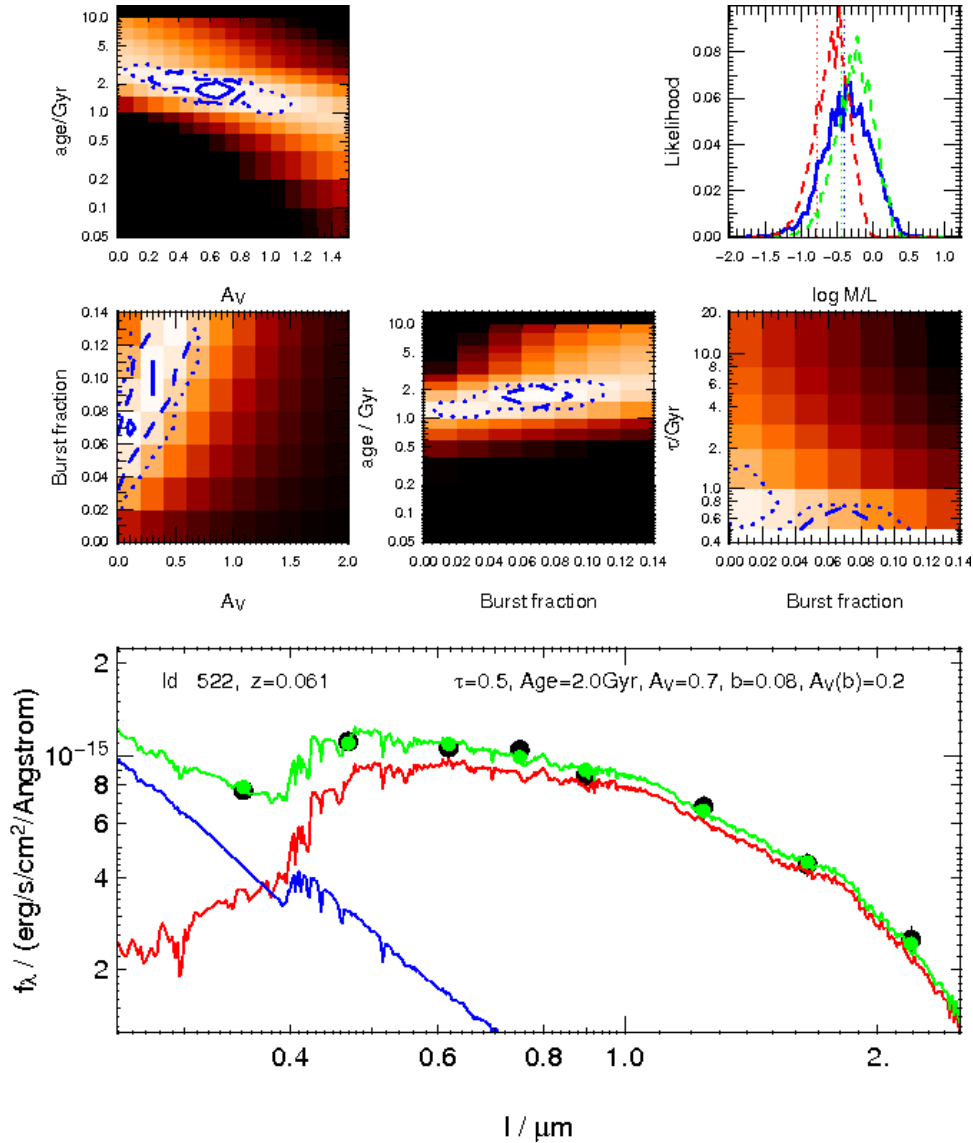


Figure 5.2: Example of SED fit result for a relatively young object at $z = 0.061$. The small panels in color scale show couples of fitting parameters plotted one against the other (age, A_V , burst fraction, and τ). Degeneracies in the fit parameters space are evident. The upper right panel shows the likelihood distribution of the mass-to-light ratio in three passbands (B, g, and K in blue, green, and red, respectively): as expected, the K band M/L is more constrained with respect to the optical ones. The bottom panel shows the observed SED (solid dots) with the best-fit overplotted as a green line (best fitting parameters are labeled on the top). Beside the best-fit SED, also the main component and the secondary burst are plotted separately, as the red and blue lines, respectively.

5.2 Computing mass-to-light ratios

each object, computing the full likelihood distribution in the 6-dimensional parameter space $(\tau, [\text{Fe}/\text{H}], t, A_V^1, \beta, A_V^2)$, the likelihood of each model being $\propto \exp(-\chi^2/2)$.

To compute the likelihood distribution of mass-to-light ratios M/L , we weight the M/L of each model by its likelihood and marginalize over all parameters. The uncertainty in M/L is obtained from the width of this distribution.

For young objects, with relatively high burst fractions, the width of the M/L distribution is usually much wider in the optical than in NIR bands, while for quiescent objects the width of the M/L distribution is very similar in all bands. On average, the width of the likelihood distribution of M/L at 68% confidence level is between ± 0.1 and ± 0.2 dex (using the B band M/L). The uncertainty in mass has a weak dependence on mass (increasing with lower S/N photometry), and it mostly depends on the spectral type: early-type galaxies have more tightly constrained masses than late types.

In Figure 5.2 we show as an example the SED fit result for a relatively young object at $z = 0.061$. Degeneracies in the fit parameters space are evident in the small panels in colour scale. Furthermore, as expected the K band M/L is better constrained than the optical ones. The bottom panel shows the observed SED together with the best-fit SED overplotted (green line), as well as the two components separately (main component and secondary burst as red and blue lines, respectively).

We estimated the galaxy stellar masses for all the objects in the I band selected catalog down to the limiting magnitude. Galaxy stellar mass functions, mass densities and number densities evolution up to $z \sim 6$ will be studied in details in a forthcoming paper (Goranova et al. in preparation).

In figure 5.1 we show the distribution of galaxy stellar masses as function of redshift for the morphological catalog used in this work. For comparison and to show the impressive statistic available we over plot the morphological catalog values used in Pannella et al. (2006) from the FDF and GOODS-S fields.

In figure 5.3 we show stellar mass density up to redshift 1 for objects with $\log M_* \gtrsim 10.8$ which corresponds to the mass completeness value for the highest redshift considered. Dashed lines represent 1σ estimate of the local mass density from Bell et al. (2003) after applying the same mass cut. The error bars represent the cosmic variance contribution, as estimated in Somerville et al. (2004), that is a factor 10 larger than statistical errors. By assuming that the mass function evolves only in normalization over this redshift range one should add 0.28 dex to the plotted values to recover total mass densities.

The mass completeness at different redshifts was estimated as the mass of a maximally old stellar population¹ having, at every redshift, an observed magnitude equal to the catalog completeness magnitude (e.g. Dickinson et al. 2003). In table 5.1 we provide the completeness mass values as a function of redshift, for the morphological catalog ($I_{814W} < 24$) as well as for the global photometric catalog ($I_{Sub} < 25$).

¹We used a dust-free, passively evolving stellar population model, ignited by an instantaneous burst of sub solar metallicity at $z = 10$.

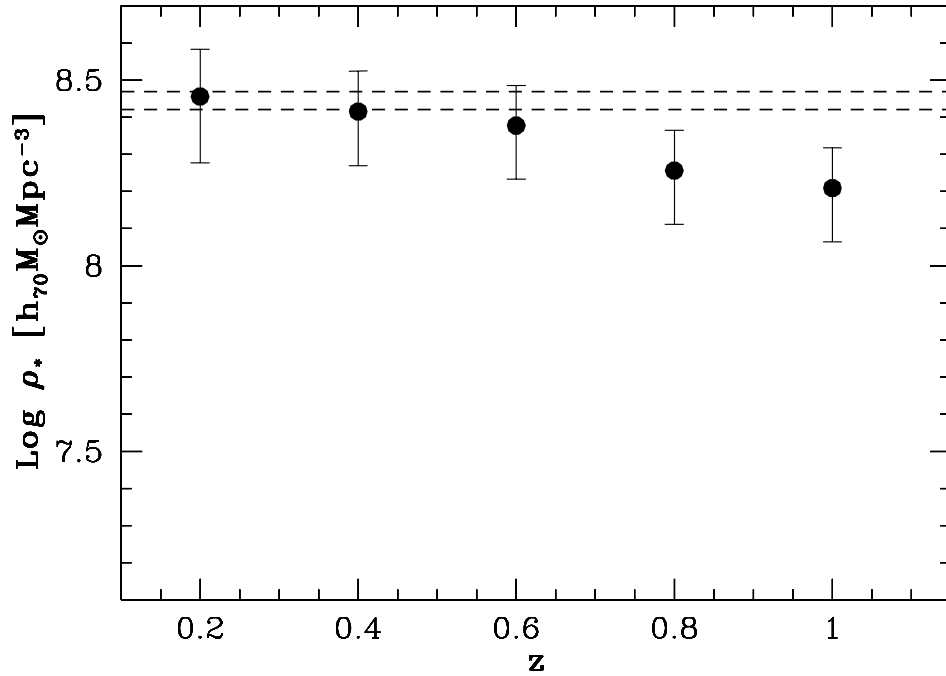


Figure 5.3: Cosmic stellar mass density up to redshift 1 for objects with $\text{Log } M_* \gtrsim 10.8$ which corresponds to the mass completeness value for the highest redshift considered. Horizontal dashed lines represent the local mass density from Bell et al. (2003) after applying the same mass cut. The error bars represent the cosmic variance contribution, as in Somerville et al. (2004). By assuming that the mass function evolves only in normalization over this redshift range one should add 0.28 dex to the plotted values to recover total mass densities.

Table 5.1: Log M_* completeness values versus redshift

z	0.25	0.45	0.65	0.85	1.05	1.25
F814W (24)	8.9	9.4	10.0	10.3	10.7	11
I_{Sub} (25)	8.6	9.1	9.7	10.0	10.4	10.7

5.3 HST Advanced Camera for Surveys imaging

The starting point of COSMOS was the allocation of an unprecedented wide Hubble Space Telescope (HST) high resolution imaging on a 2square degree patch in the sky. Imaging was performed in the F814W ACS filter. A total of 581 orbits/pointings were devoted to imaging in this filter. Within each orbit, four equal length exposures of 507 sec duration each (2028 sec

total) were obtained in a 4 position dither pattern, designed to shift bad pixels and to fill in the 90 pixel gap between the two ACS CCD arrays. Adjacent pointings in the mosaic were positioned with approximately 4% overlap in order to provide at least 3 exposure coverage at the edge of each pointing and 4 exposure coverage over approximately 95% of the survey area. This multiple exposure coverage with ACS provided excellent cosmic ray rejection.

A full description of the ACS data processing including drizzling, flux calibration, registration and mosaicing is provided in Koekemoer et al. (2007) and in Scoville et al. (2006b). The absolute registration of all ACS data in the COSMOS archive is accurate to approximately 0.05–0.10 '' over the entire field and the flux calibration of the ACS is accurate to better than 0.05% in absolute zero point. The ACS images released to the public² are sampled with 0.05 '' pixels. The measured FWHM of the PSF in the ACS I-band filter is 0.11 '' .

5.3.1 Sources extraction, star-galaxy classification and cataloging

Source extraction was performed with the SExtractor code (Bertin & Arnouts 1996) on each ACS tile in a *cold* manner: our main extraction goal was devoted the minimization of the artificial source splitting and the maximization of the number of pixels assigned to each object.

We used 348 ACS tiles, i.e. only the ones overlapping with the ground based photometry used in this work.

Taking advantage of the ACS high resolution imaging we could remove the point-like (stellar) objects using the structural parameters output by SExtractor. We namely used the full width half maximum (FWHM), the half light radius, the neural network stellarity index and the total magnitude for each object to select point-like sources: figure 3.3 in chapter 3 shows the selected sources in the total magnitude vs FWHM plane.

In figure 5.4 we show F814W band galaxy number counts, not corrected for incompleteness, compared with the available literature, and in table 5.2 we provide the plotted values. The ACS galaxy catalog has been crosscorrelated in coordinates with the ground based catalog by allowing a 1 arcsec matching radius. We removed from the final catalog all the objects for which one ground based entry had more than one entry in ACS catalog. The final morphological catalog used in this work contains 41300 objects over $\sim 0.7 \text{ } \square^{\circ}$ and results to be $\approx 90\%$ complete down to F814W = 24.

5.4 The morphological analysis

We make use of the package GIM2D (Simard et al. 1999) to fit PSF convolved Sersic (1968) profiles to the two-dimensional surface brightness distribution of each object, for all sources down to a limit of F814W=24. The PSFs used to convolve the profiles were obtained for each individual tile by stacking about 10 high S/N isolated stars.

²Publicly available at <http://irsa.ipac.caltech.edu/data/COSMOS/>

5 Bulges and disks in the last 8 Gyrs of the COSMOS

Table 5.2: Galaxy number counts not corrected for incompleteness from COSMOS in the $F814W$ ($\sim 0.7 \text{ } \square^\circ$). $\log N$ and $\sigma_{\log N}$ are given, where N is in units of $0.5 \text{mag}^{-1} \text{deg}^{-2}$.

<i>F814W</i>		
<i>mag</i>	$\log N$	$\sigma_{\log N}$
17.01	1.576	0.0969
17.51	1.801	0.0728
18.01	2.137	0.0481
18.51	2.416	0.0343
19.01	2.655	0.0258
19.51	2.867	0.0201
20.01	3.047	0.0163
20.51	3.252	0.0128
21.01	3.429	0.0104
21.51	3.63	0.0082
22.01	3.793	0.0068
22.51	3.974	0.0055
23.01	4.148	0.0045
23.51	4.318	0.0037
24.01	4.501	0.0030
24.51	4.671	0.0025
25.01	4.802	0.0021
25.51	4.872	0.0020
26.01	4.769	0.0022
26.51	4.01	0.0053

We tested our results by running also the GALFIT (Peng et al. 2002) code on some of the COSMOS ACS patches. The results from the two different codes are in excellent agreement, thus confirming the robustness both of our modelling and of the choice of flux limits (see chapter 3, section 3.1.5).

We further tested our results by running the GIM2D code on simulated images. This test was performed by adding to the real image, in a blank, pure-sky region, a fake object, as described in detail in chapter 3, section 3.1.4. The whole procedure is then performed exactly as for real objects: we find that the profile parameters of simulated objects are well recovered down to $F814W=24$ if their $\mu_e \geq \mu_{sky}$. High Sérsic index objects have very extended wings that, depending on the total flux, can fall under the sky surface brightness, thus for these objects a lower Sérsic index, total flux and effective radii are usually recovered. More details are given in chapter 3.

5.5 The evolution of the morphological mass function and mass density

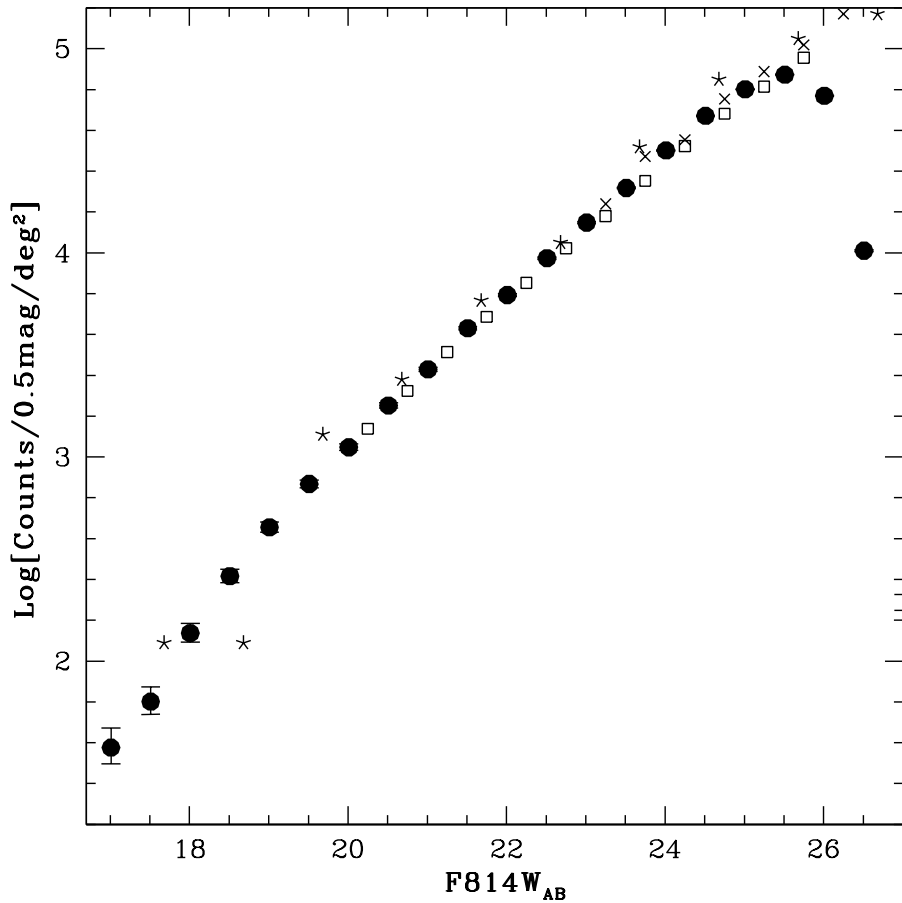


Figure 5.4: Galaxy number counts for the ACS/F814W band are plotted as filled dots. Error bars account only for poissonian errors and no correction for incompleteness has been applied. Literature data are plotted with other symbols and are taken from (Pannella et al. 2006; asterisks, FDF), (Leauthaud et al. 2007; squares, COSMOS), (Benítez et al. 2004; crosses, VV29).

5.5 The evolution of the morphological mass function and mass density

We split our sample, according to the Sérsic index value, in early-type ($n \geq 3.5$, $\approx T \leq -3$), intermediate ($2 \leq n < 3.5$, $\approx -3 < T \leq 2$) and late-type ($n < 2$, $\approx T > 2$) objects. We use here the same split as in Pannella et al. (2006), a good correlation was obtained between the average visual and automated classifications (see Fig. 3.9 in chapter 3, section 3.2.6), as

5 Bulges and disks in the last 8 Gyrs of the COSMOS

parameterized by the morphological type T and the Sérsic index n_{ser} , respectively.

We restrict our analysis to $z \leq 1.2$ to limit the bias introduced by the restframe emission band shifting, namely the effect of the morphological k-correction. A number of studies in the last years have shown, although not in a conclusive and quantitative way, that this is indeed a fair assumption (e.g. Scarlata et al. 2006; Abraham et al. 2007).

We performed extensive Monte-Carlo simulations to take into account the effect of mass uncertainties (≈ 0.2 dex) on our results. One thousand simulations of the mass catalog were generated, perturbing each mass within a gaussian of sigma equal to its error. Unless stated differently in the relevant figure captions, we use the median values of the Monte-Carlo simulations in all figures. Error bars take into account both poissonian errors on the median counts (Gehrels 1986), and 16-84th percentile values of each distribution.

In Fig. 5.5 we show the V/V_{max} corrected number density evolution split by morphological type, up to redshift 1.2, for objects in the stellar mass ranges [10.6/10.8, 10.8/11, 11/11.2, 11.2/12 in Log M_*]. The mass range is indicated in the upper right corner of each panel. By multiplying the plotted number densities by the average mass in the corresponding mass range, each panel could be interpreted as the evolution of the total mass densities contributed by objects in that stellar mass range. The dotted vertical lines show the estimated redshift completeness for the relevant mass bin.

The early-type objects always dominate the high-mass end. We find that the lower the stellar mass the more the late-type objects tend to dominate the relative contribution to the total number(mass) density.

The same trend is true by looking at increasing redshift: the higher the redshift the more the relative contribution of bulges and disks gets closer. For the lowest mass range [10.6/10.8] the transition from a bulge-dominated to a disk-dominated stellar mass budget happens around redshift 0.7; after that redshift disks are always contributing more to the total mass budget. In the second mass range (Log $M_* = 10.8/11$) the transition is not occurring before redshift 1.1.

At each redshift, a *transition mass* can be identified where the transition from a bulge-dominated to a disk-dominated stellar mass budget takes place. Based on the very good statistics available in this work, we are able to confirm the main conclusions of P06: *i*) the morphological mix at the high-mass end evolves with redshift; *ii*) the transition mass increases with redshift. At $z \sim 0.7$ we find a value of the transition mass approximately consistent with the local value $M \approx 5 \times 10^{10} M_\odot$, as measured in Bell et al. (2003) by using the concentration parameter to discriminate between early and late type objects in a complete sample extracted from local surveys. At $z \sim 1$ the disks and bulges contributions become comparable at $M \approx 1 \times 10^{11} M_\odot$.

In a fixed mass range the number densities of disks are consistent with being constant with redshift, while the early type follow the more general total declining. At a fixed redshift, the number densities of early types of different masses is very similar (in +- 0.1/0.2 dex), while the disks number densities move by one order of magnitude passing from the high to the low stellar mass range. This naturally sets the evolution of the transition mass with redshift.

5.5 The evolution of the morphological mass function and mass density

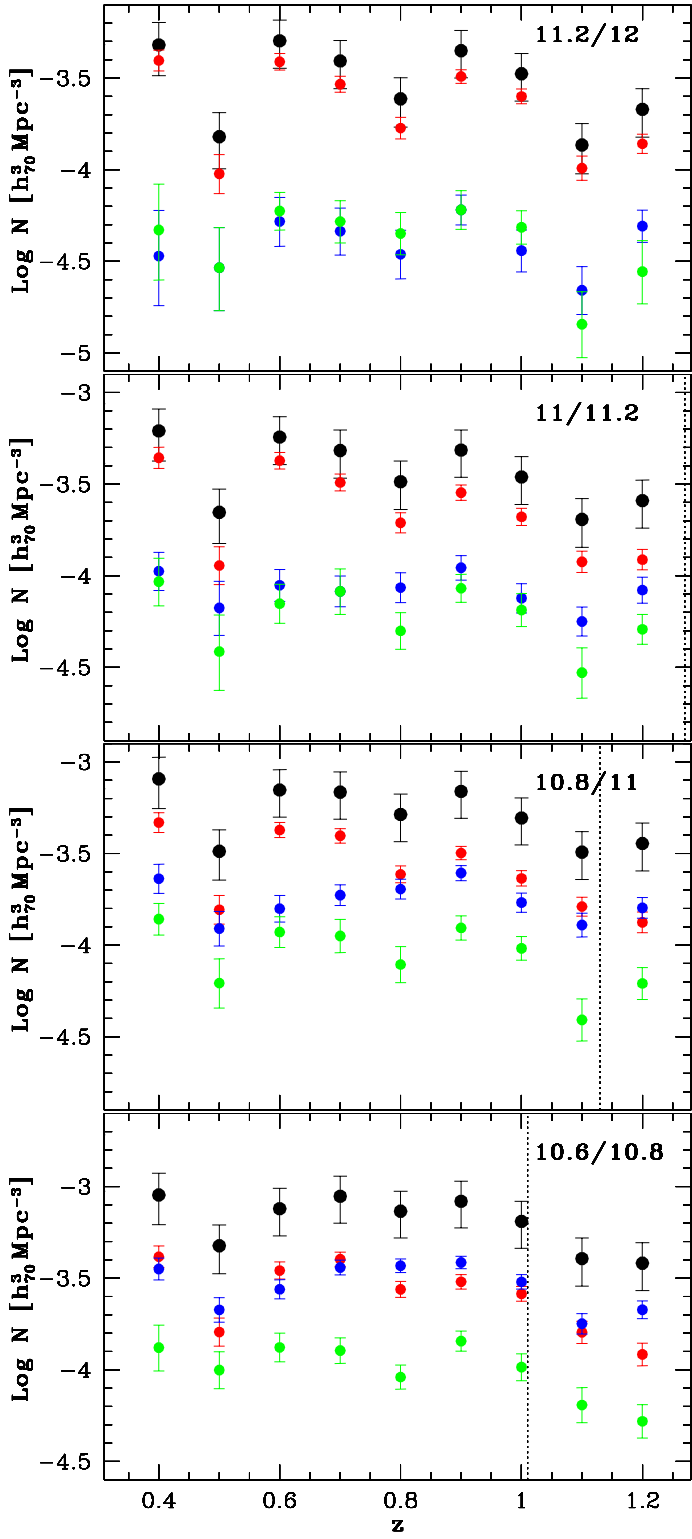


Figure 5.5: Number densities as a function of redshift and morphology. The panels show the number densities for different stellar mass bins. The mass bins are labeled in the upper right corners of each panel. Vertical dotted lines indicate the estimated completeness redshift for the relative stellar mass bin. Colors are according to the morphological split (black-total, red-bulges, green-intermediate, blue-disks).

5 Bulges and disks in the last 8 Gyrs of the COSMOS

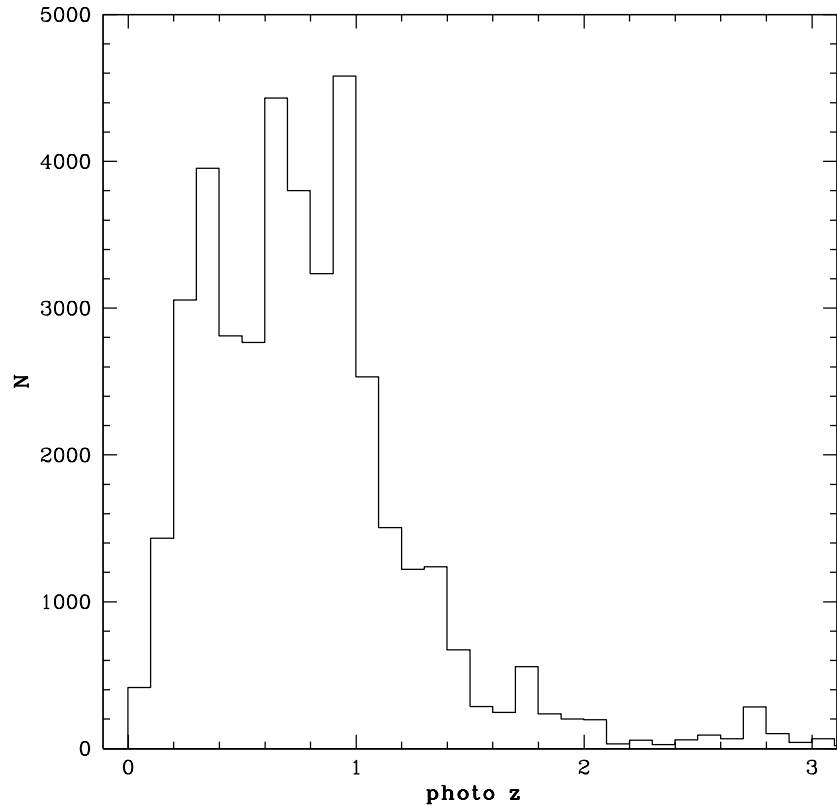


Figure 5.6: Redshift distribution of the 41300 galaxies belonging to the morphological catalog used in the present work. Overdensities at redshifts 0.4/0.7/1 are quite prominent as well as the underdensities at redshifts 0.5 and 0.8.

The slope of the redshift evolution of total number densities are consistent in all mass ranges, at least up to the common redshift completeness, meaning that the mass function in its high-mass end does not evolve in shape but only in normalization with redshift.

5.6 A hole in the sky at $z \sim 0.5$

In Fig. 5.5 there is obvious scatter around the mean number density decline in all the mass bins. However, an underdensity at $z \sim 0.5$ shows up quite strikingly. The deficit of objects is also quite evident in the global redshift distribution of our morphological catalog, as shown in fig. 5.6 It gets more and more significant with increasing stellar mass. The deficit of galaxies at this redshift is a factor of ten for the highest mass objects, and less than a factor

5.7 The environmental effect on morphological evolution

of five for objects in the lowest mass bin explored. This differential deficit is in qualitative agreement with galaxy evolution dependence on the local density as expected in current galaxy formation models (see Lee 2006 and references therein): the more underdense is the environment the later massive objects will form because there is in general a time delay in starting star formation and hence there are less small galaxy units to assemble the massive giant galaxies.

From the morphological point of view, the evolution in this underdense redshift bin is *delayed* at all stellar masses as compared with the contiguous redshift bins. The bulges fraction with respect to both the total number densities and to the disks number densities are much lower than those in the contiguous redshift bins, in agreement with the expectations of the morphology-density relation. We also note that in the highest mass bin, in this underdense region there are no massive pure disk systems.

We notice that the morphological mix in this underdense redshift bin is, in all mass ranges, very close to the morphological mix at $z \approx 1.1$, which has a comparable total number density of objects: is the morphological mix at $z \lesssim 1$ just depending on the local number density?

5.7 The environmental effect on morphological evolution

Taking advantage of the good statistics available in this study, we wish to further check the importance and role of environment on galaxy morphological evolution.

Estimating the volume density in a photometric redshift survey is not straightforward, and we try here to make it as simple and unbiased as possible.

First of all one has to decide which are the objects tracing the overdensities in a way not biased from the flux limited survey. Therefore, the objects have to be bright enough to be seen in the whole redshift range considered. Dealing with masses and morphologies, one should also take care of the selection effects introduced from the different M/L ratios associated with different stellar populations. Basically, old stellar populations, which more often but not always reside in bulges, have much higher M/L ratios with respect to young stellar populations, often but not always populating disks. A pure luminosity cut – even taking into account passive evolution – would thus preferentially cut out of the sample high M/L objects (bulges) with respect to low M/L objects (disks). To avoid this kind of bias, we use as overdensity tracers all objects with masses down to the mass completeness value at the highest redshift we are exploring (7×10^{10} solar masses).

Another issue is the relative scarcity of these objects (being in the exponential cutoff of the mass function), so one has to avoid reaching the shot noise regime when calculating number densities.

With this in mind, we proceed as follows: we first fit the number density evolution with redshift for objects more massive than 7×10^{10} solar masses, obtaining in this way an expected value of the number density at each redshift z , $\bar{\rho}(z)$. We then split the entire redshift range in slices of $\Delta z = 0.1$ (corresponding to differential depths of about about 327 comoving

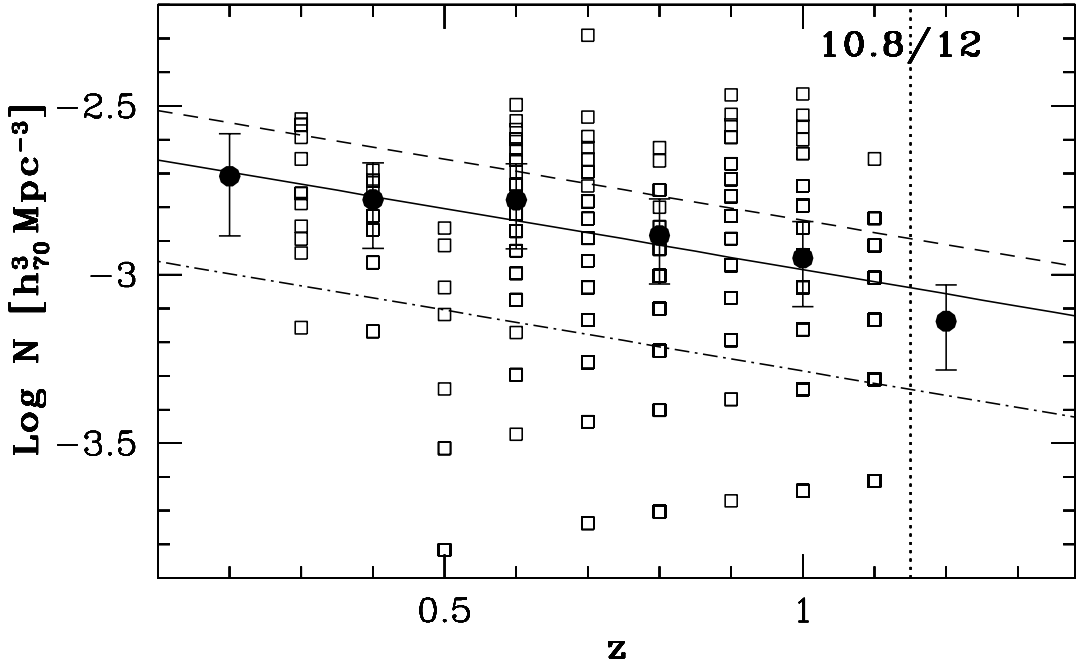


Figure 5.7: Number density evolution for objects with $\text{Log } M_* \gtrsim 10.8$. The solid line, $\bar{\rho}(z) = -2.62 - 0.36 \times z$, shows the linear fit to the filled dots (i.e. the number densities obtained over the whole field in redshift bins of $\Delta z = 0.2$). The dashed line sets the $1.4 \times \bar{\rho}(z)$ limit above which we select the overdense regions. Below the dashed-dot ($0.5 \times \bar{\rho}(z)$) line we select the underdense regions, while in between the two lines we select the medium-dense regions. The empty squares over plotted show the number densities in all the cells we have split our survey volume.

Mpc at redshift 0.5 and 244 at redshift 1). This slicing along the redshift axis turns out to be quite robust against the photo-z errors, in fact this corresponds to about 2/1.5 times the formal photo-z error at redshift 0.5/1. We then split the entire survey volume in cells of 2.8 comoving Mpc by side at each redshift slice, that is the maximum contiguous angular area we have available in the lowest redshift bin. Finally, we calculate the comoving number density of each cell at the different redshifts and assign the cell galaxy population to one of three density classes: underdense ($\rho(z) \leq 0.5 \times \bar{\rho}(z)$), medium-dense ($0.5 \times \bar{\rho}(z) < \rho(z) \leq 1.4 \times \bar{\rho}(z)$) and overdense($\rho(z) > 1.4 \times \bar{\rho}(z)$).

In Fig. 5.7 we show the number density evolution for objects with $\text{Log } M_* \gtrsim 10.8$. The solid line, $\bar{\rho}(z) = -2.62 - 0.36 \times z$, shows the linear fit to the filled dots (i.e. the number densities obtained over the whole field in redshift bins of $\Delta z = 0.2$). The dashed line sets

5.7 The environmental effect on morphological evolution

the $1.4 \times \bar{\rho}(z)$ limit above which we select the overdense regions. Below the dashed-dot line ($0.5 \times \bar{\rho}(z)$) we select the underdense regions, while in between the two lines we select the medium-dense regions. The empty squares over plotted show the number densities in all the cells we have split our survey volume.

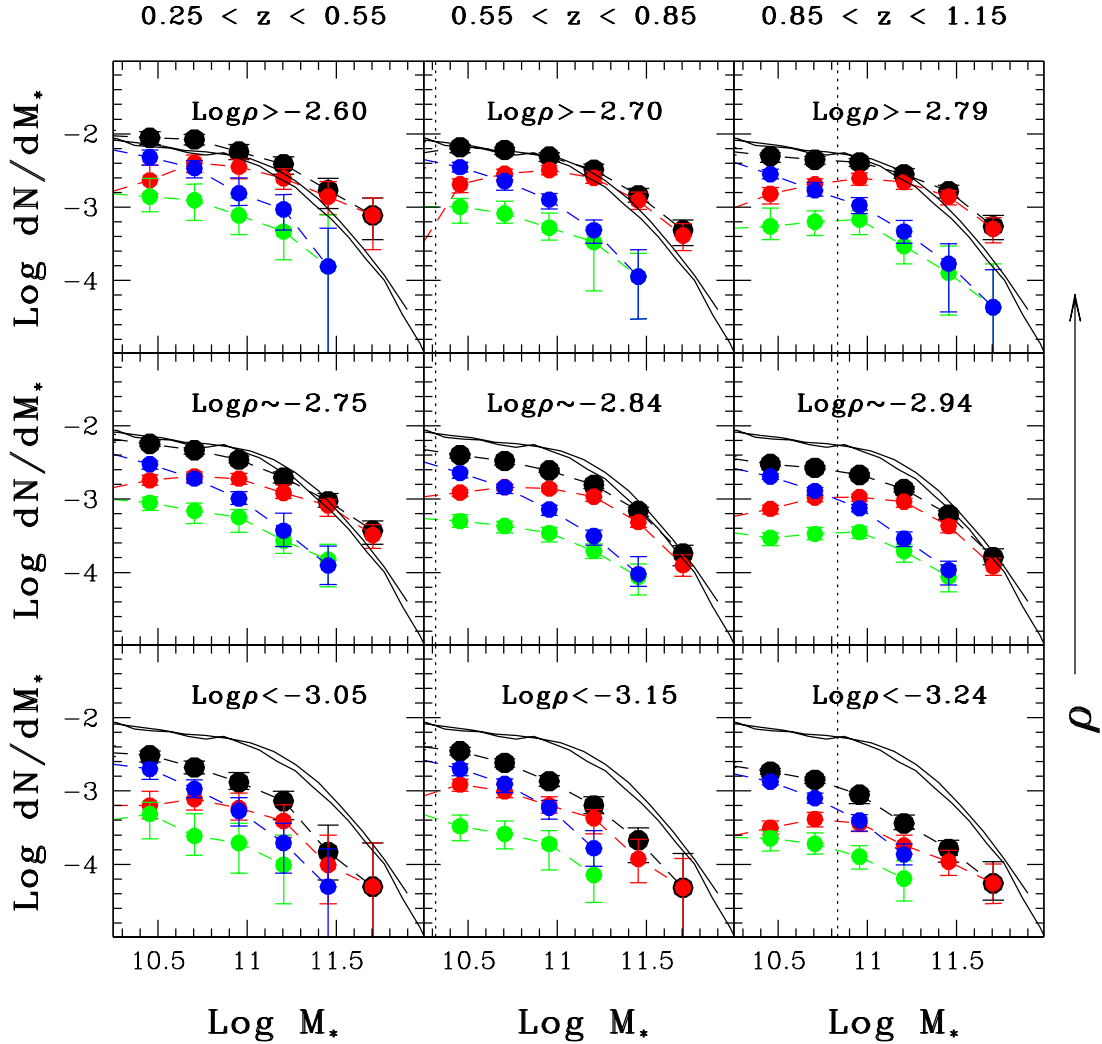


Figure 5.8: Galaxy stellar mass functions as a function of redshift, morphology and local environment. Black symbols refer to total values. The vertical axis is in units of [$h_{70}^3 \text{Mpc}^{-3} \text{dex}^{-1}$]. A vertical dotted line indicates the mass completeness limit in each redshift bin. Dashed colored lines are intended to guide the eye. Solid black lines show the local mass function determinations from Cole et al. (2001) and Bell et al. (2003).

5 Bulges and disks in the last 8 Gyrs of the COSMOS

5.7.1 8 Giga years of morphology density relation

In figure 5.8 we show the galaxy stellar mass function as a function of redshift, split by morphology and for the different environmental density defined in the previous section. Each of the panels contains about 2000 objects. Vertical dotted lines set the estimated mass completeness at the different redshifts. For reference in all panels are over plotted local estimates for the stellar mass function, which are fixed and independent from the environment. They are meant as a reference to look for differential evolution in different environments.

Let us first concentrate on the first column of figure 5.8, corresponding to the lowest redshift range. At those redshifts, the slope of the mass function is marginally evolving from the lower density regions to the higher ones, becoming shallower and consistent with the local one. This trend is in fact in good agreement with what found in the local Universe (Baldry et al. 2006).

The transition mass moves from $\text{Log } M_* = 10.7$ at high density to $\text{Log } M_* = 10.9$ at low density. In the overdense and medium-dense environments the shape of the mass function is in good agreement with the local determinations. In the overdense regions a very high mass bulge population seem to appear that overcomes the local *field* determination. Are we witnessing the first appearance of BCG/cD galaxies ?

Figure 5.8 shows that the morphologically split mass function evolves both along the redshift and the density axes, with some interesting features. For instance the total mass function, and the morphological mixtures are basically the same, up to the common mass completeness value, for overdense volumes at redshift 1 and medium-dense volumes at redshift 0.4. The transition mass is close to $\log M = 11$ at redshift 1 in medium dense volumes and it is already at that mass in the low dense environments at $z = 0.4$, and in fact the total mass is slightly higher in the first of the two panel. One could argue that having selected volumes depending on the number density of massive galaxies, the results found could just depend on a selection effect. Therefore, trying to quantify better the morphology density evolution as well as the morphological mix evolution, we integrate the mass function over the common complete mass range in the three redshift bins and in the three different environments.

In figure 5.9 we show both the bulge-to-total (lower panel) and the bulge-to-disk (upper panel) fractions at different redshifts and for different environments (low-cyan, medium-magenta, black-high).

At all redshift a morphology density relation is quite evident: more dense volumes contains also a higher relative fraction of bulges with respect to lower density volumes.

5.8 Red sequence and blue cloud up to redshift 1.15

In Figure 5.10 we show the restframe U-B color as a function of mass, redshift, morphology and environment. Morphology is indicated by different colors (red = early, green = intermediate, blue = late). The first row from the bottom shows all the different environments

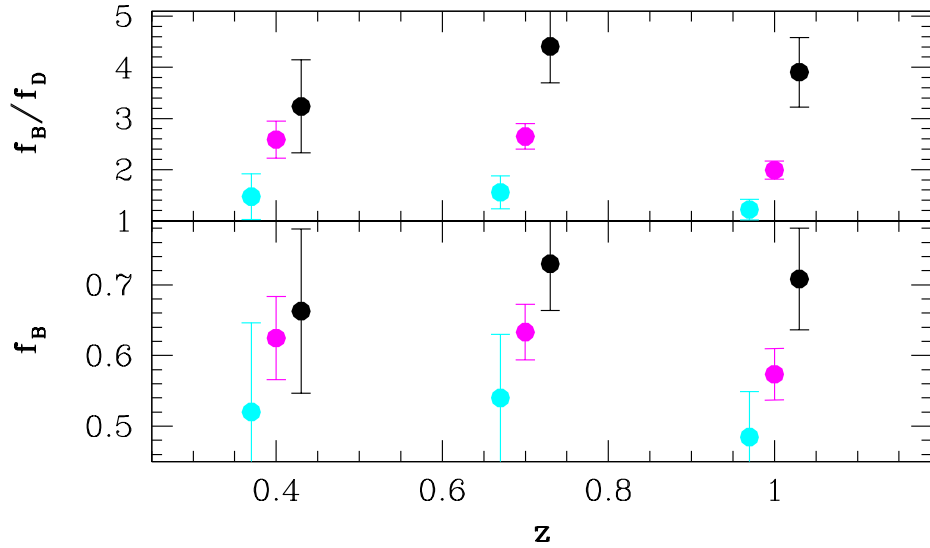


Figure 5.9: The morphology-density relation at work. The bottom panel shows the bulge fraction as function of redshift and environment. The environment variable is color coded as black-high, magenta-medium, cyan-low. The upper panel shows the numeric ratio between bulges and disks for different redshift and different environments. All the fraction are computed for objects more massive than $\text{Log } M_* > 10.8$

together. As expected, the red-sequence is becoming more and more red with decreasing redshift because of the age evolution of the stars hosted by its galaxies.

The *valley* between the red-sequence and the blue-cloud is very well defined in the lowest redshift bin, while it becomes less and less defined at increasing redshift, and mainly populated by intermediate and late-type objects.

This is more clear in Figure 5.11, where contours are used to better show the different behaviour of the three morphological classes. The contours correspond to six equally spaced levels between the minimum and maximum density of the data points of each morphological set.

In low density environments the red-sequence of bulges is quite broad and with a large scatter, pointing toward a difference in age between the red bulges. The relation gets tighter and tighter with increasing environmental density. Also, only low density regions exhibit a tail of early-type objects falling into the blue cloud. Conversely, in all environments there is a tail of disks falling into the red-sequence, but it is more pronounced in the highest densities regions.

5 Bulges and disks in the last 8 Gyrs of the COSMOS

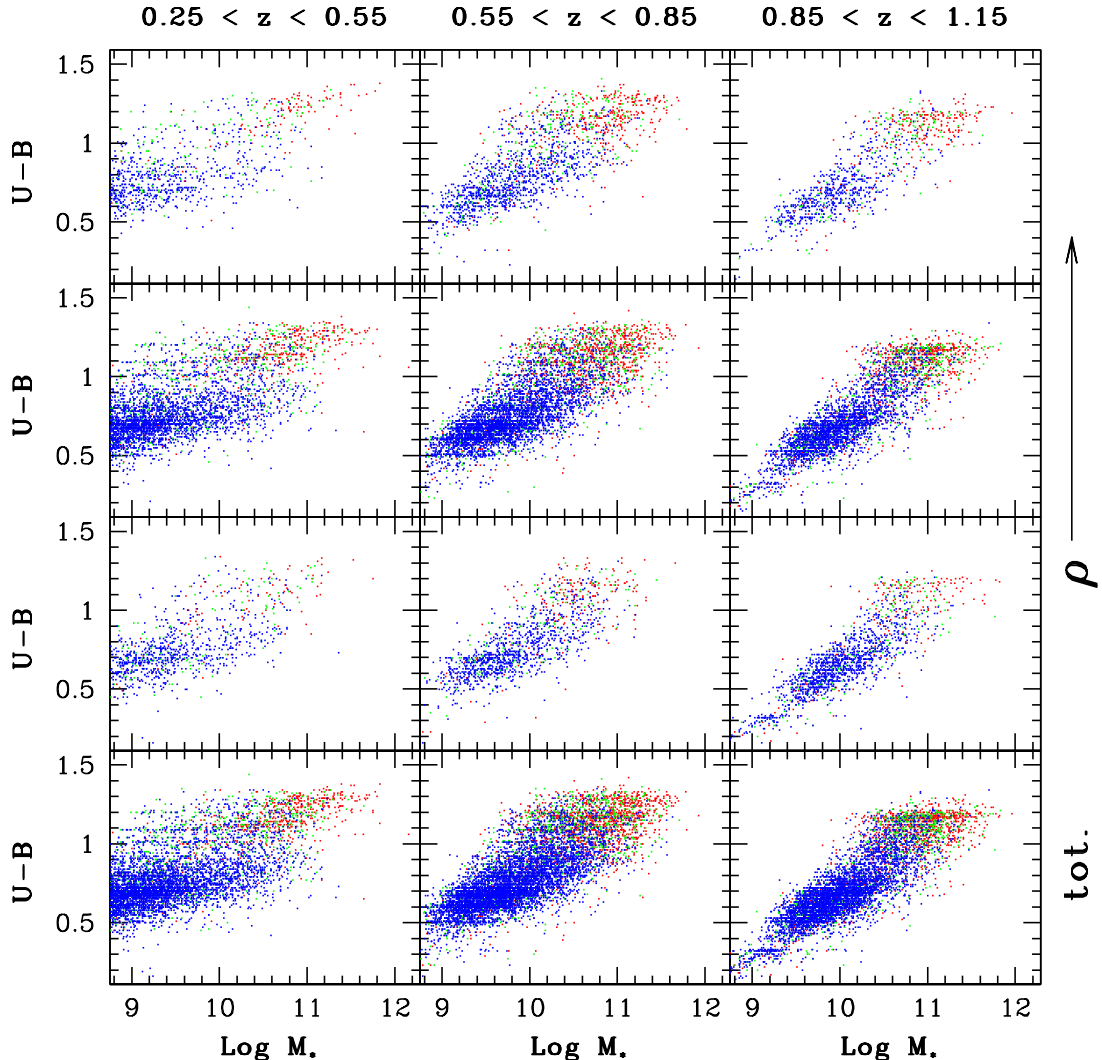


Figure 5.10: The $U-B$ restframe color as a function of mass, redshift, morphology and environment. The color coding is according to the morphological classes (red—early, green—intermediate, blue—late). The bottom row shows the total values, i.e. the first three rows from the top collapsed.

5.9 The specific star formation rate in the last 8 Gyrs

One way to explore the contribution of star formation to the growth of stellar mass in galaxies of different mass, is to study the redshift evolution of the specific SFR (SSFR) which is

5.9 The specific star formation rate in the last 8 Gyrs

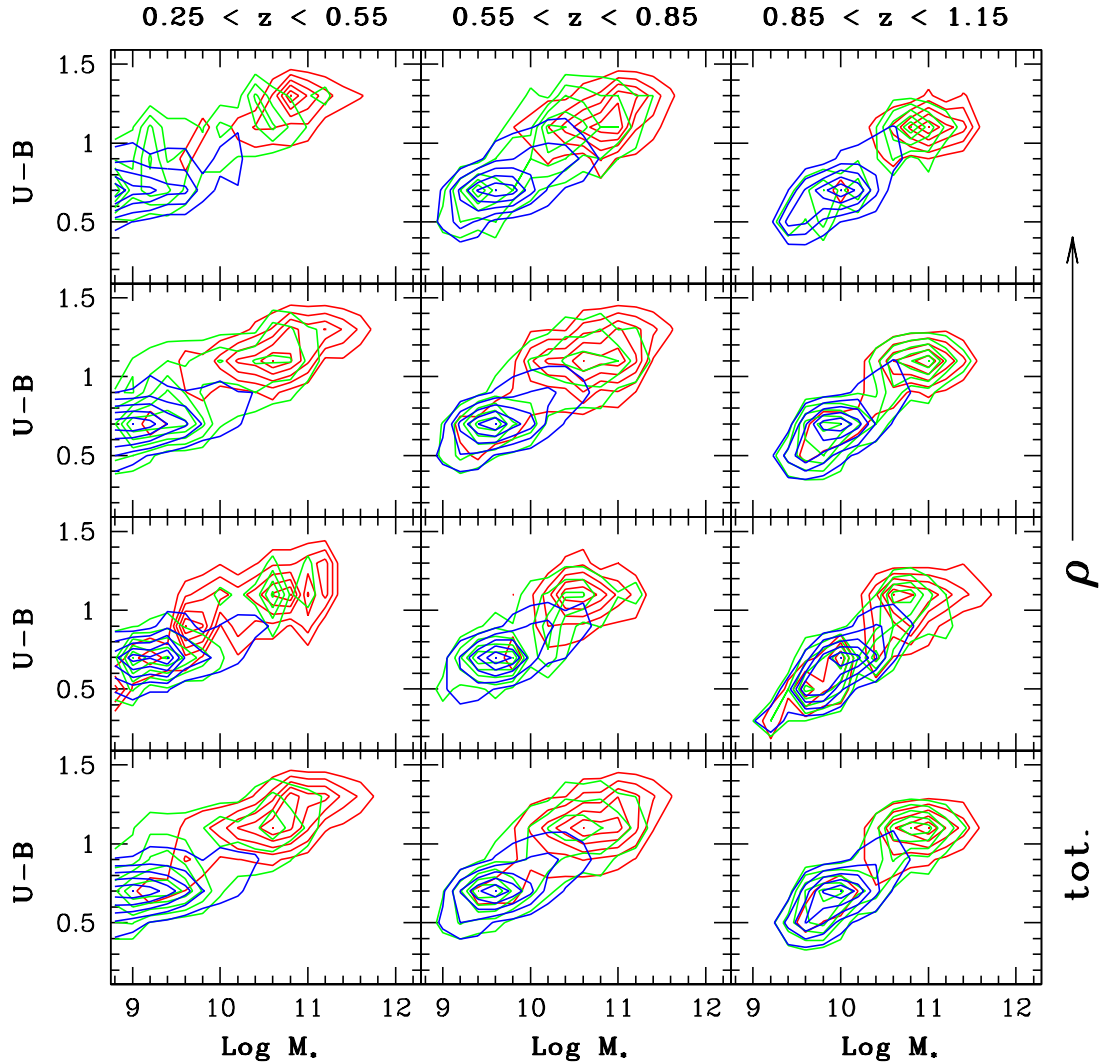


Figure 5.11: The $U - B$ restframe color as a function of mass, redshift, morphology and environment. The color coding is according to the morphological classes (red—early, green—intermediate, blue—late). The bottom row shows the total values, i.e. the first three rows from the top collapsed. Contours define the morphological classes and are drawn as explained in the text.

defined as the SFR per unit stellar mass.

Following Madau et al. (1998), the SFR of individual objects can be estimated from the restframe UV luminosity as $SFR_{2800} = 1.27 \times 10^{-28} \times L_{2800}$ in units of $M_\odot \text{yr}^{-1}$, where the

5 Bulges and disks in the last 8 Gyrs of the COSMOS

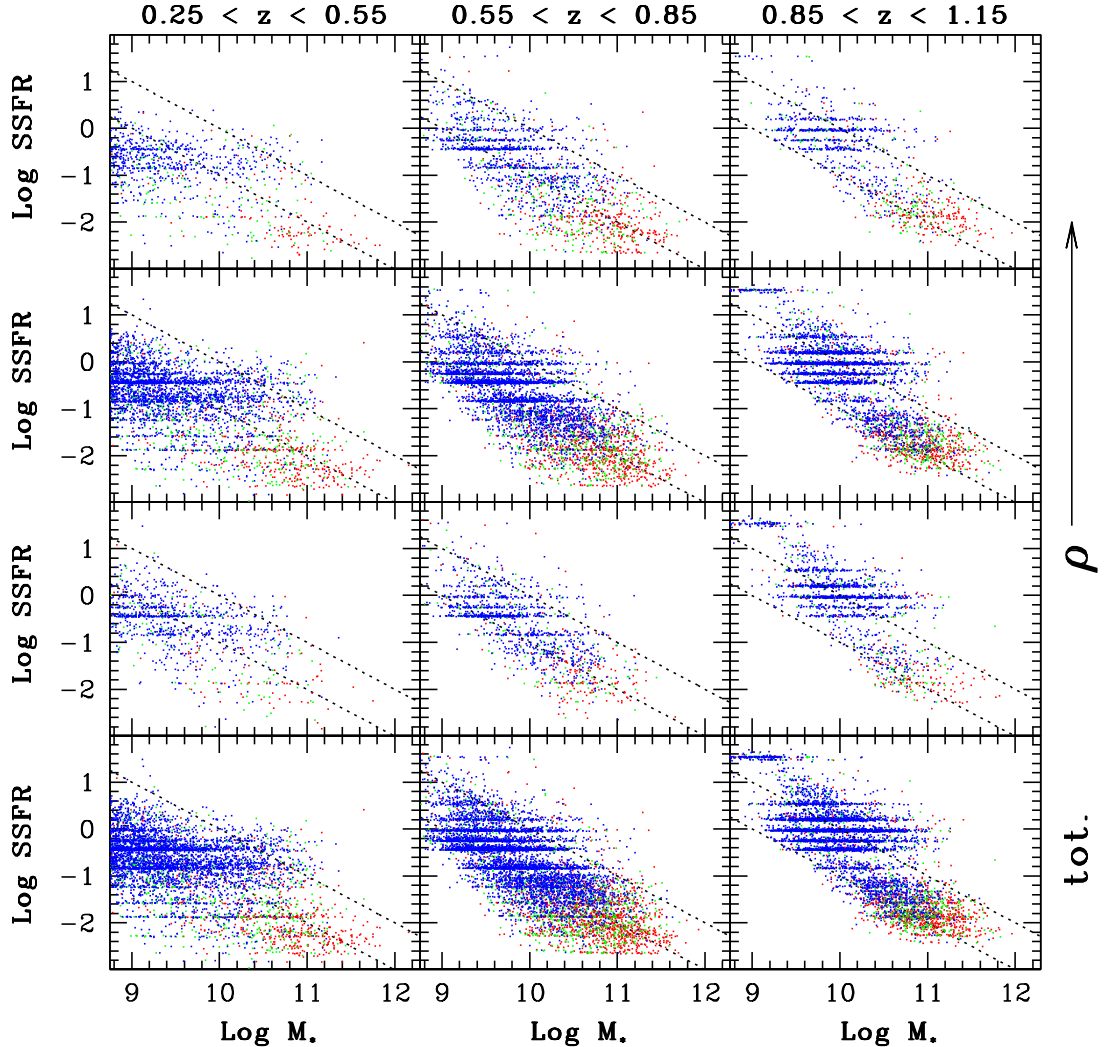


Figure 5.12: The SSFR as a function of stellar mass and morphology for three different redshift bins and in different environments. Tilted dotted lines represent constant star formation of 1 and $10 \text{ M}_\odot \text{yr}^{-1}$ and they are supposed to guide the eye.

constant factor is computed for a Salpeter IMF. The SFR is corrected by the dust attenuation obtained for the main component using the extinction curve of Calzetti (1997).

In Figure 5.12 we present the SSFR as a function of stellar mass and morphology for three different redshift bins up to redshift 1.15 and in different environments.

5.9 The specific star formation rate in the last 8 Gyrs

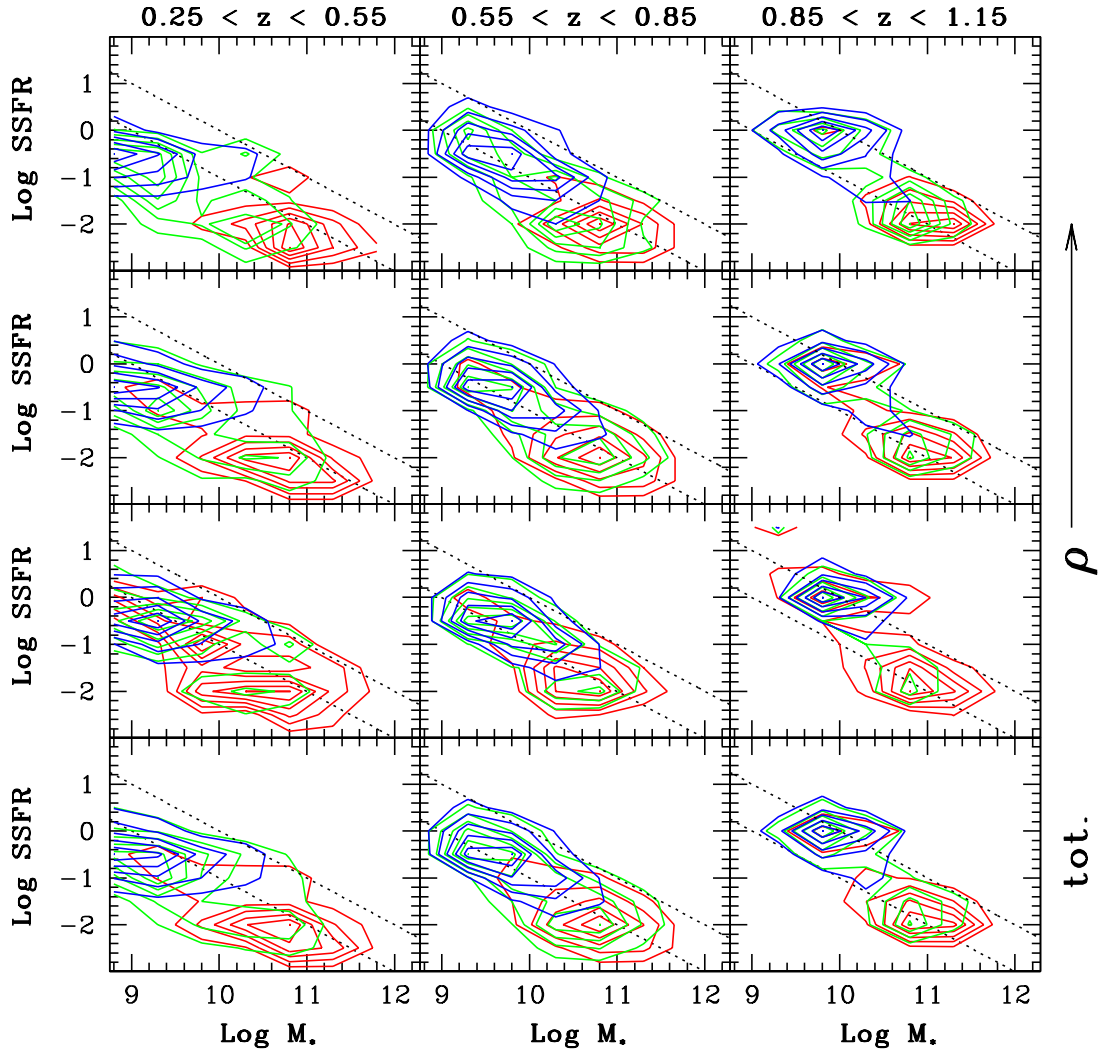


Figure 5.13: The SSFR as a function of stellar mass and morphology for three different redshift bins and in different environments. Contours define the morphological classes and are drawn as explained in the text. Tilted dotted lines represent constant star formation of 1 and $10 \text{ M}_\odot \text{yr}^{-1}$ and they are supposed to guide the eye.

The upper envelope of the SSFR is running essentially parallel to lines of constant SFR, and it is shifting to higher SFRs with increasing redshift, as it was already noted in earlier work. Note that this upper envelope is partly due to a selection effect: heavily dust obscured starbursts cannot be detected in our sample (we postpone a careful analysis of this issue to

5 Bulges and disks in the last 8 Gyrs of the COSMOS

a future work, which will make use of the recently available Spitzer Space Telescope mid-infrared observations).

Furthermore, it is evident that the most massive galaxies have the lowest amount of star formation per unit stellar mass up to the highest redshift probed, and hence they cannot have formed the bulk of their stars in this redshift range. This pushes the bulk of their star formation at much earlier cosmic epochs, in agreement with the downsizing scenario.

To better explore the different evolutionary behaviour of the three morphological classes we show in figure 5.13 the same plot, but with contour isodensity levels. In this way we better see the distribution of galaxies of morphological class and their evolution as a function of mass, redshift and environment. The red and blue clouds are very well separated in this plot at all redshifts and in all environments. The intermediate-type galaxies nicely fall between the red and blue distributions, thus confirming their nature of transition objects. The upper envelope, as well as the location of the maximum galaxy density of the early-type cloud, is increasing its star formation with redshift by not more than a factor three, while the blue cloud is moving by more than a factor ten in the same redshift range. The two clouds are very much segregated in mass: while the bulk of disks are always dominating at low masses, the early type objects dominate completely the high mass tail. Therefore, confirming the results found in P06, early-type galaxies drive the global decline of star formation in massive galaxies from redshift 1 to the local Universe.

In Figure 5.13, it is also worth noticing the evolution of the SSFR as a function of environment. At a first glance there is not much difference between the different environments. Nonetheless, at all redshifts there is a tendency of the early type objects distribution to present a plume toward the high SSFR zone, which is more pronounced at lower environmental densities.

5.10 The ages of early-type objects in different environments

In Figure 5.14 we show the ages of massive early-type galaxies as a function of redshift and for different environments as obtained from the SED fitting procedure outlined above. We cut the total sample to the common completeness limit ($\geq 7 \times 10^{10} M_{\odot}$). The dotted, dashed and solid histograms represent the high, medium and low density environments, respectively. In each panel, the difference between the mean ages in the two most extreme environments (the high and low density regions) is indicated. Such differences are significantly different from zero at all redshifts, pointing toward an earlier formation epoch of early-type galaxies in high density environments with respect to those living in a low density region.

From Figure 5.14 two things are quite evident: first, the histograms are quite similar to each other (as confirmed by a KS test) but for the oldest and youngest tails of the distribution, showing a preference of the oldest (youngest) galaxies to belong to high (low) density environments. Secondly, the width of the distributions is increasing with the cosmic clock.

These two things, together with the results discussed so far, could suggest that: i) young

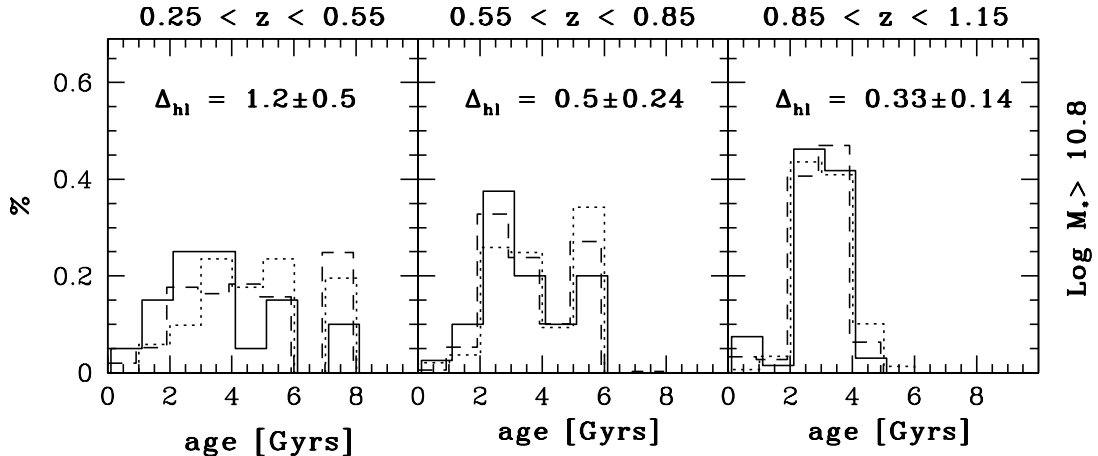


Figure 5.14: Ages of massive ($\geq 7 \times 10^{10} M_{\odot}$) early-type objects at different redshift and for different environments. The difference between the mean ages of early-type galaxies in high and low density environment is indicated in each panel. The dotted, dashed and solid histograms represent the high, intermediate and low density environments, respectively.

(bluer) massive early-type galaxies are preferentially found in low density environments, ii) the bulk of the early-type population has similar characteristic ages, colors, and SSFR, hence a very similar formation redshift; iii) the oldest objects in the Universe, or better saying the oldest stars in the Universe, happen to belong to its highest density regions.

5.11 Discussion and conclusions

In this work we have studied the evolution of the stellar mass content of disks and bulges with respect to the total mass budget up to $z \sim 1$ and its dependency from the local environments.

As expected, we find that early-type objects always dominate the high-mass end and that the lower the stellar mass the more the late-type objects tend to dominate the relative contribution to the total mass density.

At each redshift, a *transition mass* can be identified where the transition from a bulge-dominated to a disk-dominated stellar mass budget takes place. Based on the very good statistics available in this work, we are able to confirm the main conclusions of P06: *i*) the morphological mix at the high-mass end evolves with redshift; *ii*) the transition mass increases with redshift. At $z \sim 0.7$ we find a value of the transition mass approximately consistent with the local value $M \approx 5 \times 10^{10} M_{\odot}$. At $z \sim 1$ the disks and bulges contributions become comparable at $M \approx 1 \times 10^{11} M_{\odot}$.

5 Bulges and disks in the last 8 Gyrs of the COSMOS

The disks stellar mass function is consistent with being constant with redshift and declining in number densities from $\log M_* = 10.6$ to 12 by more than 1 order of magnitude. The bulges stellar mass function conversely is roughly constant in number densities at all masses, but constantly declining in the total normalization with increasing redshift. This naturally sets the evolution of the transition mass with redshift.

The slope of the redshift evolution of total number densities is consistent in all mass ranges, at least up to the common redshift completeness, meaning that the mass function in its high-mass end does not evolve in shape but only in normalization with redshift.

We have identified in the photometric redshift distribution an underdensity at $z \approx 0.5$. It gets more and more significant with increasing stellar mass. The deficit of galaxies at this redshift is a factor of ten for the highest mass objects, and less than a factor of five for objects in the lowest mass bin explored. This differential deficit is in qualitative agreement with galaxy evolution dependence on the local density: the more underdense is the environment the later massive objects will form because there is a time delay in starting star formation and hence there are less small galaxy units to assemble giant galaxies.

The morphology evolution in this underdense redshift bin is *delayed* at all stellar masses as compared with the contiguous redshift bins. The bulges fraction with respect to both the total number densities and to the disks number densities are much lower than those in the contiguous redshift bins, in agreement with the expectations of the morphology-density relation.

We notice that the morphological mix in this underdense redshift bin is, in all mass ranges, very close to the morphological mix $z \approx 1.1$, which has a comparable total comoving number density of objects. We thus argue that the morphological mix at $z \lesssim 1$ could just be depending on the local comoving number density.

We further explored the galaxy stellar mass function as a function of redshift, split by morphology and for the different environmental density.

We find that the slope of the mass function is marginally evolving from the lowest density environments to the highest density ones, becoming shallower, and consistent with the local one. This is the same trend found locally by Baldry et al. (2006)

In the overdense and medium-dense environments the mass function shape is in good agreement with the local determinations. In the overdense regions at redshift between 0.25 and 0.55 there seem to appear a very massive bulge population which overcomes the local *field* mass function determination. We argue that we could be possibly witnessing the first appearance of BGC/cD galaxies in high density regions.

The morphological split mass content evolves with both redshift and local density, with a striking feature: at different redshifts the morphological mix and the transition mass seem to be mainly depend on the stellar mass function normalization, i.e. the local number density.

We also note that in the underdense regions there are no pure disk systems more massive than $\log M_* = 11.2$, which show up only in more dense regions. This could suggest that they are the end products of high-density environments, and hence accretions, interactions and merging, and not the natural outcome of a *universal* mass function for disks' galaxies.

Finally, we have presented both the bulge-to-total and the bulge-to-disk fractions at different redshifts and for different environments, finding that a morphology–density relation is already in place at redshift 1.

In this work, for the first time to our knowledge, we have studied the evolution of galaxy colors and star formation activity as a function of morphology and environment. We have found that early and late-type galaxies in the stellar mass vs. SSFR plane (or stellar mass vs. rest-frame U-B colour) are well separated at all redshifts and in all environments. The intermediate type galaxies fall in between, confirming their nature of transition objects. At increasing redshift, the peak of the early-type galaxy distribution in such a plane is moving toward higher SSFR by a factor ≤ 3 . At the same time, the peak of the late-type galaxy distribution shifts by more than a factor ten in the same redshift range. The early- and late-type galaxy populations exhibit a significant segregation in mass: disk galaxies dominate at low masses while early-type objects completely dominate the high mass tail. Therefore, confirming the results found in P06 described in chapter 4, early-type galaxies drive the global decline of star formation present in massive galaxies from redshift 1 to the local Universe. While in general this picture seems to be quite similar in all environments, in low density regions there is a population of relatively massive, early-type galaxies, having high SSFR and blue colours.

We also explored, with the highly homogenous dataset available, the ages of the massive early-type galaxy stellar populations as a function of environment. The age distributions show significantly different mean ages at all redshifts. The results found in this work are in agreement with other recent studies. Our results suggest that young (blue) massive galaxies preferentially live in low density environments, and that most early-type galaxies have similar characteristic ages, colors, and SSFRs, hence a similar formation redshift; finally, the galaxies hosting the oldest stars in the Universe preferentially belong to the highest density regions.

Acknowledgements

We gratefully thank the entire COSMOS collaboration for the huge amount of work and high quality data released to the whole community. This research has made use of the NASA/IPAC Infrared Science Archive, which is operated by the Jet Propulsion Laboratory, California Institute of Technology, under contract with the National Aeronautics and Space Administration. Part of this work was supported by the German *Deutsche Forschungsgemeinschaft, DFG SFB 375*.

5 Bulges and disks in the last 8 Gyrs of the COSMOS

6

Further work

Abstract

In this chapter I present a few works I have been involved in, which complement the study reported in the previous chapters. I also discuss some on-going follow-up projects which extend this Thesis work to higher redshifts, to very high density environments, and to yet not addressed issues.

This last chapter is devoted to present some follow-up on-going work, most of which is complementary to what has been discussed in the previous chapters, and aimed to answer some questions raised from the study presented in this Thesis.

In section 6.2 I provide a discussion about how different star formation indicators can easily provide different results, by even an order of magnitude, thus changing the appearance and interpretation of evolutionary plots.

The environmental dependency of galaxy evolution has been studied and highlighted in this Thesis for a homogeneous sample of mainly *field* galaxies. The extension to *extreme* environments, such as galaxy clusters and galaxy voids, should be able to give more stringent constraints. In section 6.3, I describe the work done in collaboration with A. Halkola on a sample of intermediate to high redshift galaxy clusters.

The main limitation of morphological studies pursued so far is the redshift upper limit at $z \sim 1.2$. This is mostly because galaxies look different at different wavelengths and since ACS operates in the optical range, the morphological analysis of a galaxy in the restframe optical is limited to $z > 1.2$. Beyond this limit even the reddest ACS band starts mapping the NUV restframe. This wavelength domain of a galaxy spectrum is well known to be severely affected by dust attenuation and dominated by recent star formation episodes and,

6 Further work

hence, can provide a biased and transient property with respect to the optical restframe, the latter being more linked to the stellar mass. While waiting for high-resolution NIR imaging of large galaxy samples to become available, I started approaching the high redshift Universe by taking advantage of ACS sampling the UV restframe properties of high redshift star forming objects. This work has been done in collaboration with S. Noll and D. Pierini, and is described in section 6.3.

Furthermore, I was involved in studies of the cosmic star formation history and stellar mass growth up to redshift 5, as discussed in section 6.4 and 6.5.

Finally, back to the very nearby Universe, I also shared my expertise in morphological analysis for the study of massive black holes in elliptical galaxies led by N. Nowak. My contribution is briefly described in section 6.6.

6.1 The dark side of star formation: chasing the dusty Universe

Estimating star formation rates of galaxies by using a SED fitting technique is a very uncertain process. While stellar mass estimates have been found robust enough, all the other physical parameters (i.e star formation rate, dust and metals content, secondary burst fraction, luminosity-weighted age) are intrinsically degenerate and moreover heavily dependent on the ultraviolet range of the modelled spectrum. The UV light is considered a good proxy for the amount of the instantaneous star formation rate in a galaxy but unfortunately is, at the same time, the most affected by attenuation, i.e. by the amount, properties and distribution of dust present in a galaxy. In my work I applied a non specific dust attenuation correction of $A_{2800}=1$ mag. This median value, found not to depend on redshift, was derived by comparing the total stellar mass density and the integral of the cosmic SFR density at different lookback times for a heterogeneous sample of galaxies. In fact this approach reveals as good, or as bad, and accurate as the SED fitting results. An independent restframe mid-IR information is needed to provide new clues on this highly debated topic. The restframe mid-IR part of the galaxy spectrum best probes the radiation absorbed in the UV and then re-emitted by dust grains. Specific spectral windows in the mid-IR restframe (e.g. $8 \mu\text{m}$ and $15 \mu\text{m}$) have been found to tightly correlate with the galaxy star formation rate. The new upcoming MIPS surveys at $24 \mu\text{m}$ and $70 \mu\text{m}$ will hence disclose an unbiased view on the cosmic star formation rate at various redshifts.

6.1.1 The GOODS-S test

I made use of the deep $24 \mu\text{m}$ data available for the GOODS-S survey to have a preliminary handling of this issue. I selected a sample of objects in the redshift (photo-z) range 0.6/0.7 and I cross correlated this sample with the MIPS $24 \mu\text{m}$ catalog¹. The redshift range sampled

¹publicly available at <http://ssc.spitzer.caltech.edu/legacy/goodshistory.html>

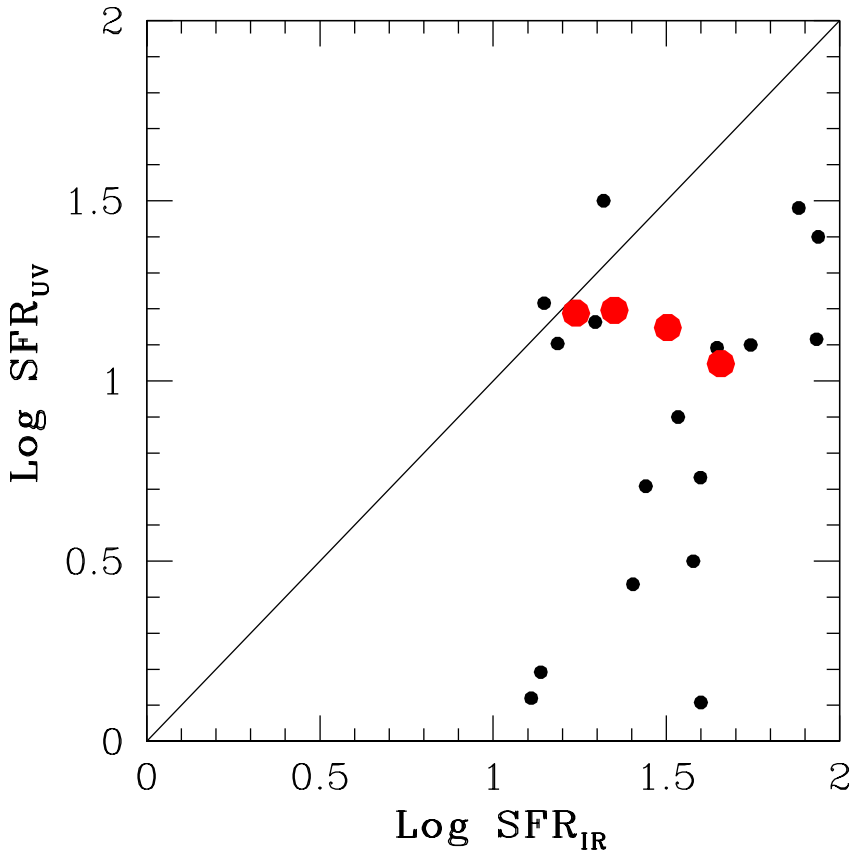


Figure 6.1: Comparison between the galaxy SFRs derived from the IR light and the UV dust corrected light. In black are marked all the GOODS-S galaxies in the redshift range 0.5/0.7 with a MIPS 24 μm counterpart detection in the publicly released catalog. In red are marked only the objects for which the cross-correlation gives an unique result.

makes the observed 24 μm corresponding to the emitted restframe at about 15 μm . Following Kennicutt (1998) this wavelength range is the best MIR proxy for the total IR emission and hence for the total SFR of a galaxy. In Fig. 6.1 we compare the SFR estimates coming from the IR light and the UV dust corrected one. Black points are showing all the sources matched in both catalogs. The trend drawn from the black points, is very similar to other literature results, and would point to a huge amount of hidden dust-obscured star formation. The angular resolution of the MIPS/SPITZER data is much higher (6 arcsec) with respect to the usual optical ground-based one (1 arcsec) and this makes the different catalogs cross-correlation a non trivial task. To have a fair, but basic, handling of this issue we decided to highlight the results obtained only from the sources for the correspondence between the two catalog was one-to-one without any doubt. The few red big dots are showing these objects.

6 Further work

Despite being only 4 objects, it seems that the two results are quite close each other and at most in within a factor 2 of uncertainty.

From this basic, but unbiased, exercise we argue that, after selecting a *fair* sample, the amount of hidden star formation, at least at a redshift about 0.6, is not dramatically high, if any and it seems to differ by at most a factor two from a UV dust corrected estimate. This result is in slight contradiction with other previous results and hence it has to be tested with a better statistical sample. The COSMOS legacy has released in these very days the SPITZER imaging over the whole field. The statistic available will allow to better understand and study how much, and when in cosmic times, hidden star formation is taking place in the Universe.

6.2 Field to Clusters variation

To better explore the morphology-density relation and in general the galaxy morphological evolution as a function of environment, I have started a collaboration with A. Halkola and S. Seitz on a project aimed at the characterization of galaxy clusters from strong lensing. I performed an accurate morphological analysis of galaxies in Abell 1689 (see Figure 6.3), a giant galaxy cluster at redshift 0.2, with the aim of estimating the galaxy velocity dispersions by means of the Fundamental Plane relation. Results have been published in Halkola et al (2006,2007). Thanks to the very accurate description of the galaxy component, we could carefully describe the cluster dark matter content and measure, for the first time by using strong lensing only, a severe truncation of galaxy dark matter halos with respect to field halos. Our results suggest that in a massive cluster environment, galaxy halos have lost more than 50% of their mass by tidal stripping.

6.2.1 Virial masses of cluster galaxies through scaling relations

Adapted from Halkola et al. 2006, "Parametric Strong Gravitational Lensing Analysis of Abell 1689", MNRAS accepted

By mean of an accurate morphological description of early-type objects in the cluster, one can aim to obtain an accurate enough measure of the object velocity dispersion, i.e. of its dynamical mass.

The velocity dispersions of cluster galaxies were determined mostly using the Fundamental Plane.

The Fundamental Plane (hereafter FP) links together, in a tight way, kinematics (velocity dispersion), photometric (effective surface brightness) and morphological (half light radius) galaxy properties (Dressler et al. 1987; Djorgovski & Davis 1987; Bender et al. 1992). We assume that the central velocity dispersion of a galaxy, as derived from the FP, is equal to the halo velocity dispersion, and that mass in disks can be neglected.

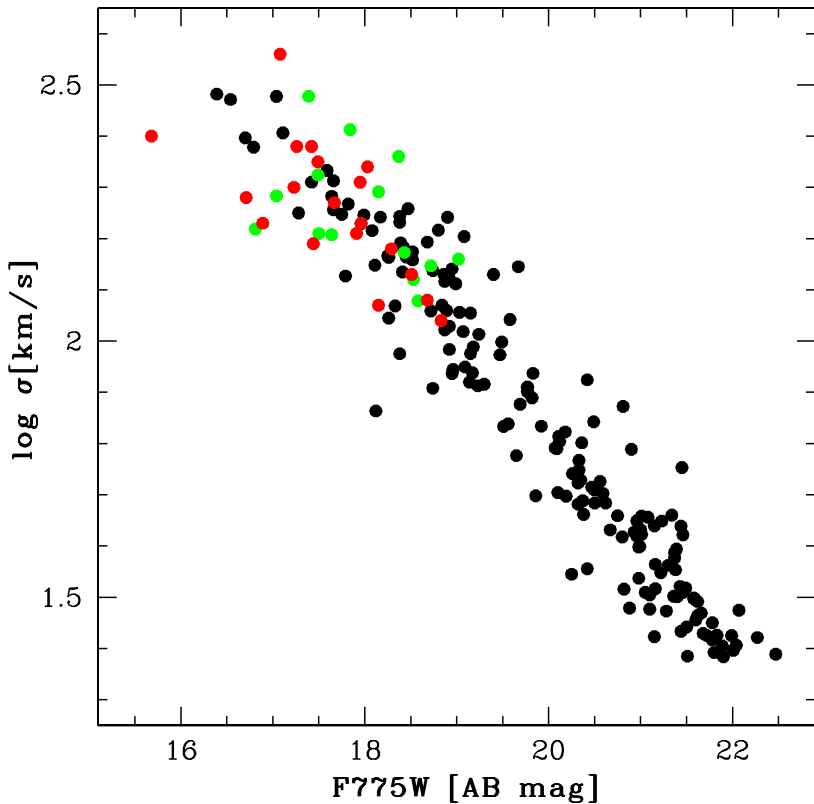


Figure 6.2: Total observed magnitude - σ relation for three $z \sim 0.2$ clusters. Red points are measured values taken from Ziegler et al. (2001) for A2218 ($z=0.18$), green points are values taken from Fritz et al. (2005) for A2390 ($z=0.23$) and full (empty) black points refer to the velocity dispersion estimates obtained in this paper for A1689 using the GIM2D (GALFIT) morphology. The literature values have been transformed to $F775W_{AB}$ magnitudes by applying relatively small colour terms (0.04,-0.4) and the AB correction (0.4).

The FP relation allows us to estimate the velocity dispersion of galaxies more accurately than the standard Faber-Jackson relation approach (Faber & Jackson 1976). We model the 2-dimensional light profiles of cluster galaxies with PSF-convolved Sersic (Sersic 1968) profiles using two packages, GALFIT (Peng et al. 2002) and GIM2D (Simard et al. 1999), to have a better handle on the systematics. The analysis was performed on the $F775W$ ACS image. 176 objects with AB magnitudes brighter than 22 were fitted. The point spread function used to convolve the models was derived by stacking stars identified in the field. The results coming out from the two completely different softwares agree very well.

In order to be able to use a FP determination for cluster galaxies at redshift ~ 0.2 in

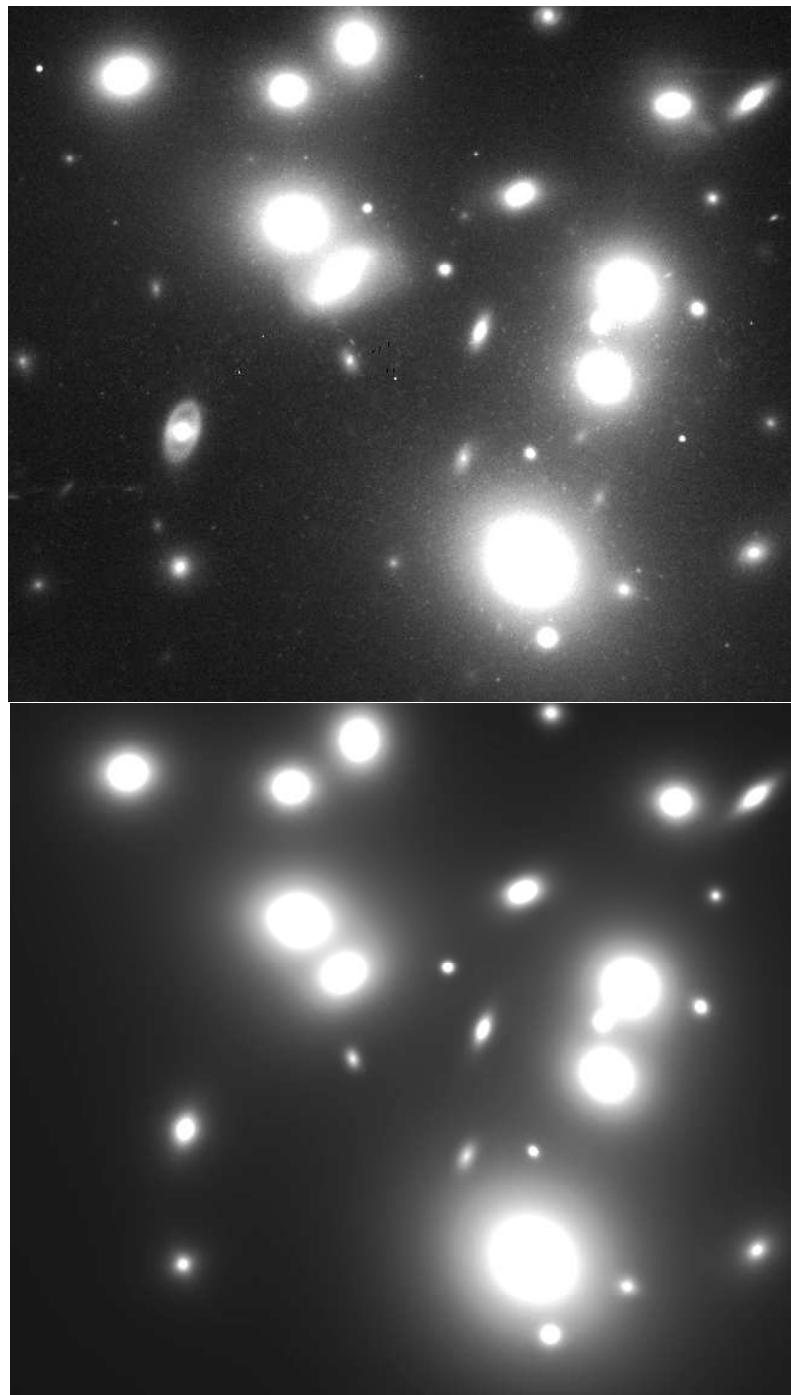


Figure 6.3: A1689 at redshift 0.186. Top panel: the *real* cluster core as imaged on a deep exposure of the ACS camera. Bottom panel: The GALFIT model for the cluster galaxy component.

6.2 Field to Clusters variation

restframe Gunn r filter (Jorgensen et al. 1996; Ziegler et al. 2001; Fritz et al. 2005), all the observed F775W_{AB} surface brightnesses (extinction corrected) were converted to restframe Gunn r_{GT} ones and corrected for the cosmological dimming. Since the observed F775W passband is close to restframe Gunn r at the redshift of A1689, the conversion factor between observed F775W and restframe Gunn r is small.

The mean observed surface brightness within r_e is:

$$\langle \mu_e \rangle_{F775W} = F775W_{observed} + 2.5 \log(2\pi) + 5 \log(r_e) - 10 \log(1+z), \quad (6.1)$$

where the last term corrects for the dimming due to the expansion of the Universe. It is then converted to restframe Gunn r_{GT} by:

$$\langle \mu_e \rangle_r = \langle \mu_e \rangle_{F775W} - A_{F775W} + K(r, F775W, z) + GT_{corr}, \quad (6.2)$$

The Galactic extinction correction A_{F775W} is calculated from the list of A/E(B-V) in Table 6 of Schlegel et al. (1998), along with their estimate of E(B-V) calculated from COBE and IRAS maps as well as the Leiden-Dwingeloo maps of HI emission. We adopted for A_{F775W} a value of 0.06.

The "k-correction colour", $K(r, F775W, z)$, is the difference between rest frame Gunn r and observed F775W magnitude and includes also the $2.5 \log(1+z)$ term. It was obtained by using an elliptical template from CWW (Coleman et al. 1980) and synthetic SEDs obtained for old stellar populations (10 Gyr, i.e. $z_f = 5$ observed at $z=0.2$) with the BC2003 Bruzual and Charlot models (Bruzual & Charlot 2003). All models give a conversion factor of approximately 0.174. The correction needed to pass from the AB photometric system to the Gunn&Thuan system is $GT_{corr} \approx 0.17$.

We used the FP coefficients from Fritz et al.. For the Gunn r band then

$$1.048 * \log R_e = 1.24 * \log \sigma - 0.82 * \log(\langle I \rangle_e) + ZP_{FP_r}, \quad (6.3)$$

where the $\langle I \rangle_e$ term, i.e. the mean surface brightness in units of L_\odot/pc^2 , is given for the Gunn r band by the equation:

$$\log \langle I \rangle_e = -0.4(\langle \mu_r \rangle_e - 26.4). \quad (6.4)$$

The zero-point of the FP ZP_{FP_r} is a quantity changing with both the cluster peculiarity and, mainly, with the cluster redshift. We used for ZP_{FP_r} the value published in Fritz et al. (2005). Their study was focused on A2218 and A2390, two massive clusters at almost the same redshift as A1689. They applied a bootstrap bisector method in estimating the ZP_{FP_r} and relative uncertainties, finding a value of 0.055 ± 0.022 .

6 Further work

Finally, we inserted the values derived from our morphological fitting procedures into the FP relation. The uncertainties on the derived velocity dispersions were estimated by taking into account the errors on the morphological parameters, the propagated photometric uncertainties, the error on the ZP_{FP_r} value and the intrinsic scatter of the FP relation, which gives the main contribution. We found that an estimate of 0.1 in $\log(\sigma)$ is a good value for the total uncertainty in velocity dispersion for objects having a velocity dispersion greater than 70 km/s. The fitted parameters for the 80 most massive galaxies are tabulated in Table 6.1.

6.3 The UV morphology of high redshift star forming galaxies

Adapted from Noll et al. 2007, "Presence of dust with a UV bump in massive, star-forming galaxies at $1 < z < 2.5$ ", A&A accepted

During the last year I have been involved in a project focused on the dust properties of high-redshift star forming galaxies. The main results have been published in Noll et al. (2007a, 2007b).

In this study, we used a sample of 108 massive, star-forming galaxies at redshift $1 < z < 2.5$, selected from the FDF Spectroscopic Survey, the K20 and the GDDS surveys, to investigate some fundamental properties of the dust extinction curve on a galaxy SED, like the slope in the rest-frame ultraviolet (UV) and the presence/absence of a broad absorption excess centred at 2175 Å (the so-called UV bump).

The spectral features of these galaxies are parametrised by two indices: the first parameter estimates the reddening in the UV and is defined as the continuum slope measured at 1750 – 2600 Å, with the exclusion of the range 1950 – 2400 Å. This proxy for the UV reddening by dust is called β_b . The second parameter characterises the apparent strength of the UV bump and is called γ_{34} . It is the difference between the continuum slopes measured at 1900 – 2175 Å (γ_3) and 2175 – 2500 Å (γ_4), respectively. A value of $\gamma_{34} \sim 1$ indicates the absence of the 2175 Å feature. Conversely, $\gamma_{34} < -2$ points to an extinction law which exhibits a significant UV bump.

These characteristics were constrained by means of a parametric description of the UV spectral energy distribution (SED) of a galaxy, as enforced by combined stellar population and radiative transfer models for different geometries, dust/stars configurations and dust properties.

In at least one third of the sample, there is a robust evidence for extinction curves with at least a moderate UV bump. The presence of particular dust particles, which are the carriers of the UV bump, is more evident in galaxies with UV SEDs suffering from heavy dust reddening.

We interpreted these results as follows. The sample objects possess different mixtures of

6.3 The UV morphology of high redshift star forming galaxies

dust grains and molecules producing extinction curves in between the average ones of the Small and Large Magellanic Cloud, where the UV bump is absent or modest, respectively. Most of the dust embeds the UV-emitting stellar populations or is distributed out of the galaxy mid-plane. Alternatively, even dust with a pronounced UV bump, as for the average Milky-Way extinction curve, can be present and distributed in the galaxy mid-plane. In this case, variations of the continuum scattering albedo with wavelength or an age-dependent extinction are not sufficient to explain the previous trend with reddening. Hence, additional extraplanar dust has to be invoked. The data suggest that the carriers of the UV bump are associated with intermediate-age stellar populations, while they survive in the harshest UV-radiation fields owing to dust self-shielding. The existence of different dust extinction curves implies that different patterns of evolution and reprocessing of dust exist at high redshift. Ignoring this may produce a non-negligible uncertainty on the star-formation rate estimated from the rest-frame UV.

6.3.0.1 Analysis of the UV morphology of high redshift galaxies

In order to investigate possible correlations between the presence of the UV bump and the UV morphology of the galaxies, I performed a morphological analysis of the sample. As I have already pointed out, at redshift larger than 1.2 even the reddest ACS band is sampling more and more the UV restrame emission of the galaxies. Thus, the morphology is more linked to the distribution of star forming regions than to the actual distribution of stars. For this reason we preferred to use a non parametric approach for this analysis.

We made use of the two indices R_T and R_A computed by GIM2D from the residuals of the best fit. These indices evaluate the bumpiness and the asymmetry of the residual image, and were used to estimate the overall smoothness of a galaxy image with respect to the best fitting model. In other words, by means of these indices we can estimate the residual substructure like spiral arms in nearby late-type galaxies (see the seminal study of Elmegreen et al. Elmegreen et al. (1992)), peculiarities and/or asymmetry in the distribution of giant star-forming regions, or interaction/mergers in high-redshift galaxies (e.g., Schade et al. Schade et al. (1995)).

Since UV morphologies of high redshift galaxies are potentially much more complex than our usual parametrisation with a Sérsic profile, we also characterised the morphologies of this galaxy sample by means of two non parametric indices, namely the concentration C and the asymmetry A of the galaxy surface brightness. The concentration parameter is given by the ratio of the radius containing 80% of the total galaxy flux to the radius containing 20% of the total flux. The asymmetry parameter is obtained by rotating the galaxy image by 180 degree from its center and then subtracting it from the original image; the total flux of this residual image is then compared with the original galaxy flux.

The C - A method was developed in the mid-nineties by Abraham et al. (Abraham et al. (1994), Abraham et al. (1996)). Subsequent works (e.g., Wu Wu (1999); Conselice et al. Conselice et al. (2000), Conselice (2003); Menanteau et al. Menanteau et al. (2006)) have

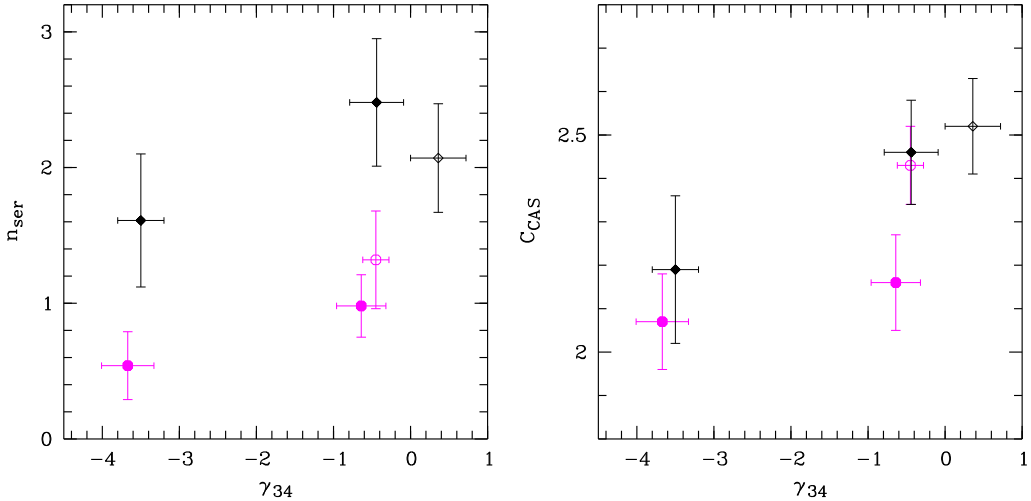


Figure 6.4: Sérsic index (top) and concentration (bottom) versus the proxy for the 2175 Å feature γ_{34} . Black (magenta) points refer to the $1 < z < 1.5$ ($2 < z < 2.5$) redshift range. Open symbols mark the subsamples with low reddening ($\beta_b < -1.5$), while the highly reddened galaxies are represented by filled symbols. Mean errors are indicated.

shown that a better morphological classification is obtained by choosing an image pivot point which minimises the measured asymmetry. We make use of the CAS parametrisation as proposed and described in detail by Conselice et al. (Conselice et al. (2000), Conselice (2003)). For our purposes in this section, it is important to say that early-type galaxies have larger concentration and lower asymmetry indices than late-type ones.

6.3.0.2 Morphological properties and extinction curve

We compared the morphological properties derived as described above for the galaxies in our sample, with the shape of their extinction curve at UV wavelengths.

We have to stress that, since the morphological parameters were determined based on the ACS i-band image of the galaxies, they correspond to different rest-frame wavelength domains, from the mid-UV to the U band, depending on the galaxy redshift.

We find that the rest-frame UV/ U -band morphology of a galaxy generally does not appear to be directly related with the shape of the extinction curve at UV wavelengths, whatever the redshift. Nevertheless, dividing our sample in “blue”/“red” objects as those having β_b greater/lower than -1.5 , blue objects at $2 < z < 2.5$ and $1 < z < 1.5$ tend to have smaller effective radii than red objects at the same redshift, whether or not a UV bump is detected in their spectra (see also Noll & Pierini (2005)).

As for the Sérsic index, there is a hint that red galaxies with evidence of a UV bump

6.3 The UV morphology of high redshift star forming galaxies

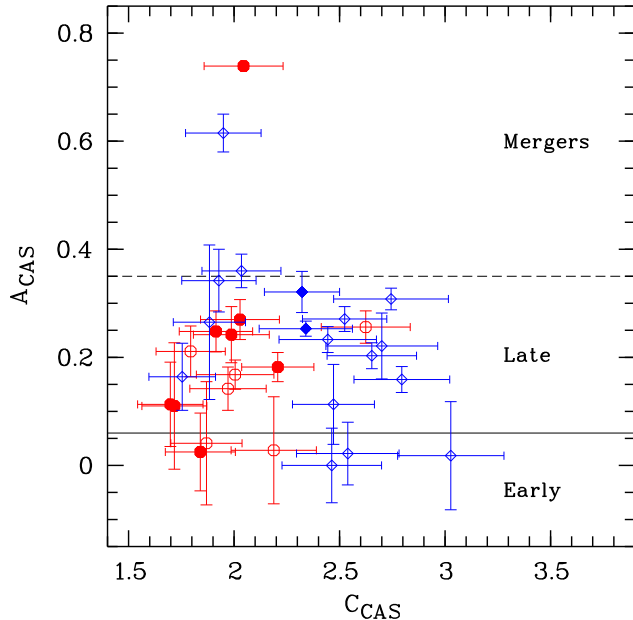


Figure 6.5: CAS parameters concentration C and asymmetry A (Conselice et al. Conselice et al. (2000), Conselice (2003)) for our sample of FDF (lozenges) and K20 galaxies (circles) at $1 < z < 1.5$. Galaxies with $\gamma_{34} < -2$ are marked by filled symbols. The solid and dashed lines separate early-type, late-type, and merging galaxies by their asymmetry (see Conselice et al. Conselice (2003)).

have a lower n_{ser} than red galaxies without UV bump in both redshift bins (see Fig. 6.4). For instance, at $1 < z < 1.5$, they exhibit an average Sérsic index of 0.54 ± 0.25 and of 0.98 ± 0.23 , respectively.

Overall, the Sérsic index seems to be larger for galaxies at higher redshifts (Fig. 6.4). Since the available high-resolution imaging probes the rest-frame UV/U-band morphology, the Sérsic profile describes the large-scale distribution of star-formation regions instead of the classical Hubble type. Hence, the azimuthally-averaged radial distribution of the rest-frame UV/U-band light traced by n_{ser} is shallower for galaxies with dust producing a significant UV bump with respect to those without it, whatever the redshift. Furthermore, it is more peaked at higher redshifts than at lower ones, even though this may be an effect of the cosmological brightness dimming. In fact, a faint component of a galaxy, like a disk, can fail detection more easily at higher redshifts, thus producing a spuriously larger value of n_{ser} .

In addition to the relatively large effective radii and low Sérsic indices, the low values of concentration of the red galaxies with evidence of a UV bump at $1 < z < 1.5$ (see Fig. 6.4) suggest that most of these galaxies are large systems with shallow radial profiles at rest-frame UV/U-band wavelengths. This is not surprising since most of the galaxies at these

6 Further work

redshifts can be classified as late types (see Fig. 6.5). However, the visual inspection of the ACS images reveals that the fraction of objects with a shallow light profile in the rest-frame UV/U-band is $40 - 70\%$ if $\beta_b > -1.5$, but only $20 - 40\%$ if $\beta_b < -1.5$. For red galaxies with a significant UV bump, this fraction becomes larger ($60 - 80\%$), though there are exceptions: CDFS-0271, the object with the strongest observed 2175 \AA absorption feature, appears as a quite compact galaxy ($R_e = 2.5 \text{ kpc}$).

Establishing the rest-frame UV morphology of a galaxy at $2 < z < 2.5$ is not possible from the available data, owing to the increased cosmological dimming. Nevertheless, we can investigate the presence of strongly distorted morphologies and/or multiple main components. These characteristics exclude the possibility of a single object with a smooth, radial surface brightness profile in the rest-frame UV. While at $1 < z < 1.5$ almost all galaxies show only one major component, at $2 < z < 2.5$ 45 – 65% of the objects seem to have two or more main components. There is not much difference between red and blue galaxies as for the fraction of objects with multiple components. However, there is a considerable difference when only red objects with strong UV bump are considered. For these galaxies, the fraction of objects with multiple components rises to 70 – 80%. This suggests that galaxies with extinction curves exhibiting a significant UV bump at $2 < z < 2.5$ are either systems with many, large star-formation complexes or merging systems. This could point to the existence of an intrinsic structural difference with respect to analogous galaxies at $1 < z < 1.5$, which appear as smooth, disc-like systems in the rest-frame UV/U-band.

6.4 The star formation rate history

Adapted from Gobasch et al. 2004, “The Star Formation Rate History in the FORS Deep and GOODS-South Fields”, ApJ, 616L, 83

The determination of the star formation rate (SFR) history of the Universe is one of the most interesting results extracted from the deep photometric and spectroscopic surveys of the last decade. A large number of measurements have been collected, at low (the Canada-France redshift survey at $z < 1$, Lilly et al. 1996), and high redshift from the Hubble Deep Field North (Madau et al. 1996), the large samples of U and B drop-out galaxies (Steidel et al. 1996), up to the most recent determinations based on I-dropouts at redshift ≈ 6 from the GOODS, UDF and UDF-Parallel ACS fields (Giavalisco et al. 2004a; Bunker et al. 2004; Bouwens et al. 2004). These studies show that the SFR (uncorrected for dust) increases from $z = 0$ to $z = 1$, stays approximately constant in the redshift range $1 - 4$, and starts to decline at larger redshifts. In all the cases quoted above the determination is based on the estimate of the total UV galaxy luminosity density, that for a given IMF is proportional to the instantaneous SFR (Madau et al. 1996, 1998). As discussed by many authors (e.g. Hopkins et al. 2001) this approach is affected by the uncertainties of dust correction, but

roughly agrees with other estimators at low to intermediate redshifts ($z \leq 1$). Theoretical models of galaxy formation and evolution can be tested against the measured SFR history (Somerville et al. 2001; Hernquist & Springel 2003).

So far, all determinations of the SFR history have suffered from some major limitations. High redshift samples have been small in number due to the limited field of view of deep pencil-beam surveys, resulting in large Poissonian fluctuations and large field-to-field variations (cosmic variance). The faint-end of the luminosity function (LF) is thusfar only poorly constrained at high redshifts, implying large completeness correction factors. Finally, the technique used to generate the high-redshift galaxy catalogues (drop-out selection, optical magnitude limited survey) might have introduced biases by selecting only specific types of galaxies and possibly missing relevant fractions of UV light (Ilbert et al. 2004).

Here we try to minimize these uncertainties and determine the SFR history of the universe with improved accuracy up to $z \approx 4.5$. Our sample of high redshift galaxies is based on two deep fields, the (I and B selected) FORS Deep Field (FDF, Heidt et al. 2003), and the (K-selected) GOODS-South field (Giavalisco et al. 2004b). Both cover a relatively large sky area, reducing the problem of cosmic variance. Both are deep enough to allow the detection of several $\times 10^3$ galaxies, thus minimizing the effect of shot noise.

We measure the star formation rate (SFR) as a function of redshift z up to $z \approx 4.5$, based on B, I and (I+B) selected galaxy catalogues from the FORS Deep Field (FDF) and the K-selected catalogue from the GOODS-South field. Distances are computed from spectroscopically calibrated photometric redshifts accurate to $\Delta z/(z_{spec} + 1) \leq 0.03$ for the FDF and ≤ 0.056 for the GOODS-South field. The SFRs are derived from the luminosities at 1500 Å. We find that the total SFR estimates derived from B, I and I+B catalogues agree very well ($\lesssim 0.1$ dex) while the SFR from the K catalogue is lower by ≈ 0.2 dex. We show that the latter is solely due to the lower star-forming activity of K-selected intermediate and low luminosity ($L < L_*$) galaxies. The SFR of bright ($L > L_*$) galaxies is independent of the selection band, *i.e.* the same for B, I, (I+B), and K-selected galaxy samples. At all redshifts, luminous galaxies ($L > L_*$) contribute only $\sim \frac{1}{3}$ to the total SFR. There is no evidence for significant cosmic variance between the SFRs in the FDF and GOODS-South field, $\lesssim 0.1$ dex, consistent with theoretical expectations. The SFRs derived here are in excellent agreement with previous measurements provided we assume the same faint-end slope of the luminosity function as previous works ($\alpha \sim -1.6$). However, our deep FDF data indicate a shallower slope of $\alpha = -1.07$, implying a SFR lower by ≈ 0.3 dex. We find the SFR to be roughly constant up to $z \approx 4$ and then to decline slowly beyond, if dust extinctions are assumed to be constant with redshift.

6.4.1 The Star Formation Rate

We compute the SFR for all 4 catalogues from the total luminosity densities l_{1500} in the 1500 Å band. First, we derive l_{1500} at a given redshift by summing the completeness corrected (using a V/V_{max} correction, see Gabasch et al. 2004a) LFs up to the 1500 Å absolute magni-

6 Further work

tude limits. Second, we apply a further correction (to zero galaxy luminosity) ZGL, to take into account the missing contribution to the luminosity density of the fainter galaxies. To this end we use the best-fitting Schechter function. For the FDF catalogues the ZGL corrections are only 2-20% in size. The small ZGL correction employed here owes itself to the faint magnitude limits probed by our deep FDF data set and the relatively flat slopes ($\alpha \approx -1.07$) of the Schechter function. Due to the brighter magnitude limit, the ZGL corrections for the GOODS catalogue can be as high as 50%. Note that if we follow i.e. Steidel et al. (1996) who find $\alpha = -1.6$ (excluded at 2σ with our fits, see Gabasch et al. 2004a), we would get much larger ZGL corrections for the same M_* , Φ_* (see the dotted line in Fig. 6.6 and the discussion below).

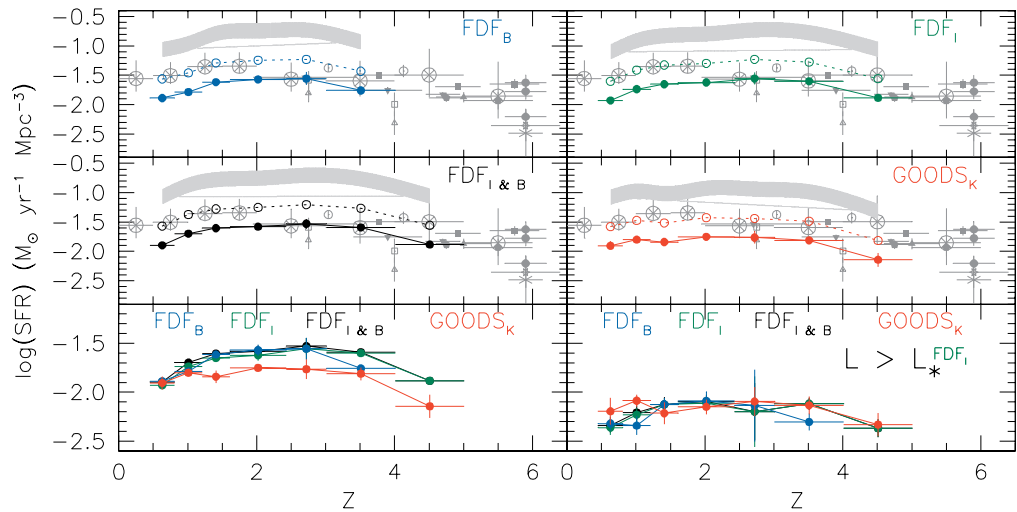


Figure 6.6: The four plots at the top show the SFR as a function of redshift derived from the 1500 Å luminosity densities computed from the B-selected (blue), I (green) and I+B-selected (black) FDF, and K-selected (red) GOODS-South field. The points are connected by the thick lines for clarity. These SFRs are based on a faint-end slope of -1.07 as derived from the FDF and GOODS data. The dotted lines show the effect of assuming a slope of -1.6. The grey-shaded region shows the effect of dust corrections with correction factors between 5 and 9, following Adelberger & Steidel (2000). The grey symbols show the results (taken from the table of Somerville et al. 2001) of Pascarelle et al. (1998, circled crosses), Steidel et al. (1996, open circles), Madau et al. (1996, open triangles), Madau et al. (1998, open squares), and (taken from Bunker et al. 2004) Iwata et al. (2003, filled triangles), Giavalisco et al. (2004a, filled squares), Bouwens et al. (2003b, filled circles), Bouwens et al. (2004, hexagonal crosses), Fontana et al. (2003b, filled pentagons), Bunker et al. (2004, open star), Bouwens et al. (2003a, inverted filled triangles). The plots at the bottom show the SFRs of the four catalogues together (left) and the SFRs derived considering the contributions of the galaxies brighter than L'_* only (right).

Finally, following Madau et al. (1998) we derive the SFR by scaling the UV luminosity

densities: $SFR_{1500} = 1.25 \times 10^{-28} \times l_{1500}$ in units of $M_{\odot} \text{yr}^{-1} \text{Mpc}^{-3}$, where the constant is computed for a Salpeter IMF. The resulting values of SFR_{1500} are shown in Fig. 6.6 as a function of redshift. Errors are computed from Monte Carlo simulations that take into account the probability distributions of photometric redshifts and the Poissonian error (Gabasch et al. 2004a). Following Adelberger & Steidel (2000), we assume that dust extinction does not evolve with redshift and is about a factor of $\sim 5 - 9$ in the rest-frame UV. A more detailed discussion of the role of dust will be given in a future paper, like an analysis based on the SFR derived at 2800 Å. Thanks to the large area covered and the faint limiting magnitudes probed, our determination of the SFR is the most precise to date, with statistical errors less than 0.1 dex for the single redshift bins spanning the range $0.5 < z < 5$.

We find that out to redshift $z \approx 3$ the SFRs derived from the I and B selected FDF, or the merged I+B catalogue, are identical within the errors ($\lesssim 0.1$ dex; see plot at the bottom left of Fig. 6.6). At larger redshifts the B-selected SFRs underestimate the true values, since B drop-outs are not taken into account. The strong evolution in both the M_* and ϕ_* parameters of the Schechter LF measured as a function of redshift by Gabasch et al. (2004a) results in a nearly constant SFR, because the strong brightening of M_* is compensated by the dramatic decrease of ϕ_* with z . Comparing the two lower panels of Fig. 6.6 shows that luminous galaxies ($L > L_*$) contribute only a third of the total SFR at all observed z , independent of the selection band.

The K-selected SFRs are similar in shape, but systematically lower by ≈ 0.2 dex at $z > 1$. This result holds independently of our completeness correction. If we consider only the contributions to the SFR down to the limiting magnitude set by the K-band, we find the same 0.2 dex difference for $1 < z \leq 3$, and 0.15 dex at $z > 3$. Fig. 6.7 shows that this result originates from the lower density of $M_{1500} > -19$ galaxies in the K-selected catalogue, as intermediate and low luminosity blue galaxies contributing to the SFR budget are more easily detected in the bluer bands than in K. In fact, the contributions to the SFR coming from the galaxies brighter than L_*^I are identical within the errors for the I and K selected catalogues (see Fig. 6.6, bottom-right panel). Therefore, cosmic variance does not play a role, as we also verified by comparing the B-band number counts in the 2 fields. They agree within 0.1 dex, which is the expected variation derived by Somerville et al. (2004) scaled to the area of the GOODS-South field. On the other hand, Gabasch et al. (2004a) show that the I-band FDF catalogue might be missing only about 10 % of the galaxies that would be detected in a deep K-band selected survey with magnitude limit $K_{AB} \approx 26$ (like in Labb   et al. 2003). The missing galaxies would be faint and likely not contributing significantly to the SFR provided their dust extinction is not exceedingly large. Independent of the selection band the SFR declines beyond $z \sim 4.5$. Our results confirm the conjecture of Kashikawa et al. (2003) that the K-selected UV LFs match the optically selected LFs at high luminosities.

The comparison with the literature shows that our results are ~ 0.3 dex lower, independent of the selection band. This difference stems from the large completeness corrections applied by, e.g., Steidel et al. (1996), derived from the steep slopes fitted to the LF. Our results scale to the literature values if similar slopes are used for the same M_* and ϕ_* . This is shown by

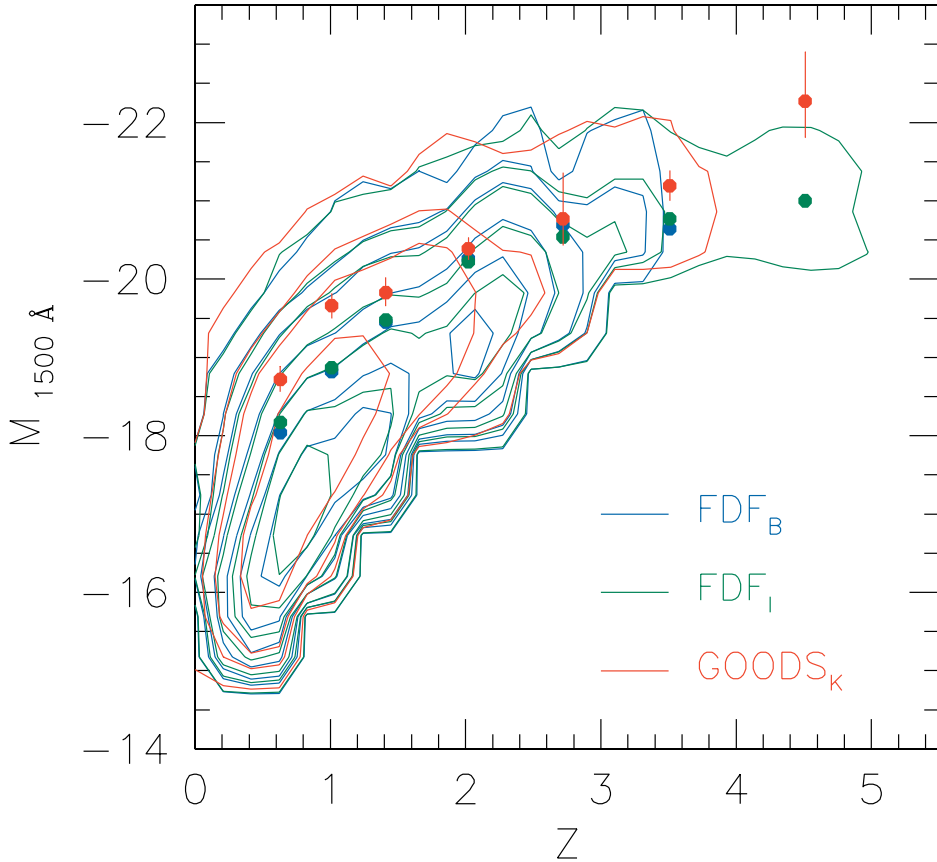


Figure 6.7: The distribution of galaxies in the rest-frame, 1500 Å absolute magnitude vs. redshift space, slightly smoothed with a Gaussian kernel. The red colors refer to the K-selected galaxies of the GOODS-South field, the blue and the green colors to B and I selected galaxies of the FDF. The lowest contour corresponds to 0.75 galaxies/arcmin²/mag per unit redshift bin; the others give the 2.5, 3.75, 6.25, 8.75, 11.25 and 13.75 galaxies/arcmin²/mag per unit redshift bin density levels. For a better comparison of the FDF and GOODS-South samples at the faint-end, we chose the completeness limit of the GOODS-South as the magnitude cut-off for all samples. The solid circles show the best-fit values of M_* , with the errorbars of the K determinations (similar or smaller errors are derived in I and B).

the dotted lines of Fig. 6.6, where we have assumed a slope of -1.6 for our data set while keeping M_* and ϕ_* the same as in our fit.

The overall agreement between the SFRs derived over a wide wavelength range (within 0.2 dex), from the optical B and I to the NIR K, sampling at $z \approx 4$ the rest-frame UV and B, shows

that we are approaching (in the optical) the complete census of the galaxies contributing to the stellar production of the universe up to this redshift. Therefore, we can expect possible biases induced by missing stellar energy distributions with redshift (Ilbert et al. 2004) to be small, when deep enough optical or NIR catalogues are available. However, we might still not take into account the possible contribution to the SFR coming from faint, highly dust-absorbed red star-forming galaxies (Hughes et al. 1998; Genzel et al. 2001) which are likely missing from optically or near-infrared selected samples. Nevertheless, it is encouraging to find that recent Spitzer results (e.g. Egami et al. 2004) indicate that the majority of the star formation has already been accounted for using the dust-corrected SFR derived from optical studies.

6.4.2 Conclusions

We have measured the SFR of the universe out to $z \approx 4.5$ with unprecedented accuracy from the FORS Deep Field and the GOODS-South Field (90 arcmin² in total). Our main conclusions are:

- The cosmic variance in the SFR history between the FDF and GOODS-South field is negligibly small. The difference between these fields is $\lesssim 0.1$ dex, consistent with theoretical expectations.
- The SFR of galaxies brighter than L_*^I is the same ($\lesssim 0.1$ dex) in B, I, (I+B) and K selected catalogues. This indicates that present optical and NIR surveys are unlikely to have missed a substantial fraction population of massive star forming objects (with the possible exception of heavily dust-enshrouded starbursts).
- The total SFR integrated over all galaxy luminosities is the same in the B, I, and (I+B) selected catalogues and is lower in the K-selected catalogue by 0.2 dex. This difference originates at luminosities lower than L_* which implies that K-selected surveys miss a significant fraction of star-forming lower-luminosity galaxies.
- At all redshifts, luminous galaxies ($L > L_*$) contribute only $\sim \frac{1}{3}$ to the total SFR, i.e. the integrated SFR of $L < L_*$ galaxies is a factor of ~ 2 higher than the one of $L > L_*$ galaxies.
- Our fits to the FDF luminosity functions suggest a flat faint-end slope of $\alpha = -1.07 \pm 0.04$ in contrast to the assumed slope of $\alpha \sim -1.6$ in the literature. This implies that past determinations have overestimated the SFR by a factor 2.
- The SFR is approximately constant over the redshift range $1 \leq z \leq 4$ and drops by about 50% around $z = 4.5$, if dust corrections constant with redshift are assumed.

6.5 The stellar mass function of galaxies to $z \sim 5$

Adapted from Drory et al. 2005, “The Stellar Mass Function of Galaxies to $z \sim 5$ in the FORS Deep and GOODS-South Fields”, ApJ, 619L, 131

6 Further work

The stellar mass of galaxies at the present epoch and the build-up of stellar mass over cosmic time has become the focus of intense research in the past few years.

Generally, this kind of work relies on fits of multi-color photometry to a grid of composite stellar population (CSP) models to determine a stellar mass-to-light ratio, since large and complete spectroscopic samples of galaxies ($z > 0$) are not yet available.

In the local universe, results on the stellar mass function (MF) of galaxies were published using the new generation of wide-angle surveys in the optical (Sloan Digital Sky Survey; SDSS, York et al. 2000; 2dF, Colless et al. 2001) and near-infrared (Two Micron All Sky Survey; 2MASS, Skrutskie et al. 1997). Cole et al. (2001) combined data from 2MASS and 2dF to derive the local stellar MF, Bell et al. (2003) used the SDSS and 2MASS to the same end.

At $z > 0$, a number of authors studied the stellar mass density as a function of redshift (Brinchmann & Ellis (2000); Drory et al. (2001a); Cohen (2002); Dickinson et al. (2003), Fontana et al. (2003a); Rudnick et al. (2003)) reaching $z \sim 3$. It appears that by $z \sim 3$, about 30% of the local stellar mass density has been assembled in galaxies, and at $z \sim 1$, roughly half of the local stellar mass density is in place. This seems to be in broad agreement with measurements of the star formation rate density over the same redshift range.

Others investigated the evolution of the MF of galaxies (Drory et al. 2004a; Fontana et al. 2004) to $z \sim 1.5$, finding a similar decline in the normalization of the MF. However, it is possible that galaxies evolve differently in number density depending on their morphology. We present a measurement of the evolution of the stellar mass function (MF) of galaxies and the evolution of the total stellar mass density at $0 < z < 5$, extending previous measurements to higher redshift and fainter magnitudes (and lower masses). We use deep multicolor data in the Forn Deep Field (FDF; I -selected reaching $I_{AB} \sim 26.8$) and the GOODS-S/CDFS region (K -selected reaching $K_{AB} \sim 25.4$) to estimate stellar masses based on fits to composite stellar population models for 5557 and 3367 sources, respectively. The MF of objects from the K -selected GOODS-S sample is very similar to that of the I -selected FDF down to the completeness limit of the GOODS-S sample. Near-IR selected surveys hence detect the more massive objects of the same principal population as do I -selected surveys. We find that the most massive galaxies harbor the oldest stellar populations at all redshifts. At low z , our MF follows the local MF very well, extending the local MF down by a decade to $10^8 M_\odot$. Furthermore, the faint end slope is consistent with the local value of $\alpha \sim 1.1$ at least up to $z \sim 1.5$. Our MF also agrees very well with the MUNICS and K20 results at $z \lesssim 2$. The MF seems to evolve in a regular way at least up to $z \sim 2$ with the normalization decreasing by 50% to $z = 1$ and by 70% to $z = 2$. Objects with $M > 10^{10} M_\odot$ which are the likely progenitors of todays $L > L^*$ galaxies are found in much smaller numbers above $z \sim 2$. However, we note that massive galaxies with $M > 10^{11} M_\odot$ are present even to the largest redshift we probe. Beyond $z \sim 2$ the evolution of the mass function becomes more rapid. We find that the total stellar mass density at $z = 1$ is 50% of the local value. At $z = 2$, 25% of the local mass density is assembled, and at $z = 3$ and $z = 5$ we find that at least 15% and 5% of

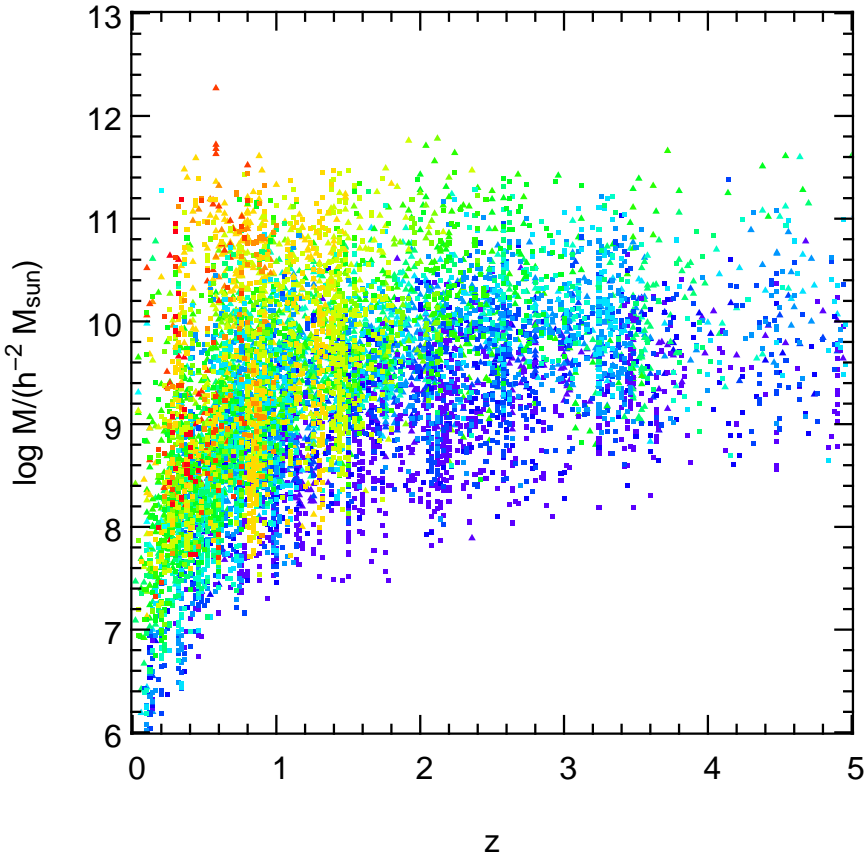


Figure 6.8: Stellar masses vs. redshift in the FDF (squares) and in GOODS-S (triangles). The luminosity-weighted mean ages of the stellar populations as determined by the CSP fit are coded by colors ranging from red for old populations (age $\gtrsim 5$ Gyr) to blue for young populations (age $\lesssim 1.5$ Gyr).

the mass in stars is in place, respectively. The number density of galaxies with $M > 10^{11} M_{\odot}$ evolves very similarly to the evolution at lower masses. It decreases by 0.4 dex to $z \sim 1$, by 0.6 dex to $z \sim 2$, and by 1 dex to $z \sim 4$.

In Fig.6.8 we show the distribution of galaxies in the mass vs. redshift plane for the FDF (squares) and GOODS-S (triangles). In addition, we code the age of each galaxy (using the best-fitting model) in colors ranging from blue for young (age $\lesssim 1.5$ Gyr) to red for old stellar populations (age $\gtrsim 5$ Gyr).

The distribution of objects from the K -selected GOODS-S sample is very similar to the distribution of the I -selected FDF down to the completeness limit of the GOODS-S sample, which is ~ 1 dex shallower in limiting mass. This indicates that present optical and near-IR surveys are unlikely to have missed a substantial population of massive objects, with the

6 Further work

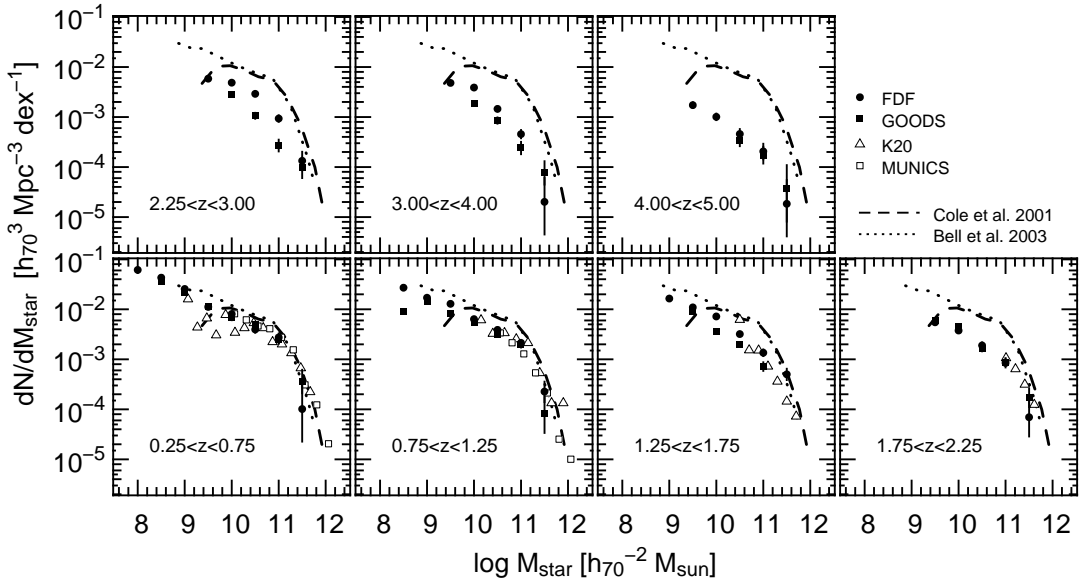


Figure 6.9: The stellar mass function (MF) as a function of redshift. The local MF of Bell et al. (2003) and Cole et al. (2001) are shown in all redshift bins for comparison. Results from the MUNICS survey (Drory et al. 2004a) and the K20 survey (Fontana et al. 2004) at $z \lesssim 2$ are also shown.

possible exception of heavily dust-enshrouded sources which may escape detection in both optical and near-IR surveys.

A striking feature of Fig. 6.8 is that the most massive galaxies harbor the oldest stellar populations at all redshifts. There always exist galaxies which are old (relative to the age of the universe at each redshift) but less massive, yet the most massive objects at each redshift are never among the youngest.

6.5.1 The stellar mass function

Fig. 6.9 shows the V_{max} -weighted mass function in seven redshift bins from $z = 0.25$ to $z = 5$. For comparison, we also show the local mass function (Bell et al. 2003; Cole et al. 2001) and the MFs to $z \sim 1.2$ of MUNICS (Drory et al. 2004a) and to $z \sim 2$ by the K20 survey (Fontana et al. 2004).

The MF of objects from the K -selected GOODS-S sample is very similar to that of the I -selected FDF down to the completeness limit of the GOODS-S sample (with the exception of a possible slightly lower normalization at $z \gtrsim 2.5$ by about 10% to 20%). This shows that near-IR selected surveys at high redshift essentially detect the more massive objects of the same principal population as do optically (I -band) selected surveys (see also Sect. 3 and Fig. 1 in Gabasch et al. 2004a). It remains to be seen what fraction of massive galaxies

(and total stellar mass density) might be hidden in dusty starbursts which appear as sub-mm galaxies.

In our lowest redshift bin, $z \sim 0.5$, the MF follows the local MF very well. The depth of the FDF ($I \sim 26.8$) allows us to extend the faint end of the MF down to $10^8 M_\odot$, a decade lower in mass than in Bell et al. (2003), with no change of slope. Furthermore, the faint end slope is consistent with the local value of $\alpha \sim 1.1$ at least to $z \sim 1.5$. Our mass function also agrees very well with the MUNICS and K20 results at $z \lesssim 2$.

The MF seems to evolve in a regular way at least up to $z \sim 2$ with the normalization decreasing by 50% to $z = 1$ and by 70% to $z = 2$, with the largest change occurring at masses of $M \sim 10^{10} M_\odot$. These likely progenitors of todays $L > L^*$ galaxies are found in much smaller numbers above $z \sim 2$. However, we note that massive galaxies with $M > 10^{11} M_\odot$ are present even to the largest redshift we probe (albeit in smaller numbers). Beyond $z \sim 2$ the evolution becomes more rapid.

It is hard to say whether the difference between the FDF and the GOODS-S field visible at $z \sim 3$ in Fig. 6.9 is significant. In fact, we find not much difference in the rest-frame UV luminosity function in the very same dataset. We think it might be related to the shallower near-IR data in the FDF compared to GOODS-S. Less reliable information on the rest-frame optical colors at young mean ages might in fact lead to an overestimation of the stellar mass. This would also explain why the two MFs become similar again at even higher z when the near-IR data in GOODS-S reach their limit, too. This would mean that the mass density in the FDF at $z \gtrsim 2.5$ might be overestimated (see below).

6.5.2 Stellar mass density and number densities

As shown in Figure 1.9 in chapter 1, this work extends the available data (Cole et al. (2001); Brinchmann & Ellis (2000); Drory et al. (2001a); Cohen (2002); Dickinson et al. (2003), Fontana et al. (2003a, 2004); Drory et al. (2004a)) on the evolution of the total stellar mass density out to $z \sim 5$.

We compute the total stellar mass density by directly summing up contributions from all objects in both fields (we obtain very similar values by means of fitting Schechter functions to the data in Fig. 6.9). We find that the stellar mass density at $z = 1$ is 50% of the local value as determined by Cole et al. (2001). At $z = 2$, 25% of the local mass density is assembled, and at $z = 3$ and $z = 5$ we find that at least 15% and 5% of the mass in stars is in place, respectively.

We also show the integral of the star formation rate determined by Steidel et al. (1999) as a dotted line. Furthermore, the dashed line shows the same quantity determined from the rest-frame UV luminosity function in the same dataset used here (Gabasch et al. 2004a). We find these measurements in agreement with each other, and with the mass densities derived here and in the literature before. However, the mass densities do show considerable scatter especially at redshifts above $z \sim 1.5$. However, as discussed above, the mass density in the FDF might be overestimated, hence reducing the scatter between our two fields. The

6 Further work

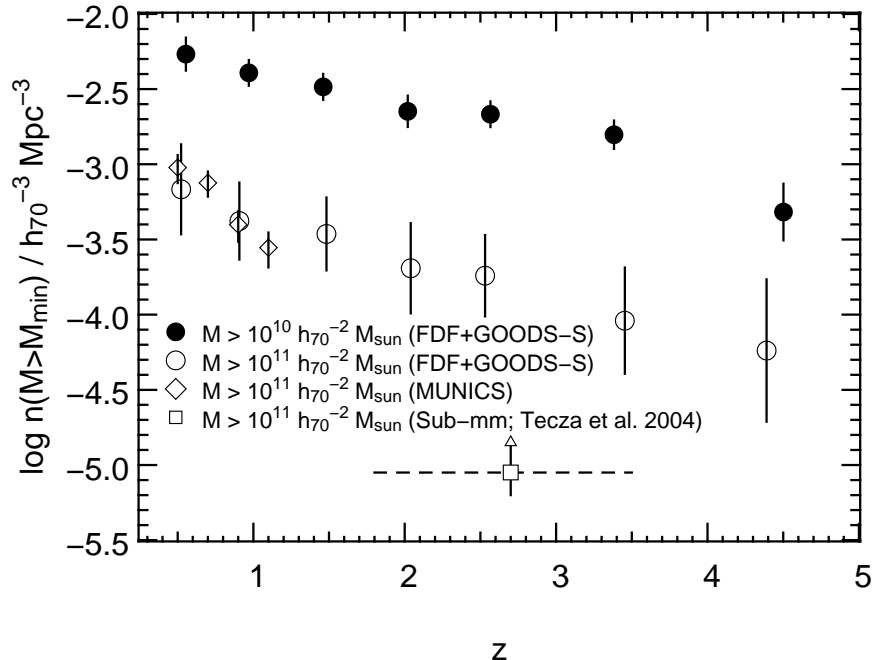


Figure 6.10: The number density of galaxies with stellar masses $M > 10^{10} M_{\odot}$ and $M > 10^{11} M_{\odot}$. Results from the MUNICS survey as well as results from Sub-mm studies are also shown.

FDF also lies above the average literature values in the redshift range in question, while the GOODS-S data seem to be in better agreement with previous measurements.

The fact that the stellar mass densities and the integrated star formation rates give consistent results is encouraging. However, dust-enshrouded starbursts at high redshift would be missing from both the SFR and the MF. However, if the number density of massive sub-mm galaxies derived by Tecza et al. (2004) of $8.9_{-3.3}^{+5.3} \times 10^{-6} \text{Mpc}^{-3}$ at $1.8 < z < 3.6$ is typical of these systems, they do not contribute significantly to the mass density at these redshifts (see below and Fig. 6.10).

Finally, Fig. 6.10 addresses the number density of massive systems as a function of redshift. We show the numbers of systems with $M > 10^{10} M_{\odot}$ and $M > 10^{11} M_{\odot}$ as full and open symbols, respectively. The number density of massive sub-mm galaxies estimated by Tecza et al. (2004) is also shown. The most striking features of Fig. 6.10 is that the number density of the most massive systems shows evolution which is very similar to the evolution of the number density at lower masses over this very large redshift range. Massive systems are present at all redshifts we probe, their number density decreasing by 0.4 ± 0.2 dex to $z \sim 1$, by 0.6 ± 0.3 dex to $z \sim 2$, and by 1 ± 0.45 dex to $z \sim 4$.

6.6 The supermassive black hole in NGC 4486a

Adapted from N. Nowak et al. 2007, “The supermassive black hole in NGC4486a detected with SINFONI at the VLT, MNRAS, in press

NGC 4486a is a low-luminosity elliptical galaxy in the Virgo cluster, close to M87. It contains an almost edge-on nuclear disc of stars and dust (Kormendy et al. 2005). The bright star $\sim 2.5''$ away from the centre makes it impossible to obtain undisturbed spectra with conventional ground-based longslit spectroscopy. However, it is one of the extremely rare cases, where an inactive, low-luminosity galaxy can be observed at diffraction limited resolution using adaptive optics with a natural guide star (NGS). This feature made NGC 4486a one of the most attractive targets during the years between the commissioning of SINFONI and similar instruments and the installation of laser guide stars (LGS). NGC 4486a is the first of our sample of galaxies observed or planned to be observed using near-infrared integral-field spectroscopy with the goal to tighten the slope of the M_\bullet - σ relation in the low- σ regime ($\lesssim 120 \text{ km s}^{-1}$) and for pseudobulge galaxies.

To derive the black hole mass in NGC 4486a, it is essential to determine the gravitational potential made up by the stellar component by deprojecting the surface brightness distribution. As NGC 4486a consists both kinematically and photometrically of two components with possibly different mass-to-light ratios Υ , we deproject bulge and disc separately.

To decompose the two components, we considered the HST images in the broad-band F850LP filter, with 2 ACS/WFC pointings of 560 seconds exposure each. The two dithers have no shift in spatial coordinates. The data were reduced by the ST-ECF On-The-Fly Recalibration system, see <http://archive.eso.org/archive/hst> for detailed information.

Moreover, we use the GALFIT package (Peng et al. 2002) to fit PSF convolved analytic profiles to the two-dimensional surface brightness of the galaxy. The code determines the best fit by comparing the convolved models with the science data using a Levenberg-Marquardt downhill gradient algorithm to minimize the χ^2 of the fit. The saturated star close to the galaxy centre has been masked out from the modelling. The observing strategy, i.e. the adopted no spatial shift between the two dithers, has allowed us to obtain a careful description of the PSF by using the TINYTim² code.

We modelled the galaxy light with a double Sérsic model with indices $n = 2.19$ for the bulge and $n = 1.67$ for the disc. In Fig. 6.11 we show the ACS image that was analysed, the bulge+disc GALFIT model and the residual image. The saturated star pops prominently up in the residual image as it was expected.

Bulge and disc were then deprojected separately using the program of Magorrian (1999) under the assumption that both components are edge-on and axisymmetric. The stellar mass

²<http://www.stsci.edu/software/tinytim/tinytim>

6 Further work

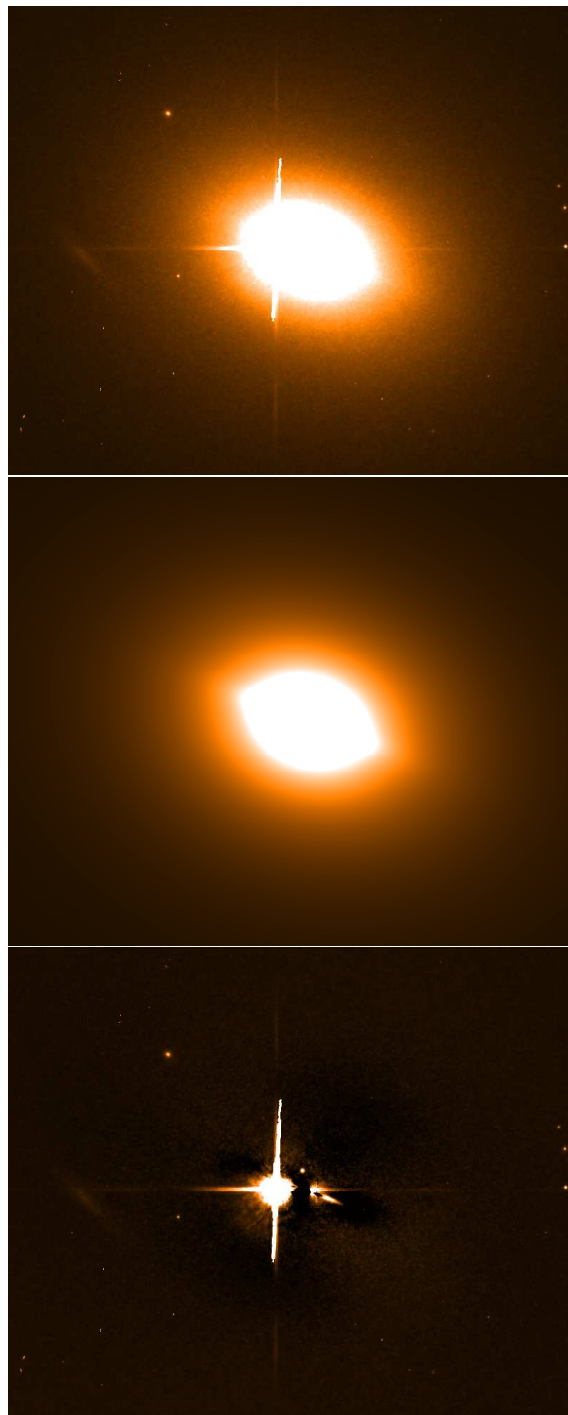


Figure 6.11: Top: the ACS F850LP image of NGC4486; middle: the bulge+disc GALFIT best model; bottom: the residual image. The star near the galaxy core pops up, as due, in the residual image.

6.6 The supermassive black hole in NGC 4486a

density then can be modelled as in Davies et al. (2006) via $\rho_* = \Upsilon_{\text{bulge}} \cdot \nu_{\text{bulge}} + \Upsilon_{\text{disc}} \cdot \nu_{\text{disc}}$, where ν is the luminosity density obtained from the deprojection and the ACS z -band mass-to-light ratio Υ is assumed to be constant with radius for both components.

The mass of the black hole in NGC 4486a was determined based on the Schwarzschild (1979) orbit superposition technique, using the code of Gebhardt et al. (2000); Gebhardt et al. (2003) in the version of Thomas et al. (2004). The dynamical mass-to-light ratios of disc and bulge agree with an old and metal-rich stellar population (Maraston 1998, 2005). Υ_{disc} tends to be larger than Υ_{bulge} which is probably due to the presence of dust in the disc.

The total stellar mass within 1 sphere of influence, where the imprint of the black hole is strongest, is $M_* = 9.84 \times 10^6 M_\odot$. If the additional mass of $M_\bullet = 1.25 \times 10^7 M_\odot$ was solely composed of stars, this would increase the mass-to-light ratio to $\Upsilon_{\text{disc}} \approx 9.1$ (6.6 if we take into account the dust-absorption), a region which is excluded by stellar population models or at least requires unrealistic high stellar ages.

Our result is in good agreement with the prediction of the M_\bullet - σ relation ($1.26^{+0.49}_{-0.35} \times 10^7 M_\odot$ using the result of Tremaine et al. 2002) and strengthens it in the low- σ regime ($\lesssim 120 \text{ km s}^{-1}$), where, besides several upper limits, up to now only three black hole masses were measured with stellar kinematics (Milky Way, Schödel et al. 2002; M32, Verolme et al. 2002; NGC 7457, Gebhardt et al. 2003).

6 Further work

Table 6.1: Table of galaxy properties from fitting cluster galaxies with a Sersic profile. The parameters of the 80 most massive galaxies are tabulated.

RA	Dec	m_{AB}^1	n_{ser}	R_e^2 (kpc)	$1 - b/a$	PA ($^\circ$)	σ_{est}^3 (km/s)
13:11:25.53	-1:20:37.0	17.13 ± 0.15	3.1 ± 0.3	8.1 ± 0.5	0.37 ± 0.02	10 ± 1	178 (224/141)
13:11:25.28	-1:19:31.1	19.09 ± 0.10	6.0 ± 0.1	2.2 ± 0.1	0.06 ± 0.01	70 ± 3	108 (136/86)
13:11:28.19	-1:18:43.8	18.75 ± 0.14	2.6 ± 0.1	2.5 ± 0.1	0.57 ± 0.03	32 ± 1	115 (144/91)
13:11:26.09	-1:19:51.9	18.39 ± 0.13	3.9 ± 0.2	2.5 ± 0.1	0.23 ± 0.01	79 ± 1	144 (181/114)
13:11:26.67	-1:19:03.8	19.64 ± 0.14	3.2 ± 0.1	1.8 ± 0.1	0.38 ± 0.01	79 ± 1	80 (100/63)
13:11:26.38	-1:19:56.5	18.33 ± 0.14	3.4 ± 0.1	1.7 ± 0.1	0.35 ± 0.01	34 ± 1	181 (228/144)
13:11:27.06	-1:19:36.8	18.25 ± 0.01	6.0 ± 0.1	4.9 ± 0.1	0.17 ± 0.01	5 ± 1	147 (185/117)
13:11:24.62	-1:21:11.1	18.24 ± 0.13	4.4 ± 0.3	2.1 ± 0.1	0.55 ± 0.03	136 ± 1	170 (215/135)
13:11:25.55	-1:20:17.2	19.17 ± 0.10	6.0 ± 0.1	2.6 ± 0.1	0.15 ± 0.02	96 ± 3	97 (122/77)
13:11:27.30	-1:19:05.1	19.62 ± 0.15	3.8 ± 0.1	1.7 ± 0.2	0.33 ± 0.01	171 ± 2	81 (102/64)
13:11:28.50	-1:18:44.8	18.64 ± 0.09	3.9 ± 0.1	3.0 ± 0.2	0.56 ± 0.03	179 ± 1	115 (144/91)
13:11:29.55	-1:18:34.6	18.25 ± 0.13	4.1 ± 0.2	2.0 ± 0.1	0.41 ± 0.01	172 ± 1	175 (221/139)
13:11:25.27	-1:20:02.9	19.65 ± 0.12	1.0 ± 0.1	1.7 ± 0.1	0.78 ± 0.01	93 ± 1	81 (102/65)
13:11:27.56	-1:20:02.5	17.74 ± 0.01	8.9 ± 0.1	8.0 ± 0.1	0.15 ± 0.01	57 ± 1	147 (185/116)
13:11:26.62	-1:19:47.9	19.69 ± 0.01	3.5 ± 0.1	2.4 ± 0.1	0.35 ± 0.01	165 ± 1	75 (95/60)
13:11:24.36	-1:21:07.5	18.83 ± 0.12	6.1 ± 0.2	1.5 ± 0.1	0.11 ± 0.02	173 ± 7	138 (174/110)
13:11:28.27	-1:19:31.5	18.38 ± 0.14	6.0 ± 0.1	2.4 ± 0.2	0.32 ± 0.02	148 ± 1	149 (188/119)
13:11:27.99	-1:20:07.7	17.66 ± 0.01	5.3 ± 0.1	3.8 ± 0.1	0.06 ± 0.01	176 ± 1	205 (259/163)
13:11:28.90	-1:19:02.5	19.00 ± 0.14	5.1 ± 0.1	3.6 ± 0.3	0.42 ± 0.01	84 ± 1	83 (105/66)
13:11:29.47	-1:19:16.5	18.77 ± 0.13	4.0 ± 0.1	1.0 ± 0.1	0.58 ± 0.02	56 ± 1	174 (220/139)
13:11:28.52	-1:19:58.4	18.27 ± 0.14	3.3 ± 0.1	2.6 ± 0.1	0.42 ± 0.02	159 ± 1	153 (192/121)
13:11:31.57	-1:19:32.7	17.04 ± 0.01	2.3 ± 0.1	4.9 ± 0.1	0.20 ± 0.01	150 ± 1	258 (325/205)
13:11:28.38	-1:20:43.4	17.75 ± 0.01	5.6 ± 0.1	7.6 ± 0.1	0.12 ± 0.01	17 ± 1	177 (223/140)
13:11:27.29	-1:20:58.4	19.06 ± 0.12	1.3 ± 0.1	2.4 ± 0.1	0.44 ± 0.03	169 ± 1	97 (123/77)
13:11:29.24	-1:19:46.9	19.53 ± 0.14	4.7 ± 0.4	0.6 ± 0.1	0.60 ± 0.02	142 ± 1	140 (176/111)
13:11:30.91	-1:18:52.5	20.28 ± 0.14	4.3 ± 0.1	0.7 ± 0.1	0.45 ± 0.01	104 ± 1	84 (106/67)
13:11:31.68	-1:19:24.6	18.82 ± 0.10	4.1 ± 0.1	3.4 ± 0.1	0.43 ± 0.04	90 ± 1	96 (121/77)
13:11:28.62	-1:20:25.1	18.41 ± 0.01	6.0 ± 0.1	2.7 ± 0.1	0.09 ± 0.01	24 ± 1	136 (172/108)
13:11:30.23	-1:20:42.7	17.11 ± 0.01	3.1 ± 0.1	5.7 ± 0.1	0.16 ± 0.01	83 ± 1	255 (321/202)
13:11:28.78	-1:20:26.5	18.38 ± 0.02	4.8 ± 0.1	7.2 ± 0.2	0.44 ± 0.05	50 ± 2	94 (119/75)

¹ Total F775W AB magnitude obtained from the surface brightness profile fitting

² Circularized physical half light radius in units of kpc

³ Estimated galaxy velocity dispersion, see text for details, and the corresponding 1σ range

Table 6.1: – continued.

RA	Dec	m_{AB}^1	n_{ser}	R_e^2 (kpc)	$1 - b/a$	PA ($^\circ$)	σ_{est}^3 (km/s)
13:11:30.44	-1:20:29.1	17.62 \pm 0.02	2.6 \pm 0.1	1.9 \pm 0.1	0.10 \pm 0.02	65 \pm 3	238 (299/189)
13:11:29.66	-1:20:27.8	16.39 \pm 0.01	1.2 \pm 0.1	10.1 \pm 0.1	0.14 \pm 0.01	144 \pm 1	303 (382/241)
13:11:28.08	-1:21:36.6	18.76 \pm 0.16	3.8 \pm 0.5	1.9 \pm 0.3	0.57 \pm 0.03	175 \pm 1	132 (166/105)
13:11:32.03	-1:18:53.6	19.06 \pm 0.17	4.5 \pm 0.3	3.5 \pm 0.5	0.05 \pm 0.01	167 \pm 6	82 (103/65)
13:11:32.88	-1:19:31.4	16.36 \pm 0.02	5.5 \pm 0.1	10.1 \pm 0.2	0.29 \pm 0.01	61 \pm 1	233 (293/185)
13:11:30.11	-1:19:55.9	18.72 \pm 0.14	2.9 \pm 0.1	1.9 \pm 0.1	0.07 \pm 0.01	107 \pm 1	135 (170/107)
13:11:28.02	-1:21:12.9	18.90 \pm 0.18	4.7 \pm 0.4	2.6 \pm 0.4	0.20 \pm 0.01	95 \pm 1	104 (131/83)
13:11:30.15	-1:20:40.1	17.66 \pm 0.01	2.5 \pm 0.1	5.3 \pm 0.1	0.36 \pm 0.01	52 \pm 1	180 (227/143)
13:11:30.40	-1:20:51.6	17.64 \pm 0.01	6.0 \pm 0.1	6.0 \pm 0.1	0.15 \pm 0.01	89 \pm 1	192 (241/152)
13:11:32.28	-1:19:46.7	17.59 \pm 0.01	5.2 \pm 0.1	4.4 \pm 0.1	0.04 \pm 0.01	144 \pm 1	215 (271/171)
13:11:32.15	-1:19:24.2	18.26 \pm 0.13	4.4 \pm 0.4	2.5 \pm 0.1	0.19 \pm 0.01	24 \pm 3	156 (196/124)
13:11:30.20	-1:20:28.4	17.54 \pm 0.01	2.5 \pm 0.1	3.2 \pm 0.1	0.13 \pm 0.01	125 \pm 6	197 (248/156)
13:11:29.18	-1:21:16.6	17.99 \pm 0.01	4.6 \pm 0.1	4.6 \pm 0.1	0.10 \pm 0.01	178 \pm 1	176 (222/140)
13:11:30.04	-1:20:15.1	19.02 \pm 0.01	3.8 \pm 0.1	2.7 \pm 0.1	0.37 \pm 0.02	116 \pm 1	86 (109/69)
13:11:30.18	-1:20:17.2	19.50 \pm 0.01	6.0 \pm 0.1	1.3 \pm 0.1	0.41 \pm 0.01	59 \pm 1	108 (136/86)
13:11:29.17	-1:20:53.8	18.95 \pm 0.12	2.7 \pm 0.1	1.0 \pm 0.1	0.19 \pm 0.01	178 \pm 1	160 (201/127)
13:11:32.83	-1:19:58.5	16.15 \pm 0.01	4.6 \pm 0.1	8.3 \pm 0.1	0.31 \pm 0.01	22 \pm 1	292 (370/230)
13:11:29.93	-1:21:00.5	18.84 \pm 0.01	5.2 \pm 0.1	1.9 \pm 0.1	0.12 \pm 0.01	25 \pm 1	114 (143/90)
13:11:32.26	-1:19:36.4	18.92 \pm 0.01	4.8 \pm 0.1	3.5 \pm 0.1	0.36 \pm 0.01	39 \pm 6	81 (102/64)
13:11:30.75	-1:20:43.6	17.82 \pm 0.01	3.5 \pm 0.1	4.2 \pm 0.1	0.12 \pm 0.01	174 \pm 1	185 (233/147)
13:11:30.56	-1:20:34.8	18.97 \pm 0.02	3.5 \pm 0.1	1.4 \pm 0.1	0.35 \pm 0.01	70 \pm 6	124 (153/100)
13:11:30.56	-1:20:45.3	18.13 \pm 0.01	4.3 \pm 0.1	2.0 \pm 0.1	0.12 \pm 0.02	92 \pm 3	173 (213/135)
13:11:29.49	-1:21:05.4	19.82 \pm 0.01	3.0 \pm 0.1	0.8 \pm 0.1	0.24 \pm 0.01	179 \pm 1	77 (98/62)
13:11:29.26	-1:21:37.3	18.77 \pm 0.09	3.1 \pm 0.1	1.9 \pm 0.1	0.53 \pm 0.03	118 \pm 1	131 (165/104)
13:11:29.30	-1:21:55.1	18.45 \pm 0.01	4.1 \pm 0.1	3.1 \pm 0.1	0.28 \pm 0.01	144 \pm 1	146 (184/116)
13:11:33.36	-1:19:16.8	20.81 \pm 0.02	2.7 \pm 0.1	0.5 \pm 0.1	0.06 \pm 0.01	167 \pm 5	77 (96/61)
13:11:33.49	-1:19:42.8	18.76 \pm 0.15	5.3 \pm 0.1	2.9 \pm 0.3	0.10 \pm 0.03	17 \pm 2	107 (135/85)
13:11:31.31	-1:21:25.0	17.79 \pm 0.01	5.0 \pm 0.1	6.3 \pm 0.2	0.09 \pm 0.01	65 \pm 2	145 (179/116)
13:11:30.21	-1:21:18.0	19.40 \pm 0.01	3.3 \pm 0.1	0.9 \pm 0.1	0.27 \pm 0.01	171 \pm 1	135 (170/107)
13:11:31.27	-1:21:27.7	18.25 \pm 0.01	3.5 \pm 0.1	1.7 \pm 0.1	0.25 \pm 0.03	61 \pm 2	175 (220/139)

¹ Total F775W AB magnitude obtained from the surface brightness profile fitting

² Circularized physical half light radius in units of kpc

³ Estimated galaxy velocity dispersion, see text for details, and the corresponding 1σ range

6 Further work

Table 6.1: – continued.

RA	Dec	m_{AB}^1	n_{ser}	R_e^2 (kpc)	$1 - b/a$	PA ($^\circ$)	σ_{est}^3 (km/s)
13:11:31.26	-1:20:52.4	18.52 ± 0.16	5.5 ± 0.1	1.8 ± 0.3	0.07 ± 0.01	41 ± 8	156 (196/124)
13:11:31.32	-1:20:44.0	19.58 ± 0.02	5.7 ± 0.2	0.9 ± 0.1	0.04 ± 0.07	18 ± 2	121 (149/97)
13:11:31.17	-1:21:27.7	19.16 ± 0.01	3.2 ± 0.1	1.6 ± 0.1	0.17 ± 0.02	138 ± 1	102 (130/82)
13:11:30.22	-1:21:42.9	18.65 ± 0.15	5.3 ± 0.1	1.4 ± 0.2	0.51 ± 0.02	24 ± 1	165 (207/131)
13:11:34.93	-1:19:24.3	18.69 ± 0.15	5.1 ± 0.1	2.6 ± 0.2	0.13 ± 0.01	2 ± 1	117 (148/93)
13:11:31.97	-1:20:58.5	18.54 ± 0.01	5.8 ± 0.1	5.1 ± 0.2	0.06 ± 0.01	24 ± 2	86 (109/68)
13:11:34.23	-1:21:01.7	18.01 ± 0.07	2.3 ± 0.2	3.1 ± 0.3	0.61 ± 0.02	177 ± 2	164 (207/130)
13:11:35.76	-1:20:12.0	18.16 ± 0.02	1.9 ± 0.1	5.1 ± 0.2	0.13 ± 0.01	15 ± 2	111 (140/88)
13:11:35.03	-1:20:04.2	18.75 ± 0.03	4.6 ± 0.1	2.9 ± 0.2	0.31 ± 0.05	11 ± 3	100 (127/79)
13:11:32.28	-1:21:37.9	18.26 ± 0.02	4.4 ± 0.1	3.4 ± 0.1	0.27 ± 0.01	120 ± 1	146 (183/116)
13:11:32.38	-1:22:10.6	18.11 ± 0.01	5.5 ± 0.1	4.1 ± 0.1	0.20 ± 0.01	63 ± 3	146 (180/115)
13:11:34.26	-1:21:18.5	19.03 ± 0.12	3.1 ± 0.1	1.8 ± 0.1	0.53 ± 0.02	90 ± 1	113 (143/90)
13:11:35.37	-1:21:18.8	18.85 ± 0.14	3.9 ± 0.1	1.7 ± 0.1	0.24 ± 0.01	66 ± 1	129 (163/103)
13:11:35.72	-1:21:09.0	19.00 ± 0.15	6.1 ± 0.3	2.8 ± 0.3	0.19 ± 0.01	167 ± 2	95 (119/75)
13:11:34.94	-1:20:58.9	18.29 ± 0.13	3.8 ± 0.2	2.5 ± 0.1	0.31 ± 0.01	117 ± 1	152 (192/121)
13:11:36.79	-1:19:42.4	19.17 ± 0.13	2.8 ± 0.1	3.0 ± 0.1	0.15 ± 0.05	43 ± 6	82 (104/65)
13:11:36.01	-1:19:57.2	19.72 ± 0.11	3.1 ± 0.3	1.3 ± 0.1	0.38 ± 0.01	170 ± 1	86 (109/69)
13:11:35.55	-1:20:42.5	18.58 ± 0.16	5.0 ± 0.2	2.2 ± 0.2	0.05 ± 0.01	90 ± 1	137 (173/109)
13:11:33.45	-1:21:53.2	18.12 ± 0.01	2.8 ± 0.1	1.4 ± 0.1	0.32 ± 0.01	15 ± 1	73 (92/58)
13:11:35.34	-1:21:12.5	19.33 ± 0.14	2.9 ± 0.2	1.8 ± 0.1	0.25 ± 0.01	24 ± 1	94 (118/75)

¹ Total F775W AB magnitude obtained from the surface brightness profile fitting

² Circularized physical half light radius in units of kpc

³ Estimated galaxy velocity dispersion, see text for details, and the corresponding 1σ range

References

- Abraham, R. G., McCarthy, P. J., Glazebrook, K., Mentuch, E., Nair, P., Yan, H., Savaglio, S., Crampton, D., Murowinski, R., Juneau, S., Le Borgne, D., Carlberg, R. G., Jorgensen, I., Roth, K., Chen, H.-W., Marzke, R. O. (2007), *The Gemini Deep Deep Survey: VIII. When Did Early-type Galaxies Form?*, ArXiv Astrophysics e-prints
- Abraham, R. G., Tanvir, N. R., Santiago, B. X., Ellis, R. S., Glazebrook, K., van den Bergh, S. (1996), *Galaxy morphology to I=25 mag in the Hubble Deep Field*, MNRAS, 279, L47
- Abraham, R. G., Valdes, F., Yee, H. K. C., van den Bergh, S. (1994), *The morphologies of distant galaxies. 1: an automated classification system*, ApJ, 432, 75
- Adelberger, K. L., Steidel, C. C. (2000), *Multiwavelength Observations of Dusty Star Formation at Low and High Redshift*, ApJ, 544, 218
- Appenzeller, I., Bender, R., Böhm, A., Drory, N., Fricke, K., Hafner, R., Heidt, J., Hopp, U., Jager, K., Kummel, M., Mehlert, D., Mollenhoff, C., Moorwood, A., Nicklas, H., Noll, S., Saglia, R., Seifert, W., Seitz, S., Stahl, O., Sutorius, E., Szeifert, T., Wagner, S., Ziegler, B. (2000), *The FORS Deep Field.*, The Messenger, 100, 44
- Arnouts, S., D'Odorico, S., Cristiani, S., Zaggia, S., Fontana, A., Giallongo, E. (1999), *The NTT SUSI deep field*, A&A, 341, 641
- Arnouts, S., Vandame, B., Benoit, C., Groenewegen, M. A. T., da Costa, L., Schirmer, M., Mignani, R. P., Slijkhuis, R., Hatziminaoglou, E., Hook, R., Madejsky, R., Rité, C., Wicenec, A. (2001), *ESO imaging survey. Deep public survey: Multi-color optical data for the Chandra Deep Field South*, A&A, 379, 740
- Arnouts, S., Walcher, C. J., Le Fevre, O., Zamorani, G., Ilbert, O., Pozzetti, L., Bardelli, S., Tresse, L., Zucca, E., Le Brun, V., Charlot, S., Lamareille, F., McCracken, H. J., Bolzonella, M., Iovino, A., Lonsdale, C., Polletta, M., Surace, J., Bottini, D., Garilli, B., Maccagni, D., Picat, J. P., Scaramella, R., Scogeggio, M., Vettolani, G., Zanichelli, A., Adami, C., Cappi, A., Ciliegi, P., Contini, T., de la Torre, S., Foucaud, S., Franzetti, P., Gavignaud, I., Guzzo, L., Marano, B., Marinoni, C., Mazure, A., Meneux, B., Merighi, R., Paltani, S., Pello, R., Pollo, A., Radovich, M., Temporin, S., Vergani, D. (2007), *The SWIRE-VVDS-CFHTLS surveys: stellar mass assembly over the last 10 Gyears. Evidence for a major build up of the red sequence between z=2 and z=1*, ArXiv e-prints, 705

References

- Böhm, A., Ziegler, B. L., Saglia, R. P., Bender, R., Fricke, K. J., Gabasch, A., Heidt, J., Mehlert, D., Noll, S., Seitz, S. (2004), *The Tully-Fisher relation at intermediate redshift*, A&A, 420, 97
- Baldry, I. K., Balogh, M. L., Bower, R. G., Glazebrook, K., Nichol, R. C., Bamford, S. P., Budavari, T. (2006), *Galaxy bimodality versus stellar mass and environment*, MNRAS, 373, 469
- Baldry, I. K., Glazebrook, K., Brinkmann, J., Ivezić, Ž., Lupton, R. H., Nichol, R. C., Szalay, A. S. (2004), *Quantifying the Bimodal Color-Magnitude Distribution of Galaxies*, ApJ, 600, 681
- Bauer, A. E., Drory, N., Hill, G. J., Feulner, G. (2005), *Specific Star Formation Rates to Redshift 1.5*, ApJ, 621, L89
- Bell, E. F., McIntosh, D. H., Katz, N., Weinberg, M. D. (2003), *The Optical and Near-Infrared Properties of Galaxies. I. Luminosity and Stellar Mass Functions*, ApJS, 149, 289
- Bell, E. F., Papovich, C., Wolf, C., Le Floc'h, E., Caldwell, J. A. R., Barden, M., Egami, E., McIntosh, D. H., Meisenheimer, K., Pérez-González, P. G., Rieke, G. H., Rieke, M. J., Rigby, J. R., Rix, H.-W. (2005), *Toward an Understanding of the Rapid Decline of the Cosmic Star Formation Rate*, ApJ, 625, 23
- Bender, R., Appenzeller, I., Böhm, A., Drory, N., Fricke, K. J., Gabasch, A., Heidt, J., Hopp, U., Jäger, K., Kümmel, M., Mehlert, D., Möllenhoff, C., Moorwood, A., Nicklas, H., Noll, S., Saglia, R. P., Seifert, W., Seitz, S., Stahl, O., Sutorius, E., Szeifert, T., Wagner, S. J., Ziegler, B. L. (2001), "The FORS Deep Field: Photometric Data and Photometric Redshifts", in *ESO/ECF/STScI Workshop on Deep Fields*, edited by S. Christiani, 327, Berlin, Springer
- Bender, R., Burstein, D., Faber, S. M. (1992), *Dynamically hot galaxies. I - Structural properties*, ApJ, 399, 462
- Benítez, N., Ford, H., Bouwens, R., Menanteau, F., Blakeslee, J., Gronwall, C., Illingworth, G., Meurer, G., Broadhurst, T. J., Clampin, M., Franx, M., Hartig, G. F., Magee, D., Sirianni, M., Ardila, D. R., Bartko, F., Brown, R. A., Burrows, C. J., Cheng, E. S., Cross, N. J. G., Feldman, P. D., Golimowski, D. A., Infante, L., Kimble, R. A., Krist, J. E., Lesser, M. P., Levay, Z., Martel, A. R., Miley, G. K., Postman, M., Rosati, P., Sparks, W. B., Tran, H. D., Tsvetanov, Z. I., White, R. L., Zheng, W. (2004), *Faint Galaxies in Deep Advanced Camera for Surveys Observations*, ApJS, 150, 1
- Bershady, M. A., Lowenthal, J. D., Koo, D. C. (1998), *Near-Infrared Galaxy Counts to J and K \sim 24 as a Function of Image Size*, ApJ, 505, 50

References

- Bertin, E. (2006), *Automatic Astrometric and Photometric Calibration with SCAMP*, in *ASP Conf. Ser. 351: Astronomical Data Analysis Software and Systems XV*, edited by C. Gabriel, C. Arviset, D. Ponz, S. Enrique, 112
- Bertin, E., Arnouts, S. (1996), *SExtractor: Software for source extraction.*, A&AS, 117, 393
- Bertin, E. (2003), *SWarp user's guide*, Swarp user's guide
- Bolzonella, M., Miralles, J.-M., Pelló, R. (2000), *Photometric redshifts based on standard SED fitting procedures*, A&A, 363, 476
- Borch, A., Meisenheimer, K., Bell, E. F., Rix, H.-W., Wolf, C., Dye, S., Kleinheinrich, M., Kovacs, Z., Wisotzki, L. (2006), *The stellar masses of 25 000 galaxies at $0.2 \leq z \leq 1.0$ estimated by the COMBO-17 survey*, A&A, 453, 869
- Bouwens, R. J., Broadhurst, T., Illingworth, G. (2003a), *Cloning Dropouts: Implications for Galaxy Evolution at High Redshift*, ApJ, 593, 640
- Bouwens, R. J., Illingworth, G. D., Rosati, P., Lidman, C., Broadhurst, T., Franx, M., Ford, H. C., Magee, D., Benítez, N., Blakeslee, J. P., Meurer, G. R., Clampin, M., Hartig, G. F., Ardila, D. R., Bartko, F., Brown, R. A., Burrows, C. J., Cheng, E. S., Cross, N. J. G., Feldman, P. D., Golimowski, D. A., Gronwall, C., Infante, L., Kimble, R. A., Krist, J. E., Lesser, M. P., Martel, A. R., Menanteau, F., Miley, G. K., Postman, M., Sirianni, M., Sparks, W. B., Tran, H. D., Tsvetanov, Z. I., White, R. L., Zheng, W. (2003b), *Star Formation at $z \sim 6$: i-Dropouts in the Advanced Camera for Surveys Guaranteed Time Observation Fields*, ApJ, 595, 589
- Bouwens, R. J., Illingworth, G. D., Thompson, R. I., Blakeslee, J. P., Dickinson, M. E., Broadhurst, T. J., Eisenstein, D. J., Fan, X., Franx, M., Meurer, G., van Dokkum, P. (2004), *Star Formation at $z \sim 6$: The Hubble Ultra Deep Parallel Fields*, ApJ, 606, L25
- Bower, R. G., Benson, A. J., Malbon, R., Helly, J. C., Frenk, C. S., Baugh, C. M., Cole, S., Lacey, C. G. (2006), *Breaking the hierarchy of galaxy formation*, MNRAS, 370, 645
- Brainerd, T. G., Blandford, R. D., Smail, I. (1996), *Weak Gravitational Lensing by Galaxies*, ApJ, 466, 623
- Brinchmann, J., Ellis, R. S. (2000), *The Mass Assembly and Star Formation Characteristics of Field Galaxies of Known Morphology*, ApJ, 536, L77
- Bruzual, G., Charlot, S. (1993), *Spectral evolution of stellar populations using isochrone synthesis*, ApJ, 405, 538
- Bruzual, G., Charlot, S. (2003), *Stellar population synthesis at the resolution of 2003*, MNRAS, 344, 1000

References

- Bundy, K., Ellis, R. S., Conselice, C. J. (2005), *The Mass Assembly Histories of Galaxies of Various Morphologies in the GOODS Fields*, ApJ, 625, 621
- Bundy, K., Ellis, R. S., Conselice, C. J., Taylor, J. E., Cooper, M. C., Willmer, C. N. A., Weiner, B. J., Coil, A. L., Noeske, K. G., Eisenhardt, P. R. M. (2006), *The Mass Assembly History of Field Galaxies: Detection of an Evolving Mass Limit for Star-Forming Galaxies*, ApJ, 651, 120
- Bunker, A. J., Stanway, E. R., Ellis, R. S., McMahon, R. G. (2004), *The star formation rate of the Universe at $z \sim 6$ from the Hubble Ultra-Deep Field*, MNRAS, 450
- Capak, P., Cowie, L. L., Hu, E. M., Barger, A. J., Dickinson, M., Fernandez, E., Giavalisco, M., Komiyama, Y., Kretchmer, C., McNally, C., Miyazaki, S., Okamura, S., Stern, D. (2004), *A Deep Wide-Field, Optical, and Near-Infrared Catalog of a Large Area around the Hubble Deep Field North*, AJ, 127, 180
- Caputi, K. I., Dunlop, J. S., McLure, R. J., Roche, N. D. (2005), *The evolution of K_s -selected galaxies in the GOODS/CDFS deep ISAAC field*, MNRAS, 361, 607
- Casertano, S., Ratnatunga, K. U., Griffiths, R. E., Im, M., Neuschaefer, L. W., Ostrander, E. J., Windhorst, R. A. (1995), *Structural Parameters of Faint Galaxies from Prerefurbishment Hubble Space Telescope Medium Deep Survey Observations*, ApJ, 453, 599
- Chen, H.-W., McCarthy, P. J., Marzke, R. O., Wilson, J., Carlberg, R. G., Firth, A. E., Persson, S. E., Sabbey, C. N., Lewis, J. R., McMahon, R. G., Lahav, O., Ellis, R. S., Martini, P., Abraham, R. G., Oemler, A., Murphy, D. C., Somerville, R. S., Beckett, M. G., Mackay, C. D. (2002), *The Las Campanas Infrared Survey. III. The H-Band Imaging Survey and the Near-Infrared and Optical Photometric Catalogs*, ApJ, 570, 54
- Cimatti, A., Daddi, E., Renzini, A. (2006), *Mass downsizing and “top-down” assembly of early-type galaxies*, A&A, 453, L29
- Cimatti, A., Daddi, E., Renzini, A., Cassata, P., Vanzella, E., Pozzetti, L., Cristiani, S., Fontana, A., Rodighiero, G., Mignoli, M., Zamorani, G. (2004), *Old galaxies in the young Universe*, Nature, 430, 184
- Cimatti, A., Pozzetti, L., Mignoli, M., Daddi, E., Menci, N., Poli, F., Fontana, A., Renzini, A., Zamorani, G., Broadhurst, T., Cristiani, S., D’Odorico, S., Giallongo, E., Gilmozzi, R. (2002), *The K20 survey. IV. The redshift distribution of $K_s < 20$ galaxies: A test of galaxy formation models*, A&A, 391, L1
- Cohen, J. G. (2002), *Caltech Faint Galaxy Redshift Survey. XVI. The Luminosity Function for Galaxies in the Region of the Hubble Deep Field-North to $z=1.5$* , ApJ, 567, 672

References

- Cole, S., Lacey, C. G., Baugh, C. M., Frenk, C. S. (2000), *Hierarchical galaxy formation*, MNRAS, 319, 168
- Cole, S., Norberg, P., Baugh, C. M., Frenk, C. S., Bland-Hawthorn, J., Bridges, T., Cannon, R., Colless, M., Collins, C., Couch, W., Cross, N., Dalton, G., De Propris, R., Driver, S. P., Efstathiou, G., Ellis, R. S., Glazebrook, K., Jackson, C., Lahav, O., Lewis, I., Lumsden, S., Maddox, S., Madgwick, D., Peacock, J. A., Peterson, B. A., Sutherland, W., Taylor, K. (2001), *The 2dF galaxy redshift survey: near-infrared galaxy luminosity functions*, MNRAS, 326, 255
- Coleman, G. D., Wu, C.-C., Weedman, D. W. (1980), *Colors and magnitudes predicted for high redshift galaxies*, ApJS, 43, 393
- Colless, M., Dalton, G., Maddox, S., Sutherland, W., Norberg, P., Cole, S., Bland-Hawthorn, J., Bridges, T., Cannon, R., Collins, C., Couch, W., Cross, N., Deeley, K., De Propris, R., Driver, S. P., Efstathiou, G., Ellis, R. S., Frenk, C. S., Glazebrook, K., Jackson, C., Lahav, O., Lewis, I., Lumsden, S., Madgwick, D., Peacock, J. A., Peterson, B. A., Price, I., Seaborne, M., Taylor, K. (2001), *The 2dF Galaxy Redshift Survey: spectra and redshifts*, MNRAS, 328, 1039
- Conselice, C. J. (2003), *The Relationship between Stellar Light Distributions of Galaxies and Their Formation Histories*, ApJS, 147, 1
- Conselice, C. J., Bershady, M. A., Jangren, A. (2000), *The Asymmetry of Galaxies: Physical Morphology for Nearby and High-Redshift Galaxies*, ApJ, 529, 886
- Cowie, L. L., Songaila, A., Hu, E. M., Cohen, J. G. (1996), *New Insight on Galaxy Formation and Evolution From Keck Spectroscopy of the Hawaii Deep Fields*, AJ, 112, 839
- Cristóbal-Hornillos, D., Balcells, M., Prieto, M., Guzmán, R., Gallego, J., Cardiel, N., Serrano, Á., Pelló, R. (2003), *K_s Number Counts in the Groth and Coppi Fields*, ApJ, 595, 71
- Daddi, E., Cimatti, A., Renzini, A., Fontana, A., Mignoli, M., Pozzetti, L., Tozzi, P., Zamorani, G. (2004), *A New Photometric Technique for the Joint Selection of Star-forming and Passive Galaxies at $1.4 < z < 2.5$* , ApJ, 617, 746
- Davies, R. I., Thomas, J., Genzel, R., Mueller Sánchez, F., Tacconi, L. J., Sternberg, A., Eisenhauer, F., Abuter, R., Saglia, R., Bender, R. (2006), *The Star-forming Torus and Stellar Dynamical Black Hole Mass in the Seyfert 1 Nucleus of NGC 3227*, ApJ, 646, 754
- De Lucia, G., Kauffmann, G., White, S. D. M. (2004), *Chemical enrichment of the intracluster and intergalactic medium in a hierarchical galaxy formation model*, MNRAS, 349, 1101

References

- De Lucia, G., Springel, V., White, S. D. M., Croton, D., Kauffmann, G. (2006), *The formation history of elliptical galaxies*, MNRAS, 366, 499
- de Vaucouleurs, G. (1948), *Recherches sur les Nebuleuses Extragalactiques*, Annales d'Astrophysique, 11, 247
- de Vaucouleurs, G., de Vaucouleurs, A., Corwin, H. G., Buta, R. J., Paturel, G., Fouque, P. (1991), *Third Reference Catalogue of Bright Galaxies*, Volume 1-3, XII, 2069 pp. 7 figs.. Springer-Verlag Berlin Heidelberg New York
- Dekel, A., Birnboim, Y. (2004), *Origin of Bimodality in Galaxy Properties: Cold and Hot Flows, Clustering and Feedback*, ArXiv Astrophysics e-prints
- Dickinson, M., Papovich, C., Ferguson, H. C., Budavári, T. (2003), *The Evolution of the Global Stellar Mass Density at $0 \leq z \leq 3$* , ApJ, 587, 25
- Djorgovski, S., Davis, M. (1987), "Fundamental Properties of Elliptical Galaxies", ApJ, 313, 59
- Djorgovski, S., Soifer, B. T., Pahre, M. A., Larkin, J. E., Smith, J. D., Neugebauer, G., Smail, I., Matthews, K., Hogg, D. W., Blandford, R. D., Cohen, J., Harrison, W., Nelson, J. (1995), *Deep galaxy counts in the K band with the Keck telescope*, ApJ, 438, L13
- Dressler, A., Faber, S., Burstein, D., et al. (1987), *Spectroscopy and photometry of elliptical galaxies—A large-scale streaming motion in the local Universe*, ApJ, 313, L37
- Dressler, A., Oemler, A. J., Couch, W. J., Smail, I., Ellis, R. S., Barger, A., Butcher, H., Poggianti, B. M., Sharples, R. M. (1997), *Evolution since $z = 0.5$ of the Morphology-Density Relation for Clusters of Galaxies*, ApJ, 490, 577
- Driver, S. P., Windhorst, R. A., Ostrander, E. J., Keel, W. C., Griffiths, R. E., Ratnatunga, K. U. (1995), *The morphological mix of field galaxies to $m_I = 24.25$ mag ($b_J \sim 26$ mag) from a deep HST WFPC2 image*, ApJ, 449, L23
- Drory, N. (2003), *Yet another object detection application (YODA). Object detection and photometry for multi-band imaging data*, A&A, 397, 371
- Drory, N., Bender, R., Feulner, G., Hopp, U., Maraston, C., Snigula, J., Hill, G. J. (2004a), *The Munich Near-Infrared Cluster Survey (MUNICS). VI. The Stellar Masses of K-Band-selected Field Galaxies to $z \sim 1.2$* , ApJ, 608, 742
- Drory, N., Bender, R., Hopp, U. (2004b), *Comparing Spectroscopic and Photometric Stellar Mass Estimates*, ApJ, 616, L103

References

- Drory, N., Bender, R., Snigula, J., Feulner, G., Hopp, U., Maraston, C., Hill, G. J., de Oliveira, C. M. (2001a), *The Munich Near-Infrared Cluster Survey: Number Density Evolution of Massive Field Galaxies to $z \sim 1.2$ as Derived from the K-Band-selected Survey*, ApJ, 562, L111
- Drory, N., Feulner, G., Bender, R., Botzler, C. S., Hopp, U., Maraston, C., Mendes de Oliveira, C., Snigula, J. (2001b), "The Munich Near-Infrared Cluster Survey – I. Field selection, object extraction, and photometry", MNRAS, 325, 550
- Drory, N., Salvato, M., Gabasch, A., Bender, R., Hopp, U., Feulner, G., Pannella, M. (2005), *The Stellar Mass Function of Galaxies to $z \sim 5$ in the FORS Deep and GOODS-South Fields*, ApJ, 619, L131
- Dubinski, J. (1998), *The Origin of the Brightest Cluster Galaxies*, ApJ, 502, 141
- Egami, E., Dole, H., Huang, J.-S., Pérez-Gonzalez, P., Le Floc'h, E., Papovich, C., Barmby, P., Ivison, R. J., Serjeant, S., Mortier, A., Frayer, D. T., Rigopoulou, D., Lagache, G., Rieke, G. H., Willner, S. P., Alonso-Herrero, A., Bai, L., Engelbracht, C. W., Fazio, G. G., Gordon, K. D., Hines, D. C., Misselt, K. A., Miyazaki, S., Morrison, J. E., Rieke, M. J., Rigby, J. R., Wilson, G. (2004), *Spitzer Observations of the SCUBA/VLA Sources in the Lockman Hole: Star Formation History of Infrared-Luminous Galaxies*, ApJS, 154, 130
- Eggen, O. J., Lynden-Bell, D., Sandage, A. R. (1962), *Evidence from the motions of old stars that the Galaxy collapsed.*, ApJ, 136, 748
- Ellis, R. S., Smail, I., Dressler, A., Couch, W. J., Oemler, A. J., Butcher, H., Sharples, R. M. (1997), *The Homogeneity of Spheroidal Populations in Distant Clusters*, ApJ, 483, 582
- Elmegreen, B. G., Elmegreen, D. M., Montenegro, L. (1992), *Optical tracers of spiral wave resonances in galaxies. II - Hidden three-arm spirals in a sample of 18 galaxies*, ApJS, 79, 37
- Faber, S. M., Jackson, R. E. (1976), *Velocity dispersions and mass-to-light ratios for elliptical galaxies*, ApJ, 204, 668
- Feulner, G., Gabasch, A., Salvato, M., Drory, N., Hopp, U., Bender, R. (2005a), *Specific Star Formation Rates to Redshift 5 from the FORS Deep Field and the GOODS-S Field*, ApJ, 633, L9
- Feulner, G., Goranova, Y., Drory, N., Hopp, U., Bender, R. (2005b), *The connection between star formation and stellar mass: specific star formation rates to redshift one*, MNRAS, 358, L1
- Fontana, A., Donnarumma, I., Vanzella, E., Giallongo, E., Menci, N., Nonino, M., Saracco, P., Cristiani, S., D'Odorico, S., Poli, F. (2003a), *The Assembly of Massive Galaxies from Near-Infrared Observations of the Hubble Deep Field-South*, ApJ, 594, L9

References

- Fontana, A., Poli, F., Menci, N., Nonino, M., Giallongo, E., Cristiani, S., D'Odorico, S. (2003b), *A European Southern Observatory Very Large Telescope Survey of Near-Infrared ($z \leq 25$) Selected Galaxies at Redshifts $4.5 < z < 6$: Constraining the Cosmic Star Formation Rate near the Reionization Epoch*, ApJ, 587, 544
- Fontana, A., Pozzetti, L., Donnarumma, I., Renzini, A., Cimatti, A., Zamorani, G., Menci, N., Daddi, E., Giallongo, E., Mignoli, M., Perna, C., Salimbeni, S., Saracco, P., Broadhurst, T., Cristiani, S., D'Odorico, S., Gilmozzi, R. (2004), *The K20 survey. VI. The distribution of the stellar masses in galaxies up to $z \sim 2$* , A&A, 424, 23
- Fontana, A., Salimbeni, S., Grazian, A., Giallongo, E., Pentericci, L., Nonino, M., Fontanot, F., Menci, N., Monaco, P., Cristiani, S., Vanzella, E., de Santis, C., Gallozzi, S. (2006), *The Galaxy mass function up to $z = 4$ in the GOODS-MUSIC sample: into the epoch of formation of massive galaxies*, A&A, 459, 745
- Ford, H. C., Clampin, M., Hartig, G. F., Illingworth, G. D., Sirianni, M., Martel, A. R., Meurer, G. R., McCann, W. J., Sullivan, P. C., Bartko, F., Benitez, N., Blakeslee, J., Bouwens, R., Broadhurst, T., Brown, R. A., Burrows, C. J., Campbell, D., Cheng, E. S., Feldman, P. D., Franx, M., Golimowski, D. A., Gronwall, C., Kimble, R. A., Krist, J. E., Lesser, M. P., Magee, D., Miley, G., Postman, M., Rafal, M. D., Rosati, P., Sparks, W. B., Tran, H. D., Tsvetanov, Z. I., Volmer, P., White, R. L., Woodruff, R. A. (2003), *Overview of the Advanced Camera for Surveys on-orbit performance*, in *Future EUV/UV and Visible Space Astrophysics Missions and Instrumentation*. Edited by J. Chris Blades, Oswald H. W. Siegmund. *Proceedings of the SPIE*, Volume 4854, pp. 81-94 (2003)., edited by J. C. Blades, O. H. W. Siegmund, volume 4854 of *Presented at the Society of Photo-Optical Instrumentation Engineers (SPIE) Conference*, 81–94
- Franceschini, A., Rodighiero, G., Cassata, P., Berta, S., Vaccari, M., Nonino, M., Vanzella, E., Hatziminaoglou, E., Antichi, J., Cristiani, S. (2006), *Cosmic evolution of the galaxy's mass and luminosity functions by morphological type from multi-wavelength data in the CDF-South*, A&A, 453, 397
- Freeman, K. C. (1970), *On the Disks of Spiral and so Galaxies*, ApJ, 160, 811
- Frith, W. J., Metcalfe, N., Shanks, T. (2006), *New H-band galaxy number counts: a large local hole in the galaxy distribution*, MNRAS, 371, 1601
- Fritz, A., Ziegler, B. L., Bower, R. G., Smail, I., Davies, R. L. (2005), *On the evolutionary status of early-type galaxies in clusters at $z \sim 0.2$ - I. The Fundamental Plane*, MNRAS, 358, 233
- Gabasch, A. (2004), *Galaxy Evolution in the Forn Deep Field*, Ph.D. thesis, Ludwig-Maximilians-Universität München

References

- Gabasch, A., Bender, R., Seitz, S., Hopp, U., Saglia, R. P., Feulner, G., Snigula, J., Drory, N., Appenzeller, I., Heidt, J., Mehler, D., Noll, S., Böhm, A., Jäger, K., Ziegler, B., Fricke, K. J. (2004a), *The evolution of the luminosity functions in the FORS Deep Field from low to high redshift. I. The blue bands*, A&A, 421, 41
- Gabasch, A., Salvato, M., Saglia, R. P., Bender, R., Hopp, U., Seitz, S., Feulner, G., Pannella, M., Drory, N., Schirmer, M., Erben, T. (2004b), *The Star Formation Rate History in the FORS Deep and GOODS-South Fields*, ApJ, 616, L83
- Gardner, J. P., Cowie, L. L., Wainscoat, R. J. (1993), *Galaxy number counts from $K = 10$ to $K = 23$* , ApJ, 415, L9
- Gardner, J. P., Sharples, R. M., Carrasco, B. E., Frenk, C. S. (1996), *A wide-field K-band survey - I. Galaxy counts in B, V, I and K*, MNRAS, 282, L1
- Gebhardt, K., Richstone, D., Kormendy, J., Lauer, T. R., Ajhar, E. A., Bender, R., Dressler, A., Faber, S. M., Grillmair, C., Magorrian, J., Tremaine, S. (2000), *Axisymmetric, Three-Integral Models of Galaxies: A Massive Black Hole in NGC 3379*, AJ, 119, 1157
- Gebhardt, K., Richstone, D., Tremaine, S., Lauer, T., Bender, R., Bower, G., Dressler, A., Faber, S., Filippenko, A., Green, R., Grillmair, C., Ho, L., Kormendy, J., Magorrian, J., Pinkney, J. (2003), *Axisymmetric Dynamical Models of the Central Regions of Galaxies*, ApJ, 583, 92
- Gehrels, N. (1986), *Confidence limits for small numbers of events in astrophysical data*, ApJ, 303, 336
- Genzel, R., Tacconi, L. J., Rigopoulou, D., Lutz, D., Tecza, M. (2001), *Ultraluminous Infrared Mergers: Elliptical Galaxies in Formation?*, ApJ, 563, 527
- Giallongo, E., Salimbeni, S., Menci, N., Zamorani, G., Fontana, A., Dickinson, M., Cristiani, S., Pozzetti, L. (2005), *The B-Band Luminosity Function of Red and Blue Galaxies up to $z = 3.5$* , ApJ, 622, 116
- Giavalisco, M., Dickinson, M., Ferguson, H. C., Ravindranath, S., Kretchmer, C., Moustakas, L. A., Madau, P., Fall, S. M., Gardner, J. P., Livio, M., Papovich, C., Renzini, A., Spinrad, H., Stern, D., Riess, A. (2004a), *The Rest-Frame Ultraviolet Luminosity Density of Star-forming Galaxies at Redshifts $z < 3.5$* , ApJ, 600, L103
- Giavalisco, M., Ferguson, H. C., Koekemoer, A. M., Dickinson, M., Alexander, D. M., Bauer, F. E., Bergeron, J., Biagetti, C., Brandt, W. N., Casertano, S., Cesarsky, C., Chatzichristou, E., Conselice, C., Cristiani, S., Da Costa, L., Dahlen, T., de Mello, D., Eisenhardt, P., Erben, T., Fall, S. M., Fassnacht, C., Fosbury, R., Fruchter, A., Gardner, J. P., Grogin, N., Hook, R. N., Hornschemeier, A. E., Idzi, R., Jogee, S., Kretchmer, C.,

References

- Laidler, V., Lee, K. S., Livio, M., Lucas, R., Madau, P., Mobasher, B., Moustakas, L. A., Nonino, M., Padovani, P., Papovich, C., Park, Y., Ravindranath, S., Renzini, A., Richardson, M., Riess, A., Rosati, P., Schirmer, M., Schreier, E., Somerville, R. S., Spinrad, H., Stern, D., Stiavelli, M., Strolger, L., Urry, C. M., Vandame, B., Williams, R., Wolf, C. (2004b), *The Great Observatories Origins Deep Survey: Initial Results from Optical and Near-Infrared Imaging*, ApJ, 600, L93
- Gilli, R., Cimatti, A., Daddi, E., Hasinger, G., Rosati, P., Szokoly, G., Tozzi, P., Bergeron, J., Borgani, S., Giacconi, R., Kewley, L., Mainieri, V., Mignoli, M., Nonino, M., Norman, C., Wang, J., Zamorani, G., Zheng, W., Zirm, A. (2003), *Tracing the Large-Scale Structure in the Chandra Deep Field South*, ApJ, 592, 721
- Glazebrook, K., Peacock, J. A., Miller, L., Collins, C. A. (1995), *An Imaging K-band survey – II. The redshift survey and galaxy evolution in the infrared*, MNRAS, 275, 169
- Halkola, A., Seitz, S., Pannella, M. (2006), *Parametric strong gravitational lensing analysis of Abell 1689*, MNRAS, 372, 1425
- Hall, P., Mackay, C. D. (1984), *Faint galaxy number-magnitude counts at high galactic latitude. I*, MNRAS, 210, 979
- Heidt, J., Appenzeller, I., Gabasch, A., Jäger, K., Seitz, S., Bender, R., Böhm, A., Snigula, J., Fricke, K. J., Hopp, U., Kümmel, M., Möllenhoff, C., Szeifert, T., Ziegler, B., Drory, N., Mehlert, D., Moorwood, A., Nicklas, H., Noll, S., Saglia, R. P., Seifert, W., Stahl, O., Sutorius, E., Wagner, S. J. (2003), *The FORS Deep Field: Field selection, photometric observations and photometric catalog*, A&A, 398, 49
- Hernquist, L., Springel, V. (2003), *An analytical model for the history of cosmic star formation*, MNRAS, 341, 1253
- Herschel, J. F. W. (1830), *Observations of Nebulae and Clusters of Stars, Made at Slough, with a Twenty-Feet Reflector, between the Years 1825 and 1833. [Abstract]*, Royal Society of London Proceedings Series I, 3, 213
- Hildebrandt, H., Bomans, D. J., Erben, T., Schneider, P., Schirmer, M., Czoske, O., Dietrich, J. P., Schrabback, T., Simon, P., Dettmar, R. J., Haberzettl, L., Hetterscheidt, M., Cordes, O. (2005), *GaBoDS: the Garching-Bonn Deep Survey. III. Lyman-break galaxies in the Chandra Deep Field South*, A&A, 441, 905
- Hopkins, A. M., Connolly, A. J., Haarsma, D. B., Cram, L. E. (2001), *Toward a Resolution of the Discrepancy between Different Estimators of Star Formation Rate*, AJ, 122, 288
- Horne, K. (1986), *An optimal extraction algorithm for CCD spectroscopy*, PASP, 98, 609

References

- Huang, J., Cowie, L. L., Luppino, G. A. (1998), *Morphological Classification of the Local I- and K-Band Galaxy Sample*, ApJ, 496, 31
- Huang, J. S., Cowie, L. L., Gardner, J. P., Hu, E. M., Songaila, A., Wainscoat, R. J. (1997), *The Hawaii K-Band Galaxy Survey. II. Bright K-Band Imaging*, ApJ, 476, 12
- Huang, J.-S., Thompson, D., Kümmel, M. W., Meisenheimer, K., Wolf, C., Beckwith, S. V. W., Fockenbrock, R., Fried, J. W., Hippelein, H., von Kuhlmann, B., Phleps, S., Röser, H.-J., Thommes, E. (2001), *The Calar Alto Deep Imaging Survey: K-band Galaxy number counts*, A&A, 368, 787
- Hubble, E. (1934), *The Distribution of Extra-Galactic Nebulae*, ApJ, 79, 8
- Hubble, E. P. (1926), *Extragalactic nebulae.*, ApJ, 64, 321
- Hughes, D. H., Serjeant, S., Dunlop, J., Rowan-Robinson, M., Blain, A., Mann, R. G., Ivison, R., Peacock, J., Efstathiou, A., Gear, W., Oliver, S., Lawrence, A., Longair, M., Goldschmidt, P., Jenness, T. (1998), *High-redshift star formation in the Hubble Deep Field revealed by a submillimetre-wavelength survey.*, Nat, 394, 241
- Ilbert, O., Tresse, L., Arnouts, S., Zucca, E., Bardelli, S., Zamorani, G., Adami, C., Cappi, A., Garilli, B., Le Fèvre, O., Maccagni, D., Meneux, B., Scaramella, R., Scoville, N., Vettolani, G., Zanichelli, A. (2004), *Bias in the estimation of global luminosity functions*, MNRAS, 351, 541
- Iwata, I., Ohta, K., Tamura, N., Ando, M., Wada, S., Watanabe, C., Akiyama, M., Aoki, K. (2003), *Lyman Break Galaxies at $z \sim 5$: Luminosity Function*, PASJ, 55, 415
- Jarrett, T. H., Chester, T., Cutri, R., Schneider, S., Skrutskie, M., Huchra, J. P. (2000), *2MASS Extended Source Catalog: Overview and Algorithms*, AJ, 119, 2498
- Jorgensen, I., Franx, M., Kjaergaard, P. (1996), *The Fundamental Plane for cluster E and SO galaxies*, MNRAS, 280, 167
- Juneau, S., Glazebrook, K., Crampton, D., McCarthy, P. J., Savaglio, S., Abraham, R., Carlberg, R. G., Chen, H.-W., Le Borgne, D., Marzke, R. O., Roth, K., Jørgensen, I., Hook, I., Murowinski, R. (2005), *Cosmic Star Formation History and Its Dependence on Galaxy Stellar Mass*, ApJ, 619, L135
- Kashikawa, N., Takata, T., Ohyama, Y., Yoshida, M., Maihara, T., Iwamuro, F., Motohara, K., Totani, T., Nagashima, M., Shimasaku, K., Furusawa, H., Ouchi, M., Yagi, M., Okamura, S., Iye, M., Sasaki, T., Kosugi, G., Aoki, K., Nakata, F. (2003), *Subaru Deep Survey. III. Evolution of Rest-Frame Luminosity Functions Based on the Photometric Redshifts for a K'-Band-Selected Galaxy Sample*, AJ, 125, 53

References

- Kauffmann, G., Charlot, S. (1998), *The K-band luminosity function at z=1: a powerful constraint on galaxy formation theory*, MNRAS, 297, L23+
- Kauffmann, G., White, S. D. M., Heckman, T. M., Ménard, B., Brinchmann, J., Charlot, S., Tremonti, C., Brinkmann, J. (2004), *The environmental dependence of the relations between stellar mass, structure, star formation and nuclear activity in galaxies*, MNRAS, 353, 713
- Kennicutt, Jr., R. C. (1998), *Star Formation in Galaxies Along the Hubble Sequence*, ARA&A, 36, 189
- Kinney, A. L., Calzetti, D., Bica, E., Storchi-Bergmann, T. (1994), *The Reddening law outside the local group galaxies: The case of NGC 7552 and NGC 5236*, ApJ, 429, 172
- Kinney, A. L., Calzetti, D., Bohlin, R. C., McQuade, K., Storchi-Bergmann, T., Schmitt, H. R. (1996), *Template Ultraviolet to Near-Infrared Spectra of Star-forming Galaxies and Their Application to K-Corrections*, ApJ, 467, 38
- Kitzbichler, M. G., White, S. D. M. (2007), *The high-redshift galaxy population in hierarchical galaxy formation models*, MNRAS, 376, 2
- Koekemoer, A. M., Aussel, H., Calzetti, D., Capak, P., Giavalisco, M., Kneib, J. ., Leauthaud, A., Le Fevre, O., McCracken, H. J., Massey, R., Mobasher, B., Rhodes, J., Scoville, N., Shopbell, P. L. (2007), *The COSMOS Survey: Hubble Space Telescope/Advanced Camera for Surveys (HST/ACS) Observations and Data Processing*, ArXiv Astrophysics e-prints
- Kormendy, J., Bruzual A., G. (1978), *The minor-axis brightness profile of the spiral galaxy NGC 4565 and the problem of massive halos*, ApJ, 223, L63
- Kormendy, J., Gebhardt, K., Fisher, D. B., Drory, N., Macchetto, F. D., Sparks, W. B. (2005), *The Nuclear Disk in the Dwarf Elliptical Galaxy NGC 4486A*, AJ, 129, 2636
- Kormendy, J., Kennicutt, R. C. (2004), *Secular Evolution and the Formation of Pseudobulges in Disk Galaxies*, ARA&A, 42, 603
- Kron, R. G. (1980), *Photometry of a complete sample of faint galaxies*, ApJS, 43, 305
- Kümmel, M. W., Wagner, S. J. (2001), *A wide field survey at the Northern Ecliptic Pole. II. Number counts and galaxy colours in B_j, R, and K*, A&A, 370, 384
- Labbé, I., Franx, M., Rudnick, G., Schreiber, N. M. F., Rix, H., Moorwood, A., van Dokkum, P. G., van der Werf, P., Röttgering, H., van Starkenburg, L., van de Wel, A., Kuijken, K., Daddi, E. (2003), *Ultradeep Near-Infrared ISAAC Observations of the Hubble Deep Field South: Observations, Reduction, Multicolor Catalog, and Photometric Redshifts*, AJ, 125, 1107

References

- Larson, R. B. (1974), *Dynamical models for the formation and evolution of spherical galaxies*, MNRAS, 166, 585
- Le Fèvre, O., Saisse, M., Mancini, D., Brau-Nogue, S., Caputi, O., Castinel, L., D'Odorico, S., Garilli, B., Kissler-Patig, M., Lucuix, C., Mancini, G., Pauget, A., Sciarretta, G., Scodéggi, M., Tresse, L., Vettolani, G. (2003), *Commissioning and performances of the VLT-VIMOS instrument*, in *Instrument Design and Performance for Optical/Infrared Ground-based Telescopes*. Edited by Iye, Masanori; Moorwood, Alan F. M. *Proceedings of the SPIE*, Volume 4841, pp. 1670-1681 (2003)., edited by M. Iye, A. F. M. Moorwood, 1670–1681
- Le Fèvre, O., Vettolani, G., Paltani, S., Tresse, L., Zamorani, G., Le Brun, V., Moreau, C., Bottini, D., Maccagni, D., Picat, J. P., Scaramella, R., Scodéggi, M., Zanichelli, A., Adami, C., Arnouts, S., Bardelli, S., Bolzonella, M., Cappi, A., Charlot, S., Contini, T., Foucaud, S., Franzetti, P., Garilli, B., Gavignaud, I., Guzzo, L., Ilbert, O., Iovino, A., McCracken, H. J., Mancini, D., Marano, B., Marinoni, C., Mathez, G., Mazure, A., Meneux, B., Merighi, R., Pellò, R., Pollo, A., Pozzetti, L., Radovich, M., Zucca, E., Arnaboldi, M., Bondi, M., Bongiorno, A., Busarello, G., Ciliegi, P., Gregorini, L., Mellier, Y., Merluzzi, P., Ripepi, V., Rizzo, D. (2004), *The VIMOS VLT Deep Survey. Public release of 1599 redshifts to $I_{AB} \leq 24$ across the Chandra Deep Field South*, A&A, 428, 1043
- Leauthaud, A., Massey, R., Kneib, J. P., Rhodes, J., Johnston, D. E., Capak, P., Heymans, C., Ellis, R. S., Koekemoer, A. M., Le Fevre, O., Mellier, Y., Refregier, A., Robin, A. C., Scoville, N., Tasca, L., Taylor, J. E., Van Waerbeke, L. (2007), *Weak Gravitational Lensing with COSMOS: Galaxy Selection and Shape Measurements*, ArXiv Astrophysics e-prints
- Lee, J. (2006), *On the Environmental Dependence of Galaxy Properties Established by the Initial Cosmological Conditions*, ApJ, 644, L5
- Lilly, S. J., Cowie, L. L., Gardner, J. P. (1991), *A deep imaging and spectroscopic survey of faint galaxies*, ApJ, 369, 79
- Lilly, S. J., Le Fevre, O., Hammer, F., Crampton, D. (1996), *The Canada-France Redshift Survey: The Luminosity Density and Star Formation History of the Universe to Z approximately 1*, ApJ, 460, L1
- Madau, P. (1995), *Radiative transfer in a clumpy universe: The colors of high-redshift galaxies*, ApJ, 441, 18
- Madau, P., Ferguson, H. C., Dickinson, M. E., Giavalisco, M., Steidel, C. C., Fruchter, A. (1996), *High-redshift galaxies in the Hubble Deep Field: colour selection and star formation history to $z \sim 4$* , MNRAS, 283, 1388
- Madau, P., Pozzetti, L., Dickinson, M. (1998), *The Star Formation History of Field Galaxies*, ApJ, 498, 106

References

- Magorrian, J. (1999), *Kinematical signatures of hidden stellar discs*, MNRAS, 302, 530
- Maihara, T., Iwamuro, F., Tanabe, H., Taguchi, T., Hata, R., Oya, S., Kashikawa, N., Iye, M., Miyazaki, S., Karoji, H., Yoshida, M., Totani, T., Yoshii, Y., Okamura, S., Shimasaku, K., Saito, Y., Ando, H., Goto, M., Hayashi, M., Kaifu, N., Kobayashi, N., Kosugi, G., Motohara, K., Nishimura, T., Noumaru, J., Ogasawara, R., Sasaki, T., Sekiguchi, K., Takata, T., Terada, H., Yamashita, T., Usuda, T., Tokunaga, A. T. (2001), *Subaru Deep Survey I. Near-Infrared Observations*, PASJ, 53, 25
- Manfroid, J., Selman, F. (2001), *Achieving 1% photometric accuracy with the ESO Wide Field Imager*, The Messenger, 104, 16
- Mannucci, F., Basile, F., Poggianti, B. M., Cimatti, A., Daddi, E., Pozzetti, L., Vanzi, L. (2001), *Near-infrared template spectra of normal galaxies: k-corrections, galaxy models and stellar populations*, MNRAS, 326, 745
- Maraston, C. (1998), *Evolutionary synthesis of stellar populations: a modular tool*, MNRAS, 300, 872
- Maraston, C. (2005), *Evolutionary population synthesis: models, analysis of the ingredients and application to high-z galaxies*, MNRAS, 362, 799
- Martini, P. (2001a), *A Deep Multicolor Survey. VI. Near-Infrared Observations, Selection Effects, and Number Counts*, AJ, 121, 598
- Martini, P. (2001b), *A Deep Multicolor Survey. VII. Extremely Red Objects and Galaxy Formation*, AJ, 121, 2301
- McCracken, H. J., Metcalfe, N., Shanks, T., Campos, A., Gardner, J. P., Fong, R. (2000), *Galaxy number counts - IV. Surveying the Herschel Deep Field in the near-infrared*, MNRAS, 311, 707
- McLeod, B. A., Bernstein, G. M., Rieke, M. J., Tollestrup, E. V., Fazio, G. G. (1995), *K-band galaxy counts*, ApJS, 96, 117
- Menanteau, F., Ford, H. C., Motta, V., Benítez, N., Martel, A. R., Blakeslee, J. P., Infante, L. (2006), *The Morphological Demographics of Galaxies in the Advanced Camera for Surveys Hubble Ultra Deep Parallel Fields*, AJ, 131, 208
- Messier, M. (1769), *A Series of Astronomical Observations Made at the Observatory of the Marine at Paris, to Wit, 1 degrees. Observations of Jupiter's Satellites in the Years 1767 and 1768. 2 degrees. Observations on the Shadows of Jupiter's Satellites. 3 degrees. On the Variation of the Belts on the Disc of That Planet. 4 degrees. Observation of a Spot on the Disc of the 3d Satellite. 5 degrees. Observation of the Belts of Saturn. 6 degrees. Observation of the Moon's Passage Over the Pleiades, in 1767. 7 degrees. Observation*

References

- of a Partial Eclipse of the Moon, January 3, and of a Total One, December 23, 1768. 8 degrees. Observations of Two Aurorae Boreales, August 6, and December 5, of the Same Year. By M. Messier, Astronomer of the Marine, F. R. S. and of the Academies of Holland and Italy*, Philosophical Transactions Series I, 59, 454
- Metcalfe, N., Shanks, T., Campos, A., McCracken, H. J., Fong, R. (2001), *Galaxy number counts - V. Ultradeep counts: the Herschel and Hubble Deep Fields*, MNRAS, 323, 795
- Metcalfe, N., Shanks, T., Weilbacher, P. M., McCracken, H. J., Fong, R., Thompson, D. (2006), *Galaxy number counts - VI. An H-band survey of the Herschel Deep Field*, MNRAS, 370, 1257
- Mignoli, M., Cimatti, A., Zamorani, G., Pozzetti, L., Daddi, E., Renzini, A., Broadhurst, T., Cristiani, S., D'Odorico, S., Fontana, A., Giallongo, E., Gilmozzi, R., Menci, N., Saracco, P. (2005), *The K20 survey. VII. The spectroscopic catalogue: Spectral properties and evolution of the galaxy population*, A&A, 437, 883
- Minowa, Y., Kobayashi, N., Yoshii, Y., Totani, T., Maihara, T., Iwamuro, F., Takami, H., Takato, N., Hayano, Y., Terada, H., Oya, S., Iye, M., Tokunaga, A. T. (2005), *Subaru Super Deep Field with Adaptive Optics. I. Observations and First Implications*, ApJ, 629, 29
- Mo, H. J., Mao, S., White, S. D. M. (1998), *The formation of galactic discs*, MNRAS, 295, 319
- Moles, M., Alfaro, E., Benitez, N., Broadhurst, T., Castander, F. J., Cepa, J., Cervino, M., Fernandez-Soto, A., Delgado, R. M. G., Infante, L., Aguerri, A. L., Marquez, I., Martinez, V. J., Masegosa, J., del Olmo, A., Perea, J., Prada, F., Quintana, J. M., Sanchez, S. (2005), *The ALHAMBRA Survey: For a systematic Study of Cosmic Evolution*, astro-ph/0504545
- Moustakas, L. A., Davis, M., Graham, J. R., Silk, J., Peterson, B. A., Yoshii, Y. (1997), *Colors and K-Band Counts of Extremely Faint Field Galaxies*, ApJ, 475, 445
- Moy, E., Barmby, P., Rigopoulou, D., Huang, J.-S., Willner, S. P., Fazio, G. G. (2003), *H-band observations of the Chandra Deep Field South*, A&A, 403, 493
- Mutchler, M., Koekemoer, A. M., Hack, W. (2002), *Drizzling Dithered ACS Images—A Demonstration*, in *The 2002 HST Calibration Workshop*, 70–80
- Noll, S., Mehlert, D., Appenzeller, I., Bender, R., Böhm, A., Gabasch, A., Heidt, J., Hopp, U., Jäger, K., Seitz, S., Stahl, O., Tapken, C., Ziegler, B. L. (2004), *The FORS Deep Field spectroscopic survey*, A&A, 418, 885
- Noll, S., Pierini, D. (2005), *Dust properties of UV bright galaxies at $z \sim 2$* , A&A, 444, 137

References

- Noll, S., Pierini, D., Pannella, M., Savaglio, S. (2007), *Presence of dust with a UV bump in massive, star-forming galaxies at $1 < z < 2.5$* , ArXiv e-prints, 707
- Nowak, N., Saglia, R. P., Thomas, J., Bender, R., Pannella, M., Gebhardt, K., Davies, R. I. (2007), *The supermassive black hole in NGC4486a detected with SINFONI at the Very Large Telescope*, MNRAS, 597–+
- Pannella, M., Hopp, U., Saglia, R. P., Bender, R., Drory, N., Salvato, M., Gabasch, A., Feulner, G. (2006), *The Evolution of the Mass Function Split by Morphology up to Redshift 1 in the FORS Deep and the GOODS-S Fields*, ApJ, 639, L1
- Papovich, C., Giavalisco, M., Dickinson, M., Conselice, C. J., Ferguson, H. C. (2003), *The Internal Ultraviolet-Optical Color Dispersion: Quantifying the Morphological K-Correction*, ApJ, 598, 827
- Pascarelle, S. M., Lanzetta, K. M., Fernández-Soto, A. (1998), *The Ultraviolet Luminosity Density of the Universe from Photometric Redshifts of Galaxies in the Hubble Deep Field*, ApJ, 508, L1
- Peng, C. Y., Ho, L. C., Impey, C. D., Rix, H.-W. (2002), *Detailed Structural Decomposition of Galaxy Images*, AJ, 124, 266
- Pickles, A. J. (1998), *A Stellar Spectral Flux Library: 1150-25000 Å*, PASP, 110, 863
- Postman, M., Lauer, T. R., Szapudi, I., Oegerle, W. (1998), *Clustering at High Redshift: Precise Constraints from a Deep, Wide-Area Survey*, ApJ, 506, 33
- Pozzetti, L., Bolzonella, M., Lamareille, F., Zamorani, G., Franzetti, P., Le Fèvre, O., Iovino, A., Temporin, S., Ilbert, O., Arnouts, S., Charlot, S., Brinchmann, J., Zucca, E., Tresse, L., Scudeggio, M., Guzzo, L., Bottini, D., Garilli, B., Le Brun, V., Maccagni, D., Picat, J. P., Scaramella, R., Vettolani, G., Zanichelli, A., Adami, C., Bardelli, S., Cappi, A., Ciliegi, P., Contini, T., Foucaud, S., Gavignaud, I., McCracken, H. J., Marano, B., Marinoni, C., Mazure, A., Meneux, B., Merighi, R., Paltani, S., Pellò, R., Pollo, A., Radovich, M., Bondi, M., Bongiorno, A., Cucciati, O., de la Torre, S., Gregorini, L., Mellier, Y., Merluzzi, P., Vergani, D., Walcher, C. J. (2007), *The VIMOS VLT Deep Survey. The Assembly History of the Stellar Mass in Galaxies: from the Young to the Old Universe*, ArXiv e-prints, 704
- Press, W. H., Teukolsky, S. A., Vetterling, W. T., Flannery, B. P. (1992), *Numerical recipes in FORTRAN. The art of scientific computing*, Cambridge: University Press, —c1992, 2nd ed.
- Rix, H.-W., Barden, M., Beckwith, S. V. W., Bell, E. F., Borch, A., Caldwell, J. A. R., Häussler, B., Jahnke, K., Jogee, S., McIntosh, D. H., Meisenheimer, K., Peng, C. Y.,

References

- Sanchez, S. F., Somerville, R. S., Wisotzki, L., Wolf, C. (2004), *GEMS: Galaxy Evolution from Morphologies and SEDs*, ApJS, 152, 163
- Röser, H.-J., Hippelein, H. H., Wolf, C. (2004), *The Heidelberg InfraRed Optical Cluster Survey (HIROCS)*, in *Clusters of Galaxies: Probes of Cosmological Structure and Galaxy Evolution*, edited by J. S. Mulchaey, A. Dressler, A. Oemler
- Rudnick, G., Rix, H.-W., Franx, M., Labbé, I., Blanton, M., Daddi, E., Förster Schreiber, N. M., Moorwood, A., Röttgering, H., Trujillo, I., van de Wel, A., van der Werf, P., van Dokkum, P. G., van Starkenburg, L. (2003), *The Rest-Frame Optical Luminosity Density, Color, and Stellar Mass Density of the Universe from $z = 0$ to $z = 3$* , ApJ, 599, 847
- Salpeter, E. E. (1955), *The Luminosity Function and Stellar Evolution.*, ApJ, 121, 161
- Saracco, P., D'Odorico, S., Moorwood, A., Buzzoni, A., Cuby, J. .., Lidman, C. (1999), *IR colors and sizes of faint galaxies*, A&A, 349, 751
- Saracco, P., Giallongo, E., Cristiani, S., D'Odorico, S., Fontana, A., Iovino, A., Poli, F., Vanzella, E. (2001), *Deep near-IR observations of the Chandra Deep Field and of the HDF South. Color and number counts*, aa, 375, 1
- Saracco, P., Iovino, A., Garilli, B., Maccagni, D., Chincarini, G. (1997), *The ESO K'-Band galaxy survey. I. Galaxy counts*, AJ, 114, 887
- Scarlata, C., Carollo, C. M., Lilly, S. J., Sargent, M. T., Feldmann, R., Kampczyk, P., Porciani, C., Koekemoer, A., Scoville, N., Kneib, J., Leauthaud, A., Massey, R., Rhodes, J., Tasca, L., Capak, P., Maier, C., McCracken, H. J., Mobasher, B., Renzini, A., Taniguchi, Y., Thompson, D., Sheth, K., Ajiki, M., Aussel, H., Murayama, T., Sanders, D. B., Sasaki, S., Shioya, Y., Takahashi, M. (2006), *COSMOS morphological classification with ZEST (the Zurich Estimator of Structural Types) and the evolution since $z=1$ of the Luminosity Function of early-, disk-, and irregular galaxies*, ArXiv Astrophysics e-prints
- Schade, D., Lilly, S. J., Crampton, D., Hammer, F., Le Fevre, O., Tresse, L. (1995), *Canada-France Redshift Survey: Hubble Space Telescope Imaging of High-Redshift Field Galaxies*, ApJ, 451, L1+
- Schirmer, M., Erben, T., Schneider, P., Pietrzynski, G., Gieren, W., Carpano, S., Micol, A., Pierfederici, F. (2003), *GaBoDS: The Garching-Bonn Deep Survey. I. Anatomy of galaxy clusters in the background of NGC 300*, A&A, 407, 869
- Schlegel, D. J., Finkbeiner, D. P., Davis, M. (1998), "Maps of Dust Infrared Emission for Use in Estimation of Reddening and Cosmic Microwave Background Radiation Foregrounds", ApJ, 500, 525

References

- Schödel, R., Ott, T., Genzel, R., Hofmann, R., Lehnert, M., Eckart, A., Mouawad, N., Alexander, T., Reid, M. J., Lenzen, R., Hartung, M., Lacombe, F., Rouan, D., Gendron, E., Rousset, G., Lagrange, A.-M., Brandner, W., Ageorges, N., Lidman, C., Moorwood, A. F. M., Spyromilio, J., Hubin, N., Menten, K. M. (2002), *A star in a 15.2-year orbit around the supermassive black hole at the centre of the Milky Way*, Nature, 419, 694
- Schwarzschild, M. (1979), *A numerical model for a triaxial stellar system in dynamical equilibrium*, ApJ, 232, 236
- Scodéglio, M., Franzetti, P., Garilli, B., Zanichelli, A., Paltani, S., Maccagni, D., Bottini, D., Le Brun, V., Contini, T., Scaramella, R., Adami, C., Bardelli, S., Zucca, E., Tresse, L., Ilbert, O., Foucaud, S., Iovino, A., Merighi, R., Zamorani, G., Gavignaud, I., Rizzo, D., McCracken, H. J., Le Fèvre, O., Picat, J. P., Vettolani, G., Arnaboldi, M., Arnouts, S., Bolzonella, M., Cappi, A., Charlot, S., Ciliegi, P., Guzzo, L., Marano, B., Marinoni, C., Mathez, G., Mazure, A., Meneux, B., Pellò, R., Pollo, A., Pozzetti, L., Radovich, M. (2005), *The VVDS Data-Reduction Pipeline: Introducing VIPGI, the VIMOS Interactive Pipeline and Graphical Interface*, PASP, 117, 1284
- Scoville, N., Aussel, H., Brusa, M., Capak, P., Carollo, C. M., Elvis, M., Giavalisco, M., Guzzo, L., Hasinger, G., Impey, C., Kneib, J., LeFevre, O., Lilly, S. J., Mobasher, B., Renzini, A., Rich, R. M., Sanders, D. B., Schinnerer, E., Schiminovich, D., Shopbell, P., Taniguchi, Y., Tyson, N. D. (2006a), *The Cosmic Evolution Survey (COSMOS) – Overview*, ArXiv Astrophysics e-prints
- Scoville, N., Benson, A., Blain, A. W., Calzetti, D., Comastri, A., Capak, P., Carilli, C., Carlstrom, J. E., Carollo, C. M., Colbert, J., Daddi, E., Ellis, R. S., Elvis, M., Ewald, S. P., Fall, M., Franceschini, A., Giavalisco, M., Green, W., Griffiths, R. E., Guzzo, L., Hasinger, G., Impey, C., Kneib, J., Koda, J., Koekemoer, A., Lefevre, O., Lilly, S., Liu, C. T., McCracken, H. J., Massey, R., Mellier, Y., Miyazaki, S., Mobasher, B., Mould, J., Norman, C., Refregier, A., Renzini, A., Rhodes, J., Rich, M., Sanders, D. B., Schiminovich, D., Schinnerer, E., Scodéglio, M., Sheth, K., Shopbell, P. L., Taniguchi, Y., Tyson, N., Urry, C. M., Van Waerbeke, L., Vettolani, P., White, S. D. M., Yan, L., Zamorani, G. (2006b), *COSMOS : Hubble Space Telescope Observations*, ArXiv Astrophysics e-prints
- Sersic, J. L. (1968), *Atlas de galaxias australes*, Cordoba, Argentina: Observatorio Astronomico, 1968
- Shaw, M. A., Gilmore, G. (1989), *The luminosity distributions of edge-on spiral galaxies. I - A two-dimensional model and its application to NGC 891 and 4565*, MNRAS, 237, 903
- Simard, L., Koo, D. C., Faber, S. M., Sarajedini, V. L., Vogt, N. P., Phillips, A. C., Gebhardt, K., Illingworth, G. D., Wu, K. L. (1999), *The Magnitude-Size Relation of Galaxies out to $z \sim 1$* , ApJ, 519, 563

References

- Skrutskie, M. F., Schneider, S. E., Stiening, R., Strom, S. E., Weinberg, M. D., Beichman, C., Chester, T., Cutri, R., Lonsdale, C., Elias, J., Elston, R., Capps, R., Carpenter, J., Huchra, J., Liebert, J., Monet, D., Price, S., Seitzer, P. (1997), *The Two Micron All Sky Survey (2MASS): Overview and Status.*, in ASSL Vol. 210: *The Impact of Large Scale Near-IR Sky Surveys*, 25
- Smail, I., Dressler, A., Couch, W. J., Ellis, R. S., Oemler, A. J., Butcher, H., Sharples, R. M. (1997), *A Catalog of Morphological Types in 10 Distant Rich Clusters of Galaxies*, ApJS, 110, 213
- Snigula, J., Drory, N., Bender, R., Botzler, C. S., Feulner, G., Hopp, U. (2002), *The Munich Near-Infrared Cluster Survey - IV. Biases in the completeness of near-infrared imaging data*, MNRAS, 336, 1329
- Soifer, B. T., Matthews, K., Djorgovski, S., Larkin, J., Graham, J. R., Harrison, W., Jernigan, G., Lin, S., Nelson, J., Neugebauer, G., Smith, G., Smith, J. D., Ziolkowski, C. (1994), *Deep imaging of the field of the $z = 4.9$ quasar PC 1247+3406, and faint galaxy counts in the K band with the Keck telescope*, ApJ, 420, L1
- Somerville, R. S., Lee, K., Ferguson, H. C., Gardner, J. P., Moustakas, L. A., Giavalisco, M. (2004), *Cosmic Variance in the Great Observatories Origins Deep Survey*, ApJ, 600, L171
- Somerville, R. S., Primack, J. R., Faber, S. M. (2001), *The nature of high-redshift galaxies*, MNRAS, 320, 504
- Steidel, C. C., Adelberger, K. L., Giavalisco, M., Dickinson, M., Pettini, M. (1999), *Lyman-Break Galaxies at $z \geq 4$ and the Evolution of the Ultraviolet Luminosity Density at High Redshift*, ApJ, 519, 1
- Steidel, C. C., Giavalisco, M., Dickinson, M., Adelberger, K. L. (1996), *Spectroscopy of Lyman Break Galaxies in the Hubble Deep Field*, AJ, 112, 352
- Steidel, C. C., Shapley, A. E., Pettini, M., Adelberger, K. L., Erb, D. K., Reddy, N. A., Hunt, M. P. (2004), *A Survey of Star-forming Galaxies in the $1.4 < Z < 2.5$ Redshift Desert: Overview*, ApJ, 604, 534
- Szokoly, G. P., Bergeron, J., Hasinger, G., Lehmann, I., Kewley, L., Mainieri, V., Nonino, M., Rosati, P., Giacconi, R., Gilli, R., Gilmozzi, R., Norman, C., Romaniello, M., Schreier, E., Tozzi, P., Wang, J. X., Zheng, W., Zirm, A. (2004), *The Chandra Deep Field-South: Optical Spectroscopy. I.*, ApJS, 155, 271
- Szokoly, G. P., Subbarao, M. U., Connolly, A. J., Mobasher, B. (1998), *The Near-Infrared Number Counts and Luminosity Functions of Local Galaxies*, ApJ, 492, 452

References

- Tecza, M., Baker, A. J., Davies, R. I., Genzel, R., Lehnert, M. D., Eisenhauer, F., Lutz, D., Nesvadba, N., Seitz, S., Tacconi, L. J., Thatte, N. A., Abuter, R., Bender, R. (2004), *SPIFFI Observations of the Starburst SMM J14011+0252: Already Old, Fat, and Rich by z=2.565*, ApJ, 605, L109
- Teplitz, H. I., Gardner, J. P., Malumuth, E. M., Heap, S. R. (1998), *Galaxy Morphology from NICMOS Parallel Imaging*, ApJ, 507, L17
- Teplitz, H. I., McLean, I. S., Malkan, M. A. (1999), *Near-Infrared Observations of the Environments of Radio-quiet QSOs at z > 1*, ApJ, 520, 469
- Thomas, J., Saglia, R. P., Bender, R., Thomas, D., Gebhardt, K., Magorrian, J., Richstone, D. (2004), *Mapping stationary axisymmetric phase-space distribution functions by orbit libraries*, MNRAS, 353, 391
- Thompson, R. I., Storrie-Lombardi, L. J., Weymann, R. J., Rieke, M. J., Schneider, G., Stobie, E., Lytle, D. (1999), *Near-Infrared Camera and Multi-Object Spectrometer Observations of the Hubble Deep Field: Observations, Data Reduction, and Galaxy Photometry*, AJ, 117, 17
- Toomre, A., Toomre, J. (1972), *Galactic Bridges and Tails*, ApJ, 178, 623
- Tremaine, S., Gebhardt, K., Bender, R., Bower, G., Dressler, A., Faber, S. M., Filippenko, A. V., Green, R., Grillmair, C., Ho, L. C., Kormendy, J., Lauer, T. R., Magorrian, J., Pinkney, J., Richstone, D. (2002), *The Slope of the Black Hole Mass versus Velocity Dispersion Correlation*, ApJ, 574, 740
- Tully, R. B., Fisher, J. R. (1977), *A new method of determining distances to galaxies*, A&A, 54, 661
- Tyson, J. A. (1988), *Deep CCD survey - Galaxy luminosity and color evolution*, AJ, 96, 1
- Väisänen, P., Tollestrup, E. V., Willner, S. P., Cohen, M. (2000), *Wide-Field J- and K-Band Galaxy Counts in the European Large-Area Infrared Space Observatory Survey Fields*, ApJ, 540, 593
- Vanzella, E., Cristiani, S., Arnouts, S., Dennefeld, M., Fontana, A., Grazian, A., Nonino, M., Petitjean, P., Saracco, P. (2002), *A VLT/FORS2 spectroscopic survey in the HDF-S*, A&A, 396, 847
- Vanzella, E., Cristiani, S., Dickinson, M., Kuntschner, H., Moustakas, L. A., Nonino, M., Rosati, P., Stern, D., Cesarsky, C., Ettori, S., Ferguson, H. C., Fosbury, R. A. E., Giavalisco, M., Haase, J., Renzini, A., Rettura, A., Serra, P., The GOODS Team (2005), *The Great Observatories Origins Deep Survey. VLT/FORS2 spectroscopy in the GOODS-South Field*, A&A, 434, 53

References

- Verolme, E. K., Cappellari, M., Copin, Y., van der Marel, R. P., Bacon, R., Bureau, M., Davies, R. L., Miller, B. M., de Zeeuw, P. T. (2002), *A SAURON study of M32: measuring the intrinsic flattening and the central black hole mass*, MNRAS, 335, 517
- White, S. D. M., Frenk, C. S. (1991), *Galaxy formation through hierarchical clustering*, ApJ, 379, 52
- Williams, R. E., Blacker, B., Dickinson, M., Dixon, W. V. D., Ferguson, H. C., Fruchter, A. S., Giavalisco, M., Gilliland, R. L., Heyer, I., Katsanis, R., Levay, Z., Lucas, R. A., McElroy, D. B., Petro, L., Postman, M., Adorf, H., Hook, R. (1996), *The Hubble Deep Field: Observations, Data Reduction, and Galaxy Photometry*, AJ, 112, 1335
- Wolf, C., Meisenheimer, K., Kleinheinrich, M., Borch, A., Dye, S., Gray, M., Wisotzki, L., Bell, E. F., Rix, H.-W., Cimatti, A., Hasinger, G., Szokoly, G. (2004), *A catalogue of the Chandra Deep Field South with multi-colour classification and photometric redshifts from COMBO-17*, A&A, 421, 913
- Wolf, C., Meisenheimer, K., Röser, H.-J. (2001), *Object classification in astronomical multi-color surveys*, A&A, 365, 660
- Wu, K. L.-K. (1999), *A quantitative study of peculiarities in galaxy morphology*, Ph.D. thesis, AA(UNIVERSITY OF CALIFORNIA, SANTA CRUZ)
- Yan, L., McCarthy, P. J., Storrie-Lombardi, L. J., Weymann, R. J. (1998), *Deep H-Band Galaxy Counts and Half-Light Radii from Hubble Space Telescope/NICMOS Parallel Observations*, ApJ, 503, L19
- Yasuda, N., et al. (2001), *Galaxy Number Counts from the Sloan Digital Sky Survey Commissioning Data*, AJ, 122, 1104
- York, D. G., Adelman, J., Anderson, J. E., Anderson, S. F., Annis, J., Bahcall, N. A., Bakken, J. A., Barkhouser, R., Bastian, S., Berman, E., Boroski, W. N., Bracker, S., Briegel, C., Briggs, J. W., Brinkmann, J., Brunner, R., Burles, S., Carey, L., Carr, M. A., Castander, F. J., Chen, B., Colestock, P. L., Connolly, A. J., Crocker, J. H., Csabai, I., Czarapata, P. C., Davis, J. E., Doi, M., Dombeck, T., Eisenstein, D., Ellman, N., Elms, B. R., Evans, M. L., Fan, X., Federwitz, G. R., Fiscelli, L., Friedman, S., Frieman, J. A., Fukugita, M., Gillespie, B., Gunn, J. E., Gurbani, V. K., de Haas, E., Haldeman, M., Harris, F. H., Hayes, J., Heckman, T. M., Hennessy, G. S., Hindsley, R. B., Holm, S., Holmgren, D. J., Huang, C., Hull, C., Husby, D., Ichikawa, S., Ichikawa, T., Ivezić, Ž., Kent, S., Kim, R. S. J., Kinney, E., Klaene, M., Kleinman, A. N., Kleinman, S., Knapp, G. R., Korienek, J., Kron, R. G., Kunszt, P. Z., Lamb, D. Q., Lee, B., Leger, R. F., Limmongkol, S., Lindenmeyer, C., Long, D. C., Loomis, C., Loveday, J., Lucinio, R., Lupton, R. H., MacKinnon, B., Mannery, E. J., Mantsch, P. M., Margon, B., McGehee, P., McKay, T. A., Meiksin, A., Merelli, A., Monet, D. G., Munn, J. A., Narayanan, V. K., Nash, T., Neilsen, E., Neswold,

References

- R., Newberg, H. J., Nichol, R. C., Nicinski, T., Nonino, M., Okada, N., Okamura, S., Ostriker, J. P., Owen, R., Pauls, A. G., Peoples, J., Peterson, R. L., Petravick, D., Pier, J. R., Pope, A., Pordes, R., Prosapio, A., Rechenmacher, R., Quinn, T. R., Richards, G. T., Richmond, M. W., Rivetta, C. H., Rockosi, C. M., Ruthmansdorfer, K., Sandford, D., Schlegel, D. J., Schneider, D. P., Sekiguchi, M., Sergey, G., Shimasaku, K., Siegmund, W. A., Smee, S., Smith, J. A., Snedden, S., Stone, R., Stoughton, C., Strauss, M. A., Stubbs, C., SubbaRao, M., Szalay, A. S., Szapudi, I., Szokoly, G. P., Thakar, A. R., Tremonti, C., Tucker, D. L., Uomoto, A., Vanden Berk, D., Vogeley, M. S., Waddell, P., Wang, S., Watanabe, M., Weinberg, D. H., Yanny, B., Yasuda, N. (2000), *The Sloan Digital Sky Survey: Technical Summary*, AJ, 120, 1579
- Zheng, W., Mikles, V. J., Mainieri, V., Hasinger, G., Rosati, P., Wolf, C., Norman, C., Szokoly, G., Gilli, R., Tozzi, P., Wang, J. X., Zirm, A., Giacconi, R. (2004), *Photometric Redshift of X-Ray Sources in the Chandra Deep Field-South*, ApJS, 155, 73
- Ziegler, B. L., Bower, R. G., Smail, I., Davies, R. L., Lee, D. (2001), *The early-type galaxy population in Abell 2218*, MNRAS, 325, 1571

Acknowledgements

After all the science in this Thesis is over, I will now take a breath to try distributing credits and honors to many persons.

First, *ubi maior*, I want to thank Ralf for all these five years he resisted having me around and also for having always, almost always, the right words at every occasion. You have been the perfect leader in all these years: often busy, never absent and always enlightening. Thanks.

Soon after comes the person that mostly took care of me and my work, Roberto. He has been very much a friend always available to discuss and talk about everything I could need, both personal and professional. That happened even if he was often very busy with management and burocratic troubles. I have always thought at you as an “older” friend of mine and never as my boss, thanks much for everything.

Special thanks go to Ulrich for being as he is, honest and constructive in his approach to all things.

Last not least in the supervising crew, I want to thank Niv for being always, after eleven am, available for discussions, clarifications, explanations and most of all for writing almost one thousand reference letters for finding me a job.

Thanks to Achim, the best system manager one can dream of, for giving me the chance to spread my stuff all over the terabyte domain ... now I will have serious problems to go anywhere else. And also for many smoking breaks of cigars and rolled cigarettes.

Most of the work presented in this Thesis would not have been possible without the efforts of Mara and Armin to whom I deserve my deep gratefulness.

Thanks to Mariele and Gabi for all the times you helped me out with papers, documents and bureaucracy. Without you and your smiles life would have been much harder here. Thanks much.

I want to thank Daniele for many many coffee & cigarettes breaks and all the times he tried hard, without success, to explain why my star formation rate indicator is the wrong one. And for the suggestions, the work done together, the english corrections and much more. You have been one of my polar stars here around. Thanks.

Frau Moretti, Bargiggia, Stefano, Anna, Luigi, Giovanna, Alessandro you have all been great *personages* in this adventure. You have all spread around leaving me alone with the Zibetto for a long time and that is not fair but I survived still as you can appreciate. I miss you all.

Acknowledgements

After the crew, the chief-in-command of this pirate italian boat in the southern bavarian see. To Gabriella my hearty thanks for being always there, stubborn and tough as a true chief: thanks for all the beers, the dinners, the late night semi-(very semi)-analitic discussions and all the rest which by the way was the best part.

Done with the munchener italians, I need to thank the other munchener ausslander, Aleksi, Yulia, Larry, Gabriela, for the nice time we spent together in these years. All our rainy barbecues were bit humid but great in the end. Thanks you all.

Thanks also to my office mates for allowing my smoky tobacco collection to be spread around and for their kindness and availability. Special thanks to Max and Stefan for the zusammenfassung of this Thesis.

In the end, I want to thank my italian polar stars. The ones that help me recognizing to be back home when in Italy: Rosita and Devid and Silvio. Keep it going like this, I need all of you.

Thanks to Grazia e Pasquale for making a revolution in their life each time we are getting closer to their place and also for letting their grand-nephew to destroy their sofas and to get all the somatics of his dad.

Last non least of this never-ending list, thanks to Leopoldo and Cristina for making all this possible.

Curriculum vitae

Personal Informations

First Name: Maurilio
Family Name: Pannella
Place of birth: Torino, Italy
Day of birth: 6 May 1970
Marital Status: Single
Nationality: Italian
Address: Max-Planck-Institut für Extraterrestrische Physik
Giessenbachstrasse D-85748
Garching b. München
Germany
Telephone: +49-89-30000-3770
Fax: +49-89-30000-3495
e-mail: maurilio@mpe.mpg.de
Research Area: Extragalactic Astronomy & Observational Cosmology

Education

September 2007 **Ph.D.** in Astronomy at the Ludwig Maximilian University of Munich, Thesis title:
Morphological evolution of galaxies over the last 8 Gyrs
Advisors: Prof. R. Bender, Dr. R.P. Saglia

Oct 2000 **Laurea** in Physics at the University “Federico II” of Naples
Thesis title: *Lyman- α emitters as tracers of the primeval Universe large scale structure*
Advisors: Prof. M.Cappaccioli, Dr. M.Arnaboldi.
Marks: 110 *cum laude*/110

Fellowships and Grants

- Sept 2005 to date** Research contract at the Max-Planck Institute for Extraterrestrial Physics, Garching
- Sept 2002 - Aug 2005** PhD fellowship of the *International Max-Planck Research School* (IMPRS) on Astrophysics
- Jan 2001 - Aug 2002** Research contract at the Astronomical Observatory of Capodimonte, Naples, in the VST Science Group

Schools

- September 2004** International Summer School “Data Analysis in Cosmology”, Valencia (Spain)
- September 2002 - March 2004** *International Max-Planck Research School on Astrophysics*, Garching (Germany)
- September 2002** Italian National School of Astrophysics: Cosmology and Relativistic Astrophysics, Asiago (Italy)
- September 2000** Italian National School of Astronomical Technologies, Astronomical Observatory of Capodimonte, Naples (Italy)

Conferences

- 2006** *Galaxies and Structures through Cosmic Times*, March 26-31, Venice, Italy; poster
MPE Dark Energy Meeting, February 27 - March 1, Ringberg Castle, Germany;
- 2005** *From Simulations to Surveys*, June 26 - July 1, Ringberg Castle, Germany; contributed talk
Stellar Populations, a Rosetta Stone for Galaxy Formation, July 4-8, Ringberg Castle, Germany;
The Origin of the Hubble Sequence, June 6-12, Vulcano Island, Italy; contributed talk

Talks

- 2006** Max-Planck Institute for Extraterrestrial Physics, Garching, Germany:
Bulges and Disks over the last 8 Gyrs, Jun 29
- 2005** “From Simulations to Surveys” conference, Ringberg Castle, Germany:
The contribution of bulges and disks to the stellar mass density evolution up to $z \sim 1$, Jun 27
“*The Origin of the Hubble Sequence*” conference, Vulcano Island, Italy:
Looking at the shaping of the Hubble fork up to $z \sim 1$, Jun 15
- 2003** Max-Planck Institute for Extraterrestrial Physics, Garching, Germany:
Intracluster Stellar Population properties from N-Body Cosmological Simulations, Feb 6

Other Professional Activities

- from 2006** Peer Reviewer for *Monthly Notices of the Royal Astronomical Society*
- 2005** Member of the Local Organizing Committee for the conference:
Stellar Populations, a Rosetta Stone for Galaxy Formation,
MPE Workshop dedicated to the 65th birthday of Alvio Renzini,
July 4-8, Ringberg Castle, Germany
- 1998** National Substitutive Service performed at the Social Services Office
of Carrara Town Hall, Italy
- 1996 - 1998** Hardware Responsible at the *G.P. Informatica sas*, Benevento, Italy

Observational & Technical Experience

Observing run	Observatory	Telescope/Instrument
4-6 March 2005	La Palma Observatory	3.5m TNG, DOLORES: optical spectroscopy (MOS)
19-21 May 2002	ESO-La Silla	3.5m NTT, EMMI: optical spectroscopy (MOS)
27-30 April 2001	ESO-La Silla	2.2m ESO/MPG, WFI: wide field imaging
20-22 April 2001 Phase II	ESO-La Silla ESO-Service Mode	3.5m NTT, EMMI: optical spectroscopy (MOS) WFI@2.2m and VIMOS_MOS@VLT
Telescope	Instrument	Reduction task
HST	ACS/WFPC2	Good experience with the MULTIDRIZZLE task
VLT	VIMOS imaging/MOS	Fair experience with the VIPGI reduction package
VLT	FORS imaging/MXU	Good experience with standard IRAF reduction packages
2.2m ESO	WFI imaging	Good experience with <i>mscred/MVM</i> -ESO pipeline
NTT	EMMI imaging/MOS	Good experience with standard IRAF reduction packages

Curriculum vitae

Publications

- 1 *Presence of dust with a UV bump in massive, star-forming galaxies at $1 < z < 2.5$,*
Noll, S., Pierini, D., **Pannella, M.**, Savaglio, S., 2007arXiv0707.0684N
- 2 *The supermassive black hole in NGC4486a detected with SINFONI at the VLT,*
Nowak, N., Saglia, R. P., Thomas, J., Bender, R., **Pannella, M.**,
Gebhardt, K., Davies, R. I., 2007arXiv0705.1758N
- 3 *The Galactic halo stellar density distribution from photometric survey data:
results of a pilot study,* Cignoni, M., Ripepi, V., Marconi, M., Alcal, J. M., Capaccioli, M.,
Pannella, M., Silvotti, R., 2007A&A...463..975C
- 4 *The Sizes of Galaxy Halos in Galaxy Cluster Abell 1689,*
Halkola, A., Seitz, S., **Pannella, M.**, 2007ApJ...656..739H
- 5 *The Evolution of Galaxy Dust Properties for $1 < z < 2.5$,*
Noll, Stefan, Pierini, Daniele, Pannella, Maurilio, Savaglio, Sandra, 2006astro.ph.12080N
- 6 *Parametric strong gravitational lensing analysis of Abell 1689,*
Halkola, A., Seitz, S., **Pannella, M.**, 2006MNRAS.372.1425H
- 7 *The Evolution of Galaxies in the FORS Deep and GOODS-S Fields,*
Drory, N., Bender, R., Feulner, G., Gabasch, A., Hopp, U., Noll, S.,
Pannella, M., Saglia, R. P., Salvato, M. 2006Msngr.125...15D
- 8 *The Evolution of the Mass Function Split by Morphology up to Redshift 1
in the FORS Deep and the GOODS-S Fields,* **Pannella, M.**, Hopp, U., Saglia, R. P.,
Bender, R., Drory, N., Salvato, M., Gabasch, A., Feulner, G., 2006ApJ...639L...1P
- 9 *The Stellar Mass Function of Galaxies to $z \approx 5$ in the FORS Deep and GOODS-South Fields,*
Drory, N., Salvato, M., Gabasch, A., Bender, R., Hopp, U., Feulner, G., **Pannella, M.**,
2005ApJ...619L.131D
- 10 *The Star Formation Rate History in the FORS Deep and GOODS-South Fields 2004,*
Gabasch, A., Salvato, M., Saglia, R. P., Bender, R., Hopp, U., Seitz, S., Feulner, G.,
Pannella, M., Drory, N., Schirmer, M., Erben, T., ApJ...616L..83G
- 11 *The Capodimonte Deep Field. Presentation of the survey and first follow-up studies,*
Alcal, J. M., **Pannella, M.**, Puddu, E., Radovich, M., Silvotti, et al., 2004A&A...428..339A

- 12 *Capodimonte Deep Field (Alcalá+, 2004),*
Alcalá, J. M., **Pannella, M.**, Puddu, E., Radovich, M., Silvotti, R., et al., 2004yCat..34280339A
- 13 *Intracluster Stellar Population Properties from N-Body Cosmological Simulations.
I. Constraints at $z = 0$,* Napolitano, Nicola R., **Pannella, Maurilio**, et al., 2003ApJ...594..172N
- 14 *CSL-1: chance projection effect or serendipitous discovery of a gravitational lens induced by a cosmic string?*, Sazhin, M., Longo, G., Capaccioli, M., Alcalá, J. M., Silvotti, R., Covone, G., Khovanskaya, O., Pavlov, M., **Pannella, M.**, Radovich, M., Testa, V., 2003MNRAS.343..353S
- 15 *Optical and near-infrared observations of the GRB020405 afterglow,*
Masetti, N., Palazzi, E., Pian, et al., 2003A&A...404..465M
- 16 *Narrowband Imaging in [O III] and Hα to Search for Intracluster Planetary Nebulae in the Virgo Cluster,* Arnaboldi, M., Freeman, K. C., Okamura, S., Yasuda, N., Gerhard, O., Napolitano, N. R., **Pannella, M.**, et al., 2003AJ....125..514A
- 17 *The Capodimonte Deep Field: research projects,*
Capaccioli, M., Alcalá, J. M., Radovich, M., Silvotti, R., **Pannella, M.**, Arnaboldi, M., Puddu, E., et al., 2003MmSAI..74..452C
- 18 *Data reduction and astrometry strategies for wide-field images:
an application to the Capodimonte Deep Field,* Alcalá, J. M., Radovich, M., Silvotti, R., **Pannella, M.**, et al. 2002SPIE.4836..406A
- 19 *Candidates for Intracluster Planetary Nebulae in the Virgo Cluster based on the Suprime-Cam Narrow-Band Imaging in [OIII] and Hα,*
Okamura, Sadanori, Yasuda, Naoki, et al., PASJ...54..883O
- 20 *A Ks-band selected galaxy sample in GOODS-S*
M. Salvato, A. Gabasch, N. Drory, G. Feulner, U. Hopp,
M. Pannella, A. Rau, S. Seitz, R. Bender, A&A submitted
- 21 *A deep galaxy catalogue in the COSMOS field*
A. Gabasch, Y. Goranova , U. Hopp, S. Noll, **M. Pannella**, MNRAS submitted
- 22 *Bulges and disks in the COSMOS during the last 8 Gyrs*
M. Pannella, A. Gabasch , Y. Goranova, N. Drory, U. Hopp, S. Noll, R.P. Saglia, R. Bender, A&A submitted